Laser-Driven Soft-X-Ray Undulator Source

Matthias Fuchs

Ludwig-Maximilians-Universität München

August 2010

Matthias Fuchs

Laser-Driven Soft-X-Ray Undulator Source

Matthias Fuchs

Dissertation
an der Fakultät für Physik
der Ludwig–Maximilians–Universität
München

vorgelegt von
Matthias Fuchs
aus Ellwangen/Jagst

München, den 04. August 2010

Erstgutachter: Prof. Dr. Florian Grüner
Zweitgutachter: Prof. Dr. Toshiki Tajima
Tag der mündlichen Prüfung: 21. September 2010

INTRODUCTION AND ABSTRACT

In order to put the results presented in this thesis into context, a short introduction is given at this point. A brief summary of the experimental results is given on page (iii).

The discovery of X-ray radiation has shed light on unexplored territories in almost all disciplines of science, ranging from chemistry, biology, physics, materials science and medicine to industrial applications. A wavelength in the Ångström range (10^{-10} m) and thus on the order of chemical bond lengths enables the radiation to resolve matter on the atomic scale. In order to simultaneously gain temporal insight into dynamics on the atomic scale, X-ray pulses with durations on the picosecond to femtosecond scale are required.

The most powerful sources capable of delivering such pulses are based on synchrotron radiation. Here, a magnetic field deflects a pulse of ultra-relativistic electrons in a direction transverse to its propagation. As a result of this acceleration, the electrons emit bursts of highly-directed synchrotron radiation.

Synchrotrons are well established facilities with excellent control over the beam parameters. The discovery of synchrotron radiation goes back into the 1940s [Elder et al., 1947]. Persistent research and a growing user community led the development from parasitic operation at high-energy accelerator facilities to dedicated high-brilliance (third generation) X-ray sources. Brilliance is a measure for the flux, focusability and transverse coherence of the radiation. The increase in brilliance has been due to both the improvement of the electron beam in terms of emittance and pulse duration as well as the evolution of the magnetic structures from bending magnets to more sophisticated insertion devices such as undulators or wigglers. The pulse duration of the X-ray emission is mainly given by that of the electron beam and is on the order of 100 ps for standard third generation synchrotron sources based on storage rings. It can reach the sub picosecond scale only with sophisticated techniques [Khan et al., 2006] and a significant loss in photon flux. The development of sources emitting more brilliant beams has recently culminated with the impressive demonstration of the world's first X-ray free-electron laser (FEL) [Emma, 2009]. FELs emit pulses of coherent radiation with significantly shorter duration than typical synchrotrons which increases the brilliance by more than six orders of magnitude. However, both of these sources are based on kilometer-scale radio-frequency accelerators, which makes them extremely costly and therefore only a few facilities exist worldwide. This means that they cannot completely serve the large user community.

In 1979, Tajima and Dawson laid the theoretical foundation for a new generation of compact particle accelerators [Tajima and Dawson, 1979]. In this scheme a laser pulse with an intensity on the order of $10^{18}\,\mathrm{W/cm^2}$ and a pulse duration of half the plasma wavelength (typically a few tens of femtoseconds) is focused into a plasma where it excites a plasma wave. The wave trails the laser pulse at its group velocity and generates accelerating electric fields which exceed the strength of those in conventional accelerators by more than three orders of magnitude. Either background plasma electrons or externally injected electrons can get trapped by these fields and – by "surfing" them – get accelerated to GeV-scale energies over distances of only a few centimeters.

However, this scheme relies on laser pulses with ultra-high intensities. Therefore, the field of laser-wakefield acceleration is very strongly dependent on advances in laser technology. Only the invention of the chirped-pulse amplification (CPA) 1985 [Strickland and Mourou, 1985] made it possible to generate laser pulses with a sufficiently high intensity. It took until the mid-1990s for lasers to become mature enough to be used as drivers allowing for wakefield-acceleration first for externally injected electrons ([Clayton et al., 1993], [Nakajima et al., 1995]), followed soon after by the acceleration of self-injected electrons [Modena et al., 1995]. In these early experiments, the thermally shaped electron spectra showed a high-energy cutoff at a few tens of MeV. The experimental developments were supported by advances in the theoretical description such as analytical models of nonlinear waves, acceleration of electrons in these waves and nonlinear evolution mechanisms for ultra-intense laser pulses in plasmas (see [Esarey et al., 1996] and references therein).

Developments in laser technology led to a decrease in pulse duration from the picosecond to the tens of femtoseconds range, while still maintaing the pulse energy and thus increasing the peak intensity. The application of such laser pulses for wakefield-acceleration resulted in a further increase in the accelerating gradient to reach 200 MV/m and extended the high-energy cutoff of the (still thermal) electron spectra to 200 MeV [Malka et al., 2002]. Meanwhile computational power became large enough to perform 3D simulations including the highly non-linear evolution of the plasma and the laser pulse which led to a deeper understanding of the processes that occur during the acceleration. 3D particle-in-cell (PIC) simuations (see for example [Dawson, 1983]) led to the discovery of a new acceleration scheme: the "bubble regime" [Pukhov and Meyer-ter Vehn, 2002], which predicted the production of quasi-monoenergetic electron beams.

In the experiments described above, electrons were accelerated in the self-modulated regime (for self-modulation, see section 2.6.4), which means that the laser pulse is longer than a plasma period. Parts of the laser pulse are interacting with the accelerated electron bunch which leads to thermal energy spectra. The development of laser pulses with ultra-high intensities and durations shorter than the plasma period resulted in 2004 in the acceleration of quasi-monoenergetic electron beams with energies of a few hundred MeV and $\sim 100\,\mathrm{pC}$ of charge [Faure et al., 2004], [Geddes et al., 2004], [Mangles et al., 2004]. Although the laser intensities in these experiments were technically not high enough to operate in the bubble regime, PIC simulations showed that the laser undergoes nonlinear processes. While propagating through the plasma these processes significantly increase the laser intensity allowing a pulse with an initially insufficient in-

tensity to drive an acceleration in the bubble regime. In 2006, electron beams of energies of 1 GeV were demonstrated using acceleration distances of only 3 cm [Leemans et al., 2006]. The shot-to-shot reproducibility of LWFA beams has increased in recent years through careful control over various parameters of the laser pulse [Mangles et al., 2007] or the gas target. One such control is the steady-state-flow gas cell scheme [Osterhoff et al., 2008], which is used as the driver for the experiments described in this thesis. New injection schemes ([Faure et al., 2006], [Geddes et al., 2008]) have the potential to further increase the stability as well as to significantly improve the electron beam quality. If sufficiently high beam qualities and staging of several acceleration sections can be shown, laser-wakefield accelerators could be potential candidates to drive future ultra-high-energy particle colliders [Schroeder et al., 2009], [Tajima, 2010]

The experimental results described in this thesis demonstrate the successful synergy between the research fields described above: the development of an undulator source driven by laser-plasma accelerated electron beams. First efforts in this new field have led to the production of radiation in the visible to infrared part of the electromagnetic spectrum [Schlenvoigt et al., 2008]. In contrast to these early achievements, the experiment described here shows the successful production of laser-driven undulator radiation in the soft-X-ray range with a remarkable reproducibility. The source produced tunable, collimated beams with a wavelength of $\sim 17\,\mathrm{nm}$ from a compact setup. Undulator spectra were detected in $\sim 70\%$ of consecutive driver-laser shots, which is a remarkable reproducibility for a first proof-of-concept demonstration using ultra-high intensity laser systems. This can be attributed to a stable electron acceleration scheme as well as to the first application of miniature magnetic quadrupole lenses with laser-accelerated beams. The lenses significantly reduce the electron beam divergence and its angular shot-to-shot fluctuations

The setup of this experiment is the foundation of potential university-laboratory-sized, highly-brilliant hard X-ray sources. By increasing the electron energy to about 1 GeV, X-ray pulses with an expected duration of $\sim 10\,\mathrm{fs}$ and a photon energy of 1 keV could be produced in an almost identical arrangement. It can also be used as a testbed for the development of a free-electron laser of significantly smaller dimension than facilities based on conventional accelerators [Gruener et al., 2007]. Such compact sources have the potential for application in many fields of science. In addition, these developments could lead to ideal sources for ultrafast pump-probe experiments due to the perfect synchronization of the X-ray beam to the driver laser.

ZUSAMMENFASSUNG

Röntgenstrahlung ist aus den heutigen Disziplinen der Wissenschaft und Technik nicht mehr wegzudenken. Seit ihrer Entdeckung Ende des 19. Jahrhunderts werden Röntgenquellen ständig zur Erzeugung immer brillanterer Strahlung weiterentwickelt. Brillanz ist dabei ein Mass der Photonenanzahl in einem bestimmten Wellenlängenbereich, der Quellgrösse und der Divergenz des Strahls.

Solch hochbrillante, durchstimmbare Röntgenstrahlung wird typischerweise von Synchrotronquellen erzeugt. Eine Synchrotronquelle besteht zum Einen aus einem Beschleuniger, der Elektronen auf relativistische Energien beschleunigt. Zum Anderen besteht sie aus einer periodischen magnetischen Struktur, genannt Undulator, die die Elektronen auf eine sinusförmige Trajektorie zwingt. Aufgrund der dadurch auftretenden Beschleunigungen emittieren die Elektronen Röntgenlicht in Form von Synchrotronstrahlung. Nachteil dieser Synchrotronquellen sind allerdings die kilometergrossen und sehr teuren Anlagen, die zur Elektronenbeschleunigung benötigt werden.

Ein neuartiger Teilchenbeschleuniger hat kürzlich nach über dreissig jährigen Forschung hoch-relativistische, quasi-monoenergetischen Elektronenpulsen über eine Beschleunigungsstrecke von nur wenigen Millimetern erzeugt. Diese neue Methode der Laserwakefield Beschleunigung basiert auf hochintensiven Laserpulsen im Tera-Watt Leistungsbereich, die in ein Gas fokussiert werden. Dabei werden die Gasatome ionisiert und es entsteht ein Plasma. Während der Laser durch dieses Plasma propagiert, regt er eine sogenannte Plasmawelle (eine Welle aus Elektronen) an, die dem Puls, ähnlich einer Wasserwelle einem Boot, hinterherläuft. Elektronen können nun auf dieser Plasmawelle "surfen" und auf hochrelativistische Energien beschleunigt werden.

Die Kombination dieser kompakten Beschleunigertypen mit einem Undulator, könnte eine kompakte Röntgenquelle erzeugen, die sogar in kleineren Laboren Platz finden kann. Die Experimente, die in dieser Dissertation beschrieben werden, stellen einen Meilenstein auf dem Weg dorthin dar: die reproduzierbare Messung von weicher Röntgenstrahlung emittiert von einer Undulatorquelle, die von laser-wakefield beschleunigten Elektronen getrieben wird. Der Hauptteil der Strahlung wird bei einem Wellenlängenbereich um 17 nm gemessen, der sich bis zu 7 nm erstreckt. Für ein Experiment, das von einem Hochleistungslaser getrieben wird, stellen spektral aufgelöste Strahlung in 70% aufeinanderfolgender Laserschüsse eine bemerkenswerte Stabilität dar. Die emittierte Strahlung soll aufgrund der voraussichtlichen Elektronenstrahlparametern eine Pulsdauern von nur 10 fs haben. Da zusätzlich der Laser perfekt zu dieser Strahlung synchronisiert ist, erfüllt eine solche Quelle mit Strahlung im harten Röntgenbereich alle Vorraussetzungen für pump-probe Experimente auf der atomaren Skala. Das Experiment, das hier beschrieben wird stellt den Grundstein für künftige Entwicklungen von Quellen im harten Röntgenbereich dar.

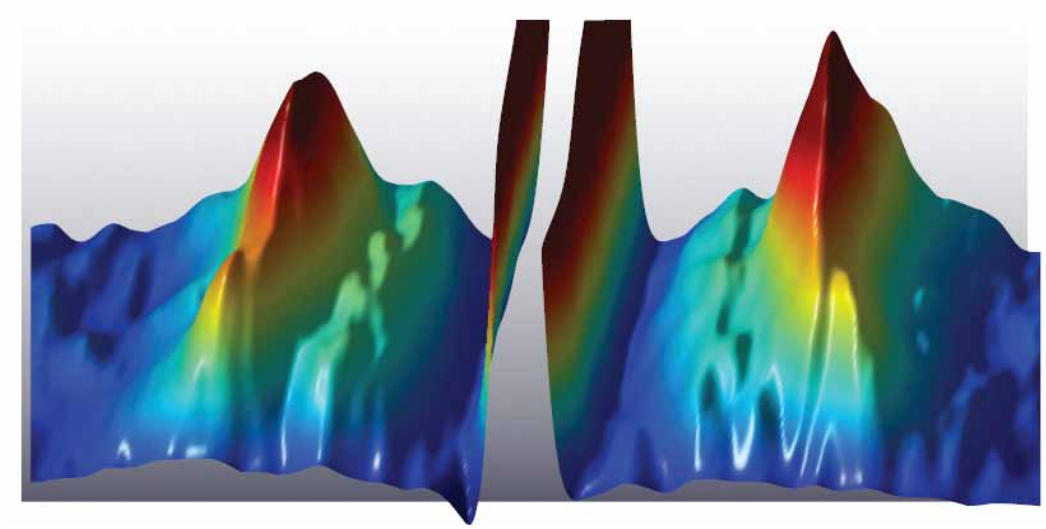

3D representation of a typical detected undulator spectrum.
The undulator radiation is spectrally resolved by a transmission grating and shows a zeroth (transmitted light) and a positive and negative first diffraction order (left/right). In each diffraction order the undulator fundamental and second harmonic peak can be seen.

Contents

1. OVERVIEW AND OUTLINE

The experiment presented in this thesis is a synergy of several different research fields. It is based on recent experimental successes in the field of laser-wakefield acceleration and on the highly-developed research fields of conventional electron acceleration and the synchrotron radiation community. Under this consideration, the thesis is structured as follows:

The relevant theoretical foundation is presented in chapters 2-4.

The experimental setups and results are described and discussed in chapters 5 & 6

In chapter 7, the experimental results are put into context and a brief overview of future developments is given.

Chapter 2 gives an overview of the theory of laser-wakefield acceleration (LWFA). The basic physics of plasma waves, their properties and how they can be harnessed for electron acceleration is briefly discussed. Current experimental results can be best explained by an acceleration in the highly non-linear "bubble" regime. So far, this regime can be mostly only described by intensive computer simulations. Analytical descriptions are subject to present research and the theory of this regime is not yet fully represented in textbooks. Therefore, a more detailed discussion of the current theoretical developments and results are given in this chapter. Additionally, a brief overview of properties of state-of-the art laser-wakefield accelerators and possible future developments is given.

Chapter 3 discusses the theory of undulator radiation. Since this is a highly-developed field, the physical processes can be described by precise analytical theories which are comprehensively covered in many textbooks. Thus, this part is only discussed very briefly. However, parts of the theoretical description that are necessary to explain the experimental findings of this thesis (which are not extensively covered in textbooks) are discussed in more detail.

Chapter 4 gives a brief overview of the theory of free-electron lasers (FELs) to the extend that the reader can appreciate possible future developments based on the experimental results presented in this thesis.

Chapter 5 describes the laser-wakefield accelerator which was used as a driver. Since the accelerator is still in an experimental status itself, details to its setup and the experimental finding are given to the extend in which the properties of the undulator source are concerned.

Chapter 6 describes the experimental observation of soft-X-ray undulator radiation from a laser-wakefield-driven undulator source. Besides the experimental setup,

simulations of undulator radiation that were necessary to explain the experimental findings are discussed in detail. The experimental results are compared to simulations and to observations of radiation from modified setups in order to gain further insights into the underlying physical processes. The undulator as a diagnostic tool is briefly discussed.

Chapter 7 puts the experimental results into context with conventional state-of-the art sources. It discusses future progress and potential properties of short to long-term developments.

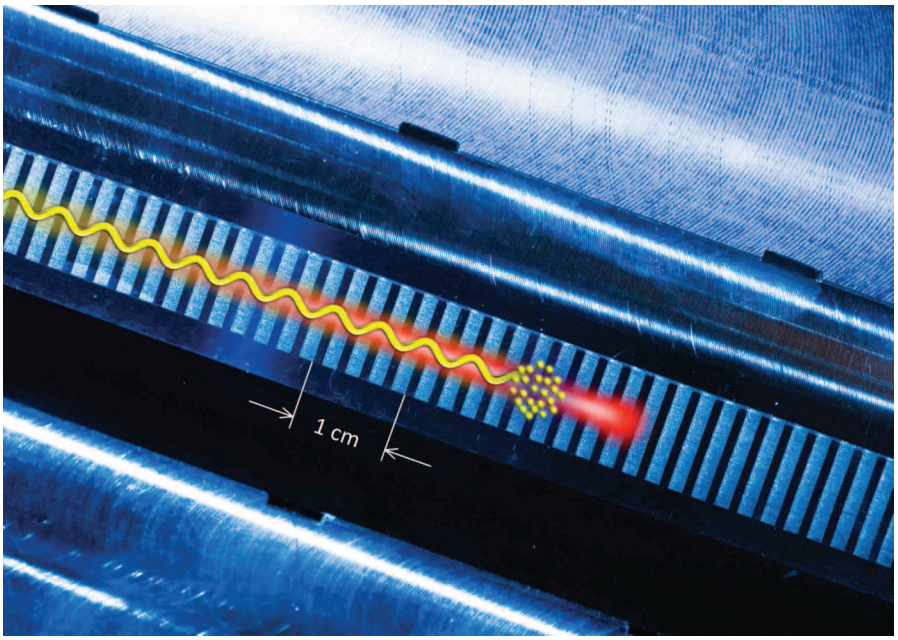

Artist's rendering of an electron bunch in an undulator.
Highly-relativistic electrons (yellow) are forced on sinusoidal trajectory by the periodic magnetic field of an undulator. As a result they emit short-wavelength radiation (red). Courtesy T. Naeser and C. Hackenberger.

2. LASER-WAKEFIELD ACCELERATION OF ELECTRONS

2.1. Introduction

The chapter discusses the physics of laser-wakefield acceleration (LWFA) of electrons. In this scheme, an ultra-short laser pulse with an ultra-high intensity is focused into a plasma, where it induces electron oscillations. Along the laser propagation direction, these excitation of longitudinal electron oscillation lead to a resonant collective electron oscillation: a plasma wave that is trailing the laser pulse at its group velocity. The wave produces strong electric fields with a longitudinal (accelerating) component, similar to a traveling wave in radio-frequency (RF) cavities. Whereas the maximum accelerating gradient of an RF-cavity is limited by the breakdown of the material to $\sim 100\,\mathrm{MV/m}$, the plasma can sustain significantly larger fields. Owing to its collective behavior, the electric field produced by the wave are approximately three orders of magnitudes larger than those in conventional accelerators. Electrons can be either self-injected or injected externally and can get accelerated to highly-relativistic energies within distances of a few centimeters. In addition to its compact dimensions, laser-wakefield accelerators are expected to emit electron bunches with intrinsically short bunch durations ($\sim 10\,\mathrm{fs}$).

This chapter is structured as follows:

- Section 2.3 covers a brief description about the plasma fundamentals necessary for the rest of the chapter. More detailed discussions of plasma physics are covered in numerous textbooks, for example see [Chen, 1984] or [Goldston and Rutherford, 1995].

- The basic physics of laser-wakefield accelerators is explained by the discussion of the generation and properties of linear plasma waves (section 2.4). The sections about laser-driven plasma waves are mainly based on the excellent reviews in [Esarey et al., 2009], [Gibbon, 2005] and [Tajima, 1985].

- Section 2.5 discusses the physics of nonlinear plasma waves which describes the plasma response for the laser parameters more closely to those used in the experiment presented below.

- It is followed by a discussion about the trapping of electrons by the plasma wave and the subsequent acceleration process as well as its limits (section 2.6).

- A list of nonlinear effects that dictate the laser evolution in the plasma is given in section 2.6.4.
- The experimental results of the electron beams used in this thesis are best described by the physics of the so-called "bubble regime". A comprehensive theory of this acceleration scheme is still subject to research and is not yet fully represented in textbooks. Therefore, a more detailed discussion is presented in section 2.6.5.
- The chapter ends with a list of state-of-the art experimental results and in the outlook near-term future projects are briefly discussed.

2.2. Overview: The Different Wakefield Regimes

Linear wakefields
Non-linear wakefields
The bubble regime

A laser-wakefield accelerator (LWFA) can be operated in different regimes depending on the intensity of the driver laser pulse. The laser pulse intensity is determined by its duration, pulse energy and the focusing geometry. Depending on the intensity, the laser causes different plasma responses: Laser pulses with a lower intensity (non- to mildly-relativistic) excite a linear plasma wave which is a sinusoidal plasma density perturbation that produces a sinusoidal electric wakefield (see section 2.4.1). For pulses with higher (relativistic) intensities, the structure of the plasma waves changes to a non-linear, spiked shape with more distinct and longer troughs and an increased (nonlinear) plasma wavelength (see section 2.5). The compression of the plasma density in the spikes causes the wakefield to longitudinally change to a "sawtooth-like" shape and to produce higher accelerating fields. Laser pulses with intensities well above the relativistic limit drive a highly non-linear plasma wave, where wavebreaking occurs immediately after the first plasma oscillation. This washes out all the downstream structure after the first plasma period, leaving behind an electron-free ionic cavity (called "bubble") which trails the laser through the plasma as a soliton-like stable structure (see section 2.6.5).
While propagating in plasma, the laser can undergo non-linear effects which can significantly alter its shape and intensity (see section 2.6.4). This evolution of the laser pulse can lead to a transition between LWFA regimes or into a mixture of several regimes.

2.3. Fundamentals

Calculation methods of plasma waves
Normalized laser intensity
The ponderomotive force
The plasma frequency
Laser propagation in plasmas

This section briefly describes the underlying fundamental definitions and processes relevant to laser-wakefield acceleration.

2.3.1. Calculation Methods

The exact calculation of laser-driven plasma wakefields is non-trivial because it requires a self-consistent approach for the computation of the wakefields, the laser fields and the particles. Therefore, analytical solutions exist only for non-evolving laser pulses in 3D for linear plasma waves and in 1D for the nonlinear case. In order to solve the 3D nonlinear problem, usually numerical codes are required and the full 3D case (nonlinear including the evolution of the laser pulse), can only be calculated by extensive simulations (see section 2.6.5).

2.3.2. Description of Laser Pulses

Most physical quantities that describe a plasma wakefield driven by a laser can be related to the intensity of the laser pulse. The most practical way to describe the intensity in LWFA theory is through the laser strength parameter $\vec{a}$ which is defined by the vector potential $\vec{A}$ of the laser, normalized by the electron rest mass energy $m_e c^2$ as:

$$\vec{a} = \frac{e\vec{A}}{m_e c^2} \tag{2.1}$$

In these normalized units, the intensity of a Gaussian laser pulse can be written as

$$a^2 = a_0^2 \exp\left(-\frac{2r^2}{r_s^2}\right) \sin^2\left(\frac{\pi z}{L}\right), \tag{2.2}$$

where r is the transverse and z the longitudinal dimension, r_s the laser spot size and L is the pulse length. The amplitude a_0 is given in practical units by

$$a_0 \simeq \lambda[\mu\mathrm{m}] \cdot \sqrt{\frac{I_0[\mathrm{W/cm^2}]}{1.4 \times 10^{18}}}, \tag{2.3}$$

with the laser wavelength λ and the peak laser intensity I_0. As discussed in the next section, a_0 is a measure for the energy gain of an electron quivering in a laser field: $a_0 = 1$ marks the transition from sub-relativistic kinetics ($a_0 \ll 1$) into the relativistic regime $a_0 \gtrsim 1$.

2.3.3. Laser-Matter Interaction

The Ponderomotive Force

The interaction of an electron with a plane, non-relativistic, electromagnetic wave results in a harmonic oscillatory motion of the electron, since the restoring force of the field is linear. In a tightly focused (and hence non-planar) ultrashort laser pulse however, the light field varies temporally as well as radially. An electron that is placed in such an inhomogeneous electromagnetic field experiences a nonlinear force which is called the ponderomotive force:

$$\vec{F}_p = -\frac{1}{4}\frac{e^2}{m_e\omega^2}\vec{\nabla}\vec{E}^2 = -m_e c^2\vec{\nabla}\left(\frac{a^2}{2}\right). \tag{2.4}$$

The ponderomotive force is directed such that charged particles are expelled from higher towards lower intensity regions of the laser pulse which is indicated by the $\vec{\nabla}\vec{E}^2$-term in eq (2.4). For a derivation of the ponderomotive force, see the Appendix, section A.1. The ponderomotive potential ($\vec{F}_p = \vec{\nabla}U_p$) equals the average kinetic energy E_{kin} that an electron gains within one oscillation period. In terms of a_0, this can be written as

$$\langle E_{\text{kin}}\rangle = U_p = \frac{a_0^2}{2}m_e c^2. \tag{2.5}$$

It can be seen that for $a_0 \gtrsim 1$, the particle quivering in the field of the laser pulse gains energy comparable to its rest energy $m_e c^2$ and has to be treated relativistically.

2.3.4. Plasmas

Plasma frequency
Plasma wavelength

A plasma is an ionized gas of positively charged ions and free, negatively charged electrons. A slight displacement of a group of electrons from their equilibrium position creates regions of net negative charge and regions of net positive charge. Such a non-uniform charge distribution produces an electric field which accelerates the electrons in the direction opposite to their displacement. When the electrons arrive at the equilibrium position, they have gained a kinetic energy equal to the potential energy of their initial displacement and overshoot. Owing to their much larger mass compared to electrons, the ions remain essentially stationary on these time-scales. This sets up an oscillation similar to a harmonic oscillator with the plasma frequency

$$\omega_{p,e} = \sqrt{\frac{4\pi e^2 n_0}{\langle\gamma\rangle m_e}}, \tag{2.6}$$

where n_0 is the electron density and m_e the electron rest mass and $\langle\gamma\rangle$ the relativistic factor averaged locally over many electrons. The plasma wavelength is defined as

$$\lambda_p = \frac{2\pi c}{\omega_p}. \tag{2.7}$$

2.3.5. Laser Propagation in Plasmas

Dispersion relation
Laser phase velocity
Laser group velocity

The propagation of an electromagnetic wave with an angular frequency on the order of the plasma frequency $\omega \simeq \omega_p$ in plasma can be described by the dispersion relation which is given by (for a derivation, see Appendix, section A.1.1):

$$\omega^2 = \omega_p^2 + c^2 k^2, \tag{2.8}$$

where $k = 2\pi/\lambda$ is the wave number of the electromagnetic wave and c the vacuum speed of light. The implication of equation (2.8) is that only waves with frequencies $\omega > \omega_p$ can propagate in plasmas, for which the plasma electron response is too slow to shield the electro-magnetic field of the laser inside the plasma. For $\omega < \omega_p$, the plasma density is overcritical which means that the electromagnetic wave gets either reflected or attenuated. Thus, an electromagnetic field of frequency ω can propagate in matter with a density below the critical density which can be calculated by setting $\omega = \omega_p$ and rewriting 2.6 as

$$n_{\text{crit}} = \frac{\langle\gamma\rangle m_e \omega^2}{4\pi e^2} \tag{2.9}$$

The plasma index of refraction η can be calculated from the dispersion relation (see Appendix, section A.1.1) and reads:

$$\eta = \sqrt{1 - \left(\frac{\omega_p}{\omega}\right)^2}. \tag{2.10}$$

It is related to the phase velocity v_{ph} and the group velocity v_{g} as follows:

$$v_{\text{ph}} = \frac{\omega}{k} = \frac{c}{\eta} \tag{2.11}$$

$$v_{\text{g}} = \frac{\mathrm{d}\omega}{\mathrm{d}k} = \eta \cdot c \tag{2.12}$$

2.4. Generation of Plasma Waves by Laser Pulses

Physical picture of plasma wave generation
Linear plasma waves

Electromagnetic pulses with a sufficiently high intensity can excite longitudinal plasma waves in underdense plasmas as their ponderomotive force expels electrons into regions of lower light intensities. For a short Gaussian laser pulse the plasma electrons are pushed transverse and forward by the head of the laser pulse and backwards by the tail,

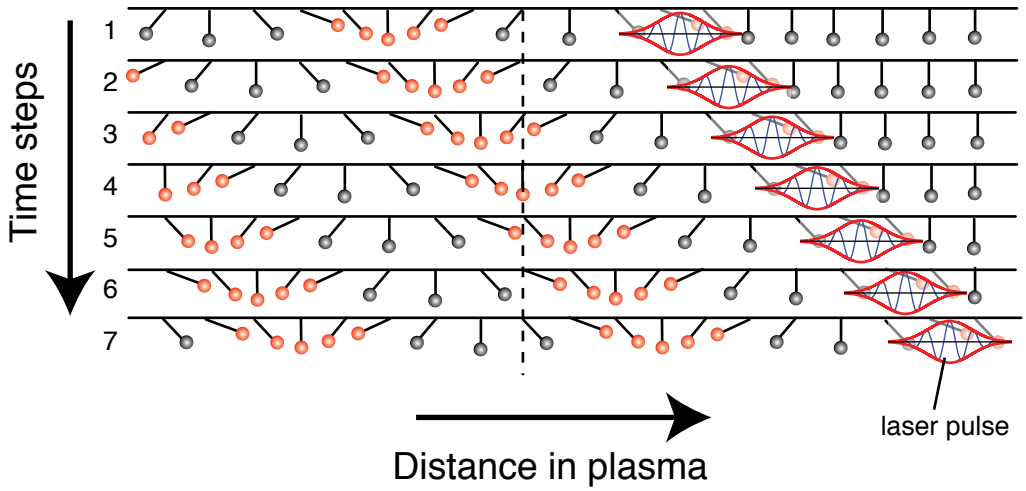

Figure 2.1. | Excitation of a longitudinal electron density wave in a plasma by a laser pulse. The figure shows a cartoon of the excitation of a plasma wave through a laser pulse. The vertical axis are time steps and the horizontal axis is the distance of the plasma in the laser propagation direction. The ponderomotive force of a laser propagating in a plasma from left to the right displaces electrons from their initial position. The stationary ion background pulls back the electron which starts to oscillate with the plasma frequency. The laser displaces the electrons (each displayed as a pendulum) in such a way that their collective motion resembles a density wave moving to the right (red dots). From the time evolution of a single electron (along the vertical dashed line), it can be seen that the electron oscillate around their initial position. It can be seen that although no matter is transported, a plasma wave with an electric accelerating field (wakefield) is trailing the laser at its group velocity. Figure based on [Dawson, 1989].

leaving behind the heavier (and for the relevant timescales inertial) ions. After the laser pulse has passed, the space-charge forces between the static ions and the electrons pull back the electrons so that they overshoot and start a longitudinal plasma oscillation. Each electron oscillates like a pendulum about its initial position. The ponderomotive force of the laser drives the electrons in phase, such that the superposition of many such pendulums generates a collective moving density perturbation (see figure 2.1). Laser pulses with a duration on the order of the plasma wavelength λ_p can thereby resonantly set up a large-amplitude plasma wave which, owing to the excitation process, trails the pulse at the group velocity of the laser. The longitudinal (accelerating) field component produced by this plasma wave follows the laser pulse and, in analogy to a the wake produced by a ship on a lake, are called wakefields. External or plasma electrons can be injected into these large fields where they are rapidly accelerated.

2.4.1. Linear Plasma Waves

Calculation of linear plasma waves
Longitudinal and transverse wakefields
Non-relativisitic wavebreaking limit

Linear plasma waves are generated by a driver laser that does not have relativistic intensities ($a_0 \ll 1$). In order to calculate the plasma response for a non-evolving laser pulse, solutions in 3D can be found by solving the linearized fluid equations: i.e. an initial background with a small perturbation is assumed (for example for the plasma density $n_0 + \delta n$, where $\delta n \ll n_0$). The linearized cold, non-relativistic fluid equations can be written as (see for example [Ruth et al., 1985]):

the continuity equation

$$\frac{\partial}{\partial t}\delta n + n_0 \vec{\nabla} \cdot \vec{u} \simeq 0, \tag{2.13}$$

the fluid momentum equation

$$\frac{\partial \vec{u}}{\partial t} \simeq \nabla\phi - \nabla a_0^2/2, \tag{2.14}$$

and Poisson's equation

$$\nabla^2\phi \simeq k_p^2 \frac{\delta n}{n_0}, \tag{2.15}$$

where n_0 is the initial plasma density, $\delta n = n - n_0$ the density perturbation, $\vec{u}$ the velocity of the perturbation, $\phi = e\Phi/(m_e c^2)$ the normalized electrostatic potential and $k_p = 2\pi/\lambda_p$ the plasma wave number. Solving eqs. (2.13), (2.14) and (2.15) for a Gaussian laser pulse (see Appendix, section A.1.2) leads to a normalized plasma density perturbation of

$$\frac{\delta n}{n_0} = -\frac{\pi}{4}\frac{a_0^2}{2}\left[1 + \frac{8}{k_p^2 r_s^2}\left(1 - \frac{2r^2}{r_s^2}\right)\right]\exp\left(-\frac{2r^2}{r_s^2}\right)\sin\left[k_p(z-ct)\right] \tag{2.16}$$

and the longitudinal electric field produced by the wake

$$E_z = -\frac{\pi}{4}\frac{m_e c\,\omega_p}{e}\frac{a_0^2}{2}\exp\left(-\frac{2r^2}{r_s^2}\right)\cos\left[k_p(z-ct)\right], \tag{2.17}$$

where r_s is the laser spot size. It can be seen that the linear plasma wave is a simple sinusoidal density perturbation associated with a sinusoidal electric field with a wavelength of λ_p, and a phase velocity v_p which is approximately the group velocity of the laser $v_g \simeq c$. Electrons injected into such a structure cannot only get longitudinally accelerated but are also transversely confined since a plasma wave also produces transverse wakefields.

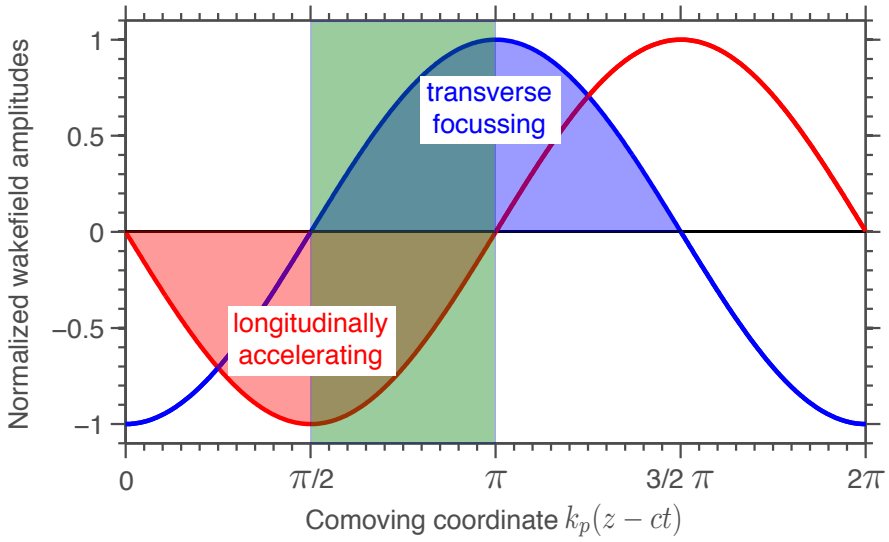

Figure 2.2. | **Normalized nonrelativistic longitudinal and transverse wakefields.** The normalized longitudinal (blue) and transverse (red) wakefield amplitude in the nonrelativistic case is plotted versus the plasma wave phase ξ. The value for the transverse wakefield amplitude is taken off-axis ($r > 0$). For electrons, a negative longitudinal field corresponds to an accelerating force, and a positive transverse field corresponds to a radially focusing force (in direction $-r$, see eqs 2.17 & 2.18). The shaded green area spans a $\lambda_p/4$-phase region of the wakefield which is both longitudinally accelerating as well as transverse focusing.

The transverse focusing force can be calculated by the Panofsky-Wenzel theorem [Panofsky and Wenzel, 1956] (which relates the axial and the transverse electromagnetic forces of a wakefield) and the transverse wakefield reads

$$W_r \sim \frac{4r}{k_p r_s^2} \exp\left(\frac{-2r^2}{r_s^2}\right) \sin\left[k_p(z-ct)\right]. \tag{2.18}$$

Both the longitudinal and the transverse fields can be seen in figure 2.2.

Properties of linear wakefields

Eqs.(2.17 & 2.18) already describe many properties unique to plasma accelerators:

The **maximum electric field** that a linear plasma wave will sustain can be estimated by assuming that all plasma electrons oscillate with the plasma frequency ω_p. Solving the linear Poisson's equation (eq. (2.15)), assuming $\delta n = n_0$ (i.e. a maximum density modulation), results in the cold, *non-relativistic* wavebreaking amplitude

$$E_0 = \frac{m_e c\, \omega_p}{e} \tag{2.19}$$

or in practical units

$$E_0[\mathrm{V/m}] \simeq 96\sqrt{n_0[\mathrm{cm}^{-3}]}, \tag{2.20}$$

which for typical densities of $n_0 = 5 \times 10^{18}$ is on the order of 200 GV/m.

Intrinsically, a **low emittance** is expected from the simple estimation (which is strictly only valid for mono-energetic electron bunches) that at the exit of the plasma accelerator the emittance ϵ can be calculated by the product of the electron beam size $\sigma_{x,y}$ and its divergence $\sigma'_{x,y}$. The electron beam size is estimated to be a fraction of the transverse wakefield dimensions which are on the order of the laser spot spot radii r_s [see eq.(2.17)]. In our case, typical laser foci are $\simeq$20 μm and from simulations electron beam sizes are expected to be $\simeq 2\mu$m. The electron beam divergence can be experimentally readily determined and it is measured to be 1 mrad (rms) for a 200 MeV electron beam [Osterhoff et al., 2008] which results in a normalized emittance of $\epsilon_n = \gamma\beta \cdot \epsilon \simeq 0.8\,\mathrm{mm\,mrad}$.
The transverse focusing forces [eq.(2.18] are zero on-axis and increase radially approximately linearly for a distance of $r \lesssim r_s/4$. The (maximum) on-axis field amplitude depends on the longitudinal distance to the laser pulse ξ, and for electrons changes from focusing to defocusing after an advance of a distance $\lambda_p/2$. Owing to the linearity of the transverse fields, the normalized emittance of the accelerated electron beam is preserved.

The **electron bunch length** is intrinsically only a fraction of one period of the accelerating structure which from equation (2.17) is shown to be on the order of the plasma wavelength λ_p. High-quality electron bunches indicate that they were accelerated in a region with linear longitudinal and transversely focusing fields, which, due to the phase shift of a factor of $\pi/2$ of the fields is only the case over a distance of $\lambda_p/4$. For the plasma densities used in the experiment described below, $\lambda_p \simeq 15\,\mu\mathrm{m}$ which gives an estimated upper limit for the electron bunch duration of only a few tens femtoseconds.

2.5. Nonlinear Plasma Waves

Calculation of nonlinear plasma waves
Quasi-static approximation (QSA)
Non-linear plasma wavelength
Maximum non-linear wakefield amplitude for a given driver

Plasma waves that are driven by laser pulses with sufficiently high intensities become nonlinear. For intensities of $a_0 > 1$, the quiver velocity of the electrons in the laser field becomes relativistic which also influences the shape of the plasma wave: it is no longer sinusoidal, but its waveform steepens and the plasma wavelength increases. In comparison to the linear case, this leads to larger electric fields that the wave can sustain, in which electrons can get accelerated to substantially higher energies. Nonlinear plasma waves can analytically only be calculated in 1D (corresponding to a transversely infinitely extended laser beam size) using the quasi-static approximation (QSA) [Sprangle et al., 1990]. This approximation assumes that the plasma response does not significantly change the laser pulse during the time it takes the pulse to transit a plasma electron. This means that the approximation is valid only for laser pulses with pulse durations that are shorter than the time it takes for them to evolve in the plasma. In

this approximation, the fluid response to a static laser field is calculated at a fixed time, and in a next step the laser evolution due to this altered plasma fluid is determined by solving the wave equation. Nonlinear plasma waves can be calculated starting from the longitudinal parts of the cold *relativistic* fluid equations [Sprangle et al., 1990]:

the electron fluid momentum equation

$$\frac{d(\gamma\beta_z)}{dt} = c\frac{\partial\phi}{\partial z} - \frac{c}{2\gamma}\frac{\partial a^2}{\partial z}, \tag{2.21}$$

and the continuity equation

$$\frac{\partial n}{\partial t} + c\frac{\partial(n\beta_z)}{\partial z} = 0, \tag{2.22}$$

where $\phi = e\Phi/(m_e c^2)$ is the normalized electrostatic potential, n the plasma density and $a = a(z)$ the normalized laser pulse intensity. The normalized longitudinal and transverse plasma fluid velocities are given by $\beta_z = v_z/c$ and $\beta_\perp = v_\perp/c$, respectively. The relativistic factor associated with the electrons is given by $\gamma = (1-(\beta_z^2+\beta_\perp^2))^{-1/2}$ and the plasma wave propagates with a phase velocity β_p. The expressions can be greatly simplified by a transformation into a frame that is co-moving with the plasma-wave velocity. With a laser pulse as the driver, the wave moves with the group velocity of the laser ($\beta_p \simeq \beta_g$) and therefore the co-moving frame has the coordinates $\xi = z - v_g t$ and $\tau = t$. The application of the QSA allows the fluid momentum and continuity equations to be integrated (see Appendix, section A.1.3) which leads to:

$$\gamma(1 - \beta_g\beta_z) - \phi = 1 \tag{2.23}$$

$$n(\beta_g - \beta_z) = n_0\beta_g \tag{2.24}$$

These equations, in combination with the Poisson's equation (eq. 2.15) lead to the quasistatic cold fluid equation for the electrostatic potential ϕ

$$\frac{\partial^2\phi}{\partial\xi^2} = k_p^2\gamma_g^2\left[\beta_g\left(1 - \frac{1+a^2}{\gamma_g^2(1+\phi)^2}\right)^{-1/2} - 1\right], \tag{2.25}$$

where $\gamma_g = (1-\beta_g^2)^{-1/2}$.

In the case of $\gamma_g \gg 1$ (which means low plasma densities and high laser intensities, see equation 2.35), this can be simplified to

$$\frac{\partial^2\phi}{\partial\xi^2} = \frac{k_p^2}{2}\left(\frac{1+a^2}{(1+\phi)^2} - 1\right), \tag{2.26}$$

and the plasma fluid quantities can be written as

$$\frac{n}{n_0} = \frac{(1+a^2)+(1+\phi)^2}{2(1+\phi)^2}, \tag{2.27}$$

$$u_z = \frac{(1+a^2)-(1+\phi)^2}{2(1+\phi)}, \tag{2.28}$$

$$\beta_z = \frac{(1+a^2)-(1+\phi)^2}{(1+a_0^2)+(1+\phi)^2}, \tag{2.29}$$

The properties of a nonlinear plasma wave computed with eqs.(2.26)-(2.29) can be seen in fig.(2.3). The field of nonlinear waves can exceed that of the cold non-relativistic wavebreaking limit (E_0, eq 2.19) because of their deviation from the sinusoidal shape of linear waves: the electron density shows sharply peaked crests which are separated by wide troughs, the electric field shows a characteristic "sawtooth" profile and the plasma wavelength elongates (see figure 2.3).

Analytically, the **general characteristics of nonlinear plasma waves** can be determined by solving equation (2.25) in the region behind the driver laser ($\xi \leqslant 0$). Since here $a = 0$, the analysis yields the properties (independent of the driver) of a nonlinear plasma wave of a given amplitude $E_{\max}$. The wave becomes nonlinear if its amplitude is larger than the non-relativistic wavebreaking limit ($E_{\max} > E_0$). The electrostatic potential produced by the wave oscillates between

$$\phi_m = \frac{\hat{E}_{\max}^2}{2} \pm \beta_p \sqrt{\left(1+\frac{\hat{E}_{\max}^2}{2}\right)^2 - 1} \tag{2.30}$$

where $\hat{E}_{\max} = E_{\max}/E_0$ and the $\pm$ gives the maximum and the minimum values $\phi_{\max}$ and $\phi_{\min}$ at the position $\xi_{\max}$ and $\xi_{\min}$, respectively (see fig.(2.4)). The potential has a periodicity of [Esarey et al., 2009]

$$\lambda_{\mathrm{N}p} = \lambda_p \begin{cases} 1 + \dfrac{3}{16}\left(\dfrac{E_{\max}}{E_0}^2\right) & \text{for } \dfrac{E_{\max}}{E_0} \gg 1 \\ \dfrac{2}{\pi}\left(\dfrac{E_{\max}}{E_0} + \dfrac{E_0}{E_{\max}}\right) & \text{for } \dfrac{E_{\max}}{E_0} \ll 1 \end{cases} \tag{2.31}$$

which is the nonlinear plasma wavelength. Using equation 2.34, this can be written for $a_0 \gg 1$ as

$$\lambda_{\mathrm{Np}} \simeq \left(\frac{2\sqrt{a_0}}{\pi}\right)\lambda_p. \tag{2.32}$$

The amplitude of the plasma wave $E_{\max}$ depends on the driver. For a linearly polarized laser with a temporally square pulse profile with an amplitude of a_0 and an optimal length of $L \simeq \lambda_{\mathrm{N}p}/2$, the maximum amplitude is given by [Esarey et al., 2009]

$$\hat{E}_{\max} = \frac{E_{\max}}{E_0} = \frac{a_0^2/2}{\sqrt{1+a_0^2/2}}. \tag{2.33}$$

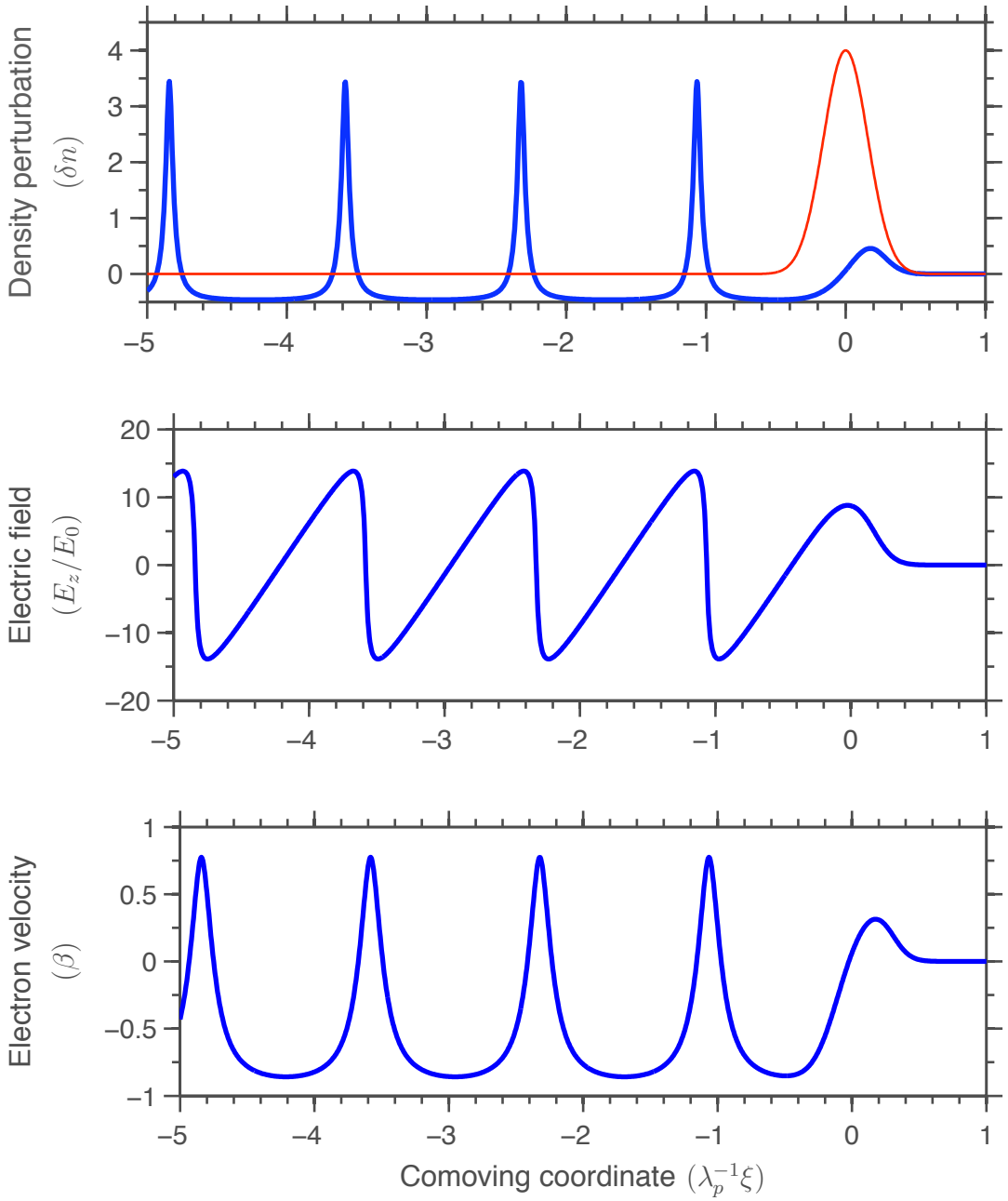

Figure 2.3. | **Nonlinear plasma wave properties.** The figure shows the plasma density perturbation $\delta n/n_0 = (n_0 - n)/n_0$, the electric field normalized to the cold wavebreaking limit E_z/E_0 and the plasma fluid velocity $\beta_z = v_z/c$ of a nonlinear plasma wave with a phase velocity of $\beta_p = 0.95$. The graphs are computed by numerically solving eqs (2.26) - (2.29). The co-moving coordinate ξ is normalized to the non-relativistic plasma wavelength λ_p. The wave is driven by a Gaussian laser pulse $a^2(\xi)$ centered at $\xi = 0$ (depicted red in Fig.2.3**a**) with an amplitude $a_0 = 2$ and a pulse duration of $L = k_p^{-1}$. The laser pulse is moving to the right.

2.6. Acceleration of Electrons in Laser Wakefields

2.6.1. Wavebreaking and Maximum Electric Field

Nonlinear wavebreaking field
Laser group velocity in the nonlinear regime

The maximum electric field that a nonlinear plasma wave can sustain is given by the wavebreaking field E_{WB}. Wavebreaking occurs if the electron fluid velocity of the plasma v_z reaches the velocity of the plasma wave v_p, causing the density (eq.(2.24)) to become singular. This results in the maximum field that a nonlinear wave can sustain before it breaks of [Akhiezer and Polovin, 1956]

$$E_{\mathrm{WB}} = \sqrt{2(\gamma_p - 1)} \cdot E_0. \tag{2.34}$$

The plasma wave velocity γ_p is approximately the laser group velocity γ_p which can be calculated from the nonlinear dispersion relation to be [Decker and Mori, 1994]:

$$\gamma_g = \frac{\omega}{\omega_p}\sqrt{\frac{a_0^2+2}{2}} = \sqrt{\frac{n_{\mathrm{crit}}}{n_0}}\sqrt{\frac{a_0^2+2}{2}}, \tag{2.35}$$

where $n_{\mathrm{crit}} = (m_e\omega_p^2)/(4\pi e^2)$ is the critical density (see section 2.3.5). This means that the velocity depends on both the laser intensity a_0 and the plasma density n_0. Transverse (3D) effects of the laser beam, such as Rayleigh diffraction can decrease the longitudinal laser group velocity to [Esarey and Leemans, 1999]

$$\gamma_g \simeq \left(\frac{\omega_p^2}{\omega^2} + 2\frac{c^2}{\omega^2 w_0^2}\right)^{-1/2}, \tag{2.36}$$

where w_0 is the laser focal spot size. The plasma wave moves with a velocity close to the laser group velocity $\gamma_p \simeq \gamma_g$ and for typical densities in the laser-wakefield regime $\gamma_p = 10 \ldots 100$. Such velocities lead to significant increase in accelerating fields in comparison to linear plasma waves (see eq. 2.34). From equation (2.33) it can be seen that a sufficiently high laser peak intensity a_0 can drive a high amplitude plasma wave and can even lead to wavebreaking (if $E_{\mathrm{max}} > E_{\mathrm{WB}}$) for $a_0 \geqslant 2\sqrt{\gamma_p}$ (assuming $a_0 \gg 1$ and $\gamma_p \gg 1$).

2.6.2. Electron Trapping and Acceleration

Phase-space picture of acceleration
Acceleration distance & maximum electron energies
Electron bunch duration
Minimum injection momentum

The trapping and acceleration of electrons in a wakefield can be best explained in the phase-space of the plasma wave. Fig.(2.4) shows the phase-space trajectories of test electrons with different initial kinetic energies under the influence of the fields of a plasma wave driven by a laser with the same parameters as in fig.(2.3). The motion of a test electron is given by (see [Esarey and Pilloff, 1995] and Appendix equation (A.49)):

$$H(p_z, \xi) = \sqrt{p_z^2 + 1 + a^2} - \beta_p p_z - \phi(\xi) \tag{2.37}$$

The electron orbits are defined by $H(p_z, \xi)$=h_0, where h_0=const is the initial kinetic energy of the test electron. Electrons with an initial velocity of at least the plasma wave velocity ($\beta_z \gtrsim \beta_p$) at the position of the potential minimum $\phi_{\min}$=$\phi(\xi$=$\xi_{\min})$ (backside of the bucket) become trapped as discussed below and execute rotations in phase-space (white-colored trajectories in fig.(2.4)). However, the trapping process itself is not described in this model. Electrons with a velocity of exactly β_p at $\xi_{\min}$ and an energy of $H_s(\gamma_s, \phi)$=$H(\gamma_p, \phi_{\min})$ move on an orbit called the separatrix (dotted red trajectory in Fig.(2.4)) which separates trapped from background electrons. Background electrons (black trajectories in Fig.(2.4)) that do not have a sufficiently high velocity to become trapped slip backward with respect to the plasma wave, whereas electrons with energies that are too high cannot interact efficiently with the wave and slowly overtake the wake. The separatrix is characterized by its width (in the ξ-dimension) which is the distance between the position of two minima of the potential $\xi_{\min}$ and is given by the nonlinear plasma wavelength $\lambda_{\mathrm{N}p}$, equation (2.31). The height is given by the difference between the maximum and minimum electron momenta at the position of the potential peak $\xi_{\max}$ which can be calculated by solving equation (2.37) for H=H_s in a region behind the laser, where a=0. This results in [Esarey et al., 2009]

$$p_m = \beta_p \gamma_p (1 + \gamma_p \Delta\phi) \pm \gamma_p \sqrt{(1 + \gamma_p \Delta\phi)^2 - 1}\,, \tag{2.38}$$

where + and - stand for the maximum and the minimum momentum, $\Delta\phi = \phi_{\max} - \phi_{\min} = 2\beta_p[(1+\hat{E}^2_{\max}/2)^2 - 1]^{1/2}$ is the difference between the maximum and minimum potential, derived from equation (2.30). Typically, electrons get trapped at the back of a plasma period (i.e. at $\xi = \xi_{\min}$), where the plasma density is highest, as discussed below. They get trapped at this position if they have a minimum momentum of [Schroeder et al., 2006]

$$p_t = \beta_p \gamma_p (1 - \gamma_p \phi_{\min}) - \gamma_p \sqrt{(1 - \gamma_p \phi_{\min})^2 - 1}\,, \tag{2.39}$$

which indicates that the minimum initial momentum p_t required for electrons to become trapped by the plasma wave depends on the the plasma density n_0 and the laser intensity a_0 (implicit through both the potential of the wave (eqs.(2.30)&(2.33)) and the wave phase velocity γ_p, equation (2.35)). Thus, for higher laser intensities and higher plasma densities (and therefore lower γ_p) electrons with a lower initial momentum become trapped as can be seen in fig.(2.5). This can be understood since for higher plasma densities the wave velocity is slower and for higher laser intensities the separatrix becomes larger both allowing electrons with smaller initial velocities to become trapped.

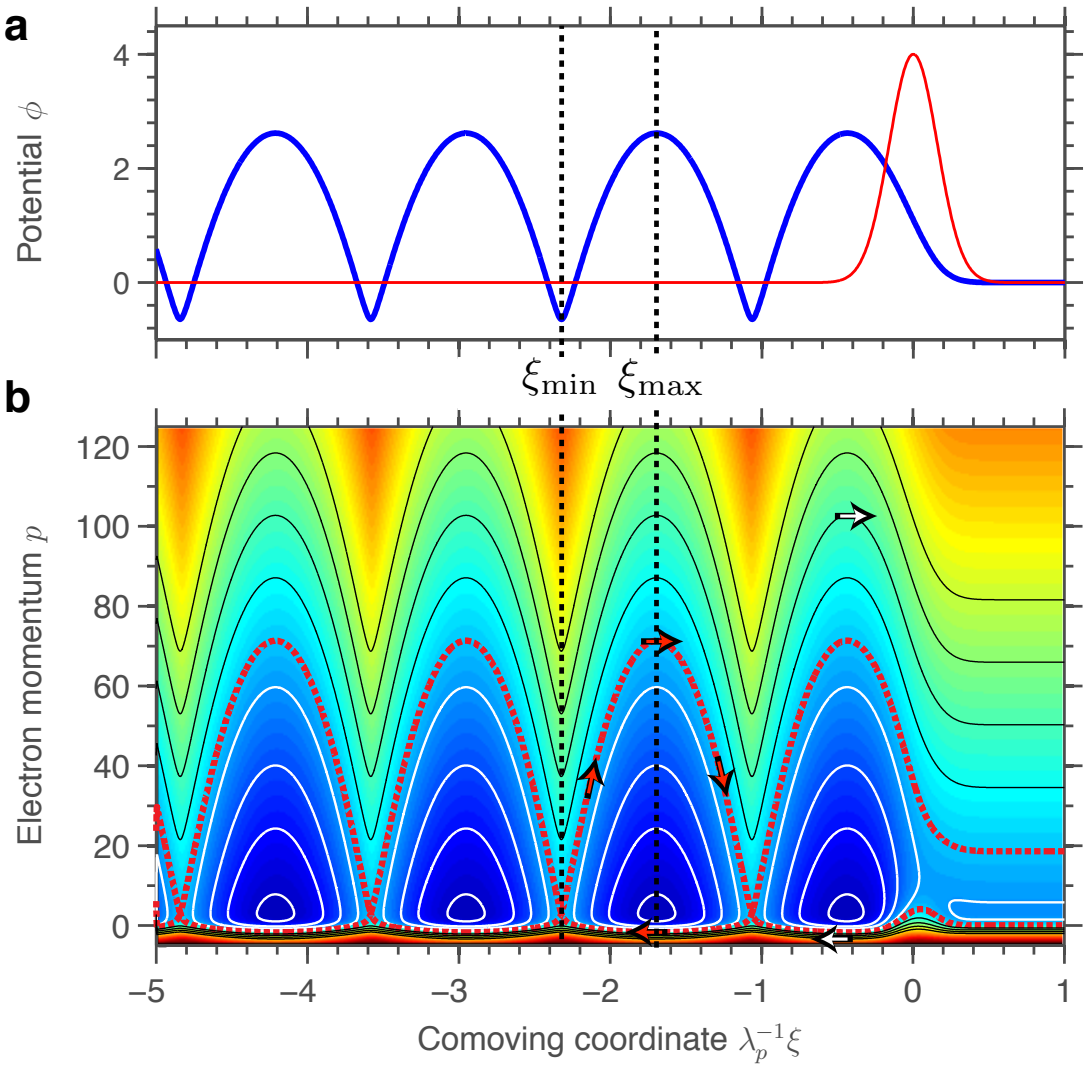

Figure 2.4. | **Phase space picture of a nonlinear plasma wave.** **a)** Potential of the plasma wave (blue), driven by the laser pulse (red). The position of the potential minium $\phi_{\min}$ is labeled as $\xi_{\min}$, the maximum $\phi_{\max}$ as $\xi_{\max}$. **b)** Phase space trajectories of test electrons with different initial kinetic energies. The separatrix shown as red dashed line separates trajectories of electrons that are trapped (white trajectories) from those that are not trapped (black lines) by the fields of the wave. The laser and plasma parameters are those of fig.(2.33).Trapping is not included in this model and therefore electrons that are initially outside the separatrix will continue to stay outside. As discussed below, trapping occurs if background electrons (with a momentum $p = 0$) gain enough energy to get inside the separatrix (for example by scattering or the field of a second laser beam) or if the separatrix is lowered (for example by a drop of the plasma wave phase velocity).

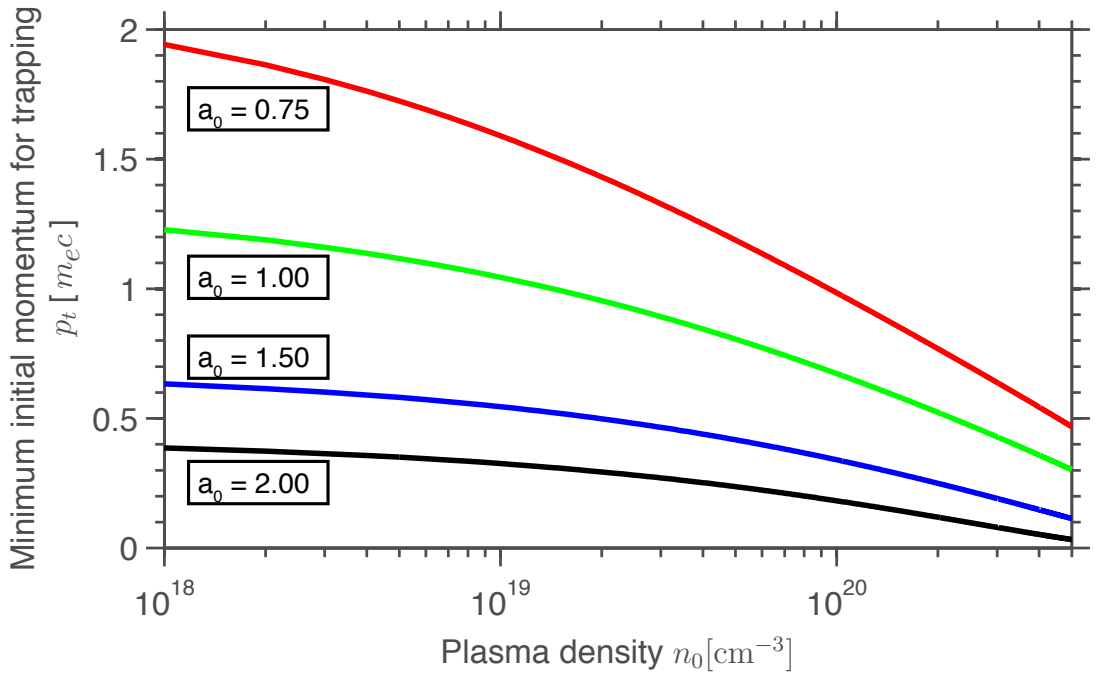

Figure 2.5. | **Minimal injection momentum.** The initial momentum required for an electron to become trapped by a plasma wave for different laser intensities a_0 plotted against the plasma density n_0. The driver laser is assumed to have a central wavelength of 800 nm.

Electrons that lie on the separatrix reach the highest momentum which in the linear case can be written as [Esarey and Pilloff, 1995]

$$\gamma_{\max} \simeq 4\gamma_p^2 \hat{E}_{\max} \tag{2.40}$$

The energy that the electron gains ($p_{\max} - p_{\min}$, eqn 2.38) is given by $\gamma_{\max} \simeq 2\gamma_p^2 \hat{E}_{\max}$ [Tajima and Dawson, 1979].

For nonlinear waves, the maximum energy is given by [Esarey and Pilloff, 1995]

$$\gamma_{\max} \simeq 2\gamma_p^2 \hat{E}_{\max}^2, \tag{2.41}$$

which implies that electrons can gain higher energies if they are trapped in nonlinear plasma waves. Since $\gamma_p^2 \sim n_0^{-1}$ (eq 2.35), lower plasma densities allow for higher electron energies even though for higher densities the accelerating field gradients are larger. This can be understood by estimating the distance it takes for an electron moving with the speed of light to outrun the accelerating (back half) part of the the plasma wave (moving with γ_p and therefore slightly slower than c). This distance is called the **dephasing length** and in the linear case reads [Tajima and Dawson, 1979], [Esarey et al., 2009]

$$L_d = \gamma_p^2 \lambda_p \simeq \frac{\lambda_p^3}{\lambda^2}, \tag{2.42}$$

which indicates that $L_d \sim n_0^{-3/2}$.

The maximum energy can be estimated by assuming that the electrons are accelerated by the maximum field $E_{\max} \sim n_0^{1/2}$, equation (2.33), over the whole dephasing length which results in

$$W_{\max} = eE_{\max}L_d \sim \frac{1}{n_0}. \tag{2.43}$$

Therefore higher electron energies can be achieved by a lower plasma density, but since the accelerating fields get smaller a longer distance is required.

2.6.3. Limits

Depletion
Dephasing
Diffraction
Beam loading

There are several processes that limit the maximum energy gain of the accelerated electrons. In the following, each process is discussed including an estimate on the maximum acceleration distance that it allows. With this, the maximum possible electron energies can be roughly estimated by assuming that the electrons experience the maximum possible accelerating field $E_{\max}$, equation (2.33), given for a certain plasma density and laser intensity over the respective acceleration distance $W_{\max} = eE_{\max}L_{\mathrm{acc}}$

Electron dephasing. Since the laser beam (and therefore the plasma wave) propagates in a plasma with a velocity $v < c$, electrons can get accelerated to higher velocities than the group velocity of the laser pulse. They can outrun the accelerating fields of the plasma wave and get decelerated which is called dephasing. Since the longitudinal (accelerating) and the transverse focusing fields of the plasma wave are out of phase by a factor of $\pi/2$ with respect to each other [Akhiezer and Polovin, 1956], both linear accelerating and transverse focusing fields only exist in a quarter of the plasma wave period. Therefore, the dephasing length is reached after the electron beam outruns the plasma wave by a distance of $\simeq\lambda_p/2$. The length can be estimated by assuming an electron moving with c and the plasma wave moving with the group velocity of the laser: $L_d/v_p = (L_d + \lambda_{\mathrm{Np}}/2)/c$. Using equation 2.35, this leads to

$$L_d = \frac{\lambda_{\mathrm{Np}}^3}{\lambda^2}\left(\frac{a_0^2+2}{2}\right). \tag{2.44}$$

This equation can be simplified for $a_0^2 \ll 1$ and in the case of $a_0^2 \gg 1$, a lengthy calculation including relativistic effects leads to [Esarey et al., 2009]:

$$L_d = \begin{cases} \dfrac{\lambda_p^3}{\lambda^2} & \text{for } a_0^2 \ll 1 \\ \dfrac{\sqrt{2}}{\pi}\dfrac{\lambda_p^3}{\lambda^2}\dfrac{a_0}{N_p} & \text{for } a_0^2 \gg 1 \end{cases} \tag{2.45}$$

and a corresponding maximum energy gain of [Esarey et al., 2009]

$$\Delta W_d\,[\mathrm{MeV}] = \begin{cases} 1260 \cdot \dfrac{I\,[\mathrm{W/cm^2}]}{n_0\,[\mathrm{cm^{-3}}]} & \text{for } a_0^2 \ll 1 \\ 1260 \cdot \dfrac{2}{\pi N_p} \dfrac{I\,[\mathrm{W/cm^2}]}{n_0\,[\mathrm{cm^{-3}}]} & \text{for } a_0^2 \gg 1, \end{cases} \tag{2.46}$$

where N_p is the number of plasma periods behind the driver laser.

In the linear regime ($a_0 \ll 1$), the maximum acceleration distance is mainly limited by the dephasing length. This can be overcome by using a nonuniform axial (along the acceleration distance) plasma density. Especially for an axially increasing plasma density, the phase velocity of the plasma wave also increases [Sprangle et al., 2001]. This means that the dephasing length (and thus the maximum energy gain) can be extended. For appropriate tapering of the plasma density, the acceleration limit is given by the pump depletion (see below).

In the nonlinear regime ($a_0 \gg 1$), the dephasing and the pump depletion lenghts become comparable which means that an increase of the dephasing length does not lead to higher energy gains. Therefore a simpler setup with no density tapering can be employed, leading to energy gains comparable to the linear gain, but using higher accelerating gradients and therefore shorter channel lengths.

For the parameters of the experiment described below (laser power $P = 20\,\mathrm{TW}$ at a wavelength of 800 nm, laser intensity of $I \simeq 2 \cdot 10^{18}\,\mathrm{W/cm^2}$ and correspondingly $a_0 \simeq 1$, a plasma density of $n_0 \simeq 5 \cdot 10^{18}\,\mathrm{cm^{-3}}$ and correspondingly $\lambda_p \simeq 15\,\mu\mathrm{m}$) the dephasing length is calculated to be $L_d = 5.2\,\mathrm{mm}$ and a correspondingly maximum energy gain of $\Delta W_d = 500\,\mathrm{MeV}$. However, this has to be considered only as a coarse approximation since the laser intensity $a_0 \simeq 1$ which is in between the limits of the estimations given above (the formula in the limit $a_0 \ll 1$ has been used for the calculation).

Laser diffraction. Without any forms of optical guiding, the laser pulse undergoes Rayleigh diffraction which increases the beam size and correspondingly decreases the laser intensity. Since a plasma wave can only by driven by a sufficiently intense laser, the acceleration distance is limited to a few Rayleigh lengths (Z_R)

$$L_{\mathrm{diff}} \simeq \pi Z_R, \tag{2.47}$$

where $Z_R = \pi w_0^2/\lambda$, with λ being the laser wavelength and w_0 the rms laser spot size. In this case, the energy gain is limited to

$$\Delta W_{\mathrm{diff}}\,[\mathrm{MeV}] \simeq 740 \frac{\lambda}{\lambda_p} \frac{1}{\sqrt{1 + a_0^2/2}} \cdot P\,[\mathrm{TW}]. \tag{2.48}$$

To overcome this limitation, the laser pulse can be kept focused beyond the Rayleigh length by a medium with an index of refraction that is higher on-axis

than off-axis ($\partial\eta(r)/\partial r < 0$) [Sprangle et al., 1992]. The index of refraction for a laser pulse in a plasma depends on both the radial plasma density and implicitly on the radial laser intensity through the relativistic mass increase of the electron in the laser field:

$$\eta(r) = \sqrt{1 - \left(\frac{\omega_p}{\omega}\right)^2} \simeq 1 - \frac{4\pi e^2}{2\,\omega^2}\frac{n(r)}{\gamma(r) m_{e,0}}. \tag{2.49}$$

This suggests that a radially increasing appropriate plasma density profile $n(r)$ as well as radially different electron energies $\gamma(r)$ can form such a channel. The first possibility can be achieved by a second laser pulse or an electrical discharge in a gas that ionizes and heats electrons. The hot electrons expand and form a channel that has a radial plasma density distribution with a minimum (and thus a maximum index of refraction) on axis. This can be used as a **plasma waveguide** to guide the laser beam over several Rayleigh lengths [Butler et al., 2002; Geddes et al., 2004].

Laser pulses with a sufficiently high powers ($P{>}P_{\mathrm{crit}}[\mathrm{GW}] \simeq 17.4(\omega/\omega_p)^2$) undergo **relativistic self-focusing** and can also be guided in a plasma (for relativistic self-focussing, see section 2.6.4).

A plasma waveguide has several advantages over the relativistic self-guiding regime. Since the channel does not require a high laser power $P{>}P_{\mathrm{crit}}$, it can be operated at lower intensities with the advantage of not having to rely heavily on nonlinear effects which may result in a more stable regime.

In the case of the experimental parameters given above, the limit of the energy gain given by the laser diffraction is $\Delta W_{\mathrm{diff}} = 660\,\mathrm{MeV}$. It can be seen that in this case the dephasing is limiting the acceleration rather than the diffraction. However, for a slightly lower plasma density, the dephasing length can be increased and the maximum energy gain is limited by laser diffraction.

Pump depletion. As the laser excites a plasma wave, it transfers energy to it and starts to deplete [Horton and Tajima, 1986],[Ting et al., 1990]. The depletion length can be estimated by assuming that the laser pulse energy is completely transferred to the plasma wave. In the 1D case, assume a plasma wave with an electric field of E_{max} (energy density of E_{max}^2) over a length of L_{pd} and a laser pulse with a longitudinal square profile over a pulse length of $L = \lambda_{\mathrm{Np}}/2$ (for λ_{Np}, see equation (2.31)). With a laser electric field E_L, this can be computed by: $E_{\mathrm{max}}^2 L_{\mathrm{pd}} \simeq E_L^2 L$ which results in a depletion length of [Esarey et al., 2009]

$$L_{pd} = \begin{cases} \dfrac{2}{a_0^2}\dfrac{\lambda_p^3}{\lambda^2} & \text{for } a_0^2 \lesssim 1 \\[2ex] \dfrac{\sqrt{2}\,a_0}{\pi}\dfrac{\lambda_p^3}{\lambda^2} & \text{for } a_0^2 \gg 1 \end{cases} \tag{2.50}$$

and a corresponding maximum energy gain of [Esarey et al., 2009]

$$\Delta W_{pd}\,[\mathrm{MeV}] = \begin{cases} 3.4\times10^{21}\cdot\dfrac{1}{\lambda\,[\mu\mathrm{m}]\,n_0\,[\mathrm{cm}^{-3}]} & \text{for } a_0^2 \ll 1 \\ 400\cdot\dfrac{I\,[\mathrm{W/cm}^2]}{n_0\,[\mathrm{cm}^{-3}]} & \text{for } a_0^2 \gg 1. \end{cases} \tag{2.51}$$

Since both the dephasing as well as the diffraction lengths can be extended by either target engineering or certain physical effects, the pump depletion sets the upper limit of the single-stage energy gain. In order to run a laser-plasma accelerator beyond pump depletion, it has to be operated over several stages, each driven by a "fresh" laser pulse.

For the experimental parameters given above, the depletion length is given by $L_{pd} \simeq 12\,\mathrm{mm}$ which leads to a maximum energy gain of $\Delta W_{pd} \simeq 850\,\mathrm{MeV}$.

Beam loading. The electric fields of the plasma wave can be significantly modified by the fields of the highly dense injected electron bunches. This is referred to as beam loading and can set severe limitations on the number of accelerated electrons, the quality of the accelerated beam and the efficiency of the process. The maximum number of electrons that can be loaded into a wave bucket can be estimated by calculating the number of electrons in a small axial region ($\ll \lambda_p$) which produce an electric field that cancels out the accelerating field of the plasma wave. For a linear wakefield far from wavebreaking ($E_{\max}<E_0$), this number is calculated to be [Katsouleas et al., 1987]

$$N_{\max} \simeq 5\times10^5 \frac{E_{\max}}{E_0} A[\mathrm{cm}^2]\sqrt{n_0[\mathrm{cm}^{-3}]}, \tag{2.52}$$

where A is the cross-sectional area of the bunch (i.e. the transverse area over which the fields of the bunch and the plasma wave interact. The equation assumes $A \gg \pi/k_p^2$; $1/k_p$ is the skin depth).

The energy spread of an infinitesimally short electron beam can be estimated by assuming that the front of the bunch is accelerated by the whole electric field of the plasma wave and gains an energy $\Delta\gamma_{\max}$, whereas the back of the bunch experiences only the accelerating field shielded by the front and gains an energy of $\Delta\gamma_{\min}$. Since the reduction in accelerating field for the electrons at the back of the bunch is linear in the number of electrons N contained in the bunch, the relative energy spread can be estimated as [Katsouleas et al., 1987]

$$\frac{\Delta\gamma_{\max}-\Delta\gamma_{\min}}{\Delta\gamma_{\max}} = \frac{N}{N_{\max}}. \tag{2.53}$$

The efficiency of transferring wake energy into accelerated electron energy can be estimated by the maximum decrease of the electric field of the plasma wave due to

the loaded electron bunch (which is at the back of the bunch) and can be written as [Katsouleas et al., 1987]

$$\eta_b = \frac{N}{N_{\max}} \left(2 - \frac{N}{N_{\max}} \right), \tag{2.54}$$

which means that for $N \rightarrow N_{\max}$, the efficiency approaches 100% but also the energy spread approaches 100%. Therefore the electron beam quality sets an upper limit on the number of accelerated electrons in a bunch. However, these are only 1D estimations and laser pulses with higher energies over a larger focal spot (same intensities) can lead to a decrease of the beam loading effect.

2.6.4. Evolution of an Intense Laser Pulse in a Plasma

Self-modulation
Relativistic self-focusing
Ponderomotive self-channeling
Filamentation
Self-steepening

High-intensity laser pulses undergo a substantial evolution as they propagate through plasma. Owing to their large electric fields, they modify the plasma density and can accelerate electrons to relativistic energies within a single optical cycle. The propagation and evolution of a laser beam in a plasma is mainly governed by the index of refraction η which depends on the electron density n_e, the electron relativistic mass γm_e and the laser frequency ω as:

$$\eta = \sqrt{1 - \left(\frac{\omega_p}{\omega}\right)^2} = \sqrt{1 - \frac{4\pi e^2}{\omega^2} \frac{n_e}{\gamma m_e}}\,. \tag{2.55}$$

The laser group velocity and its phase velocity are given by

$$v_g = \eta \cdot c \qquad \text{and} \qquad v_{\text{ph}} = \frac{c}{\eta}. \tag{2.56}$$

Self-modulation. Long laser pulses with a duration of $L > \lambda_p$ undergo self-modulation since the plasma wave (excited by the laser) has an electron density profile that is periodic with the plasma wavelength. Along the axis, this leads in regions of lower plasma density to a higher index of refraction (see eq.[2.55]) and in regions with a high density to a lower index of refraction compared to the index of refraction of the undisturbed plasma background. As a consequence, laser pulses that extend over several plasma periods get transversely diffracted at high density sections and focused in the electron-void areas. This causes the axial intensity of the pulse to get modulated with a period of λ_p and eventually the laser to break up. These laser beamlets, spaced at λ_p resonantly excite a large plasma wave. However,

accelerated electron bunches in these wakefields directly interact with the laser pulse which causes a growth of the emittance and leads to broad energy spectra.

Relativistic self-focusing. For laser intensities of $a_0 > 1$, the laser transversely accelerates electrons to relativistic velocities which results in an increase of the relativistic electron mass. For a typical laser pulse, the transverse intensity profile peaks on axis and drops for a larger radius which leads to the strongest acceleration of electrons on axis (with an associated largest relativistic mass). From equation 2.55, it can be seen that this translates into a higher index of refraction on axis than off axis. Correspondingly, the phase fronts of the laser pulse propagate slower on axis than they do off axis (phase velocity: $v_{\mathrm{ph}} = c/\eta$) which results in a focusing effect. In this way, a laser with sufficiently high power ($P{>}P_{\mathrm{crit}}[\mathrm{GW}] \simeq 17.4(\omega/\omega_p)^2$) can undergo relativistic self-focusing which can cancel out the Rayleigh diffraction and thus the pulse can be guided in a plasma over distances $> Z_R$. However, this does not work for laser pulses with duration $c\tau_L < \lambda_p$ since the ponderomotive force pushes electrons at the front of the pulse which leads to an increase in electron density. This cancels out the decrease in plasma frequency due to the relativistic mass increase and the head of the short pulse starts to erode by diffracting similar to a low-intensity beam. However, it is possible for the front edge of the laser to deplete before it starts to diffract which leads to laser pulse etching and can effectively relativistically guide short pulses (see section 2.6.5)

Ionization-induced defocusing. The ionization of gas atoms changes the plasma density. For laser intensities that are just slightly above the ionization threshold (for example lasers that are not yet focused to a diffraction limited spot), the ionization probability has both a radial and an axial dependency. The highest (on-axis) intensity results in the highest ionization yield and therefore the highest plasma density on-axis. This leads to a transverse gradient of the index of refraction with a minimum on-axis and therefore to the defocusing of the laser beam. The effect depends on the type of gas chosen as a target: for hydrogen the required laser intensity is $I_{\mathrm{H}^+} = 1.4 \times 10^{14}\,\mathrm{W/cm^2}$ and the rising edge of the laser completely ionizes the gas for intensities $I > 10^{15}\,\mathrm{W/cm^2}$ which leads to a uniform density distribution and therefore to no defocusing. A higher laser intensity is required for gases with higher atomic numbers. For example helium fully ionizes at $I_{\mathrm{He}^{++}} \simeq 10^{16}\,\mathrm{W/cm^2}$. This effect can be mitigated by a preformed plasma channel or at a well defined vacuum-plasma transition (present for example in gas jets), where the laser can be focused to a diffraction limited spot in vacuum before it enters the plasma [Auguste et al., 1994; Gibbon, 2005].

Ponderomotive self-channeling. Owing to its radial ponderomotive force, a laser pulse expels electrons from the axis, creating a channel with a low plasma density on axis. This leads to a radial gradient of the refractive index with a maximum on-axis. However, for laser powers $P{<}P_{\mathrm{crit}}$ this effect is not sufficiently strong to guide the laser by itself, and for $P{\rightarrow}\ P_{\mathrm{crit}}$ guiding is achieved predominantly by relativistic self-focusing but is enhanced by self-channeling [Esarey et al., 2009].

Filamentation. Through relativistic self-focusing in plasmas of relatively high densities, lasers with powers significantly above P_{crit} can generate not only a single, but multiple ion channels across the transverse beam profile. The laser expels electrons and leaves behind a plasma channel. The fields of long laser pulses ($c\tau_L > \lambda_p$) in combination with the electric fields of the channel and the magnetic fields produced by the current of electrons that enter into the channel can interact and accelerate these electrons in forward direction (direct laser acceleration) [Pukhov et al., 1999]. Owing to the magnetic field produced by these electrons, currents that have the same propagation directions attract each other and form filaments. If the transverse laser focal spot is much larger than the skin depth of the plasma ($w_0 \gg 1/k_p$), small perturbations in the beam current and laser intensity can form several filaments, each of the size of $1/k_p$. Due to the background plasma, these filaments are shielded from each other and they do not attract one another. However, for a slightly smaller laser spot size, the filaments can coalesce and form a single "super-channel" [Pukhov and Meyer-ter Vehn, 1996]. In order to suppress filamentation and thus a deterioration of the accelerated electrons, short laser pulses which do not interact with the electron beam are more suited for acceleration. Experimentally, for the bubble regime it was found in [Thomas et al., 2009] that a minimum laser spot size in terms of its pulse duration of $w_0 \gtrsim c\tau_L$ is required in order to suppress filamentation and produce monoenergetic electron beams.

Self-steepening & self-shortening. Self-steepening and self-shortening are the result of two effects: (1) The increase in relativistic mass of electrons under the influence of high laser intensities leads to an increase of the index of refraction. For longitudinally varying laser intensity profiles, this leads to regions with different local *group* velocities along the laser pulse (a higher intensity part of the laser moves with a higher group velocity: $v_g = \eta \cdot c$) [Decker and Mori, 1994; Esarey et al., 2000]. (2) in regions with a lower plasma density, the index of refraction is increased which also increases the local group velocity. In the bubble regime (see section 2.6.5) the laser pushes a compressed electron sheet in front, like a snow-plough, leaving behind a low plasma density. Thus, the lower-intensity leading edge of the laser experiences a high electron density (and therfore has a lower local group velocity). The longitudinal central region of the laser with the peak intensity experiences a low density. For longitudinal Gaussian laser intensity, both of these effects lead to a higher local group velocity for the (longitudinal) central part of the pulse compared to the leading edge. This results in a compression of the pulse. It increases the intensity gradient at the front of the laser pulse (self-steepening) and leads to a higher overall peak intensity.

2.6.5. 3D Theory and the Bubble Regime

3D theory
Particle-in-cell (PIC) code
The bubble
3D scalings derived from PIC simulations

The experiments described in this thesis are conducted with an electron accelerator that is operated in the so-called "bubble"-regime [Pukhov and Meyer-ter Vehn, 2002]. A comprehensive theory of this acceleration scheme is still subject to research and is not yet fully represented in textbooks. Therefore, a more detailed discussion is presented in this section.

The bubble acceleration mechanism relies on the non-linear evolution of the laser pulse and requires a 3D nonlinear description. Since both the motion of electrons under the influence relativistically intense laser pulses ($a_0 \geqslant 1$) and the laser pulse evolution become highly nonlinear, only few accurate analytical solutions in 1D and 2D exist. Owing to these non-linearities, numerical simulations generally must be used to describe the physical processes in 3D and to predict scaling laws for parameters such as electron energy, energy spread, the accelerated charge, etc with laser intensity and plasma parameters.

Particle-in-Cell (PIC) (eg.: [Dawson, 1983; Hockney and Eastwood, 1988]) codes are a commonly used tool to simulate plasma accelerators. PIC codes solve the Maxwell's equations as well as the relativistic equations of motion for particles in an electromagnetic field and are therefore very fundamental, since only very few assumptions are made. In order to describe the large amount of particles in a plasma, the code represents their distribution as macro-particles, each of which can be viewed as finite-sized cloud of an ensemble of many real particles of the same species at the same velocity. In this description, rather than solving the whole 6D particle phase-space grid at each step, only regions where particles are present must be solved; only the Maxwell's equations are solved on a 3D spatial (configuration) grid. The macro-particles can move continuously under the influence of the electromagnetic field. This creates charge densities and currents which are used to solve Maxwell's equations on the discretized configuration grid, in order to calculate the fields that act on the macro-particles in the next step. This method allows for a highly parallelized computation, but the high longitudinal resolution (given by a fraction of the laser wavelength: $\simeq 1\mu$m) that needs to be resolved, requires a large amount of computational time for typical laser-plasma accelerators (of few-cm length and 10^{18} particles/cm^{-3}) even on large computer clusters.

PIC codes allow one to investigate the properties and scalings even of highly nonlinear wakefields in 3D. In the previous section, nonlinear plasma waves have only been discussed in the 1D limit which assumes a transverse laser beam size much larger than the plasma wavelength. However, the 3D shape of a plasma wave driven by a laser beam of the transverse size $r_s \approx \lambda_p$ deviates significantly from a sinusoidal wave form. Laser beams with a transverse Gaussian intensity distribution that is peaked on-axis drive a stronger plasma wave on-axis than off-axis. This leads to a longer nonlinear plasma wavelength [see eq.(2.31)] on-axis than for larger radii, resulting in transversely

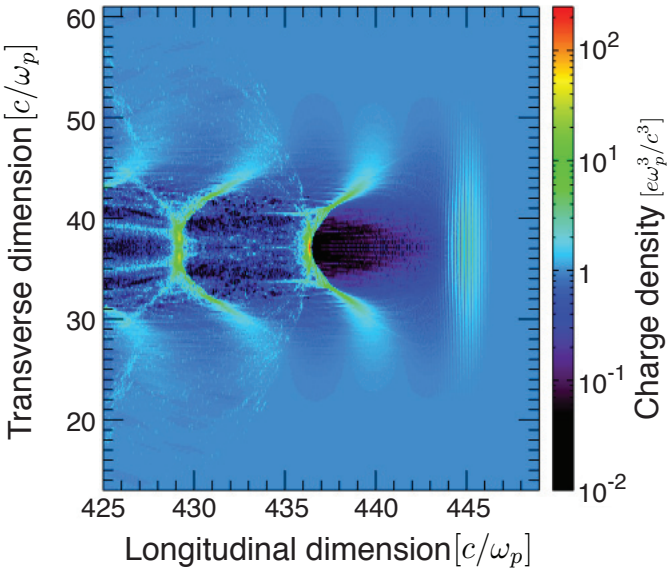

Figure 2.6. | 3D PIC simulation of a laser-wakefield accelerator. The figure shows a PIC simulation of the plasma-density distribution in a laser-wakefield accelerator. The laser pulse (moving from left to right) can be seen from the rapid oscillations in plasma density (on the right-hand side of the figure) with a wavelengths of one-half of the laser wavelength which are a result of the fast component of the ponderomotive force. It is trailed by a plasma wave that shows the transverse "horseshoe"-like shapes typical for the nonlinear regime. The parameter chose for this simulation are: $n_e = 5 \cdot 10^{18}\,\mathrm{cm}^{-3}$, $\tau_L = 40\,\mathrm{fs}$ (FWHM), $a_0 = 2.7$, $\lambda_L = 800\,\mathrm{nm}$, and $\omega_0 = 23\,\mu\mathrm{m}$ (FWHM). Figure courtesy of T. Mehrling.

"horseshoe"-shaped plasma wavefronts (see figure 2.6). Owing to these curved shapes, the threshold for wavebreaking is lowered, since the wave starts to break transversely [Bulanov et al., 1997] which can obviously not be described in 1D.

The Bubble Regime

In contrast to the linear ($a_0 \ll 1$) and the quasi-linear ($a_0 \gtrsim 1$) regime where electrons undergo mostly longitudinal plasma oscillations, their oscillations become transverse-dominated for highly nonlinear laser intensities ($a_0 \gg 1$). The laser field is so strong that it radially expels all electrons from a region around the axis, leaving behind a uniformly-dense column of ions. This regime was first described as the blowout-regime for electron beams [Rosenzweig et al., 1991] and for lasers [Mora and Antonsen, 1996] as driver. The ions, which remain stationary on the relevant time scales, pull back on the electrons causing them to return to the axis after about a plasma period; they overshoot and thereby create a plasma wave. If the laser intensity is sufficiently high, the wave breaks after the first oscillation which washes out all downstream features, leaving behind only a single ionic cavity. This cavity is a stable structure that trails the laser pulse at approximately its group velocity through the plasma. With the use of 3D PIC simulations this "**bubble**"-regime was explored for laser pulses shorter than λ_p as a

possibility to produce high-quality, ultrarelativistic electron bunches with small energy-spreads and low emittances [Pukhov and Meyer-ter Vehn, 2002]. The bubble provides fields that have ideal focusing and acceleration properties for electrons: at a certain longitudinal position, the accelerating field is constant with the transverse distance from the axis ($r_\perp$) and varies linearly with the distance to the laser pulse ξ, whereas the transverse fields are linear with the the radius $r_\perp$ and constant along ξ. Therefore, the bubble produces fields that are suited for an emittance-preserving acceleration even for a transverse finite-sized electron beam. These properties are due to the spherical shape of the bubble which is filled with a uniform ion background. The fields are given by [Kostyukov et al., 2004; Lu et al., 2006]

$$E_z(\xi) \simeq \frac{\xi}{2} k_p E_0 \tag{2.57}$$

$$E_r(r_\perp) - B_\Theta(r_\perp) = \frac{r_\perp}{2} k_p E_0 \tag{2.58}$$

where E_0 is the non-relativistic wavebreaking limit (eq 2.19). The maximum axial electric field is at the bubble radius $\xi = R$ and for a matched laser spot size (eq 2.60) has the amplitude of $E_{max}/E_0 = \sqrt{a_0}$.

Typical pulse lengths and intensities of laser systems used in LWFA experiments initially do not reach the threshold to operate in the bubble regime. However, during the pulse propagation in the plasma, the laser undergoes nonlinear evolution, such as self-steepening, self-shortening and self-focussing (see section 2.6.4) This results in a significantly higher laser intensity which can lead to a wake in the "bubble-like" regime with its typical ponderomotive blowout of electrons from the axis. The effect can be seen in PIC simulations that are explaining recent experimental results (see figure 2.8 and [Faure et al., 2004]).

Self-Injection into the Bubble Fields

Electrons can become self-injected directly into the accelerating phase of the bubble fields. In order to describe the injection process, electrons originating from different distances to the laser propagation axis have to be distinguished. Electrons, initially located off-axis, are mostly hit by the outer regions of the laser and get scattered outwards, never to return to the axis which means that they do not contribute to the acceleration process and their energy is lost. Most electrons that are transversely expelled by the laser from a region close to the axis wrap around the cavity in half circles. They compose a highly dense electron sheath of radius R around the bubble center $\xi = 0$ (see fig.2.7), that forms the boundary of the bubble. On the backside of the bubble, the trajectories of these electrons cross, leading to a strongly peaked electron density. For a sufficiently high laser intensity of $a_0 \gtrsim 2$, the bubble shape can be approximately modeled as a sphere [Kostyukov et al., 2004; Lu et al., 2006]. The electric potential produced by this cavity filled with uniformly dense, positive ions has a minimum at its radius and (increases toward and) peaks at its center. The electron density peak at the backside of the cavity further decreases this potential which leads to a global minimum, thus making it

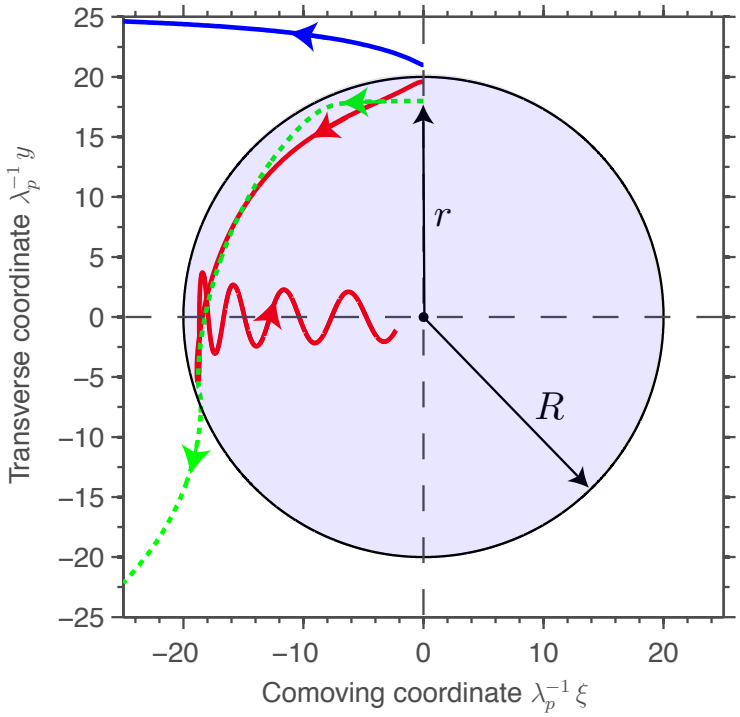

Figure 2.7. | Calculated trajectories of electrons with different initial conditions under the fields of a bubble. The bubble is modeled after [Kostyukov et al., 2009] as a sphere with a radius R having a uniform ion background (for the equations of motion, see Appendix section A.2). Electron trajectories under the influence of the bubble fields are numerically solved for the initial conditions: $p_y = 0$, $p_z = 0$ and a distance $r > R$ (blue), $r = R$ (red), $r < R$ (green) at $\xi = 0$. Only electrons with an initial position $r \leqslant R$ and a sufficiently small negative momentum can become trapped. However, since the electron moving on the green trajectory ($r < R$) traverses the fields of the bubble in the region $\xi > 0$, it has negative momentum p_z at $\xi = 0$ and therefore the probability of getting trapped is decreased. Not considered in this model is the electric potential from the electron density spike trailing the bubble. All distances are normalized to k_p.

most likely for electrons to get trapped in this region. Since these electrons are strongly accelerated to longitudinal velocities larger than β_p, some of them entering this region can get scattered into the bubble by the potential of this density peak and wavebreaking occurs. In order for electrons to get trapped by the bubble, their longitudinal velocity has to be at least that of the bubble ($\beta_z \gtrsim \beta_p$). This condition can be written in terms of only plasma and bubble parameters, namely the plasma wavelength λ_p, the bubble radius R and its phase velocity β_p [Kostyukov et al., 2009]

$$k_p R \gtrsim \sqrt{2}\gamma_p, \tag{2.59}$$

where $k_p = 2\pi/\lambda_p$ and $\gamma_p = (1 - \beta_p^2)^{-1/2}$. Therefore, electrons can only get trapped in a bubble with a sufficiently large radius R which is approximately the same as the laser

spot size w_0. PIC simulations have shown that a laser spot size matched to the laser intensity and the plasma wavelength oscillates only slightly if [Lu et al., 2007]

$$k_p R \simeq k_p w_0 = 2\sqrt{a_0}. \tag{2.60}$$

However, even for bubbles with sufficiently large radii, not all electrons entering the region of the potential minimum at the cavity backside will get trapped [Kostyukov et al., 2009]. Depending on their previous trajectories, they have gained different longitudinal momenta upon their arrival at the back of the bubble. This momentum can be determined by the electron's initial distance to the axis r_ξ at the position $\xi = 0$, where it is maximally displaced from the axis, its transverse momentum $p_r = 0$, and it is about to return toward the axis (see figure 2.7). The equations of motion of electrons under the influence of the bubble potential (which is modeled as a sphere with a radius R and a uniform ion background after [Kostyukov et al., 2009]) are numerically solved for different initial distances to the axis (for the equations see Appendix section A.2). The results can be seen in figure 2.7.

It can be seen that electrons at a distance $r > R$ at the longitudinal position $\xi = 0$ are deflected by the electron sheath surrounding the bubble and do not return to the axis and are lost. In this model, electrons that are located at $r = R$ (initially at rest: $p_r = p_z = 0$) are transversely pulled by the fields of the bubble into its outer rim and thus into its longitudinally accelerating fields. As they drift back through the bubble (in the co-moving frame ξ) they are accelerated in forward direction. By the time they have reached its back side they have gained enough momentum so that their longitudinal velocity is that of the bubble ($\beta_z = \beta_p$). These electrons are injected into the bubble and can be accelerated to high energies by its fields. The electrons get trapped at a position close to the axis, where their transverse momentum is maximal and thus undergo strong betatron motion during the acceleration which can be seen in figure 2.7.

Electrons that are inside the perimeter of the bubble ($r < R$) at the position $\xi = 0$, have already traversed parts of the decelerating (accelerating in direction $-\xi$) region of the bubble. Therefore, in contrast to the electrons at the border of the bubble, they are not at rest at the position $\xi = 0$, but have a momentum in the negative ξ-direction. If the magnitude of this momentum is too high the electrons cannot reach the phase velocity of the bubble, and therefore the probability of getting trapped decreases significantly.

This simple model does not consider two important processes that are known to exist from PIC simulations: (1) The Coulomb scattering of electrons at the potential produced by the electron density spike at the back of the bubble which can cause electrons that initially did not have a sufficiently high velocity to get trapped. (2) The space-charge fields of the captured electrons alter the fields of the bubble (beam loading) which can either lead to a termination of the injection or a change of its shape and continuous trapping. Which alternative occurs depends on the initial condition of several parameters such as the laser intensity, the focal spot size, the plasma density and the interplay of complex phenomena. Such phenomena include the evolution of the laser, the self-injection and shape of the trapped electron bunch, and their influence on the wake. However, a rigorous formalism of these processes is still subject to research and therefore

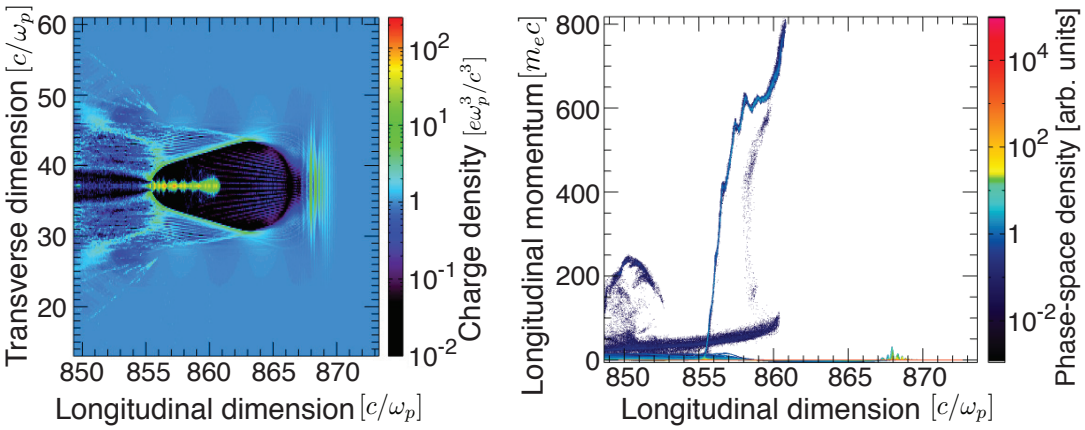

Figure 2.8. | 3D PIC simulation of a laser-wakefield accelerator after injection. The left-hand side of the figure shows the plasma density distribution of a laser-wakefield accelerator after injection (at a later time step compared to that shown in figure 2.6, using the same parameters). It can be seen that the laser pulse which has undergone a significant evolution (for comparison see figure 2.6) drives a bubble-like accelerating structure. The injected electrons cause the bubble structure to elongate which leads to a decreased velocity of the backside of the bubble and to continuous injection (see the main text). The right-hand side of the figure shows the electron spectrum along the longitudinal bubble coordinate. It can be seen that electrons that got injected at a later time (that are at a distance further back within the bunch) are accelerated over a shorter distance which causes their energy to be lower. Electron spectra qualitatively similar to that shown in this figure are detected in the experiments (see section 5.3), however they cannot be measured time-resolved along the electron bunch. Figure courtesy of T. Mehrling.

conclusions and parameter scans have to be simulated by PIC codes. If the self-injection is not terminated, these simulations show that the fields of the trapped electron bunch cause the back of bubble to elongate. As a result, the backside of the bubble is moving with a slower velocity than the front which effectively lowers the trapping threshold (at the backside) causing electrons to be injected continuously throughout the whole acceleration distance [Kalmykov et al., 2009; Kostyukov et al., 2009] (see figure 2.8). Electrons that got trapped at different times are accelerated over different distances and therefore the energy spectrum of the accelerated electron bunch usually consists of a narrow peak at high energies (electrons that got trapped first) with a broad background. In the second scenario, the repelling fields of the trapped electrons can also terminate the injection of additional electrons and the shape of the bubble is only slightly changed [Kalmykov et al., 2009].

Scalings for the Bubble Regime

By means of PIC simulations, it was found that short laser pulses with matched profiles in both transverse and longitudinal dimensions, evolve little and can be self-guided over

many Rayleigh lengths [Decker and Mori, 1994; Lu et al., 2007]. This scheme is based on relativistic self-guiding and thus the laser power has to be above the critical power $P > P_{\mathrm{crit}}$ (see section 2.6.4). Although the front of short pulses is not self-guided (see section 2.6.4), the laser can efficiently transfer energy to the wakefield and stay focused over many Rayleigh lengths. This is possible if the leading edge of the pulse locally pump depletes before it starts to diffract. The body of the pulse is guided in the low electron density channel. For a laser with a sufficiently high intensity gradient, the blowout of the plasma electrons happens mostly at the pulse front and, owing to this energy transfer, gets locally depleted. This causes the front edge to slowly etch backward resulting in a continuously decreasing pulse duration until the laser is fully depleted. For the highest efficiency, the time (distance) it takes for the laser to be completely eroded should be matched to the dephasing length of the electrons which sets a requirement on the minimal pulse duration. Furthermore, a spherical shape of the bubble with wakefields ideal for electron acceleration is achieved for intensities of $a_0 \gtrsim 4$. Therefore, the duration of the laser pulse needs to be sufficiently long to reach dephasing but not too long in order not to interact with the accelerated electron bunch. Additionally, it requires an appropriate (matched) spot size for a large enough bubble to ensure self-injection as well as a sufficiently high intensity in order to be in the bubble regime and drive a spherically shaped bubble.

Scalings for the **maximum energy gain** in the bubble regime can be estimated by assuming the linear accelerating field [eq.(2.57)] of a spherical bubble over the dephasing length of the bubble radius R which leads to [Lu et al., 2007]

$$\Delta E[\mathrm{GeV}] \simeq 1.7 \left(\frac{0.8}{\lambda_0[\mu\mathrm{m}]}\right)^{4/3} \left(\frac{10^{18}}{n_p[\mathrm{cm}^{-3}]}\right)^{2/3} \left(\frac{P[\mathrm{TW}]}{100}\right)^{1/3}. \tag{2.61}$$

Similar considerations, based on analytical and numerical studies have lead to [Gordienko and Pukhov, 2005]

$$\Delta E[\mathrm{MeV}] \simeq 0.1 \left(\frac{c\tau_L}{\lambda_0}\right) \sqrt{P[\mathrm{GW}]}, \tag{2.62}$$

where λ_0 is the laser wavelength, n_p the plasma density, P the laser power and τ_L the pulse duration. For the parameters of the experiment described below (laser power $P = 20\,\mathrm{TW}$ at a wavelength of $\lambda = 800\,\mathrm{nm}$, $a_0 = 1$, and a plasma density of $n_0 \simeq 5 \cdot 10^{18}$), equation 2.61 gives a maximum electron energy gain of $\Delta E = 340\,\mathrm{GeV}$. An energy of $\approx 220\,\mathrm{MeV}$ is detected in the experiments described below (see section 5.3), however the laser pulses utilized as driver do not fulfill the for equation 2.61 required $a_0 \gtrsim 2$.

The maximum **number of accelerated electrons** can be estimated by the energy balance between the field energy in the first bucket and the energy of N electrons at maximum kinetic energy. The result given in reference [Lu et al., 2007]

$$N \simeq 2.5 \times 10^9 \, \frac{\lambda_0[\mu\mathrm{m}]}{0.8} \sqrt{\frac{P[\mathrm{TW}]}{100}}, \tag{2.63}$$

has similar scaling (differing only in the coefficients) to the result given in reference

[Gordienko and Pukhov, 2005]

$$N \simeq 8.4 \times 10^9 \, \frac{\lambda_0[\mu\mathrm{m}]}{0.8} \sqrt{\frac{P[\mathrm{TW}]}{100}}. \tag{2.64}$$

For the experimental value given above, equation 2.63 leads to $N \simeq 1 \cdot 10^9$ electrons or a charge of 180 pC (the experiment described below typically show a charge of 10 pC).

These scalings suggest that lower plasma densities lead to higher electron energies. However, the critical power to get relativistic self-focusing P_{crit} (see section 2.6.4) increases with lower density and thus, a higher laser power is needed to ensure enough self-focusing before the laser diffracts. Furthermore, the bubble velocity increases for a lower plasma density, resulting in a higher threshold for the electron velocity in order to get self-injection. Therefore, a separation of the injection and the acceleration by either external injection or new injection schemes as discussed in the next section may be more attractive.

Disadvantages of the Bubble Regime

Although the self-injection process in the bubble regime contributes to the simplicity of the scheme, it comes with some intrinsic disadvantages: the injection mechanism is based on an interplay of many complex, highly nonlinear processes and therefore it is hard to control. As a result, the reproducibility of the electron beam and its properties are not (yet) sufficiently high for certain fields such as high-energy physics or free-electron lasers (FELs), both of which require short electron bunches with a high amount of charge, small energy spread and a very low emittance. The relatively high energy spread of a few percent is mainly caused by several factors:

(1) The not well-defined (sometimes even continuous) injection of electrons into the bubble field results in an acceleration over different distances and by different acceleration phases for individual electrons, thus leading to a large energy spread.

(2) The transverse injection results in strong betatron oscillations of the electrons during the acceleration. This leads to emission of synchrotron radiation which can extend into the hard X-ray range and decreases the electron energy. The radiated power depends on the transverse focusing force of the bubble fields (which increases linearly with the distance to the central axis) and thus on the initial transverse momentum of the electron. Therefore, electrons injected with different transverse momenta move on betatron trajectories with different amplitudes and emit radiation with different powers. As a result, even though electrons in a longitudinal slice of the beam experience the same accelerating field, they lose a different amount of energy through betatron radiation. This leads to an axially uncorrelated energy spread in the electron bunch which can increase the normalized energy spread throughout the electron beam [Michel et al., 2006b]. Furthermore, the transverse trapping leads to high transverse momenta and therefore to a relatively high transverse emittance.

(3) The electric field of the injected electrons screen the bubble fields for electrons that are injected at a later point in time (beam loading). This modifies (mainly) the

accelerating field of the bubble which results in a different energy gain for electrons at different longitudinal positions in the beam. A trapezoidal density profile of the accelerated bunch can flatten the accelerating field over the distance of the beam and thus minimize this effect [Tzoufras et al., 2008]. A larger bubble radius (which requires a higher laser power, eq.[2.60]) can sustain a higher number of electrons to be trapped or can mitigate the beam loading effects and thus decrease the energy spread for a more moderate beam current [Tzoufras et al., 2008].

(4) The extraction point of the electron beam from the accelerating fields and therefore the plasma is crucial to achieve a small energy spread. The beam should be accelerated over a distance slightly longer than the dephasing length and should be extracted when it is longitudinally symmetric about the position of the maximum momentum in phase-space $\xi_{\max}$ (see fig.[2.4]).

A comprehensive understanding of the bubble regime (including the injection mechanism) and the feasibility of achieving electron beams with a sufficiently high quality (enough electrons with a sufficiently small energy spread and a low emittance) is still an open topic and subject to present-day research.

2.7. Discussion

The estimations and formulas derived in the previous sections for the respective LWFA regimes can be used for comparison with experimental results. The experiments described below (see section 5.3) are usually performed with plasma densities of $n_0 \simeq 5 \times 10^{18}\,\mathrm{cm}^{-3}$ which corresponds to a plasma wavelength of $\lambda_p \simeq 15\mu\mathrm{m}$. With equation (2.36), the 3D plasma wave phase velocity can be estimated to be $\gamma_p \simeq 4.7$. In order to get electron injection for this plasma density in the case of a **nonlinear wakefield**, according to 1D theory, the laser has to drive a plasma wave with an amplitude of $E_{\max} \simeq E_{\mathrm{WB}}$. Through equations (2.33) & (2.34), this results in a required minimal laser intensity of $a_0 \simeq 4$. In order to drive an accelerator in a pure **bubble** regime and to get self-injection at these plasma densities, it can be calculated with equation (2.59) that the bubble radius has to be $R \geqslant 16\,\mu\mathrm{m}$. In order to drive such a bubble, a laser intensity of $a_0 \simeq 11$ is required (see equation (2.60)). However, experiments demonstrate the acceleration of self-injected electron beams with laser pulses of significantly smaller intensities.

Current state-of-the art laser systems typically cannot reach the required intensities to operate in a pure bubble regime. Therefore both the analytical model of the electron injection in a pure bubble regime (equation (2.59)) and the 1D theory of nonlinear wakefields (eqs.(2.33 & 2.34)) cannot completely describe the underlying processes. Additionally, a comprehensive description of multidimensional wavebreaking and its dependence on various parameters is currently lacking. Therefore, various aspects of the process can only be described separately or by means of PIC simulations. In 3D, the plasma wave shows transversely "horseshoe" -shaped plasma wavefronts which lead to transverse electron trapping [Bulanov et al., 1997], much different from 1D wavebreaking. Specifically, when the curvature radius of the wavefronts is comparable to the electron fluid

displacement, the injection resembles rather a thermalization [Gordienko and Pukhov, 2005]. PIC simulations show that the threshold can be lowered by almost one order of magnitude in comparison to longitudinal wavebreaking [Pukhov and Meyer-ter Vehn, 2002]. Furthermore, through the complex nonlinear evolution of a laser pulse in the plasma (self-focusing, self-steepening, etching, etc, see section 2.6.4) the phase velocity of the plasma wave can be lower as analytically estimated (equation (2.36)) and the laser intensity can increase. These effects can lead to a decrease of the required laser intensity to get electron self-injection. Moreover, the bubble can get elongated through beam loading which leads to a lower phase velocity of the backside of the bubble, thereby causing an additional decrease of the injection threshold.

The lack of a comprehensive theory complicates the task of selecting parameters to achieve the injection and acceleration of high quality electron beams. Therefore, only constraints on the parameters which arise from the separate descriptions (each with different underlying physical phenomena) of the whole process, can be given: The upper limit of the **laser beam spot size** should be on the order of the plasma skin depth $w_0 \simeq 1/k_p$ in order not to undergo filamentation ([Thomas et al., 2009] & see section 2.6.4). However, the bubble regime requirement for getting electron injection requires a minimum (matched) beam size of $w_0 \gtrsim \sqrt{2}k_p^{-1}\gamma_p$ [Kostyukov et al., 2009]. Furthermore, the **laser pulse duration** should be less than the laser focal spot size $c\tau_L \lesssim w_0$, in order for the laser not to interact with the the accelerated electrons and to mitigate filamentation and the deterioration of the electron beam. The lower boundary for the pulse duration is given by the maximum energy gain that the electrons can reach before the laser pump depletes through etching of its front edge (see section 2.6.5). The **plasma density** should be chosen high enough to get a sufficiently slow plasma wave phase velocity in order for electrons to get trapped. On the other hand, the density should not be chosen too high in order to suppress filamentation and continuous trapping by a low injection threshold. PIC simulations describe the complete acceleration process, including dynamic nonlinear effects such as the laser evolution as well as the plasma feedback onto the laser, and thus can be used for a more detailed selection of parameters. However, since these simulations are very computationally intensive, it is difficult to do the extensive parameter scans that are necessary to determine the precise parameters.

2.7.1. Electron Beam Properties and Experimental Results

Electron bunch duration
Electron beam emittance
Maximum accelerated charge & energy spread

The following section gives a brief overview of the electron beam quality and state-of-the art experimental results.

Electron Bunch Duration

In addition to the small accelerator dimensions of LWFAs, the accelerated electron bunches are assumed to be of an intrinsically ultrashort duration, on the order of just a few femtoseconds. This estimation is based on the fact that the electron bunch length is a fraction of the accelerating structure which is on the order of the plasma wavelength (which, depending on the plasma density, is a few tens of femtoseconds). More precisely, high-quality electron bunches (in terms of few-percent energy spread and small emittances) indicate a termination of the acceleration process at a phase where both the longitudinal as well as the transverse electric fields are linear. Since the accelerating and the transverse focusing fields are out of phase by a factor of $\pi/2$, this requirement is fulfilled for approximately a quarter of the plasma period (see figure 2.2). Therefore $\lambda_p/4 \simeq$10 fs can be regarded as an estimation for an upper boundary on the electron pulse duration. This intuitive picture is confirmed by 3D Particle-in-Cell simulation, from which pulse durations of 10 fs [Lu et al., 2007] and even sub-10 fs [Geissler et al., 2006; Pukhov and Meyer-ter Vehn, 2002], depending on the laser and plasma parameters, can be deduced. However, the electron bunch duration has not yet been measured to sufficiently high resolution. Measurements using the electro-optical sampling technique [Debus et al., 2010; van Tilborg et al., 2006] yield a pulse duration of $\sim$50 fs, but this method is limited by the bandwidth of the electro-optical crystals and therefore has to be considered as an upper boundary. Furthermore, the accelerated electron bunch is perfectly synchronized to the driver laser which is also true for X-ray radiation of lightsources driven by these bunches and could thus be used as a low time-jitter trigger for ultrafast pump-probe experiments.

Transverse Electron Beam Emittance

Simulations and transverse wakefield dimensions (see section 2.4.1) indicate a geometric (non-normalized) transverse emittance on the order of $\epsilon \simeq 1\,\mu$m mrad. This estimation is based on the assumption that the transverse emittance can be determined in the focus of the beam ($\alpha_{\mathrm{Twiss}} = 0$) by the product of the electron beam size and divergence. The electron beam size in the plasma accelerator is estimated to be a few μm. Imaging experiments that use the betatron radiation emitted by the electron bunch suggest a source size of below 3 μm [Mangles et al., 2009]. The divergence of an electron beam with an energy of 200 MeV after exiting the plasma is measured to be $\simeq$ 1mrad [Osterhoff et al., 2008]. This leads to the aforementioned estimate of the transverse emittance. This assumption is only valid for monoenergetic electron beams as well as a beams with Gaussian spatial- and transverse-electron-momentum distributions. Due to the linear transverse wakefields and the immediate coupling of the self-injected electrons to the accelerating phase, their transverse momentum at the moment of injection is conserved during the acceleration process which means that the normalized emittance ($\epsilon_n = \beta\gamma\,\epsilon$) is expected to be a constant. However, similar to the bunch duration, the electron beam emittance has not yet been experimentally measured with sufficiently high precision. An upper value of $\epsilon_n = 2.7 \pm (0.9)$ mm mrad for 55 MeV electron beams is given by [Fritzler

et al., 2004], using the pepper-pot technique. Simulations indicate that an accelerator driven by laser beams composed of transverse higher-order Hermite-Gaussian modes the emittance can be lowered. In the quasi-linear regime $a_0 \simeq 1$, such pulses could be used to both decrease the transverse momentum of electrons during their injection and tailor the strong transverse wakefields which can lead to a better control of the transverse emittance [Michel et al., 2006a].

Charge & Energy Spread

The ultimate limit on the amount of charge accelerated to a certain electron energy is given by the transfer of driver-laser energy to the electrons via the plasma wave. However, distortions of the bubble shape and screening of the accelerating fields by other electrons set a limit on the maximum charge in high-quality electron beams. The shaping of the injected electron distribution can mitigate the deterioration of the beam quality (energy spread, emittance, etc) by such effects: The accelerating fields in the bubble regime are flat over the whole electron bunch for a triangular-shaped bunch density profile which leads to a low energy spread [Tzoufras et al., 2008]. The maximum number of electrons in such a **triangular-shaped** bunch distribution is given by [Tzoufras et al., 2008]:

$$Q[\mathrm{nC}] = 4.7 \times 10^6 \frac{E_0}{E_{\max}} \sqrt{\frac{1}{n_0[\mathrm{cm}^{-3}]}}\, (k_p R)^4 \simeq 7.5 \times 10^7 \sqrt{\frac{1}{n_0[\mathrm{cm}^{-3}]}}\; a_0^{3/2}, \qquad (2.65)$$

where a matched laser spot size (eq 2.60) and $E_{\max}$ for a matched laser from equation (2.57) were used. For an accelerator with a plasma density of $n_0 = 1.2 \times 10^{18}\mathrm{cm}^{-3}$ and a 200 TW laser (to ensure a pure bubble regime), this leads to an accelerated charge of 550 pC which is just slightly below the value calculated with the scaling found in [Lu et al., 2007] (eq 2.63).

Experimentally beams with a charge of typically a few hundred pico-Coulomb and few-percent energy spread have been measured [Faure et al., 2004; Geddes et al., 2004; Mangles et al., 2004]. The relatively high energy spread due to the electron injection mechanism can be decreased by separating the injection process from the acceleration (see section 2.7.2): Experiments with the counter-propagating injection scheme have shown energy spreads of $\simeq 1\%$ although with a charge of only 10 pC [Rechatin et al., 2009]. Another scheme with a plasma density downramp as electron injector holds promise to accelerate electron bunches with 0.1% energy spread [Geddes et al., 2008].

Maximum Energy Gain

Laser diffraction can be overcome by guiding of the pulse (see section 2.6.3). Experiments using a plasma channel as a guide, resulted in a maximum accelerated electron energy of 1 GeV [Leemans et al., 2006].

2.7.2. Advanced Injection Schemes

Counter-propagating pulse injection
Plasma density transitions

Most electron beam parameters in the bubble regime (see section 2.6.5) are determined by highly nonlinear processes which leads to self-trapping and is therefore difficult to control. A separation of the injection process from the subsequent acceleration promises a higher quality in crucial electron beam parameters: (1) A controlled injection could lead to short electron bunches with a low energy spread, since the trapping occurs at a well-defined position without any further (continuous) injection. (2) The transverse emittance can be decreased through a longitudinal rather than a transverse injection. (3) The control over the injection process gives a possibility to shape the injected electron beam and thus counteracting beam loading which is a reason for a high energy spread and a deterioration of the electron beam through a deformation of the accelerating structure. The subsequent acceleration can be performed in a quasi-nonlinear wakefield ($a_0 \simeq 1$) which does not rely that heavily on non-linear effects and thus is easier to control and stabilize. Additionally, the separate injection schemes require lower laser intensities.

Electron Injection by Colliding Laser Pulses

In this scheme, two counter-propagating laser pulses are employed: a high-intensity pump pulse that drives a wakefield with an amplitude well below wavebreaking and a less intense, counter-propagating injection pulse [Esarey et al., 1997]. When the two laser pulses collide, they form a beat wave with a slow phase velocity. Background electrons with an initial momentum too low to get trapped are longitudinally accelerated by the ponderomotive force associated with the slow beat wave. They can gain a sufficiently high momentum to get trapped in the large amplitude plasma wave driven by the pump pulse and can get accelerated to high energies. Since the amplitude of the pump pulse is not high enough to lead to wavebreaking on its own, electron injection occurs only in the well-defined region, where the colliding pulses overlap.

In this scheme, the duration of the injection and thus the number of injected electrons as well as their injection momentum can be controlled by the amplitude of the injection pulses and the duration of the counter-propagating pulse, respectively. The electron energy gain can be controlled by the delay between the colliding injection pulses and therefore by the acceleration distance left in the plasma. The control over the injection can lead to higher beam quality in terms of pulse duration, energy spread and emittance. First promising results using the two-laser scheme [Faure et al., 2006] have matured into the acceleration of an electron beam with an FWHM-energy spread of 1%, however with a relatively low charge of only 10 pC [Rechatin et al., 2009].

Electron Injection via a Density Downramp

One other promising possibility to get control over the electron injection is to implement a longitudinal plasma density downramp into the gas target [Bulanov et al., 1998]. The local phase velocity of a plasma wave that is moving through a density downramp decreases. It can be reduced to approximately the plasma fluid velocity which leads to the injection of cold background plasma electrons.

The reduction of the phase velocity can be understood by looking at the distance of the electric potential peak of the plasma wave ($\xi_{\max}$ in fig.2.4) with respect to the driver laser which is approximately at a distance $\Delta\xi \simeq \lambda_p/2$. In the region with the higher plasma density before the density downramp, the distance $\Delta\xi$ is smaller than in the region of the lower plasma density, since the plasma wavelength gets longer for a lower density ($\lambda_p \sim n_e^{-1/2}$). Therefore, even though the group velocity of the driver laser increases for lower densities, the local phase velocity of a plasma wave going through a density transition *decreases*. The local phase velocity of the wave is given by [Esarey et al., 2009]

$$\frac{v_p}{c} \simeq 1 - \frac{\xi}{2n_e}\frac{\mathrm{d}n_e}{\mathrm{d}z}, \tag{2.66}$$

where $\xi < 0$ is a distance in the wake, measured from the driving laser pulse. Thus, for a density downramp ($\mathrm{d}n_e/\mathrm{d}z < 0$), the wake phase velocity decreases. In 3D PIC simulation it can be seen that a density reduction from $4.4\times10^{18}\,\mathrm{cm}^{-3}$ to $2.75\times10^{18}\,\mathrm{cm}^{-3}$ over a distance of 10 μm (considering a laser wavelength of 1 μm) leads to trapping of an abundant number of electrons at the density transition [Brantov et al., 2008].

In order to accelerate electrons to high energies, the plasma density is kept constant and below the wavebreaking limit after the transition, and thus the accelerator region is directly connected to the injector. Since the electrons are injected into the accelerating phase of the wakefield, no external timing or beam transport is needed. The electrons are injected at a well-defined position with a certain transverse and longitudinal momentum distribution. Subsequently, they get equally accelerated by the same wakefield phase, leaving their initial transverse momenta and the absolute longitudinal momentum spread constant. Since their longitudinal momentum increases, this leads to electron beams with a small relative energy spread as well as a small transverse emittance.

Experimentally, the downramp-injector part of the scheme has been shown to deliver low energy electron beams with a relatively low longitudinal and transverse momentum spread and a high amount of charge [Geddes et al., 2008].

2.8. LWFA: List of Symbols

Symbol	Description
a_0	Amplitude of laser pulse intensity normalized to $m_e c^2$
λ, ω	Central wavelength, angular frequency of laser pulse
$k = 2\pi/\lambda$	Wavenumber of the laser pulse
η	Plasma index of refraction
v_{ph}, v_{g}	Phase/ group velocity of the laser pulse
λ_p, ω_p	Plasma period / plasma frequency
λ_{Np}	Non-linear plasma period
$k_p = 2\pi/\lambda_p$	Wavenumber of the plasma wave
n_0	Unperturbed plasma (electron) density
$\delta n = n - n_0$	Plasma density perturbation
$\xi = z - v_p t$	Co-moving coordinate (distance from position of laser pulse)
$\phi = e\Phi/(m_e c^2)$	Normalized potential of plasma wave
E_z	Longitudinal electric field of the plasma wave
E_0	Nonrelativistic wavebreaking limit
E_{max}	Maximum electric field amplitude of plasma wave
E_{WB}	Wavebreaking limit for nonlinear plasma wave
ξ_{min}, ξ_{max}	Position of wakefield potential minimum/maximum
L_d	Dephasing length
L_{dp}	Pump depletion length
R	Radius of bubble

2.9. Back of the envelope formulas

- plasma frequency:

$$\omega_{p,0} = \sqrt{\frac{e^2 n_0}{m_e \epsilon_0}} = 5.7 \times 10^4 \sqrt{n_0\,[\mathrm{cm}^{-3}]}$$

- non-relativisitc plasma wavelength:

$$\lambda_{p,0}[\mu\mathrm{m}] = \frac{2\pi c}{\omega_{p,0}} = 3.33 \times 10^{10} \left(n_0[\mathrm{cm}^{-3}]\right)^{-1/2}$$

- normalized vector potential of the laser field:

$$a_0 \simeq \lambda[\mu\mathrm{m}] \cdot \sqrt{\frac{I_0[\mathrm{W/cm}^2]}{1.4 \times 10^{18}}},$$

- laser power $P = \pi r_0^2 I_0/2$: (r_0 is the laser spot size)

$$P[\mathrm{GW}] \simeq 21.5 \times \left(\frac{a_0 r_0}{\lambda}\right)^2$$

- cold non-relativistic (linear) wavebreaking limit: (all plasma electrons oscillate with ω_p which corresponds to $\delta n = n_0$)

$$E_0\,[\mathrm{V/m}] \simeq 96\sqrt{n_0\,[\mathrm{cm}^{-3}]}$$

- cold relativistic (nonlinear) wavebreaking limit

$$E_{\mathrm{WB}} = \sqrt{2(\gamma_p - 1)}\cdot E_0$$

- plasma wave phase velocity

$$\gamma_p = \frac{\omega}{\omega_p}\sqrt{\frac{a_0^2+2}{2}}$$

- critical power for relativistic self-focusing:

$$P_{\mathrm{crit}}[\mathrm{GW}] \simeq 17.4\left(\frac{\omega}{\omega_{p,0}}\right)^2$$

- dephasing length ($a_0 \ll 1$)

$$L_d \simeq \frac{\lambda_p^3}{\lambda^2}$$

- energy gain limited through dephasing (analytical formula) ($a_0 \ll 1$)

$$\Delta W_d \simeq 1260\cdot\frac{I\,[\mathrm{W/cm}^2]}{n_0\,[\mathrm{cm}^{-3}]}$$

- energy gain limited through dephasing (numerical, bubble regime) ($a_0 > 2$)

$$\Delta E[\mathrm{GeV}] \simeq 1.7\left(\frac{0.8}{\lambda_0[\mu\mathrm{m}]}\right)^{4/3}\left(\frac{10^{18}}{n_p[\mathrm{cm}^{-3}]}\right)^{2/3}\left(\frac{P[\mathrm{TW}]}{100}\right)^{1/3}$$

- number of accelerated electrons (numerical, bubble regime) ($a_0 > 2$)

$$N \simeq 2.5\times 10^9\,\frac{\lambda_0[\mu\mathrm{m}]}{0.8}\sqrt{\frac{P[\mathrm{TW}]}{100}}$$

plasma density n_0 [cm^{-3}]	5×10^{18}
plasma frequency $\omega_{p,0}$ [Hz]	1.3×10^{14}
plasma wavelength $\lambda_{p,0}$ [μm]	15
laser frequency ω [Hz] ($\lambda = 800$nm)	2.36×10^{15}

Conversions

- pressure in plasma density (for H):
  100 mbar $\simeq 2.5 \cdot 10^{18}\ \frac{1}{\mathrm{cm}^3}$
- charge:
  $1\,\mathrm{nC} \simeq 6 \times 10^9$ electrons
- photon energy E_{ph} to wavelength:
  $\lambda[\mathrm{nm}] = 1240/E_{ph}[\mathrm{eV}]$

3. UNDULATOR RADIATION THEORY (UR)

3.1. Introduction

The chapter discusses the physics of undulator radiation (UR). The radiation is emitted from relativistically propagating electrons that get transversely accelerated by a sinusoidal magnetic field (produced by an undulator) and emit a brilliant, highly-directed beam of synchrotron radiation. Undulator radiation can be widely tunable, currently ranging in wavelength from microwaves, through terahertz radiation and infrared, to the visible spectrum, to ultraviolet, to X-rays. Additionally, it is linearly polarized and has a narrow spectral bandwidth.

The properties of this radiation can be calculated by starting from the emission of a single relativistic electron under any arbitrary motion. In order to get a simple analytical expression, several approximations that take advantage of the undulator radiation characteristics can be made: owing to the highly collimated beams, the small-angle and far-field approximations can be applied. The periodicity of the undulator field leads to a further simplification (section 3.3). The photon beam size and divergence of the emission of a single electron or filament electron beam (that is an electron beam in which all electrons have the same energy and travel along the same trajectory) can be approximated by Gaussian distributions (section 3.4.1). The radiation from an electron beam with a finite transverse emittance ("thick" electron beam) can be calculated by a convolution of the electron beam distribution with the emission of a single electron (section 3.5.2). The brilliance (section 3.5.1) is a measure of the flux, focusability and transverse coherence of the undulator radiation. Furthermore, the brilliance can in many aspects be thought of a photon phase-space distribution. Since it is invariant under any linear transformation of the phase space, it can be used to propagate the radiation over a distance or through optical components by the Ray-Transfer Matrix formalism (see sections 3.5.3, 3.7).

The fundamentals of synchrotron radiation are described only briefly since they are presented comprehensively in many textbooks, see for example [Onuki and Elleaume, 2003] or [Clarke, 2004]. The properties as well as the propagation of undulator radiation is discussed in more detail since they are necessary for the explanation of the experimental results. The section about the propagation of the undulator radiation is based on [Kim, 1989] but slightly extended to give explicit expressions that are necessary for the model to describes the experimental observations.

3.2. Overview

Undulators are devices that consist of alternating magnetic dipoles which produce sinusoidal transverse magnetic fields with amplitude B_0 and period λ_u (see fig 3.1). They are characterized by the deflection parameter which is defined as [Onuki and Elleaume, 2003]

$$K = \frac{eB_0\lambda_u}{2\pi mc^2} \simeq 0.93\ B_0[\mathrm{T}]\,\lambda_u[\mathrm{cm}] \tag{3.1}$$

In the rest frame of the relativistic electrons moving through this field, λ_u is contracted by the Lorentz factor γ which is defined as the total electron energy E in units of the electron rest energy $m_o c^2$. The undulator field causes the electrons to oscillate transversely with an amplitude proportional to K, and as a result of this acceleration to emit radiation. In the laboratory frame, this emission occurs in a narrow cone in the forward direction. The measured wavelength is once more reduced by a factor of γ because of the Doppler shift which varies with the detection angle θ. Taking into account the reduced longitudinal electron velocity caused by the transverse quivering motion, the detected wavelength for the n-th harmonic is

$$\lambda_n = \frac{\lambda_u}{2n\gamma^2}\left(1 + \frac{K^2}{2} + \gamma^2\theta^2\right). \tag{3.2}$$

Typical values are: $\lambda_u \simeq$ few cm, $\gamma \simeq 10,000$ and $K \simeq 1$, leading to an emission wavelength in the X-ray range.

3.3. Radiation of a Charge under arbitrary Motion

Radiation of a moving charge
Electric field in the near- and the far-field
Approximations for a linear undulator
Electric fields in the time and frequency domain
Undulator harmonics

An electron emits radiation at the time τ and the position $\vec{R}(\tau)$. An observer located at the position $\vec{r}$ detects the electric field at the time t after it has travelled a distance $\vec{D}(\tau)$ of

$$t = \tau + \frac{D(\tau)}{c}, \tag{3.3}$$

where $\vec{D}(\tau)$ is the distance between the electron and the observer at the time τ and $\hat{n}$ is the normalized unit vector pointing from the electron to the observer:

$$\hat{n}(\tau) = \frac{\vec{r} - \vec{R}(\tau)}{|\vec{r} - \vec{R}(\tau)|} = \frac{\vec{D}(\tau)}{D(\tau)} \tag{3.4}$$

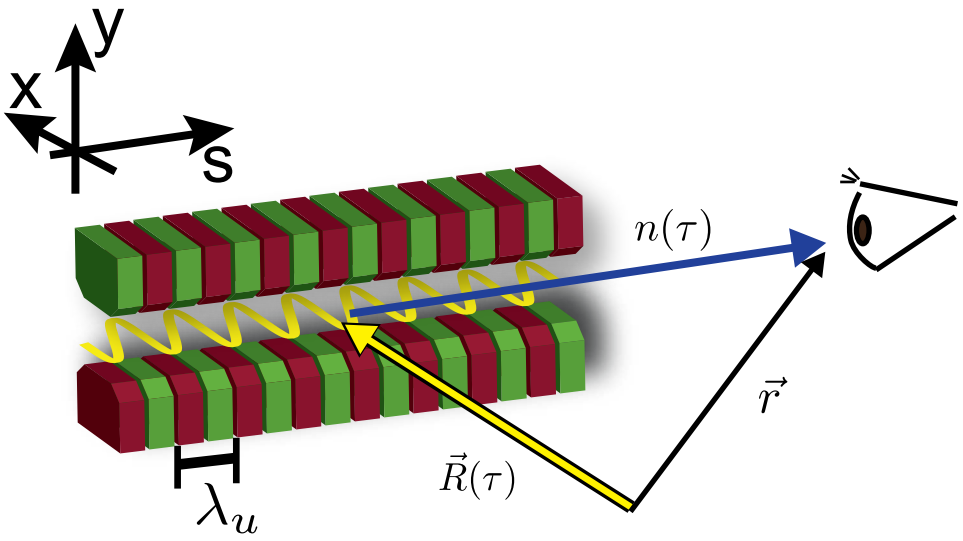

Figure 3.1. | **Coordinate system.** An electron is moving along the s-axis through an undulator on a transverse (in x-direction) sinusoidal trajectory (yellow). Its position at the time τ is $\vec{R}(\tau)$. An observer at the position $\vec{r}$ detects the radiation emitted by the electron. The undulator has a period of λ_u.

The emitted electric field of a charged particle under any arbitrary motion moving with relativistic speeds can be derived from the Liénard-Wiechert potentials [Jackson, 1998] and in the frequency domain it reads [Onuki and Elleaume, 2003]:

$$\vec{E}(\vec{r},\omega) = \frac{\mathrm{i}e\omega}{4\pi c\epsilon_0}\int_{-\infty}^{\infty}\frac{\vec{\beta}-\hat{n}\,(1+\mathrm{i}c/(\omega D))}{D}\exp\left[\mathrm{i}\omega\left(\tau+\frac{D}{c}\right)\right]\mathrm{d}\tau, \tag{3.5}$$

where $\vec{\beta}$ is the velocity of the electron, normalized to the speed of light c. Numerically, this equation can be efficiently solved using the Fast Fourier Transform algorithm (FFT). Most simulations that are performed to compare to the experimental results (see section 6.2) are conducted with the code SRW [Chubar and Elleaume, 1998] which evaluates this near-field equation. Analytical results, however, can be obtained with the **far-field approximation**, in which velocity fields are neglected and $\hat{n}$ is a constant [Onuki and Elleaume, 2003]. With this approximation, the field can be written in the time domain as [Feynman et al., 1970; Onuki and Elleaume, 2003]

$$E(\vec{r},t) = \frac{e}{4\pi\epsilon_0 cD\cdot(1-\vec{\beta}\hat{n})}\frac{\mathrm{d}}{\mathrm{d}\tau}\left(\frac{\hat{n}\times(\hat{n}\times\vec{\beta})}{1-\vec{\beta}\hat{n}}\right)\Bigg|_{\mathrm{ret}} = \frac{e}{4\pi\epsilon_0 cD}\,\hat{n}\times\left(\hat{n}\times\frac{\mathrm{d}^2}{\mathrm{d}t^2}\vec{R}(\tau(t))\right), \tag{3.6}$$

where $|_{\mathrm{ret}}$ indicates that the expression is evaluated at the retarded time. It can be seen that the field is proportional to the apparent acceleration of electron as seen by the observer, projected into the plane normal to the direction of emission $\hat{n}$. In the

frequency domain, the field can be written as [Onuki and Elleaume, 2003]

$$\vec{E}(\vec{r},\omega) = \frac{-\mathrm{i}e}{2c\epsilon_0 D}\,\exp\left(\mathrm{i}\frac{\omega}{c}\hat{n}\vec{r}\right)\vec{H}(\hat{n},\omega), \tag{3.7}$$

where

$$\vec{H}(\hat{n},\omega) = \frac{\omega}{2\pi}\int_{-\infty}^{\infty}(\hat{n}-\vec{\beta})\exp\left[\mathrm{i}\omega\left(\tau-\frac{\hat{n}\vec{R}}{c}\right)\right]\mathrm{d}\tau. \tag{3.8}$$

Most physical quantities, such as the flux, brilliance as well as size and divergence of the radiation can be described by the dimensionless vector $\vec{H}$. It can be shown that equation (3.7) is the Fourier transform of the electric field seen by the observer in time domain, equation (3.6).

In the case of a periodic structure, such as an undulator, $\vec{H}$ can be decomposed into a sum, where each term describes a narrow frequency range around the resonance frequency of the corresponding harmonic. In the case of a long undulator (many undulator periods N_u), $\vec{H}$ can be approximated as [Onuki and Elleaume, 2003]

$$\vec{H}(\theta_x,\theta_z,\omega) \simeq N_u\sum_{n=1}^{\infty}(-1)^{n(N_u-1)}\,\vec{h}_n(\theta_x,\theta_z)\,\mathrm{sinc}\left[\pi N_u\left(\frac{\omega}{\omega_1}-n\right)\right] \tag{3.9}$$

where n is the number of the harmonic of the radiation, $\mathrm{sinc}(x) = \sin(x)/x$, and ω_1 is the frequency of the fundamental. In the case of a linear undulator $\vec{h}_n$ can be written as

$$\begin{aligned}\vec{h}_n(\theta_x,\theta_z) &= \frac{n}{\lambda_1}\int_0^{+\lambda_u}\begin{pmatrix} K/\gamma\cos(2\pi(s/\lambda_u))-\theta_x \\ -\theta_z\end{pmatrix} \\ &\times \exp\left[\mathrm{i}2\pi n\left(\frac{s}{\lambda_u}+\frac{-2\gamma\theta_x K\sin(2\pi(s/\lambda_u))+K^2/4\sin(4\pi(s/\lambda_u))}{2\pi(1+(K^2/2)+\gamma^2(\theta_x^2+\theta_y^2))}\right)\right]\mathrm{d}s,\end{aligned} \tag{3.10}$$

where λ_u is the undualtor period, K the deflection parameter (see equation 3.1) and λ_1 the wavelength of the fundamental (see equation 3.2).

The spectral characteristics of the undulator radiation are described by electric fields in the time and frequency domains (equation 3.6 & 3.7). Owing to the sinusoidal magnetic field of the undulator, the electrons are forced onto a sinusoidal trajectory and thus undergo a periodic acceleration. The electric field seen by an observer (fig 3.2) is proportional to the acceleration of the apparent motion $\mathrm{d}^2/\mathrm{d}t^2\vec{R}(\tau)$ (the acceleration seen by the observer) of the electron (equation 3.6). The electron executes not only a transverse oscillation but also a longitudinal oscillation which in the electron rest frame resembles a figure-eight motion. Thus the emitted electric field in the time domain is not composed of a pure sinusoidal shape (but for $K < 1$ the shape is very close). The electric field in the frequency domain is the Fourier analysis of the field in the time domain. Its observable, the angular spectral flux, is proportional to $|\vec{H}(\theta_x,\theta_z,\omega)|^2$ (equation 3.11).

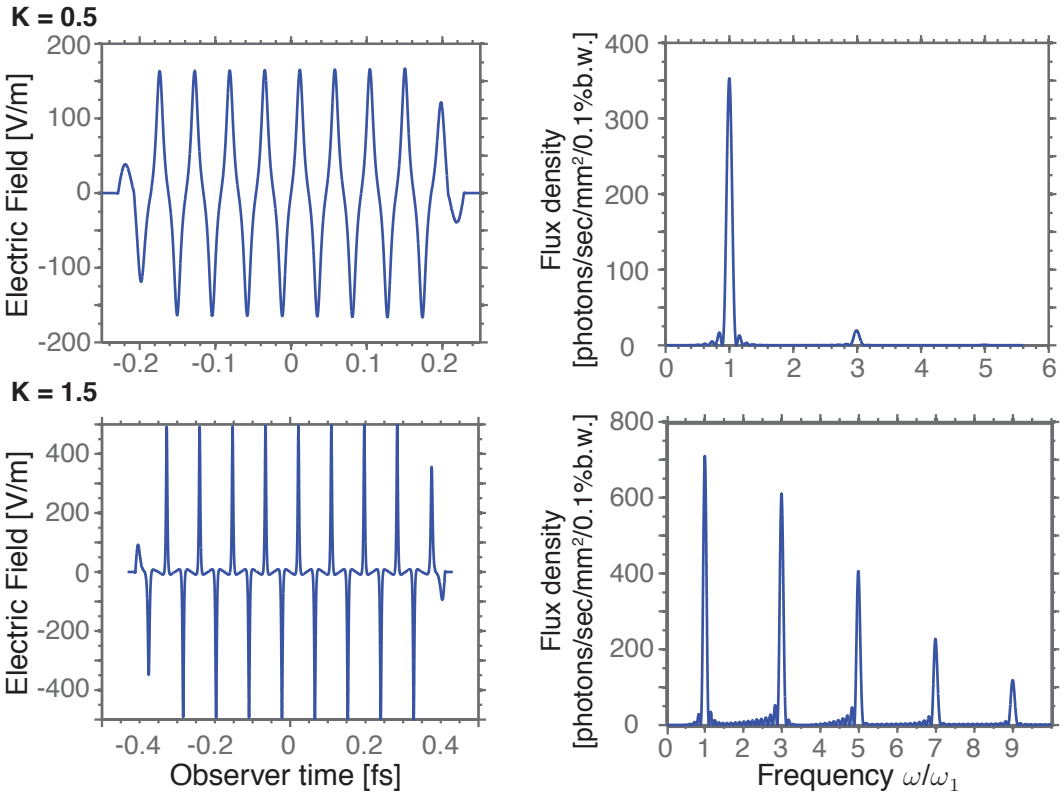

Figure 3.2. | **Electric fields in the time domain and the corresponding spectral flux density.** The left hand side depicts the electric fields of a single electron in the time domain and the right hand side the associated angular spectral flux for a $K = 0.5$ (upper) and a $K = 1.5$ undulator (lower part of the figure). Both fields are observed on-axis.

For the largely sinusoidal shape of the temporal field in the case of $K < 1$, the Fourier transform mainly consists of the fundamental and has small contributions from higher harmonics (see upper part of fig 3.2). For $K > 1$, the figure-eight motion of the electron gets more pronounced. In this case, the apparent electron trajectory (and acceleration) and thus the electric field strongly deviate from a pure sinusoidal shape: it exhibits a spiked temporal structure. Physically, this means that the transverse deflection of the electron (amplitude $\propto K$) is larger than the angle of the radiation emission cone and the observer only detects short flashes of radiation, similar to wiggling a searchlight beam. This regime is called the wiggler regime. In order to Fourier analyze this temporal structure, a higher number of harmonics must be used, as can be seen in the lower part of fig 3.2. Since the temporal shape of every period of the observed field has a point-symmetry, the spectrum is made up of only odd harmonics.

However, for radiation that is detected off-axis, the point-symmetry is not valid anymore. The temporal shape in fig 3.3 shows that the distance between two successive (positive and negative) peaks becomes asymmetric, since they are emitted at different distances to the observer. Thus the spectrum also consists of even harmonics. Further-

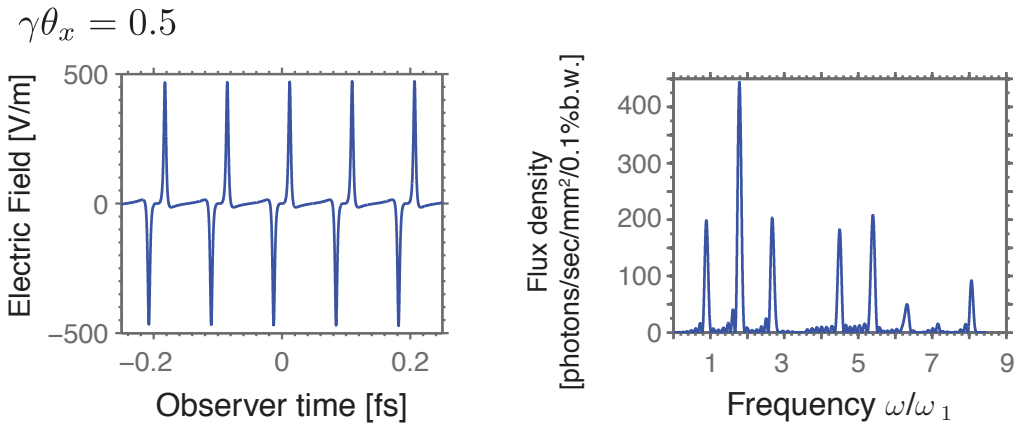

Figure 3.3. | **Off-axis fields in the time domain and the corresponding spectral flux density.** $K = 1.5$ undulator . Observation angle $\gamma\theta_x = 0.5$, $\gamma\theta_y = 0$; ω_1 is the on-axis resonance frequency

more, it can be seen in the spectrum (right hand side in 3.3) that the amplitudes of the odd components get smaller and are shifted to smaller frequencies with a larger angle, as can be expected from the resonance condition, equation (3.2).

3.4. Angular Spectral Flux of a Filament Electron Beam

Angular Spectral Flux
Approximation by a Gaussian beam
UR beam size & divergence
On-axis flux
Angle-integrated flux

The angular spectral flux ($\mathrm{d}\Phi/\mathrm{d}\Omega$) is the experimentally observable quantity that describes the angular and spectral characteristics of the undulator radiation. With eq.(3.9), it can be shown that the angular spectral flux at a narrow frequency band around the harmonic frequencies ω_n is the sum over angular spectral fluxes of each harmonic ($\mathrm{d}\Phi_n/\mathrm{d}\Omega$) [Onuki and Elleaume, 2003]:

$$\begin{aligned} \frac{\mathrm{d}\Phi}{\mathrm{d}\Omega}(\theta_x, \theta_z, \omega) &= \alpha \frac{I}{e} |\vec{H}(\theta_x, \theta_z, \omega)|^2 \\ &\simeq \sum_{n=1}^{\infty} \frac{\mathrm{d}\Phi_n}{\mathrm{d}\Omega}(\theta_x, \theta_z, \omega) \end{aligned} \tag{3.11}$$

where $\alpha = 1/137$ is the fine-structure constant. The angular spectral flux for each harmonic n reads

$$\frac{\mathrm{d}\Phi_n}{\mathrm{d}\Omega}(\theta_x, \theta_z, \omega) = \alpha \frac{I}{e} N^2 \underbrace{|\vec{h}_n(\theta_x, \theta_z)|^2}_{\text{lobe function}} \underbrace{\mathrm{sinc}(\pi N_u (\omega/\omega_1 - n))^2}_{\text{interference function}}, \tag{3.12}$$

where $\omega_1(\theta_x, \theta_z)$ is the resonance frequency as a function of the observation angle θ.

The shape of the angular spectral flux for each harmonic is determined by the "lobe function" $|\vec{h}_n|^2$ (equation (3.10)) which describes the electric field emitted by a single undulator period and the "interference function" $\mathrm{sinc(x)}^2$ which is the superposition of the phases of the radiation from each period. Typical (small) errors in a real undulator field predominantly influence the phases of the radiation from each period and therefore the interference term can not be expressed as a $\mathrm{sinc(x)}^2$ function. However, for a mathematically perfect undulator, the interference term is only nonzero in a narrow bandwidth around frequencies ω_n that satisfy the resonance condition (equation (3.2)) which for off-axis angles ($\Psi^2 = \theta_x^2 + \theta_y^2$) is the case for correspondingly lower frequencies.

The radial symmetry of this term is a consequence of the periodicity of the field and it is responsible for the circular, cone-shaped angular emission pattern. The radiation amplitude along these circular emission rings is given by $|\vec{h}_n(\theta_x, \theta_z)|^2$ which describes the angular intensity (lobe) structure for each harmonic. This function depends on the undulator magnetic field.

Thus, the typical parabolic shapes of the angular undulator spectra for each harmonic (see figure 3.5) are due to the interference term, whereas the intensity distributions (only odd harmonics on-axis, even harmonics peak only off-axis, and the lobe structure with nods of higher harmonics) are given by the lobe function. The spectral width of the radiation is described by the interference term: on axis, the $\mathrm{sinc(x)}^2$ shows a narrow peak at each harmonic with width $\simeq 1/nN_u$. The height of the harmonics is given by $|\vec{h}_n(0,0)|^2$ (which is zero for even harmonics on axis). The divergence of the radiation is determined by the angular shape of the flux around the resonance frequencies. It is also mainly given by the interference function, since it varies much more rapidly with θ than the lobe function which can be regarded as a constant in this case. Therefore, the divergence of odd harmonics is the width of the $\mathrm{sinc(x)}^2$-term at resonance frequencies ω_n (which depend on the angle through the resonance condition).

At the exact resonance frequencies of each harmonic $\omega_n = n\omega_1$, $\mathrm{sinc}(x) \to 1$ and the angular flux can be written as

$$\frac{\mathrm{d}\Phi_n}{\mathrm{d}\Omega}(\theta_x, \theta_z, \omega_n) = \alpha \frac{I}{e} N_u^2 |\vec{h}_n(\theta_x, \theta_z)|^2. \tag{3.13}$$

3.4.1. Approximation by a Gaussian beam

The analytical description can be simplified by approximating the undulator radiation beam size and divergence by Gaussian distributions. For resonance frequencies ω_n, the sinc(x) function of the angular spectral flux (equation (3.12)) can be approximated by a Gaussian distribution $\exp(-\theta^2/(2\sigma_{r'}^2))$ which leads for a filament electron beam to a rms **divergence** of [Onuki and Elleaume, 2003]

$$\sigma_{r'} \simeq \sqrt{\frac{\lambda_n}{2L}} = \frac{1}{2\gamma}\sqrt{\frac{1}{nN_u}\left(1 + \frac{K^2}{2}\right)}, \tag{3.14}$$

where $L = N_u \lambda_u$ is the length of the undulator and λ_n the wavelength of the radiation (equation (3.2)) . It can be seen that a smaller emission angle results not for only higher

electron energies γ, but also for a higher harmonic number n as well as more undulator periods N_u. As can already be seen from equation (3.12), undulator radiation is emitted in a much narrower cone than bending magnet radiation ($\sigma_{r',\mathrm{bend}} \simeq 1/\gamma$) because of the interference of the radiation from individual undulator periods.

In a similar way, the waist of the **photon beam size** of a filament electron beam (in the middle of the undulator at $s = 0$) at resonance wavelengths can be approximated by a Gaussian distribution with a standard deviation of

$$\sigma_r \simeq \sqrt{\frac{\lambda_n L}{2\pi^2}}. \tag{3.15}$$

A photon beam emittance for undulator radiation in the Gaussian approximation can be defined by the product of equation (3.14) and equation (3.15) [Onuki and Elleaume, 2003]

$$\epsilon_{\mathrm{ph}} = \sigma_r \sigma_{r'} \simeq \frac{\lambda}{2\pi}. \tag{3.16}$$

However, equations (3.14 & 3.15) are just approximations. The exact beam size, divergence and photon beam emittance have to be calculated by means of the second order moments (variance) $\sigma_x^2 = \langle x^2 \rangle$ and $\sigma_{x'}^2 = \langle \theta_x^2 \rangle$ which lead to the following definition of the photon beam emittance [Onuki and Elleaume, 2003]:

$$\epsilon_{\mathrm{ph}} \geqslant \frac{\lambda}{4\pi}. \tag{3.17}$$

In the Gaussian approximation, the angular spectral flux can be written as [Clarke, 2004]

$$\frac{\mathrm{d}\Phi}{\mathrm{d}\Omega}(\vec{\Psi}, \omega_n) = \left.\frac{\mathrm{d}\Phi}{\mathrm{d}\Omega}\right|_{\vec{\Psi}=0} \exp\left(-\frac{\vec{\Psi}^2}{2\sigma_{r'}^2}\right), \tag{3.18}$$

where $\vec{\Psi} = (\theta_x, \theta_y)$.

The **on-axis flux density** (the amplitude in equation 3.18) can be calculated from equation (3.13) for $\omega = \omega_n$ to be [Onuki and Elleaume, 2003]

$$\left.\frac{\mathrm{d}\Phi}{\mathrm{d}\Omega}\right|_{\vec{\Psi}=0} = \frac{\mathrm{d}\Phi_n}{\mathrm{d}\Omega}(0, 0, \omega_n) = \alpha \frac{I}{e} N_u^2 \gamma^2 F_n(K), \tag{3.19}$$

where

$$F_n(K) = \frac{n^2 K^2}{(1 + K^2/2)^2} \left[J_{(n-1)/2}\left(\frac{nK^2}{4 + 2K^2}\right) - J_{(n+1)/2}\left(\frac{nK^2}{4 + 2K^2}\right)\right]^2, \tag{3.20}$$

which can be seen in fig 3.4. For $n = 1$ and $K < 1$, it can be approximated as $F_n(K) \simeq K^2/(1+K^2/2)$. For a small undulator parameter ($K < 1$) a formula in practical units for the on-axis spectral flux of the fundamental in units of [Photons/sec/0.1%b.w./mrad^2] is given by [Onuki and Elleaume, 2003]:

$$\left.\frac{\mathrm{d}\Phi}{\mathrm{d}\Omega}\right|_{\vec{\Psi}=0} \simeq 1.744 \times 10^{14} \cdot N_u^2 \, E^2[\mathrm{GeV}] \, I[\mathrm{Amp}] \, \frac{K^2}{1 + K^2/2}. \tag{3.21}$$

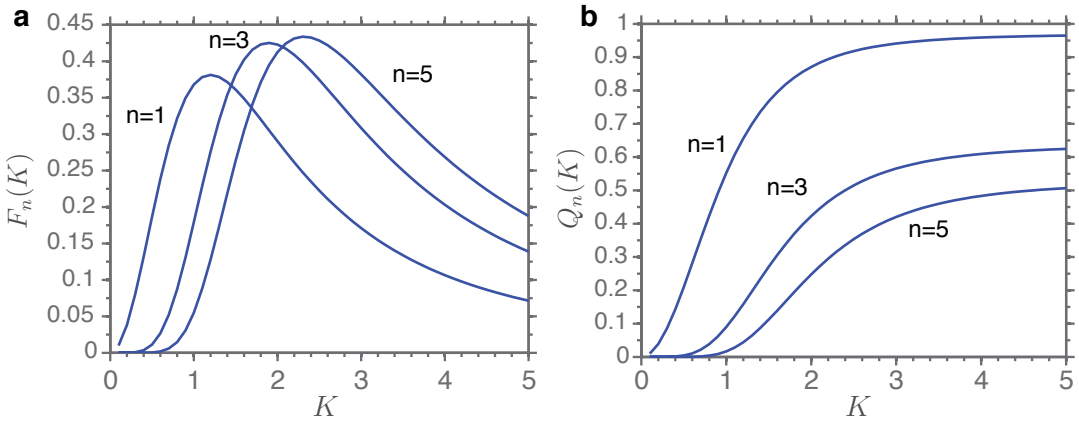

Figure 3.4. | **Functions $F_n(K)$ and $Q_n(K)$.** **a** shows the function $F_n(K)$ and **b** the function $Q_n(K)$ versus the undulator parameter K for different harmonics n. For $K < 1$, $Q_n(K)$ can be approximated by $Q_n(K) \simeq K^2$

The total spectral flux for each harmonic can be calculated by integrating equation (3.12) over all angles

$$\Phi_n(\omega) = \int_{-\infty}^{\infty}\int_{-\infty}^{\infty} \frac{\mathrm{d}\Phi_n}{\mathrm{d}\Omega}(\theta_x, \theta_z, \omega)\ \mathrm{d}\theta_x\, \mathrm{d}\theta_z, \tag{3.22}$$

which in the Gaussian approximation can be written as

$$\Phi(\vec{\Psi}, \omega_n) = \left.\frac{\mathrm{d}\Phi}{\mathrm{d}\Omega}\right|_{\vec{\Psi}=0} 2\pi\sigma_{r'}^2. \tag{3.23}$$

This leads to an **angle-integrated spectral flux** at $\omega = \omega_n$ of

$$\Phi|_{\omega=\omega_n} = \frac{\pi}{2}\alpha N_u \frac{I}{e} Q_n(K), \tag{3.24}$$

where $Q_n(K) = (1 + K^2/2)F_n(K)/n$ (see fig. 3.4). In practical units for, for the fundamental and a small undulator parameter ($K < 1$), this can be written in units of [Photons/sec/0.1%b.w.] as [Onuki and Elleaume, 2003]:

$$\Phi|_{\omega=\omega_1} \simeq 1.431 \times 10^{14} \cdot N_u\, I[\mathrm{Amp}]\, K^2. \tag{3.25}$$

The integration of equation (3.12) at a frequency slightly below the resonance $\omega_n' = \omega_n(1 - 1/(nN_u))$ leads to an angle integrated flux which is almost twice the flux at the resonance frequency: $\Phi_n(\omega_n') \simeq 2 \cdot \Phi_n(\omega_n)$. However, the radiation for smaller frequencies is emitted on a cone with a dip on axis, in the forward direction (see figure 3.5), leading to a higher divergence. The radiation with the smallest divergence is emitted at the resonance frequency.

3.5. Finite-Emittance Electron Beams & Propagation of Undulator Radiation

A finite-emittance electron beam ("thick" beam) with many electrons can be best described by its brilliance since the total brilliance is just the sum of the brilliances of each electron. The brilliance can in many aspects be thought of as a photon phase-space distribution. For an incoherent source, the total brilliance can be calculated by the convolution of the electron beam distribution with the single-electron brilliance. Since it is an invariant under any linear transformation of the phase space, it can be used to propagate the radiation over a free distance or through optical components and the flux can be calculated by integrating the brilliance.

3.5.1. Brilliance of a Filament Electron Beam

A radiation source is completely characterized by its brilliance distribution $\mathcal{B}$ which can be described by the Wigner function [Wigner, 1932] and can be interpreted as an analog of a phase space density for photons.

$$\mathcal{B}(\vec{x},\vec{\Psi},s,\omega) = \frac{\epsilon_0\omega^2}{2\pi^2 ch}\frac{I}{e}\int_{-\infty}^{\infty}\int_{-\infty}^{\infty}\left(\vec{E}(\vec{x}+\frac{\vec{\xi}}{2},s,\omega)\right)\left(\vec{E}^*(\vec{x}-\frac{\vec{\xi}}{2},s,\omega)\right)\exp\left(\mathrm{i}\frac{\omega}{c}\vec{\Psi}\vec{\xi}\right)\mathrm{d}^2\vec{\xi}, \tag{3.26}$$

where $\vec{x}=(x,y)$ and $\vec{\xi}$ a spatial integration variable. However, since the brilliance is not an observable in the quantum-mechanical sense and for example can be negative, it cannot strictly be interpreted as a phase-space density. For a more detailed discussion see [Onuki and Elleaume, 2003].

The brilliance is connected to the spectral angular and spatial flux densities by

$$\frac{\mathrm{d}\Phi}{\mathrm{d}\Omega}(\hat{n},\omega) = \int_{-\infty}^{\infty}\int_{-\infty}^{\infty}\mathcal{B}(\vec{x},\vec{\Psi},s,\omega)\,\mathrm{d}^2\vec{x} \tag{3.27}$$

$$\frac{\mathrm{d}\Phi}{\mathrm{d}\mathcal{S}}(\vec{x},s,\omega) = \int_{-\infty}^{\infty}\int_{-\infty}^{\infty}\mathcal{B}(\vec{x},\vec{\Psi},s,\omega)\,\mathrm{d}^2\vec{\Psi}, \tag{3.28}$$

and to the total flux by

$$\Phi(\omega) = \int_{-\infty}^{\infty}\int_{-\infty}^{\infty}\mathcal{B}(\vec{x},\vec{\Psi})\,\mathrm{d}^2\vec{x}\;\mathrm{d}^2\vec{\Psi}. \tag{3.29}$$

Gaussian Approximation of the Brilliance of a Filament Electron Beam

Similar to the flux, the brilliance at resonant odd frequencies ω_n can be approximated by spatial and angular Gaussian distributions. In the undulator middle ($s = 0$), for a **filament electron beam** it can be written as [Kim, 1989]

$$\mathcal{B}_n^0(\vec{x}, \vec{\Psi}, 0, \omega_n) = \mathcal{B}_n^0(\vec{o}, \vec{o}, 0, \omega_n) \exp\left(-\frac{\vec{x}^{\,2}}{2\sigma_r^2} - \frac{\vec{\Psi}^2}{2\sigma_{r'}^2} \right), \tag{3.30}$$

where σ_r and $\sigma_{r'}$ are the standard deviations given by equations (3.14)& (3.15). The **on-axis brilliance** $\mathcal{B}_n^0|_0$ can be written under consideration of equation (3.29 and the photon emittance (equation (3.16)) in terms of the total flux as

$$\mathcal{B}_n^0|_0 = \mathcal{B}_n^0(\vec{o}, \vec{o}, 0, \omega_n) \simeq \frac{\Phi_n(\omega_n)}{(2\pi\sigma_r\sigma_{r'})^2} = \frac{\Phi_n(\omega_n)}{(\lambda/2)^2}, \tag{3.31}$$

where $\Phi_n(\omega)$ is the angle-integrated spectral flux (equation (3.24)).

3.5.2. Brilliance of a Thick Electron Beam

For undulator radiation from an electron beam with a finite transverse emittance (a "thick" electron beam), the total emitted electric field is given by the sum of the electric fields emitted by each electron. For an uncorrelated Gaussian electron distribution with a temporal pulse length much longer than the emitted wavelength ($\sigma_l \gg \lambda$), each electron emits radiation incoherently to that of all other electrons in the beam. As a result, the brilliance of each electron can simply be added up if all electrons in the bunch (independent of their transverse position or angle) are subject to the same acceleration which is true in the case of undulators. Therefore, the total brilliance, equation (3.26), can be written as the convolution of the particle distribution $f(\vec{X}_e, \vec{\psi}_e, s)$ and the brilliance of a single electron $\mathcal{B}^0$ [Kim, 1989]

$$\mathcal{B}(\vec{x}, \vec{\Psi}; s) = \int_{-\infty}^{\infty} \int_{-\infty}^{\infty} \mathcal{B}^0(\vec{x} - \vec{X}_e, \vec{\Psi} - \vec{\psi}_e; s, \omega)\, f(\vec{X}_e, \vec{\psi}_e, s)\, \mathrm{d}^2\vec{X}_e\, \mathrm{d}^2\vec{\psi}_e\,. \tag{3.32}$$

In addition to the Gaussian approximation of the brilliance of the single electron emission (equation (3.30)), the electron beam can also be well approximated by Gaussian distributions as

$$f(\vec{X}_e, \vec{\psi}_e, s) = \frac{1}{(2\pi)^2\epsilon_x\epsilon_y} \exp\left(-\frac{x^2}{2\sigma_x^2} - \frac{\theta_x^2}{2\sigma_{x'}^2} - \frac{y^2}{2\sigma_y^2} - \frac{\theta_y^2}{2\sigma_{y'}^2} \right). \tag{3.33}$$

The convolution of two Gaussian functions results in a Gaussian function with a standard deviation that is the root-mean-square of the initial distributions. Thus the **brilliance**

of an electron beam with a finite transverse emittance can be approximated as

$$\mathcal{B}_n(\vec{x},\vec{\Psi},0,\omega_n) \simeq \mathcal{B}_n(\vec{o},\vec{o},0,\omega_n)\ \exp\left(-\frac{x^2}{2\Sigma_x^2}-\frac{\theta_x^2}{2\Sigma_{x'}^2}-\frac{y^2}{2\Sigma_y^2}-\frac{\theta_y^2}{2\Sigma_{y'}^2}\right), \tag{3.34}$$

where the photon beam size and divergence of the radiation emitted by a thick electron beam are

$$\Sigma_{x,y} = \sqrt{\sigma_{x,y}^2+\sigma_r^2} \tag{3.35}$$

$$\Sigma_{x',y'} = \sqrt{\sigma_{x',y'}^2+\sigma_{r'}^2}, \tag{3.36}$$

with $\sigma_{x,y}$ the horizontal and vertical electron beam size, σ_r the single-electron undulator beam size (equation (3.15)), $\sigma_{x',y'}$ the electron beam divergence and $\sigma_{r'}$ the single-electron UR divergence (equation (3.14)). The on-axis brilliance for a thick electron beam is given by

$$\mathcal{B}_n|_0 = \mathcal{B}_n(\vec{o},\vec{o},0,\omega) \simeq \frac{\Phi_n(\omega)}{(2\pi)^2\Sigma_x\Sigma_{x'}\Sigma_y\Sigma_{y'}}, \tag{3.37}$$

where $\Phi_n(\omega)$ is given by equation (3.24). It can be seen that the effect of a thick electron beam is to smear out the on-axis brilliance (and thus the on-axis flux density), whereas the total integrated brilliance (flux) is conserved.

From equation (3.37), it can be seen that the highest peak brilliance for a thick beam can be achieved, for a matched electron beam size and divergence, given by the following condition: the electron beam must be focused into the center of the undulator (of length L) with an electron beam "Rayleigh length" of $L/2\pi$ [Wiedemann, 2002], resulting in the Twiss parameters $\alpha_{\text{Twiss}} = 0$ and $\beta_{\text{Twiss}} = \sigma_r/\sigma_{r'} = L/(2\pi)$. (For a short description of the Twiss parameters, see section 3.8).

3.5.3. Propagation of Undulator Radiation

The brilliance can in many aspects be thought of as the phase-space distribution of the undulator radiation photons. Since it is an invariant under any linear transformation of the phase space, the propagation of the UR through free drifts or optical components can be calculated by linear operations on the brilliance:

$$\mathcal{B}(\vec{x}_2,\vec{\varphi}_2,s_2) = \mathcal{B}(\vec{x}_1,\vec{\varphi}_1,s_1), \tag{3.38}$$

where the coordinates are transformed by the transfer matrix $\mathcal{M}$ (see section 3.7)

$$\begin{pmatrix}\vec{x}_2\\ \vec{\varphi}_2\end{pmatrix} = \mathcal{M}\begin{pmatrix}\vec{x}_1\\ \vec{\varphi}_1\end{pmatrix}. \tag{3.39}$$

For example, propagation through a free drift distance is calculated by

$$\mathcal{B}(\vec{x},\vec{\varphi},s+\ell) = \mathcal{B}(\vec{x}-\ell\cdot\vec{\varphi},\vec{\varphi},s). \tag{3.40}$$

The spatial flux density after a free drift of length ℓ can be calculated by integration of the brilliance (see equation (3.28)) which leads to (for a detailed calculation: see Appendix, section B.1)

$$\frac{\mathrm{d}\Phi}{\mathrm{d}\mathcal{S}} = \frac{\Phi}{2\pi(\sigma_r^2 + \ell^2\sigma_{r'}^2)} \exp\left(-\frac{x^2+y^2}{2(\sigma_r^2 + \ell^2\sigma_{r'}^2)}\right). \tag{3.41}$$

Inserting the divergence of the UR from a single electron (equation (3.14)), it can be seen that the photon beam size after a free drift of length ℓ changes to

$$\sigma_r(s=\ell) = \sqrt{\sigma_{r,0}^2 + \ell^2\sigma_{r'}^2} = \sqrt{\frac{\lambda L}{2\pi^2} + \frac{\lambda}{2L}\ell^2}, \tag{3.42}$$

where L is the undulator length and λ the wavelength of the emitted radiation. This is the standard deviation of a Gaussian function resulting from the convolution of the photon beam size at the undulator center $\sigma_{r,0}$ and the product of the divergence and the drift distance, analogous to the propagation of Gaussian beams in optics [Saleh and Teich, 1991].

UR by a Thick Electron Beam after a Drift

Similarly, UR from thick electrons beams can be propagated. As shown in Appendix, section B.2, carrying out the convolution in the center of the undulator and propagating the resulting brilliance is equivalent to first separately propagating the single-electron brilliance and the electron beam to the observation point and then performing the convolution. For a **thick electron beam**, after a drift of a distance ℓ, the

UR **divergence** is:

$$\Sigma_{x',y'} = \sqrt{\sigma_{x',y'}^2 + \frac{\lambda}{2L}} \tag{3.43}$$

and the UR **beam size** is:

$$\Sigma_{x,y}(\ell) = \sqrt{\sigma_{x,y}^2(\ell) + \frac{\lambda L}{2\pi^2} + \frac{\lambda}{2L}\ell^2}, \tag{3.44}$$

where $\sigma_{x',y'}$ are the rms electron beam divergences, $\sigma_{x,y}(\ell)$ the rms electron beam sizes at the position ℓ, and $\sigma_r^2(0)$ the single-electron rms UR beam size in the undulator center.

The experimentally observable quantity, the on-axis spatial spectral flux, can thus be written as

$$\left.\frac{\mathrm{d}\Phi}{\mathrm{d}\mathcal{S}}\right|_{\vec{x}=0} = \frac{\Phi_n}{2\pi\,\Sigma_x(s)\,\Sigma_y(s)}, \tag{3.45}$$

where Φ_n is the total flux, given by equation (3.24). Similarly, the the on-axis angular spectral flux is

$$\left.\frac{\mathrm{d}\Phi}{\mathrm{d}\Omega}\right|_{\vec{\Psi}=0} = \frac{\Phi_n}{2\pi\Sigma_{x'}\Sigma_{y'}}. \tag{3.46}$$

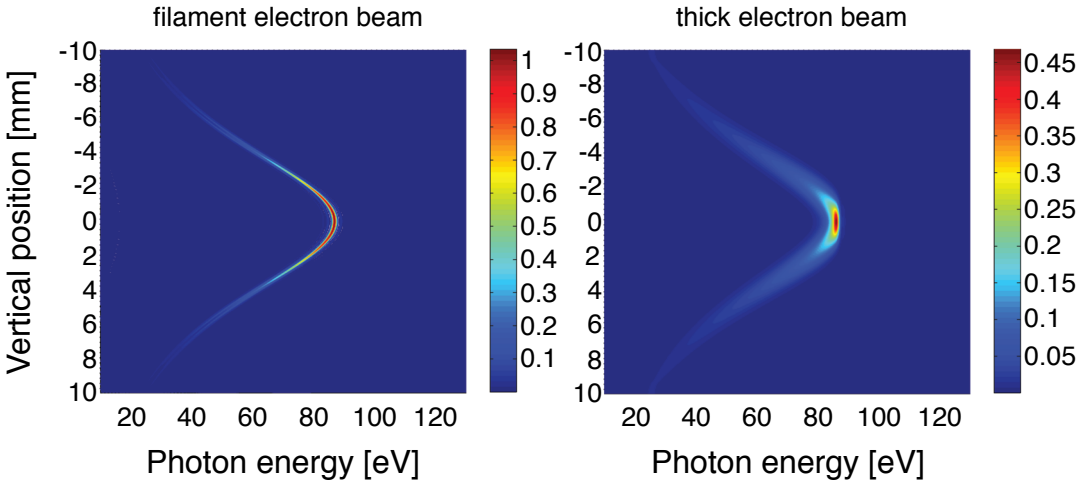

Figure 3.5. | **Spatial spectral flux.** The figure shows the vertical spatial spectral flux of the undulator fundamental (at horizontal position 0) for a filament and a finite-emittance electron beam for an undulator with a period of 5 mm and a $K = 0.5$. In both cases, an electron beam with an energy of 230 MeV and the same current have been used. The geometrical emittance in the right-hand side figure is $\epsilon = 1$nm rad. Color-coded is the spatial spectral flux which in both cases is normalized to the peak flux of the filament electron beam.

These Gaussian approximations are only valid for radiation at the resonance frequency ω_n. It can be seen that a finite-emittance electron beam smears out (and decreases) the on-axis flux. However, the integrated total flux is equal to that of an zero-emittance beam (of the same number of electrons).

3.6. Discussion

Total undulator flux
Undulator divergence and beam size
On-axis flux of zero and finite-emittance beams
Bandwidth of radiation
Longitudinal and transverse coherence

3.6.1. Undulator Flux

The **total angle-integrated flux** emitted by an electron beam with a current I and an undulator with a number of periods N_u and an undulator parameter K can be written for the undulator fundamental and for $K < 1$ as (see equation 3.24)

$$\Phi_n = \frac{\pi}{2}\alpha N_u \frac{I}{e} K^2, \tag{3.47}$$

where $\alpha = 1/137$ is the fine-structure constant.

It can be seen that the flux can be linearly increased by a higher number of undulator periods and a higher number of electrons in the bunch. For $K < 1$, the flux increases quadratically with the undulator parameter K. The angle-integrated flux is equal for a filament (zero-emittance) and a finite-emittance electron bunch (both of the same charge).

Divergence and Beam Size

The divergence and beam size of the undulator flux in a Gaussian approximation can be written as

$$\Sigma_{x,y} = \sqrt{\sigma_{x,y}^2 + \sigma_r^2} \tag{3.48}$$

$$\Sigma_{x',y'} = \sqrt{\sigma_{x',y'}^2 + \sigma_{r'}^2}, \tag{3.49}$$

where $\sigma_{x,y}$ and $\sigma_{x',y'}$ are the respective electron beam size and divergence, and the intrinsic (single-electron) undulator beam size and divergence are given by

$$\sigma_r = \sqrt{\frac{\lambda_n L}{2\pi^2}} \tag{3.50}$$

$$\sigma_{r'} = \sqrt{\frac{\lambda_n}{2L}} \tag{3.51}$$

for an undulator of length L and an emission wavelength λ_n.

On-Axis Flux for a Zero and Finite-Emittance Beam

In the Gaussian approximation, the angular spectral flux can be written as ($\vec{\Psi} = (\theta_x, \theta_y)$)

$$\frac{\mathrm{d}\Phi}{\mathrm{d}\Omega}(\vec{\Psi}, \omega_n) = \left.\frac{\mathrm{d}\Phi}{\mathrm{d}\Omega}\right|_{\vec{\Psi}=0} \exp\left(-\frac{\theta_x^2}{2\Sigma_{x'}^2} - \frac{\theta_y^2}{2\Sigma_{y'}^2}\right), \tag{3.52}$$

where the on-axis flux is given by

$$\left.\frac{\mathrm{d}\Phi}{\mathrm{d}\Omega}\right|_{\vec{\Psi}=0} = \frac{\Phi_n}{2\pi\Sigma_{x'}\Sigma_{y'}}. \tag{3.53}$$

It can be seen that for a finite-emittance electron beam, the flux gets washed out and the on-axis flux gets decreased.

Using equations 3.47 and 3.51, it can be seen that for a zero-emittance (filament) electron beam the on-axis flux (for $K < 1$) can be written as

$$\left.\frac{\mathrm{d}\Phi}{\mathrm{d}\Omega}\right|_{\vec{\Psi}=0} = \alpha\frac{I}{e}N_u^2\gamma^2\frac{K^2}{1 + K^2/2}, \tag{3.54}$$

which is equal to equation 3.19.

It can be seen that although the angle-integrated flux does not depend on the electron energy γ, owing to the smaller emission cones ($\sigma_{r'} \propto 1/\gamma$) of the radiation at higher electron energies the on-axis flux scales with γ^2. A practical consequence of this can be seen in the results of the simulations describing the experimental measurements (see section 6.2) in the shift of the spectral peak of the sum of on-axis fluxes of a range of electron energies to higher photon energies.

3.6.2. Bandwidth of Undulator Radiation

The bandwidth of the single-electron undulator emission is broadened by several (independent) effects and the overall bandwidth can be written as

$$\frac{\Delta\lambda}{\lambda} = \sqrt{\left(\frac{\Delta\lambda}{\lambda}\right)^2_{\text{nat}} + \left(\frac{\Delta\lambda}{\lambda}\right)^2_{\Delta\gamma} + \left(\frac{\Delta\lambda}{\lambda}\right)^2_{\epsilon}}. \tag{3.55}$$

The natural (single-electron) bandwidth is given by

$$\left(\frac{\Delta\lambda}{\lambda}\right)_{\text{nat}} \simeq \frac{1}{nN_u}, \tag{3.56}$$

where N_u is the number of undulator periods and n the harmonic number.

The magnitude of the individual contributions to the broadening can be estimated by the resonance condition of the emitted wavelength

$$\lambda = \frac{\lambda_u}{2n\gamma^2}\left(1 + \frac{K^2}{2} + \gamma^2\theta^2\right), \tag{3.57}$$

which leads to the estimation of the broadening due to electron energy spread σ_γ of

$$\left(\frac{\Delta\lambda}{\lambda}\right)_{\Delta\gamma} = 2 \cdot \frac{\sigma_\gamma}{\gamma}. \tag{3.58}$$

The influence of the electron beam emittance originates from both a finite divergence and a finite size of the electron beam. Using the last term of equation 3.57, the broadening of the bandwidth by an electron beam with a divergence of $\sigma_{x'}$ can be estimated to be

$$\left(\frac{\Delta\lambda}{\lambda}\right)_{\sigma_{x'}} = \frac{(\gamma\sigma_{x'})^2}{1 + K^2/2}. \tag{3.59}$$

The increase in bandwidth due to a finite-sized electron beam originates from the fact that an observer (located sufficiently close to the source) detects the radiation emitted from various electron under a different angle. This can be estimated with formula (3.59) by using instead of $\sigma_{x'}$ an angle of $\theta = \sigma_x/d$, where σ_x is the electron beam size and d the distance of the observer to the undulator source.

Typically the undulator spectrum is observed through a finite-sized slit (or correspondingly an acceptance angle of θ_{slit}) which increases the bandwidth by

$$\left(\frac{\Delta\lambda}{\lambda}\right)_{\theta_{\mathrm{slit}}} = \frac{(\gamma\theta_{\mathrm{slit}})^2}{1+K^2/2}. \tag{3.60}$$

There is a significant difference between the broadening through electron-energy spread and both the broadening through emittance effects and the observation after a finite-sized slit: the latter two effects broaden the bandwidth only toward longer wavelengths than the resonance wavelength, whereas the broadening due to the energy spread is symmetrically about the resonance wavelength.

For a discussion of the expected undulator bandwidth in the experiment described below, see section 6.1.1.

3.6.3. Longitudinal and Transverse Coherence

For undulator radiation, the transverse and longitudinal coherence can be considered separately. In the case of a longitudinal extended monoenergetic (filament) electron beam, photons from different electrons are coherent with each other, if they are emitted from a region that is smaller than the radiation wavelength. The intensity of the radiation from a filament beam of uncorrelated electrons with a Gaussian longitudinal distribution with an rms pulse length of σ_s can be written as [Onuki and Elleaume, 2003]

$$|\vec{H}|^2 = |\vec{H}_0|^2 \left[N_e + N_e(N_e-1)\exp\left(-\frac{\sigma_s^2}{(\lambda/2\pi)^2}\right)\right], \tag{3.61}$$

where λ is the wavelength of the radiation. For a bunch length of $\sigma_s < 0.8\lambda$, the term proportional to N_e^2 dominates and the emission is called coherent. In the X-ray range, the electron pulse length is typically longer than the emitted wavelength, but coherent emission can nevertheless be achieved by a process called microbunching (see section 4).

For an electron beam with a finite transverse emittance, the degree of coherence can be determined by the phase-space area occupied by the radiation. The transversely coherent flux can be written as [Kim, 1989]

$$\Phi_{\mathrm{coh}} = \left(\frac{\lambda}{2}\right)^2 \mathcal{B}|_0. \tag{3.62}$$

It can be seen that the peak brilliance (given by equation (3.37)) is a direct measure of the transverse coherence which for a thick beam leads to

$$\Phi_{\mathrm{coh}} = \frac{\sigma_r^2\sigma_{r'}^2}{\Sigma_x\Sigma_{x'}\Sigma_y\Sigma_{y'}}\Phi_{\mathrm{tot}}. \tag{3.63}$$

Thus, the transverse degree of coherence is the ratio of the total radiation to the single electron phase-space area.

3.7. ABCD-Matrix Formalism

The ABCD-Matrix formalism allows the raytracing of an optical system for paraxial rays. The rays are described by a vector consisting of their position and angle with respect to the optical axis. The effect of individual optical components on the rays can be described by a 2x2 matrix, the ray-transfer matrix.

$$\begin{pmatrix} x_2 \\ \theta_2 \end{pmatrix} = \begin{pmatrix} A & B \\ C & D \end{pmatrix} \begin{pmatrix} x_1 \\ \theta_1 \end{pmatrix} \tag{3.64}$$

Since the position and angle of the ray at the input an output plane are related by two linear algebraic equations, the whole optical system can be described by a the product of the matrices of each individual optical element:

$$\begin{pmatrix} A & B \\ C & D \end{pmatrix} = \mathcal{M}_n \cdot ... \cdot \mathcal{M}_2 \cdot \mathcal{M}_1 \tag{3.65}$$

Some examples of ray-transfer matrices are given for

- a free drift space of length s

$$\mathcal{M}_s = \begin{pmatrix} 1 & s \\ 0 & 1 \end{pmatrix} \tag{3.66}$$

- a thin lens with focal length f

$$\mathcal{M}_f = \begin{pmatrix} 1 & 0 \\ -1/f & 1 \end{pmatrix} \tag{3.67}$$

3.8. Twiss Parameters

An electron beam with an emittance ϵ can be described as an ellipse in phase space as [Wiedemann, 2007]:

$$\gamma_{\text{Twiss}} x^2 + 2\alpha_{\text{Twiss}} x\theta + \beta_{\text{Twiss}} \theta^2 = \epsilon, \tag{3.68}$$

where α, β and γ are the so-called Twiss parameters. The electron beam propagating along a beamline can be described by transforming these parameters, i.e. they describe the transformation of the phase-space ellipse under the influence of optical components (dipole magnets, quadrupole magnets, ...) or free-drifts in a beamline. They are related to each other by

$$\alpha_{\text{Twiss}}(s) = -\frac{1}{2}\beta'_{\text{Twiss}}(s) \tag{3.69}$$

$$\gamma_{\text{Twiss}}(s) = \frac{1 + \alpha_{\text{Twiss}}(s)}{\beta_{\text{Twiss}}(s)}, \tag{3.70}$$

where s is the distance along the beamline. Their practical meaning can be seen in figure 3.6: The beam size at a position s is given by

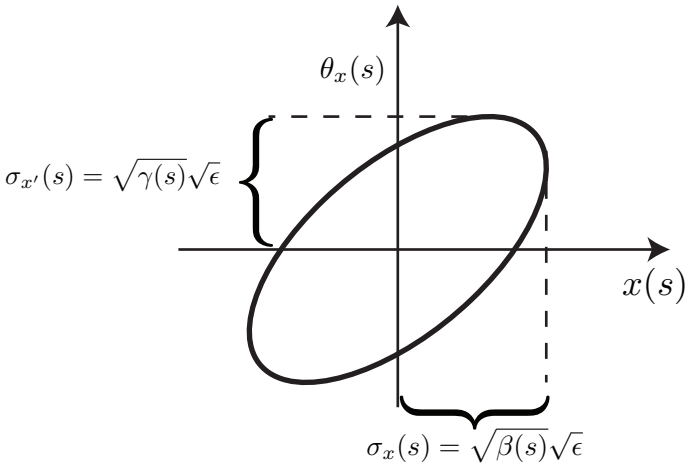

Figure 3.6. | **Phase-space representation of an electron beam.** The electron beam size and the beam divergence are given in terms of the Twiss parameters.

$$\sigma_x(s) = x(s)|_{\max} = \sqrt{\beta_{\text{Twiss}}(s)}\sqrt{\epsilon} \tag{3.71}$$

and the divergence of an electron beam is given by

$$\sigma_{x'}(s) = \theta(s)|_{\max} = \sqrt{\gamma_{\text{Twiss}}(s)}\sqrt{\epsilon} \tag{3.72}$$

The electron beam is in focus for $\alpha_{\text{Twiss}} = 0$, where the beam size and divergence can be written as:

$$\sigma_x \sigma_{x'} = \epsilon \tag{3.73}$$

The electron beam can be propagated through a beam line by transforming the Twiss parameters using ABCD-transfer-matrices $\mathcal{M}$ similar as discussed in section 3.7:

$$\begin{pmatrix} \beta_1 & -\alpha_1 \\ -\alpha_1 & \gamma_1 \end{pmatrix} = \mathcal{M} \begin{pmatrix} \beta_0 & -\alpha_0 \\ -\alpha_0 & \gamma_0 \end{pmatrix} \mathcal{M}^T. \tag{3.74}$$

3.9. Undulator: List of Symbols

Symbol	Description
$\vec{D}(\tau)$	Distance emitter to observer
$\hat{n} = \vec{D}/\lvert\vec{D}\rvert$	Normalized emission direction
$\vec{x} = (x, y)$	Distances
$\vec{E}$	Emitted electric field
$\vec{H}$	Dimensionless vector of electric field
$\vec{\Psi} = (\theta_x, \theta_y)$	Observation angles
σ_r , $\sigma_{r'}$	UR photon beam size, divergence (RMS)
$\sigma_{x,y}$, $\sigma_{x',y'}$	Electron beam size, divergence (RMS)
Σ_x , $\Sigma_{x'}$	UR photon beam size, divergence of a thick electron beam (RMS)
n	harmonic number
λ_n	Wavelength of n-th harmonic emission
λ_u	Undulator period
$K \propto \lambda_u B$	Undulator parameter
N_u	number of undulator periods
Φ_n	Total photon flux of harmonic n
$\mathrm{d}\Phi/\mathrm{d}\Omega\lvert_{\vec{x}=0}$	On-axis spatial flux
$\mathcal{B}$	Brilliance

4. FREE-ELECTRON LASER (FEL) THEORY

This section gives a brief overview over free-electron laser (FEL) theory to the extent relevant for the discussion of future developments of X-ray sources based on the experiment described in this thesis.

In contrast to conventional lasers where the amplification of the beam is achieved by transitions of excited electrons in bound atomic or molecular states, FELs use a beam of relativistic "free" (unbound) electrons as gain medium. Typical lasers consists of a gain medium inside an optical cavity which is composed of highly reflective mirrors. However, since it is extremely difficult to produce mirrors in the X-ray range, FELs have to get full amplification in a single pass. The basic 1D theory of this single-pass, high-gain "SASE" (self-amplified spontaneous emission) regime is discussed below.

Although (spontaneous) undulator radiation and FEL radiation originate from a similar setup (electrons propagating through a sinusoidal magnetic field), FELs emit *coherent* radiation whereas the undulator emission discussed in the previous chapter is incoherent. One of the main advantages of this coherent radiation is the significantly higher brilliance compared to spontaneous emission as discussed in section 3.6.3: the intensity of coherent emission scales quadratically with the number of electrons N_e, whereas the spontaneous radiation scales only linear with N_e. In order for radiation to be emitted coherently, it has to originate from electrons that are located at a distance smaller than wavelength of the emitted radiation (see section 3.6.3). The electron pulse duration is typically longer than the wavelength for radiation in the X-ray range. However, coherent emission can nevertheless be achieved by "microbunching" where electrons are self-arranged by the FEL process into sufficiently small regions within the bunch (as discussed below).

The physical processes that take place in an FEL can be best seen in figure 4.1. Electrons propagating through the undulator interact with the radiation field originating from electrons further back in the bunch. The energy transfer from the electrons into the light field can be calculated by [Schmüser et al., 2008]

$$\frac{\mathrm{d}W}{\mathrm{d}t} = \vec{v} \cdot \vec{F} = -ev_x E_x, \tag{4.1}$$

where v_x is the transverse electron velocity and E_x the transverse electric field of the radiation field. It can be seen that if v_x is parallel to E_x, the electron transfers energy into the light field and gets decelerated. For anti-parallel electron velocity and electric field vectors, electrons get accelerated by the light field (see figure 4.1**a**). Through the interaction between the electrons with its magnetic field, the undulator acts as an energy-dispersive device: the higher-energy electrons move on "shorter" trajectories since their

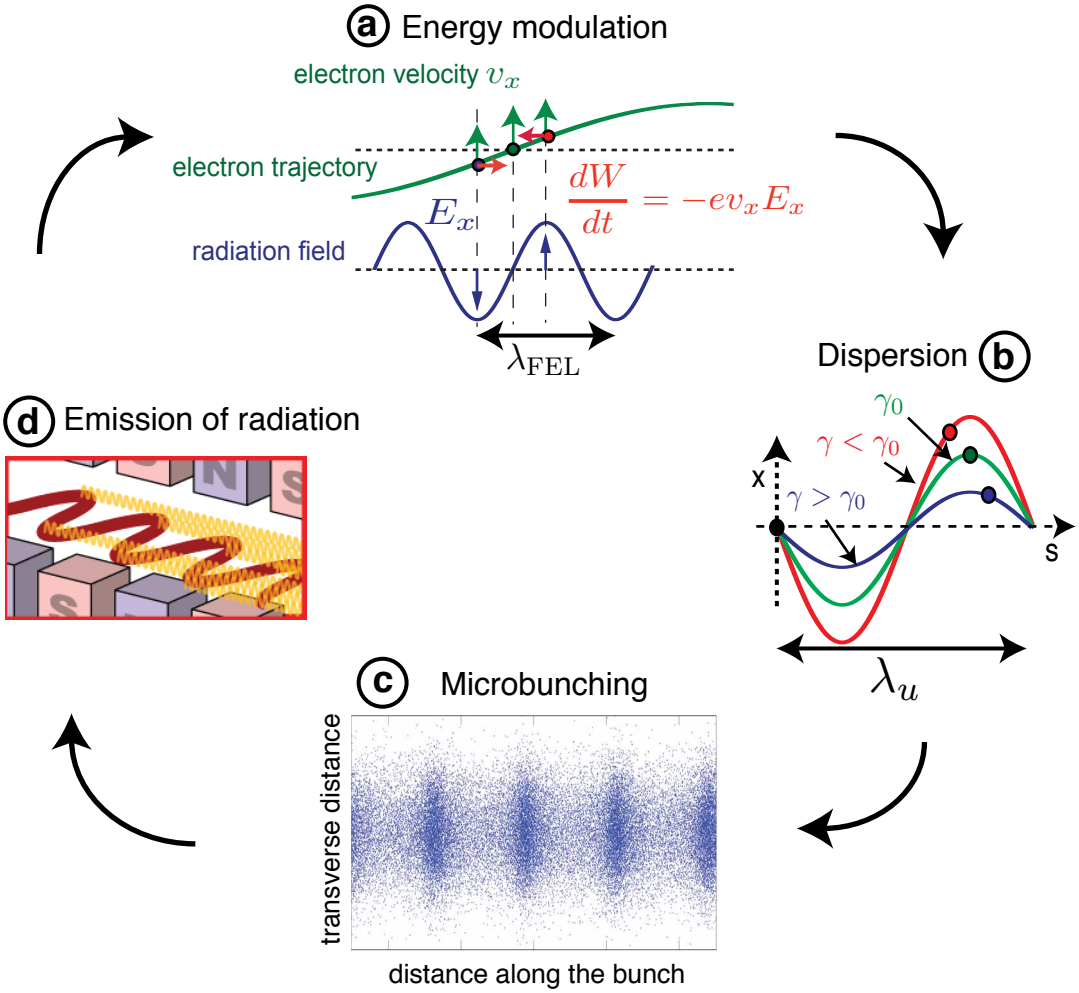

Figure 4.1. | **Principle of the FEL process.** The interaction of electrons with the radiation field (**a**) leads to a correlated change in electron energies. The undulator acts as an dispersive element (**b**) which results in microbunching of the electron bunch (**c**). This leads to an increase in the intensity of the emitted radiation (**d**), which in turn causes a stronger modulation of the electron energies (**a**). An FEL cycles through these processes every undulator period, which leads to its self-amplifying, exponentially-growing gain (as can be seen in figure 4.2). The amplification process is terminated when the space charge forces of the electrons within the microbunches balance the forces of the interaction between the electrons and the radiation field and a maximum possible microbunching of the electron beam is reached. The graph in (**c**) is a result of a 1D FEL simulation (courtesy of T. Seggebrock). Figure (**d**) is taken from wikipedia.

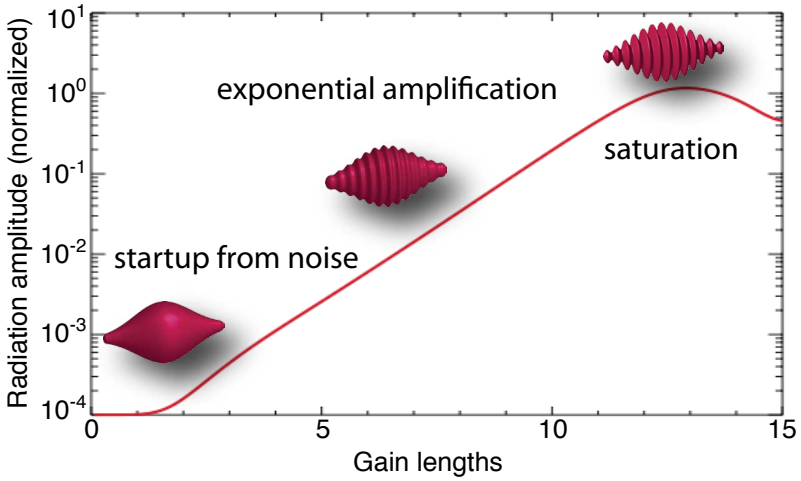

Figure 4.2. | Amplitude of FEL radiation field versus distance along undulator. The figure shows the exponential increase of the FEL radiation field versus the distance along the undulator normalized to the gain length L_{g0}. A cartoon of the electron bunch distribution at various positions is shown in red. The radiation amplitude starts out from noise emitted by a randomly distributed electron bunch. Through the interaction with the radiation field the electron bunch gets microbunched which leads to an increased emission of radiation and to an exponential amplification. When the electron bunch is maximally microbunched, the radiation amplitude reaches saturation. If the electron bunch continues propagating in the undulator the field starts to transfer energy back into the electron bunch and the radiation amplitude starts to oscillate.

transverse deflection (and thus the transverse amplitude of the trajectory) is smaller (transverse amplitude $\propto K/\gamma$ [Huang and Kim, 2007]). Additionally, electrons with a higher energy propagate faster in comparison to lower-energetic electrons and thus advance in the relative bunch coordinate, whereas the slower electrons fall back within the bunch.

In the electron bunch, this dispersion leads to regions of increased density with a periodicity of the wavelength of the electric field (λ_{FEL}) separated by regions of decreased density: the so-called microbunching (see figure 4.1(c)). Owing to this increase in density of electrons in a region $< \lambda_{\mathrm{FEL}}$, the emitted radiation is coherent to a higher degree which means that the intensity of the emission is also increased. This leads to a stronger microbunching and in turn to a stronger emission. This process results in an exponential growth of the emitted FEL radiation along the undulator length which can be seen in figure 4.2. In the SASE regime, the FEL starts out from noise (spontaneous undulator radiation) and reaches saturation after a single pass through the undulator. However, for X-ray FELs this saturation length requires several tens of meters of undulator.

A mathematical 1D treatment of the process shows that the emitted power grows with

the distance along the undulator s as [Schmüser et al., 2008]

$$P = \exp\left(\frac{s}{L_{g0}}\right), \tag{4.2}$$

where the power gain length L_{g0} is defined as

$$L_{g0} = \frac{1}{4\pi\sqrt{3}}\frac{\lambda_u}{\rho}. \tag{4.3}$$

The Pierce parameter ρ is a central parameter in the FEL theory which is defined as

$$\rho = \frac{1}{2\gamma}\left[\frac{I_{\text{peak}}}{I_A}\left(\frac{A_u\lambda_u}{2\pi\sigma_r}\right)^2\right]^{1/3} \propto \frac{1}{\gamma}\left(\frac{I_{\text{peak}}}{I_A}\right)^{1/3}\lambda_u^{4/3}, \tag{4.4}$$

where γ is the relativistic factor, I_{peak}/I_A is the peak current of the electron bunch normalized to the Alfvén current $I_A = 17\,\text{kA}$, λ_u the undulator period and σ_r the transverse electron beam size. The Bessel function factor is given by $A_u = K/\sqrt{2}\,[J_0(\xi) - J_1(\xi)]$ where J_i are Bessel functions which depend on the undulator K parameter through $\xi = K^2/(4 + 2K^2)$. The scaling in equation (4.4) is valid with the assumption of a constant maximum on-axis magnetic undulator field B_0 ($K \propto B_0\lambda_u$) which leads to γ, λ_u and I_{peak} as free parameters. The electron beam size σ_r has to be chosen small to reach a high current density. However, an electron beam size that is too small causes a high beam divergence which leads to an increase of the transverse electron velocities at the expenses of the longitudinal velocities and thus results in an effective increase in the longitudinal energy spread. Bearing these effects in mind, σ_r has to be optimized under consideration of a matched electron beam optics and is effectively not a free parameter.

Typically 15 - 25 gain lengths (L_{g0}) of undulator is required to reach saturation. With a large Pierce parameter ρ, a small saturation length can be achieved (as can be seen from equation (4.3)). Laser-wakefield accelerated (LWFA) electron bunches hold the potential to provide extremely large peak currents. In combination with a small-period undulator, an FEL driven by LWFA beams with relatively small electron energies could reach Pierce parameters that are almost an order of magnitude larger than that of conventional FELs (at similar emission wavelengths). In addition to the the compact sizes of the laser-wakefield accelerator, this could lead to an FEL with significantly smaller dimensions than its conventional counterpart.

In order to undergo an FEL process, the amplification of the radiation intensity has to be large enough to overcompensate any losses (such as diffraction as discussed below). Especially for a single-pass FEL without an optical resonator, this requires electrons beams with a sufficiently high peak current but also a sufficiently high beam quality (such as small energy spread and a small emittance). From a theoretical analysis including degrading effect such as space charge, diffraction and energy spread the requirements on the electron beam quality can be quantified. An upper limit for the relative rms electron beam energy is given by [Schmüser et al., 2008]

$$\frac{\sigma_\gamma}{\gamma} < 0.5 \cdot \rho \tag{4.5}$$

In order to quantify the requirements on the transverse electron beam emittance, an electron beam size matched to get maximum overlap with the FEL radiation is considered. However, since diffraction losses still occur, a gain length L_g smaller than the Rayleigh range z_R is required. The demand of $L_g \approx z_R/2$ in combination with the consideration of an upper limit of transverse electron momenta (that increase the effective energy spread as discussed above) leads to a maximum tolerable emittance of [Schmüser et al., 2008]

$$\epsilon < \frac{\lambda_{\mathrm{FEL}}}{4\pi}. \tag{4.6}$$

This is equal to the emittance of the photon beam emittance of a Gaussian beam as discussed in section 3.4.1. Particularly in the case of short-wavelength FELs, this requirement cannot be fully satisfied which leads to a decrease in transverse coherence (and thus in brilliance) in comparison to theoretical predictions.

From these requirements, it can be seen that the radiation measured in the experiment described is purely spontaneous undulator emission since the energy spread of the electron beam ($\approx 3.5\%$) violates the requirement for an FEL process (typical X-ray FEL parameters are $\rho = 0.01\%$ ... 0.5% [Gruener et al., 2007]).

5. LASER-WAKEFIELD ELECTRON ACCELERATOR

The chapter describes the laser-wakefield accelerator that was used as driver for the undulator source described in the next chapter. The experimental setup relevant for the undulator measurements is described in section 5.1 & 5.2 and the experimental results in section 5.3. For a more detailed discussion, please refer to [Osterhoff, 2008b].

Affiliated publication

- J. Osterhoff, A. Popp, Zs. Major, B. Marx, T. P. Rowlands-Rees, M. Fuchs, M. Geissler, R. Horlein, B. Hidding, S. Becker, E. A. Peralta, U. Schramm, F. Gruner, D. Habs, F. Krausz, S. M. Hooker and S. Karsch, Generation of Stable, Low-Divergence Electron Beams by Laser-Wakefield Acceleration in a Steady-State-Flow Gas Cell. *Phys. Rev. Lett.* **101**, 085002 (2008)

5.1. Laser System

Pulse energy
Pulse duration
Contrast

The laser-wakefield accelerator (LWFA) is driven by the ATLAS laser facility at the Max-Planck-Institut für Quantenoptik. The system delivers pulses on target of 850 mJ energy with a 37 fs FWHM-duration (~ 20 TW) at a central wavelength of ~ 800 nm with a repetition rate of 10 Hz. It is based on titanium-doped sapphire crystals and utilizes the chirped-pulse amplification (CPA) scheme [Strickland and Mourou, 1985], which allows the creation of laser pulses with ultrahigh intensities: temporally stretched laser pulses with a (temporally) correlated, linear photon energy distribution (chirp) are amplified to high intensities without destroying optical components and subsequently (temporally) compressed to a pulse with an ultrahigh intensity. Additionally, the amplification using this technique results in a good beam quality since non-linear effects, such as self-phase modulation or self-focusing are avoided. The contrast of the laser pulse peak intensity to the amplified spontaneous emission background (ASE) on the few picosecond timescale is on the order of 10^{-8} (for further details, see [Osterhoff, 2008b]). The ATLAS laser system is currently being upgraded to pulses with an energy of ~ 2 J and a duration of ~ 20 fs.

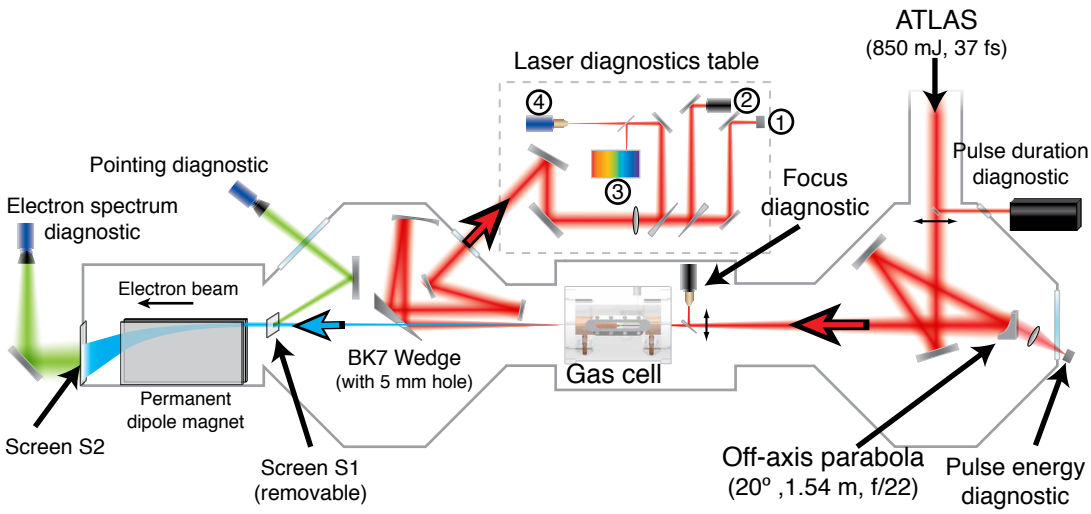

Figure 5.1. | **Setup of the laser-wakefield accelerator.** The laser pulse(red) is focused into a gas cell, where it accelerates electrons (blue). After exiting the gas, the laser can be characterized outside of the vacuum chamber on the diagnostics table. The diagnostics are: 1: Pulse energy, 2: Alignment diagnostic, 3: Laser spectrometer, 4: Laser mode diagnostic. The pointing, divergence and spectrum of the electron beam can be characterized. Viewgraph taken from [Osterhoff, 2008b].

5.2. Experimental Setup

Focal geometry
Normalized vector potential a_0
Laser diagnostics
Electron diagnostics

The laser beam is focused by an off-axis parabola in a $f/22$- geometry over a distance of $f = 1.54\,\mathrm{m}$ to a spot size of $23\,\mu\mathrm{m}$ (FWHM) into the gas cell. The laser energy within the transverse area of $23\,\mu\mathrm{m}$ diameter was measured to be 61% of the total energy [Osterhoff, 2008b]. For the laser parameters described in section 5.1, this leads to an average vacuum FWHM focal intensity of $1.9 \times 10^{18}\,\mathrm{W/cm^2}$ and to a normalized laser vector potential of $a_0 = 0.94$.

Before focusing, the laser pulse duration can be characterized by a second-order autocorrelator (SwampOptics GRENOUILLE) as well as the pulse energy can be measured. The precise laser alignment and the focus quality are inspected for attenuated beams with a stationary 8-bit CCD camera using a microscope objective. The pointing fluctuations of the laser beam at the focus position was measured to be approximately half a focus spot size.

The laser is focused into the gas cell (see below), where it accelerates electrons and gets modulated as described in section 2.6.4. The laser beam after the exit of the gas cell is routinely diagnosed for its beam profile and position, its spectrum as well as its pulse

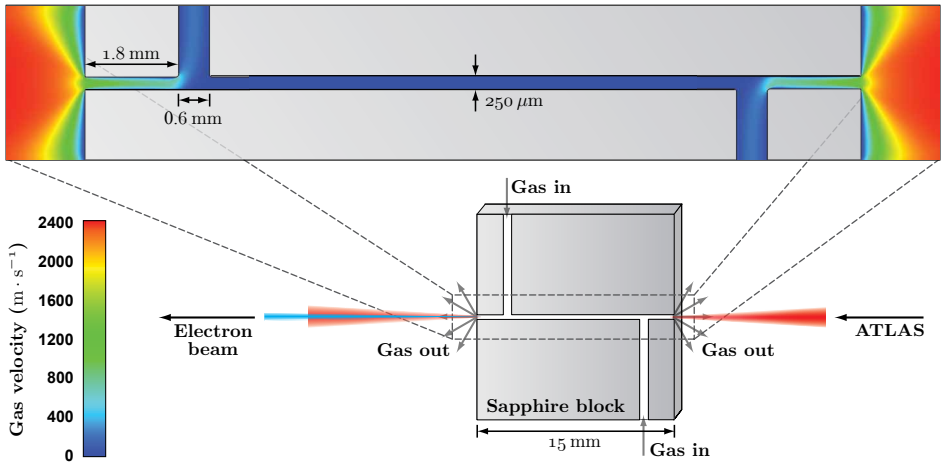

Figure 5.2. | **Gas cell.** The upper part of the figure shows the velocity distribution of the gas in the gas cell, simulated with the fluid-dynamics code FLUENT. The lower part of the figure shows the layout of the gas cell. Viewgraph taken from [Osterhoff, 2008b].

energy. In order to do so, the laser is reflected out of the chamber onto a diagnostics table by an uncoated BK7 wedge with a hole of 5 mm, which does not disturb the electron beam.

The gas cell consists of a cylindrical channel with a diameter 250 µm and 15 mm length. The hydrogen gas from a reservoir is filled into the channel through 0.6 mm thick inlets, located at a distance of 1.8 mm from both exits (see figure 5.2). Half-profiles of the channel and inlets are laser-machined into two sapphire plates, which are pressed together to form a gas cell. The upper part of figure 5.2 shows the almost perfectly stationary and homogenous gas density profile between the two inlets. This in combination with a high stability in laser parameters leads to very reproducible shot-to-shot experimental conditions, which is a reason for the stable electron beams (see section 5.3). The gas cell was operated in pulsed mode with $\sim$ 200 ms filling time to reach steady-state.

Electron Diagnostics

Two diagnostics at different positions allow the characterization of the accelerated electron beam: The beam pointing and divergence can be measured with the help of a scintillating phosphor screen, located at a distance of 1.12 m after the exit of the accelerator (S1 in figure 5.1). This screen can be removed from the beam path in order to ensure the propagation of undisturbed electron beams for characterization of different properties. The screen is imaged with an objective lens onto a 12-bit CCD camera (Point Grey Research Scorpion 1600 x 1200 pixels). The diagnostic is capable of capturing structures down to $\sim$ 150 µm.

The electron spectrum can be diagnosed by a second scintillating screen (S2) located

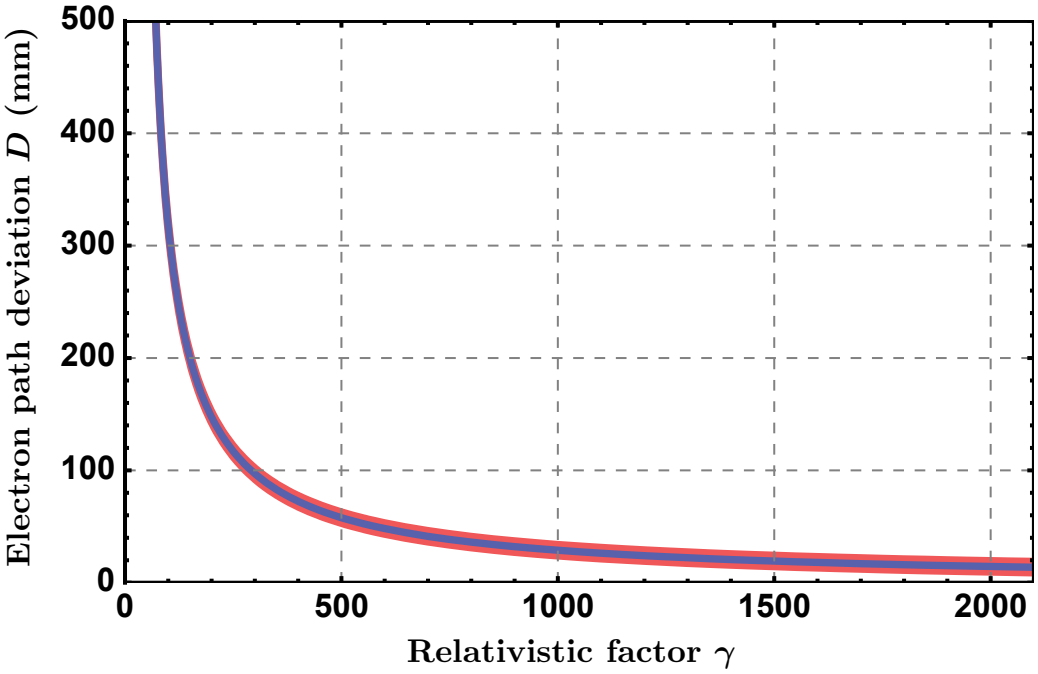

Figure 5.3. | **Deflection of the electron beam after the magnetic dipole.** The figure shows the energy-dependence of the electron-deflection for the spectrometer setup used in these experiments. An electron entering the dipole magnet with an angle of 0 (blue line) and $\pm 1.4\,\mathrm{mrad}$ (red lines) with respect to the defined ∞-energy axis can lead to different deduced energies. Figure taken from [Osterhoff, 2008b].

after a 37 cm-long dipole magnet with a field of $\sim 450\,\mathrm{mT}$. The screen is imaged by a 12-bit PCO Pixelfly QE CCD camera. An absolute calibration in charge of the spectrum diagnostics was performed at a conventional accelerator [Buck et al., 2010]. Since the energy calibration of the setup could not be done with well-defined electron beams, the electron spectra are deduced from the deflection of the electrons by the dipole magnet: The fields of the magnet were characterized by a Hall-probe measurement. These fields were used in a single-particle tracking code to map the electron deflection onto a corresponding electron energy. However, this method of determining the energy is conditional on the divergence and the angle of the electron beam with respect to the defined ∞-energy axis. An analytical model was used in [Osterhoff, 2008b] to estimate the error in the deduced electron energy of a beam that is entering the spectrometer under an angle with respect to the ∞-energy axis. The result for a typical value of $\pm 1.4\,\mathrm{mrad}$ (which arises from beam pointing measurements at screen S1, directly in front of the spectrometer entrance) can be seen in figure 5.3.

Since the electrons are energy-dispersed only in the vertical direction, the spectral properties of the (horizontal) transverse beam structure can be characterized as can be seen in figure 5.4.

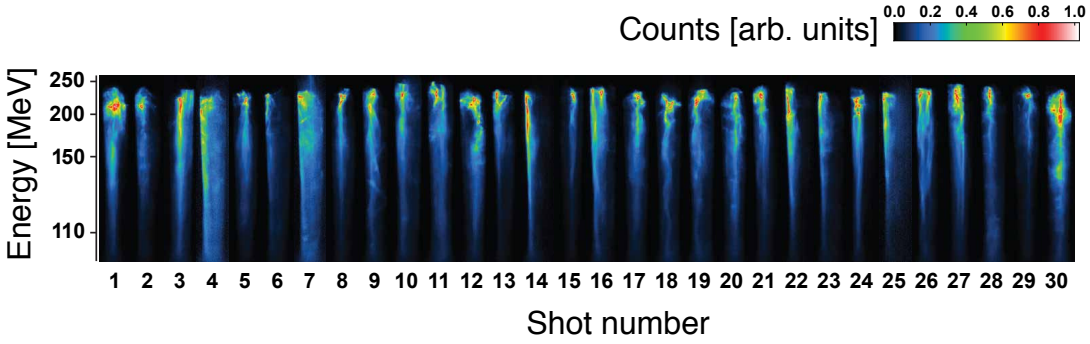

Figure 5.4. | Time series of energy-dispersed electron beams of consecutive laser shots. Each vertical line corresponds to a separate electron beam produced by consecutive driver laser shots. The vertical dimension is the deflection of the electron beam by the dipole magnet of the spectrometer and corresponds to the energy distribution of the electron beam. Color-coded are the CCD counts, which are normalized for each shot. The horizontal dimension corresponds to the divergence of the electron beam. It can be seen that the quasi-monoenergetic features located at around 220 MeV show a significantly smaller divergence than the spectral background. Figure from [Osterhoff, 2008b].

5.3. Properties of the LWFA Electron Beams

Spectral distribution
Charge
Energy spread of the peaks
Divergence
Shot-to-shot pointing

A stable regime for electron acceleration has been found for a plasma density of $n_e \sim 7.3 \times 10^{18}\text{cm}^{-3}$. In this regime, electron beams that show similar spectra in 80% of consecutive driver laser shots have been produced. Fluctuations in the laser as well as the target gas properties in the remaining 20% are responsible for differently shaped spectra. Typical electron spectra have a quasi-monoenergetic feature at an energy of $\sim$ 220 MeV on top of a broad background (see figure 5.5). Shots taken in a run over 40 consecutive driver laser shots show that the energy of the peaks varies around 214 MeV with a standard deviation of 6%, whereas the energy of the high-energy cutoff around 234 MeV has a standard deviation of 3% [Osterhoff et al., 2008][1]. The energy fluctuations agree with the observation that undulator radiation produced by only the high-energy part of the electron spectra results in a smaller wavelength variation than

[1]Note that the electron energies given in [Osterhoff et al., 2008] are a factor of 0.93 too low. This has been found by the wavelength analysis of the undulator radiation, produced by these electrons (see next chapter). A thorough characterization of the magnetic dipole of the electron spectrometer has shown a slightly higher average field strength of 458 mT (than 450 mT used in [Osterhoff et al., 2008]), which leads to higher electron energies for the same electron deflection distance.

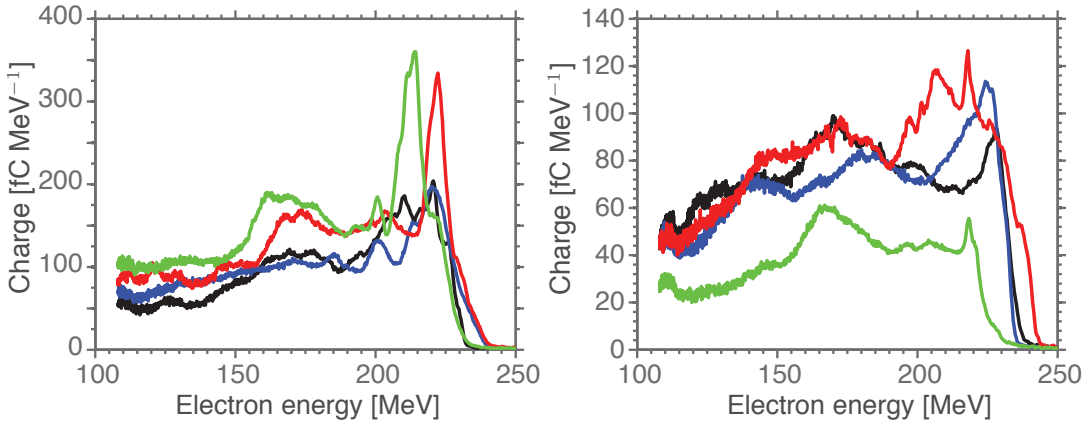

Figure 5.5. | **Typical electron beam spectra.** The figure shows spectra of some typical shots of figure 5.4. The left-hand side shows spectra with more pronounced quasi-monoenergetic features than the spectra on the right-hand side. Any correlation between laser and plasma parameters and the occurrence of the pronounced quasi-monoenergetic features has not yet been found and is still subject to research.

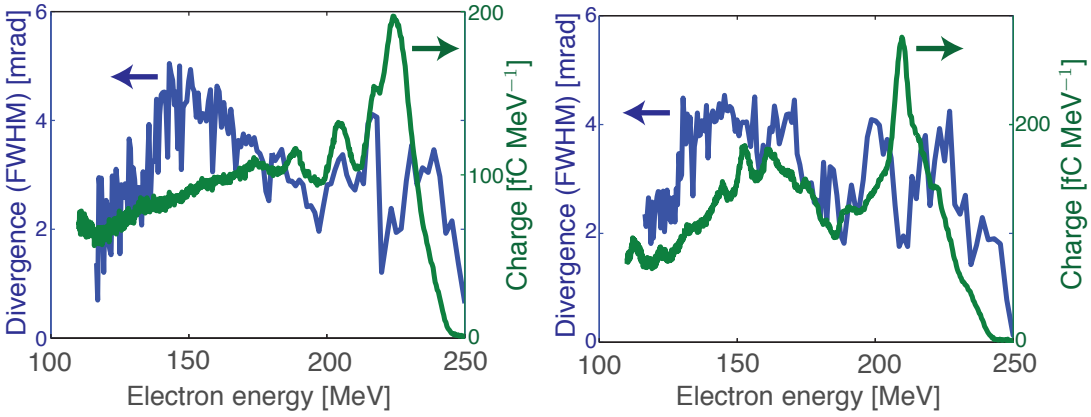

Figure 5.6. | **Energy-dependent divergence of LWFA beams.** The figure shows the electron spectra (green; scale on right hand side) and the energy-dependent divergence (blue; scale on the left) of the LWFA electron beams used in the experiment described below. It can be seen that the quasi-monoenergetic features of the beams have the smallest divergence of $\sim 700\,\mu\mathrm{rad}$ (rms).

radiation produced from the spectral region around the quasi-monenergetic features (see section 6.2). The peaks of the electron spectra show a relative energy spread of 8.2% (FWHM).

In the spectrally-resolved transverse beam profiles (figure 5.4), it can be seen that the quasi-monoenergetic features of the beams have a significantly lower divergence than the background (see also figure 5.6). The integrated charge of the electron beams is 12 pC with $4 \pm 1.6\,\mathrm{pC}$ in the peak and $8 \pm 2\,\mathrm{pC}$ in the background.

The electron beam profile of a single shot can be seen in figure 5.7. An analysis of 74 consecutive shots shows an average rms-divergence of 0.9 ± 0.2mrad [Osterhoff

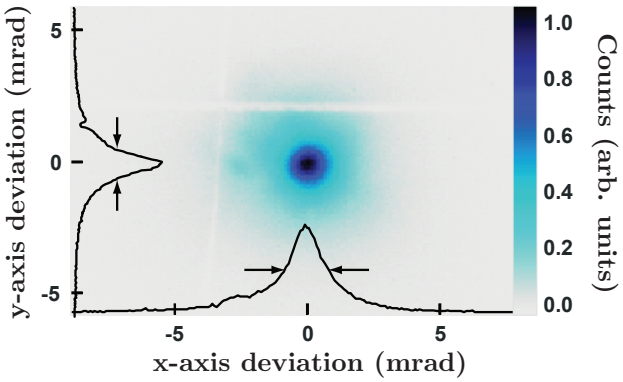

Figure 5.7. | **Electron beam divergence.** The figure shows the electron beam profile detected with the scintillating screen S1 at a distance of 1.12 m after the exit of the accelerator. The divergence of this shot is 0.7 mrad, assuming a Gaussian profile [Osterhoff et al., 2008]. The white lines in the figure arise from pen markers used for spatial calibration.

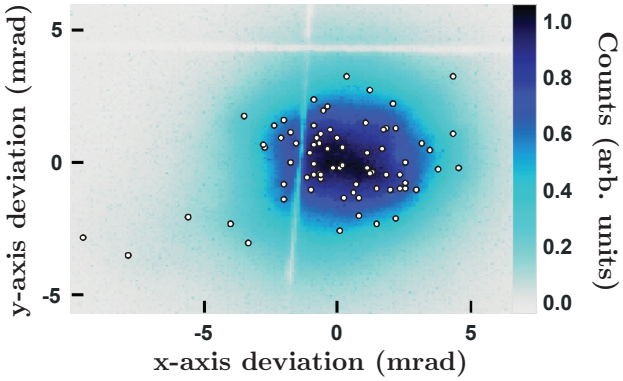

Figure 5.8. | **Shot-to-shot pointing of the electron beam.** The figure shows the signal detected at screen S1, summed up over 74 consecutive electron shots. The dots correspond to the peak positions of each shot and the color-coding corresponds to the overall count distribution. From this an rms shot-to-shot pointing fluctuation of 1.4 mrad (y-axis) and 2.2 mrad (x-axis) can be deduced. [Osterhoff et al., 2008]. The laser polarization is along the x-axis. The white lines in the figure arise from pen markers used for spatial calibration.

et al., 2008]. Note that this diagnostics is not sensitive to electron energies and thus the divergence is deduced from the whole transverse beam distribution, which means that the lower divergent quasi-monenergetic features cannot be distinguished from the beam background. The shot-to-shot pointing of the electron beam can be seen in figure 5.8. An rms-fluctuation of 2.2 mrad along the axis of the laser polarization and 1.4 mrad perpendicular to the laser-polarization axis can be deduced from a series of 74 consecutive shots.

6. EXPERIMENTAL UNDULATOR RADIATION RESULTS

The chapter discusses the experimental observation of soft-X-ray undulator radiation from a laser-wakefield-driven undulator source. The experimental setup is described in section 6.1, simulations of undulator radiation that explain the experimental findings are discussed in section 6.2 and the experimental results compared for different utilized setups are reported in section 6.3.

Affiliated publications:

- T. Eichner, F. Grüner, S. Becker, M. Fuchs, D. Habs, R. Weingartner, U. Schramm, H. Backe, P. Kunz, W. Lauth, Miniature magnetic devices for laser-based, table-top free-electron lasers. *Phys. Rev. STAB*, **10**, 082401 (2007).
- R. Weingartner, M. Fuchs, A. Popp, S. Raith, S. Becker, S. Chou, M. Heigoldt, K. Khrennikov, J. Wenz, B. Zeitler, Zs. Major, J. Osterhoff, F. Krausz, S. Karsch, F. Grüner, Imaging laser-wakefield-accelerated electrons using miniature magnetic quadrupole lenses. *to be published.*
- M. Fuchs, R. Weingartner, A. Popp, Zs. Major, S. Becker, J. Osterhoff, I. Cortrie, B. Zeitler, R. Horlein, G.D. Tsakiris, U. Schramm, T.P. Rowlands-Rees, S.M. Hooker, D. Habs, F. Krausz, S. Karsch, F. Grüner, Laser-driven soft-X-ray undulator source. *Nat. Phys.*, **5**, 826–829 (2009).

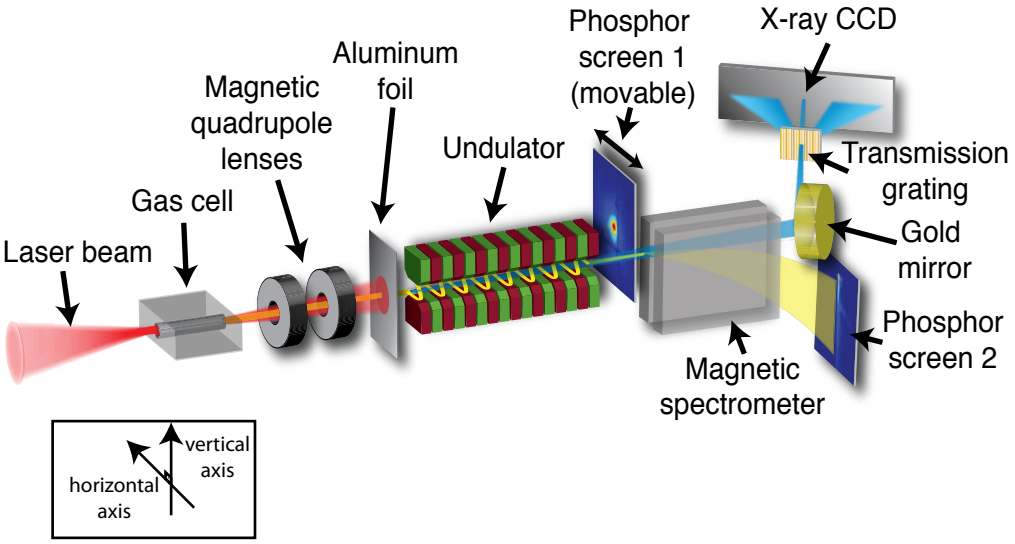

Figure 6.1. | **Experimental setup.** A laser pulse from the ATLAS laser facility (red) is focused into a hydrogen-filled gas cell, where it accelerates electrons to energies of about 200 MeV (yellow). The electron beam is collimated by a pair of miniature permanent magnetic quadrupole lenses. A 15 μm thick aluminum foil blocks the laser as well as plasma radiation. The electrons emit soft X-ray radiation by propagating through a 30 cm long undulator. The undulator radiation is collected and horizontally focused by a spherical gold mirror with a radius of curvature of 10 m in grazing incidence configuration. It is subsequently analyzed by an X-ray spectrometer consisting of a 1000 lines/mm transmission grating and an X-ray CCD camera. The pointing and divergence of the electron beam can be diagnosed by a phosphor screen at a distance of 1.12 m after the exit of the accelerator. The electron spectrum can be measured by a second phosphor screen (at a distance of 1.94 m from the accelerator) after the electron beam has been energy-dispersed by a dipole magnet. The distance from the accelerator to the lenses is ≈ 30 cm, from the lenses to the undulator ≈ 15 cm, from the undulator center to the gold mirror ≈ 1.4 m, from the gold mirror to the grating ≈ 1.04 m and from the grating to the CCD detector ≈ 30 cm.

6.1. Setup and Components

The setup of the experiment is shown in figure 6.1. It is composed of three main parts: (1) the electron accelerator and associated diagnostics, (2) the electron beam transport to collimate the electron beam and the undulator to produce radiation and (3) the undulator radiation diagnostics. The components (2) and (3) are described in detail in the following section, for further information on the LWFA accelerator see the previous chapter.

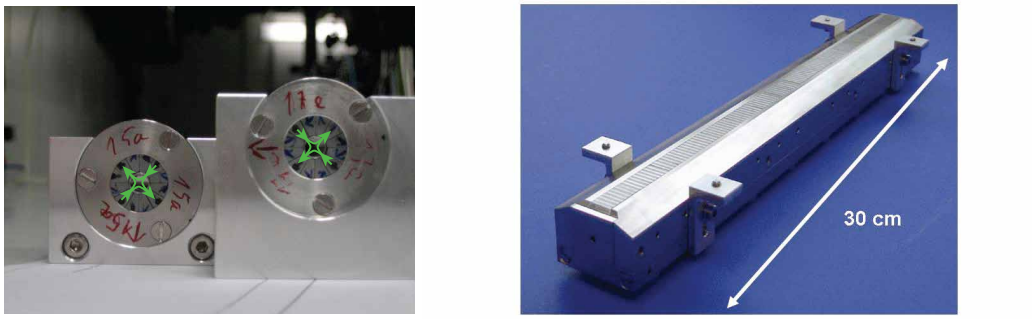

Figure 6.2. | **Photograph of magnetic lenses and undulator.** The left-hand side of the figure shows the magnetic quadrupole lenses. They have a magnetic field gradient of ≈500 T/m over an inner bore radius of 6 mm and a length of 17 mm and 15 mm, respectively. The green lines depict the quadrupole fields. The right-hand side shows a photograph of the lower half of the undulator. It has a magnetic field period of 5 mm over a total length of 30 cm.

6.1.1. Miniature Magnetic Quadrupole Lenses and Undulator

Properties of the miniature magnetic quadrupole lenses
Properties of the short-period undulator
Estimation of the undulator radiation linewidth

Both the miniature permanent magnetic quadrupole lenses (PMQs) and the undulator have been specifically designed for the experiment described below. The high-gradient miniature PMQs with a length of only a few centimeters and the 30 cm-long, short-period undulator are designed to realize a compact overall setup [Eichner et al., 2007]. The small dimensions of the setup are necessary to take full advantage of the unique properties of laser-wakefield accelerated electron beams, such as their ultrashort pulse duration. The large intrinsic divergence of the LWFA electron beam causes the bunch to elongate due to path length differences during the propagation over the distance from the accelerator to the undulator (see figure 6.7). This can be mitigated by collimating the beam at a distance as close as possible to the exit of the accelerator. Owing to their large field gradients, this can be achieved by the compact PMQs. Typical electromagnetic lenses have significantly smaller field gradients. Therefore, they have to be placed further away and have to be of an increased length in order to have the same collimating effect as the miniature permanent magnetic quads and cannot counteract the bunch elongation equally well.

The PMQs as well as the undulator have been commissioned at the conventional electron accelerator facility “Mainzer Mikrotron” (MAMI) [Eichner et al., 2007].

The ≈500 T/m magnetic field gradients of the **miniature PMQs** ensure a sufficiently high strength to focus electron beams with energies of several hundred MeV to a few GeV, despite their compact lengths. In order to realize such high gradients, magnetic fields of 1.5 T at the tip of the poles are produced by NdFeB permanent magnets in

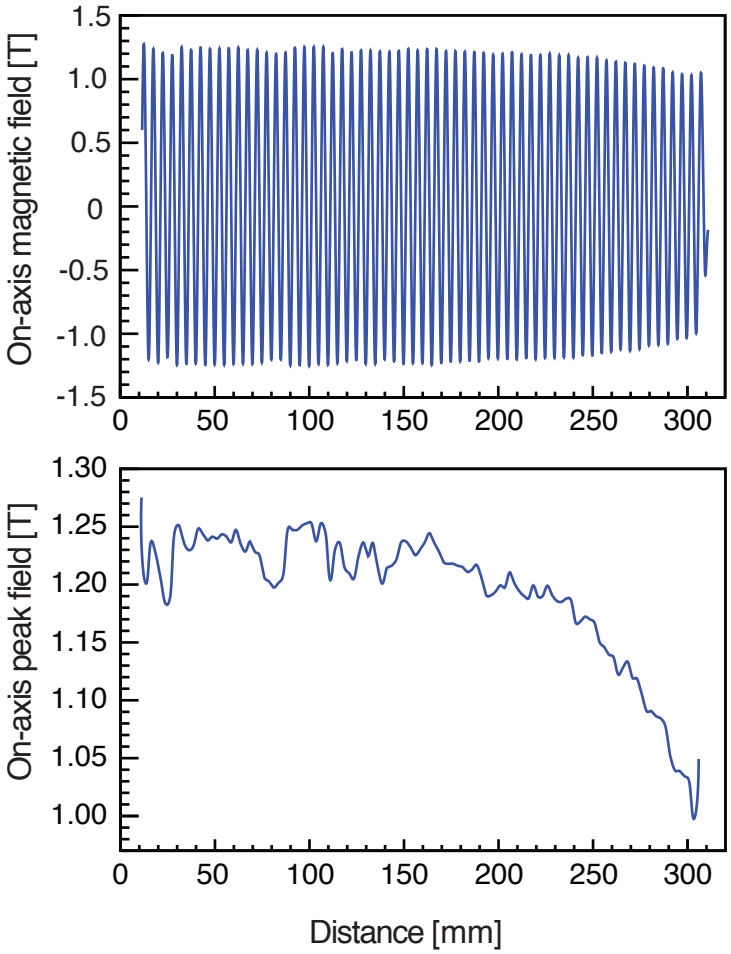

Figure 6.3. | **Measured undulator field.** The upper part of the figure shows the undulator magnetic field for a gap of 1.2 mm measured with a hall probe. The lower part shows the distribution of the absolute peak value of the amplitude along the undulator. Note the zoomed-in scale in the lower figure.

a Halbach configuration [Halbach, 1980] over a bore radius of 3 mm. A sophisticated tuning method of the lenses [Becker et al., 2009] proved to be able to minimize their higher order magnetic moments. This is important to minimize any deteriorating effect on the electron beam emittance.

The **undulator** is built with NdFeB permanent magnets arranged in a Halbach hybrid geometry which utilizes saturated CoFe plates to guide the magnetic field. It consists of 60 periods, each with a length of 5 mm. The distance between the poles was set to 1.2 mm which is a tradeoff between a high magnetic field (and thus a high photon yield, see equation 6.15) and a gap that is sufficiently large to minimize the risk of electrons hitting the undulator magnets which can thereby lose their magnetization. In such a configuration the undulator produces an on-axis magnetic field with an amplitude of $B_0 \simeq 1.2$ T which results in deflection parameter of $K \simeq 0.55$ (3.1). A slight decrease of magnetic field toward one side of the undulator was observed with a Hall probe

measurement, leading to a mean field of $B_0 = 1213\,\mathrm{mT}$ with an rms deviation of 29.5 mT (figure 6.3). These field variations can be somewhat flattened by tuning of the magnetic flux distribution [Eichner, 2007]. However, a 2.4 % fluctuation is tolerable since the bandwidth of the produced undulator radiation is dominated by other effects: In our case, the main contributions to the on-axis undulator radiation bandwidth are

$$\frac{\Delta\lambda}{\lambda} = \sqrt{\left(\frac{\Delta\lambda}{\lambda}\right)^2_{\mathrm{nat}} + \left(\frac{\Delta\lambda}{\lambda}\right)^2_{\Delta B} + \left(\frac{\Delta\lambda}{\lambda}\right)^2_{\Delta\gamma} + \left(\frac{\Delta\lambda}{\lambda}\right)^2_{\epsilon}}, \tag{6.1}$$

where the terms describe broadening due to:
the natural linewidth of a $N_u = 60$ period undulator

$$\left(\frac{\Delta\lambda}{\lambda}\right)_{\mathrm{nat}} \simeq \frac{1}{nN_u} = 1.7\,\% \tag{6.2}$$

the fluctuations in magnetic field B of 2.4 %, expressed in terms of the undulator deflection parameter K

$$\left(\frac{\Delta\lambda}{\lambda}\right)_{\Delta K,\mathrm{fluct}} = \frac{K^2}{1+K^2/2}\frac{\Delta K}{K} = 0.6\,\%. \tag{6.3}$$

Furthermore, an electron bunch with a finite transverse beam size experiences different undulator magnetic field along its vertical axis. The vertical undulator magnetic field changes according to $B(z) = B_0 \cdot \cosh(2\pi z/\lambda_u)$ [Wille, 2000] which leads for a typical electron beam size of 450 µm (see table 6.1) to a magnetic field of 1412 mT at $z = 450\mu\mathrm{m}$. This $\Delta B_0/B_0 \simeq 14\%$ over the beam width leads to an increase in the integrated detected linewidth of

$$\left(\frac{\Delta\lambda}{\lambda}\right)_{\Delta K,B-\mathrm{var}} = \frac{K^2}{1+K^2/2}\frac{\Delta K}{K} = 3.7\,\%, \tag{6.4}$$

the electron-energy spread of the quasi-monoenergetic features of $\simeq 8$ % FWHM ($\simeq 3.4\%$ (rms)) of the beams utilized in this experiment [Osterhoff et al., 2008]

$$\left(\frac{\Delta\lambda}{\lambda}\right)_{\Delta\gamma} = 2\cdot\frac{\sigma_\gamma}{\gamma} \simeq 6.8\,\%. \tag{6.5}$$

The broadening due to emittance effects $(\Delta\lambda/\lambda)_\epsilon$ depends on electron beam size and divergence which owing to the chromaticity of the magnetic lenses vary with the electron energy (see section 6.2). The linewidth broadening due to this effect for energies around the peak energy can be deduced from undulator simulations of finite-emittance electron beams (see section 6.2.5) and are on the order of a few per cent.

6.1.2. Electron Beam Transport

Setup: Collimation of the electron beam
Effects on the divergence and angular fluctuations of the beam
Energy acceptance of the lens setup
Steering of the electron beam
Suppression of the increase in electron pulse duration

After exiting the plasma accelerator, the electron beam is collimated by a doublet of miniature permanent magnet quadrupole lenses. The lenses have proven to be a critical system component for three reasons: (1) They reduce the divergence and the effective angular shot-to-shot fluctuation of the electron beam (see section below and figure 6.4). This way, they prevent electrons from hitting the undulator walls and enable a higher reproducibility of the undulator radiation. Note that collimating the beam does not modify the intrinsic pointing fluctuations of the LWFA bunch, however, it reduced the effective spatial shot-to-shot variation on target. (2) The chromatic effects of the magnetic lenses onto the electron beam leads to an effective energy-band-pass filter for the undulator radiation (see section 6.2). This decreases both the photon-energy bandwidth and spectral fluctuations of the radiation. (3) The collimation of the beam mitigates the elongation of the electron bunch due to path-length differences occurring in a free drift during the transport from the accelerator to the undulator and thus ensure the conservation of its ultrashort pulse duration (see figure 6.7).

Collimation

The effect of the collimation of the electron beam through the magnetic lenses in comparison to freely drifting beams can be seen in figure 6.4. The lenses were set to collimate an electron energy of $\simeq 210$ MeV which corresponds to the energy of the quasi-monoenergetic peak of the spectral electron distribution. Despite the chromatic effects of the lenses, a clear reduction in divergence and angular shot-to-shot fluctuations can be seen which results in an increased reproducibility of the beam (for further details, see [Weingartner et al.]).

Magnetic Quadrupole Lens Setup

In section 3.5.2 it can be seen that the highest brilliance for a thick electron beam can be achieved, if the electron beam is focused into the undulator center ($\alpha_{\mathrm{Twiss}} = 0$) with a Twiss parameter of $\beta_{\mathrm{Twiss}} = L/(2\pi)$ matched to the undulator length L. However, in order to account for the wide range of energies and the energy fluctuations of the LWFA electron beams, a setup that collimates the beam was chosen for this experiment. The energy acceptance of the setup is mainly given by the beam size at the exit of the undulator which (vertically) has to be smaller than the undulator gap, in order not to hit the undulator magnets with the electron beam. In figure 6.5, it can be seen, that the acceptance for the β-matched setup is significantly smaller than that of the (collimating) setup used in the experiment. An additional drawback of the β-matched setup is that

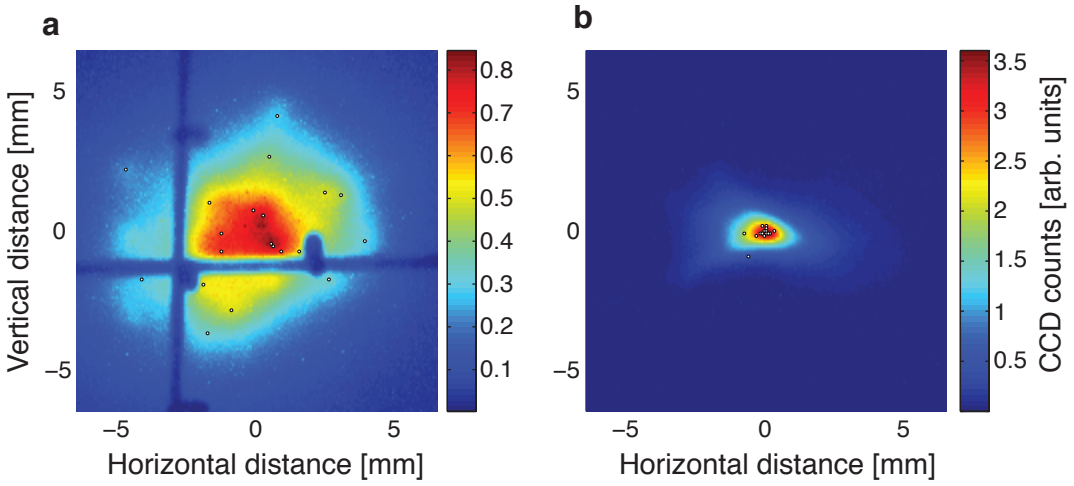

Figure 6.4. | **Angular shot-to-shot fluctuation.** The angular shot-to-shot fluctuations are measured at the pointing diagnostics screen S1 at a distance of 1.12 m after the exit of the accelerator. Color-coded is the sum over 20 consecutive shots without lenses (**a**) and 47 consecutive shots after the collimation with the magnetic lenses (**b**), where the dots indicate the position of the peak of each shot. The FWHM-fluctuations at this distance are for the free-drifting beam vertically 5.3 mm and horizontally 5.2 mm, whereas the application of the lenses reduce these values to 0.9 mm (vertical) and 1.2 mm (horizontal) [Weingartner et al.].

the produced undulator radiation is emitted with a relatively high divergence and has to be focused in both dimensions. In the soft-X-ray range, focusing with relatively high efficiencies can only be realized by a setup of grazing incidence mirrors which is highly prone to pointing fluctuations. The magnetic lens setup used in this experiment proved that it is possible to focus the undulator radiation by means of a convergent electron beam with a focus at the detector (see section 6.2) and thus, in principle, no additional mirrors are need for focusing (see chapter 7). However, in order to keep the setup as simple as possible, only a doublet instead of a triplet of magnetic lenses was used which leads to an elliptical beam profile with a larger horizontal diameter. These larger horizontal beam sizes were collected and focused by a grazing incidence gold mirror (see figure 6.1).

The lenses used in the experiment were a 17 mm long lens with a gradient of 481 T/m and a 15 mm long lens with a gradient of 485 T/m. The appropriate distances between the accelerator exit and the first lens (D_1) as well as the distance between both lenses (D_2) are found with the help of a code for designing particle optical systems [Makino and Berz, 1999]. The distances for collimating electron beams of various energies and the corresponding electron beam sizes and divergences in the undulator center can be seen table 6.1.

An additional advantage of the magnetic lenses is that they allow to steer the electron beam (see figure 6.6). This is crucial for the fine alignment of the electron beam with respect to the undulator.

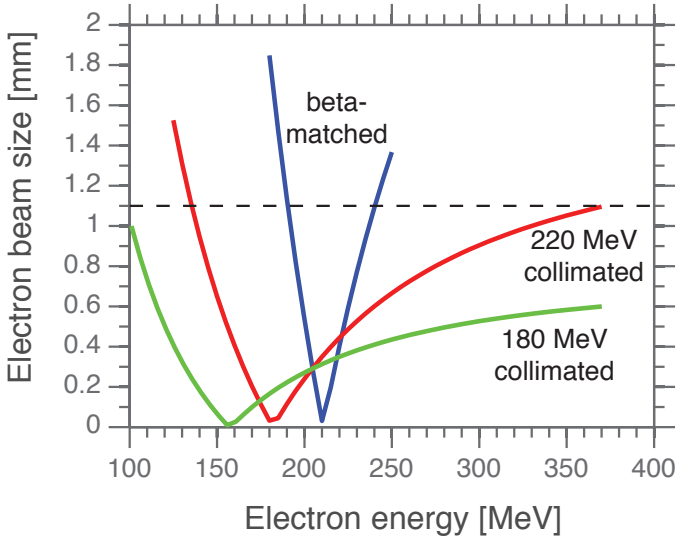

Figure 6.5. | **Electron beam size for two lens setups.** Calculated electron beam sizes at the undulator exit versus the electron energy for a β-matched lens setup (blue) and the lenses set to collimate 180 MeV (green) and 220 MeV (red) as used in the experiment. The undulator gap of 1.2 mm is indicated by the dashed line.

E [MeV]	D_1 [cm]	D_2 [cm]	h-size [μm]	v-size [μm]	h-div [μrad]	v-div [μrad]
150	20.15	1.00	323.05	148.57	17.17	9.37
160	21.36	1.15	341.52	158.09	15.70	8.41
170	22.57	1.30	360.13	167.71	13.76	7.36
180	23.79	1.46	377.34	176.12	17.10	8.21
190	25.00	1.61	395.99	185.76	15.11	7.09
200	26.20	1.77	413.38	194.36	17.74	7.57
210	27.41	1.92	432.00	203.99	15.74	6.46
220	28.62	2.07	450.60	213.61	13.85	5.50
230	29.82	2.23	468.20	222.23	16.12	5.90
240	31.03	2.38	486.78	231.80	14.35	5.07
250	32.24	2.53	505.34	241.33	12.72	4.45
without lenses			718.73	718.73	1000.00	1000.00

Table 6.1. | **Distances of lens setups for different electron energies.** The distance between the accelerator exit and the first lens (D_1) and between the two lenses (D_2) for lens setups that collimated an electron beam with an energy E. The horizontal and vertical beam size (h-size and v-size) as well as the horizontal and vertical divergences (h-div and v-div) are given in the undulator center for an geometrical emittance of $\epsilon = 1\,\mu\mathrm{m}\,\mathrm{mrad}$.

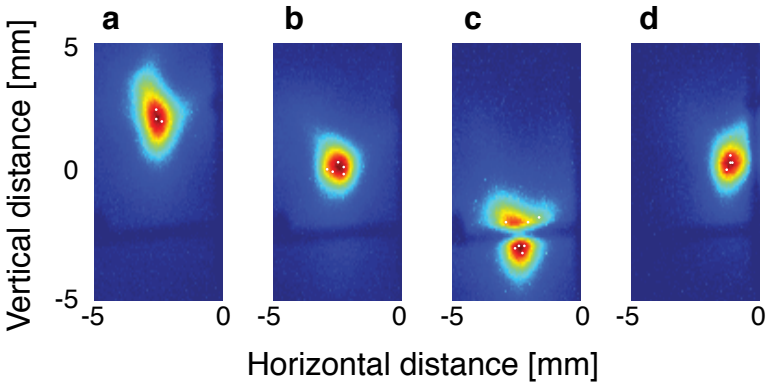

Figure 6.6. | Steering of the electron by translation of the magnetic lenses. Demonstration of the steering of the electron beam through a translation of a few micrometer of the magnetic lenses in vertical **a, b, c** and horizontal **d** direction. The horizontal black line arises from pen marks used for spatial calibration.

Mitigation of the Increase in Electron Pulse Duration through Beam Transport

Laser-wakefield accelerated electron beams are expected to have an ultrashort pulse duration on the order of $\sim 10\,\mathrm{fs}$ (see section 2.7.1). Since the undulator is positioned $\sim 50\,\mathrm{cm}$ after the exit of the accelerator, the influence of degrading effects that elongate the bunch duration during beam transport, such as space-charge effects, path-length differences due to angular spread and chromatic effects of the lenses as well as energy spread have to be taken into account. Figure 6.7 shows the bunch-duration evolution of a 10 fs ($\sim 3\,\mu\mathrm{m}$) long electron bunch along our setup simulated by a tracking algorithm [GPT, 2009], which includes all degrading effects mentioned above. According to this simulation, a bunch with a longitudinal rms-length of $2.95\,\mu\mathrm{m}$ (9.8 fs) elongates to $3.06\,\mu\mathrm{m}$ (10.2 fs) over the distance of our beamline (including the magnetic lenses), which extends from the exit of the accelerator to the exit of the undulator (at $\sim 0.8\,\mathrm{m}$).

In our case, the predominant effect in the growth of bunch duration is the path length difference due to a finite emittance electron beam, i.e. the path-length difference of an electron with a finite divergence in comparison to a on-axis reference electron with zero divergence. In the case of a free drift (no magnetic lenses, green curve in figure 6.7), the path difference grows perpetually along the whole setup. For our beamline with lenses (red curve in figure 6.7), the path difference increases similar to the free drift until the bunch reaches the first lens. Then it grows rapidly, since the first lens is defocusing in the horizontal direction which leads to an even larger path-length difference. After the second lens (which is focusing in the vertical dimension), the electron beam is collimated (see the yellow envelope in figure 6.16) and therefore no more path length difference is accumulated which means that the bunch duration remains almost constant. Thus, in order to conserve the ultrashort pulse durations, the highly-divergent LWFA electron beams should be collimated as close to the accelerator exit. This is only possible for thin lenses with a large field gradient such as the miniature magnetic quadrupole lenses

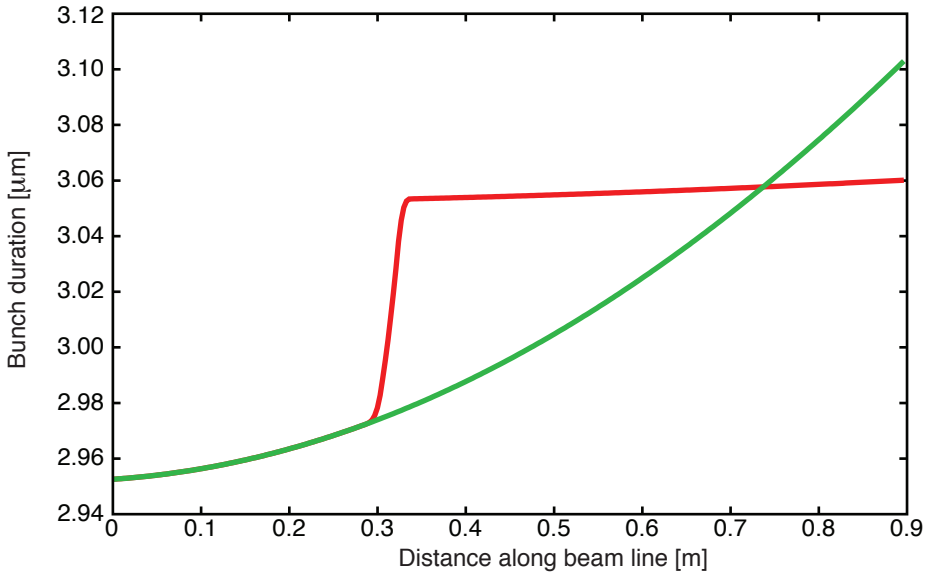

Figure 6.7. | **Simulation of the evolution of the electron bunch duration along the beamline.** The red curve shows the bunch-duration evolution of an electron bunch that is propagating through the beamline including the magnetic lenses, (which are positioned at 28 cm and 32 cm; the undulator from 50-80 cm), and the green curve shows the growth of the duration of a free-drifting bunch. Both curves are simulated with a tracking code [GPT, 2009] with an initial bunch duration of 10 fs, an initial RMS-divergence of 1 mrad and rms-source size of 2 µm, a charge of 5 pC and an energy of 210 MeV with an rms-energy spread of 3.5 %.

used in this experiment (see section 6.1.1).

An analytical beam-transport calculation of an electron with an initial divergence of 1 mrad (one standard deviation of the divergence distribution) and a zero-divergence electron, both propagating through the lens setup, leads to a path-length difference of $\sim 0.5\,\mu m$ ($\sim 2.4\,fs$). A convolution with the whole temporal Gaussian bunch distribution of 10 fs rms gives an increase in bunch duration of 0.3 fs, which agrees very well with the simulated results.

The elongation of the bunch duration due to electron-energy spread and the resulting time of arrival differences for electrons with different energies can be neglected in our case. The simulated durations for a bunch without energy spread does not significantly differ from a bunch with an RMS energy-spread of 3.5% (corresponding to the width of the effective electron spectrum, see section 6.2). An analytical upper limit for two zero-emittance electrons with energies of 200 and 210 MeV, respectively, yields an arrival-time difference of 0.8 fs. Simulations for a bunch with a charge of 5 pC show that space-charge effects also do not have a significant influence on the duration. Space charge primarily leads to the development of an energy chirp along the bunch hence increase the initial energy spread [Grüner et al., 2009] as well as increase the initial beam divergence due to Coulomb explosion. Yet, for the relatively small charge of 5 pC, the transverse bunch expansion is mainly driven by the initial divergence.

6.1.3. Undulator Radiation Diagnostics

Transmission curves of XUV and optical band-pass filters
Electron beam scattering through a thin aluminum foil
X-ray spectrometer
Calibration of X-ray spectrometer
Deduction of photon number from CCD counts

Filters

The properties of the undulator radiation were mainly characterized by an X-ray spectrometer. Since the X-ray CCD camera used in this spectrometer, is very sensitive to optical light, the undulator radiation has to be separated from any laser light as well as from any background radiation. This task was performed by several filters: a 15 μm thick, several 150 and 450 nm thick aluminum[1] as well as several 150 and 450 nm thick zirconium foils[1] which could be used each of its own or in a combination of several foils. The thick Al foil was used to block the remaining laser light that exits the accelerator as well as any plasma radiation which in our case has a relatively high intensity in the XUV range. This mainly originates from recombination radiation of oxygen in the sapphire (Al_2O_3) capillary walls. The foil was placed directly in front of the undulator in order to separate this background radiation from the subsequently produced undulator signal. Since the laser beam is still very small and intense at that distance, the foil has to be chosen sufficiently thick, in order to resist puncture by laser ablation which could lead to a leakage of laser light that could destroy the CCD camera. However, it has to be chosen thin enough as to not significantly deteriorate the electron beam emittance via multiple Coulomb scattering as it passes through. The increase of the angular distribution of a filament electron beam traversing a medium of thickness x with a so-called radiation length of X_0 can be estimated by [Amsler and *et al.*, 2008]

$$\sigma_\theta\,[\mathrm{rad}] = \frac{13.6}{\beta E\,[\mathrm{MeV}]}\sqrt{\frac{x}{X_0}}\left[1 + 0.038\ln\left(\frac{x}{X_0}\right)\right], \tag{6.6}$$

where E and β are the electron energy and the normalized electron velocity, respectively. For an aluminum foil ($X_0 = 8.9\,\mathrm{cm}$) of the thickness $15\,\mu$m, the increase in angular distribution is $\sigma_\theta = 0.54\,\mathrm{mrad}$. However, this drastic increase in emittance does not significantly influence the result of the experiment described below, since the high electron energy spread is largest degrading effect, as discussed in section 6.3.2.

The thin (few hundred nm-thick) foils are placed directly in front of the entrance slit of the X-ray spectrometer. The transmission curves of thin aluminum and zirconium foils in the soft-X-ray as well as in the optical wavelength range can be seen in figures 6.8 & 6.9.

However, due to XUV radiation emitted from the plasma in the accelerator, the undulator radiation could only be detected without background if the thick Al foil was

[1] All ultra-thin filters are obtained from Lebow Company, USA

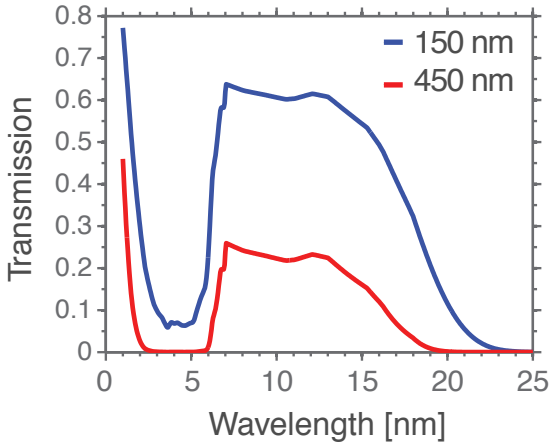

Figure 6.8. | **Transmission curves of zirconium.** The experimentally determined transmission curves of zirconium in the soft-X-ray range for different filter thicknesses [CXRO].

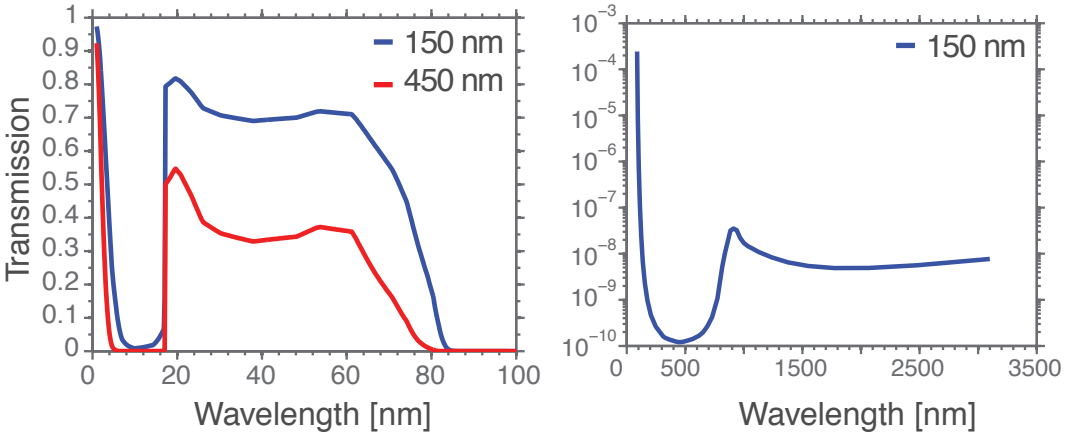

Figure 6.9. | **Transmission curves of aluminum.** Left-hand side: experimentally determined transmission curves for Al foil of thickness 150 and 450 mm in the soft-X-ray range [CXRO]. Right-hand side: calculated transmission curve for a wider wavelength range with constants used from [Rakić, 1995]

placed in the beam path (the transmission of 15 μm Al in the XUV is about 10^{-10}). With the thin Al and Zr foils, it could be excluded that the radiation detected in the diffraction orders of the X-ray spectrometer is scattered optical light and verified to be in the soft-X-ray range.

A gold mirror was used to collect and horizontally focus the undulator radiation onto the X-ray CCD camera. It was set up in a grazing incidence configuration with an angle of $\alpha = 9°$ for which the reflection curve can be seen in fig 6.11. In this configuration, the mirror shows different focusing properties for the meridian plane (in our case horizontal) and the sagittal plane (vertical). A result of a raytracing of an undulator beam through the beamline is shown in figure 6.10. The horizontal and vertical focal lengths of the

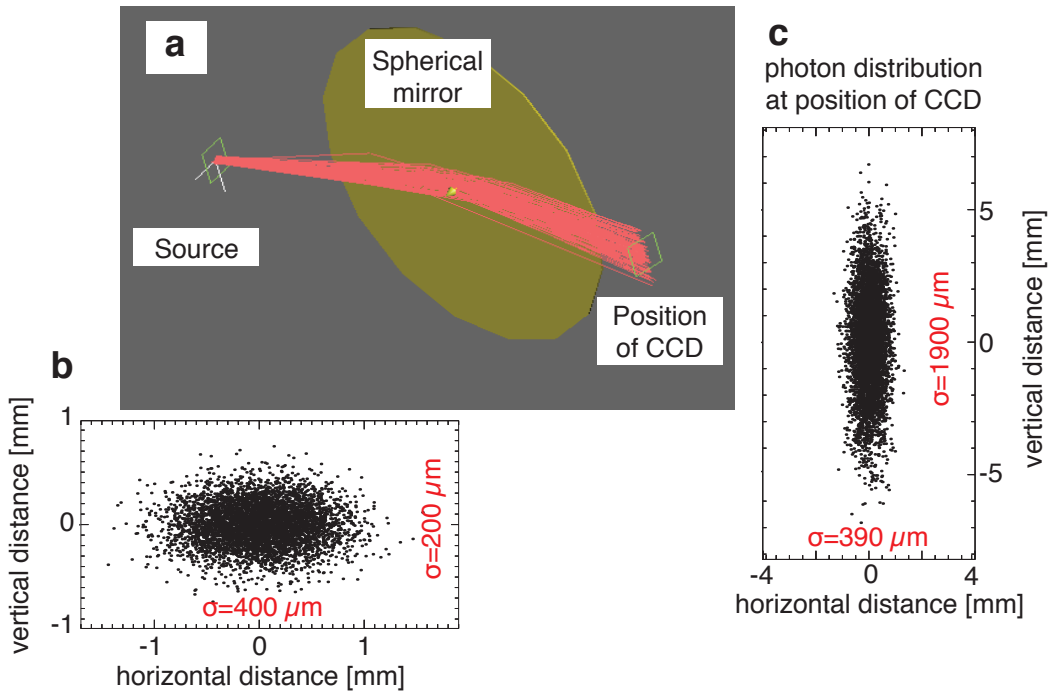

Figure 6.10. | **Raytracing of the imaging with the spherical mirror.** The setup (**a**) shows the undulator emission (Source) being focused by a spherical gold mirror onto the position of the CCD. In order to clearly illustrate the focusing of the mirror, the size of the mirror is exaggerated with respect to the propagation distances before (1.4m) and after the mirror (1.35m). The figure shows the raytracing of the source with the (typical undulator) horizontal and vertical dimensions of $\sigma_h = 400\mu\text{m}$ (rms) and $\sigma_v = 200\mu\text{m}$ (rms) (**b**) and a divergence of $700\mu\text{rad}$ (rms) through the beamline with a spherical gold mirror with a radius of curvature of $R = 10\,\text{m}$. The resulting distribution at the position of the CCD (**c**) clearly shows the focusing in the horizontal dimension. The results were obtained with the raytracing code SHADOW [Welnak et al., 1994] embedded in the X.O.P. environment [Dejus and del Rio, 1996].

mirror with a radius of curvature $R = 10\,\text{m}$ (used in the setup) are given by [Kirkpatrick and Baez, 1948]:

$$f_h = R\frac{\sin(\alpha)}{2} = 0.78\,\text{m} \tag{6.7}$$

$$f_v = \frac{R}{2\sin(\alpha)} = 32\text{m}. \tag{6.8}$$

The distances from the undulator center to the mirror and from the mirror to the CCD camera are $\sim 1.4\,\text{m}$ and $\sim 1.34\,\text{m}$, respectively. This means that the mirror horizontally images the undulator center approximately in a 1:1 geometry onto the CCD. The image plane of the setup is $\sim 0.4\,\text{m}$ downstream of the CCD position, which is also confirmed by raytracing. The focal lengths are extremely sensitive to the angle of incidence α which was not adjusted to a very high accuracy since the mirror was used to compensate

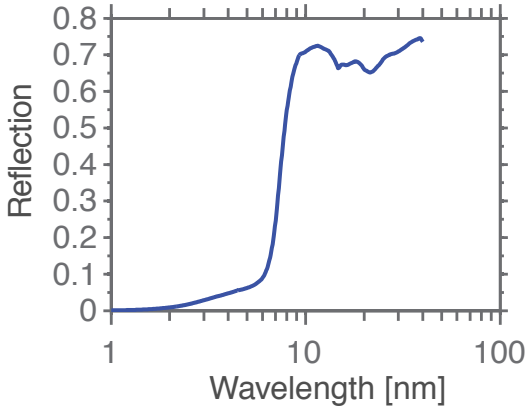

Figure 6.11. | **Reflection of gold mirror.** The experimentally determined reflection of gold in a grazing incidence angle of 9° [CXRO]. The cutoff in reflectivity for small wavelength is around 7.5 nm.

for errors in the setup. The large vertical focal length leads to a virtual image at a position of −1.46 m. This means that the vertical divergence of the undulator radiation is practically not changed by the mirror.

X-ray Spectrometer

The X-ray spectrometer consists of an entrance slit with a variable width, a transmission grating and an X-ray CCD camera. The transmission grating is similar to the ones used in the *Chandra* X-Ray Observatory satellite for the Low Energy Transmission Grating (LETG). It consists of free-standing 1000 lines-per-millimeter gold wires held by a two support meshes: perpendicular to the grating wires is a "fine" supporting structure of gold wires with 2.5 μm thickness and a period of 25.4 μm and this whole structure is held by a triangularly-shaped "coarse" supporting structure made of wires with a width of 68 μm [Predehl et al., 1992], [CXC, 2009]. This sophisticated structure ensures that no optical radiation contaminates the diffraction orders of the XUV signal. The whole grating consists of about 80 of these triangles. From the efficiency curve (fig 6.12), it can be seen that approximately 10 % of the soft-X-ray radiation is diffracted into the first diffraction order.

For the detection of the radiation a Princeton Instruments PI-SX:400 back-illuminated X-ray CCD camera with 1340x400 pixels, each of the size 20x20 μm was used. The quantum efficiency curve can be seen in fig 6.13.

Wavelength Calibration of the X-ray Spectrometer

XUV radiation from the plasma, filtered through the 450 nm Al was used for the wavelength calibration of the X-ray spectrometer. The filtered radiation can be seen in figure 6.14 and a lineout integrated over the whole CCD camera in figure 6.15. In order to minimize the error in the calibration, the slit was closed to a width $\sim 150\,\mu$m.

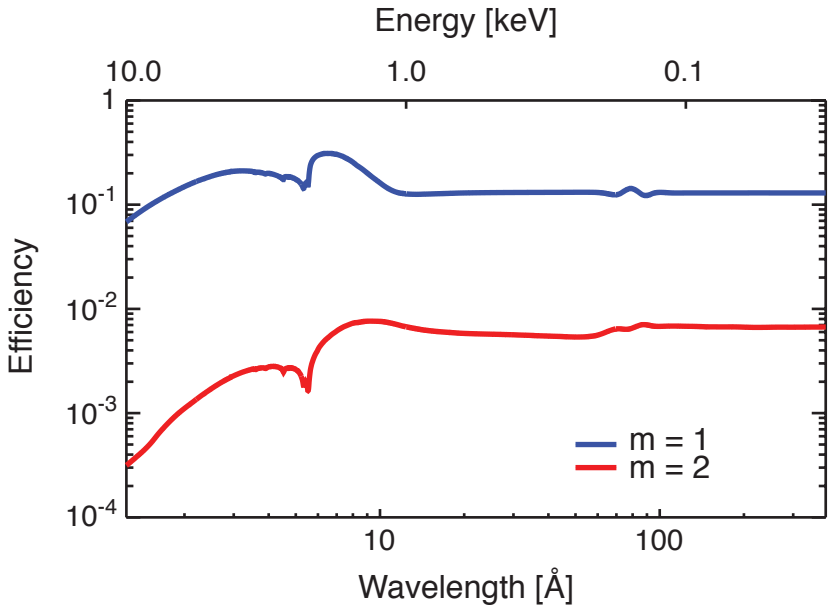

Figure 6.12. | **Efficiency of transmission grating.** The wavelength-dependent grating efficiency is given for the first (blue) and the second (red) diffraction order. In both cases, the given efficiency is the sum of the positive and the negative diffraction order. The values are calculated by an analytical model of the grating including the supporting structures and verified by calibration [CXC, 2009].

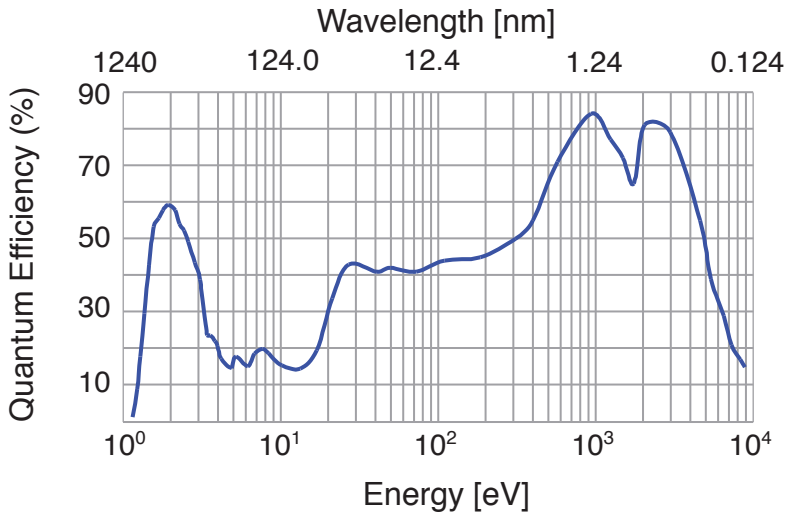

Figure 6.13. | **CCD Quantum Efficiency.** The plot shows the wavelength-dependent quantum efficiency of the X-ray CCD camera used in the experiment [PI]

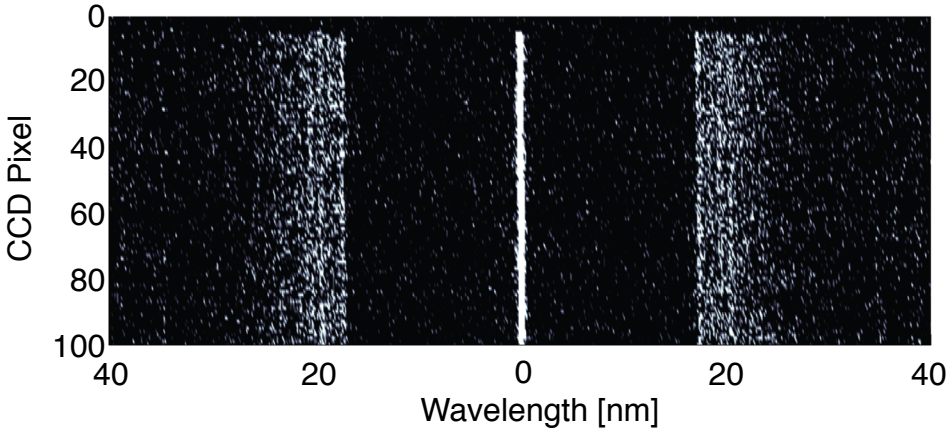

Figure 6.14. | **Spectrally-resolved plasma radiation.** The figure shows the spectrally-resolved radiation originating from the plasma of the accelerator, filtered by a 450 nm thick aluminum foil.

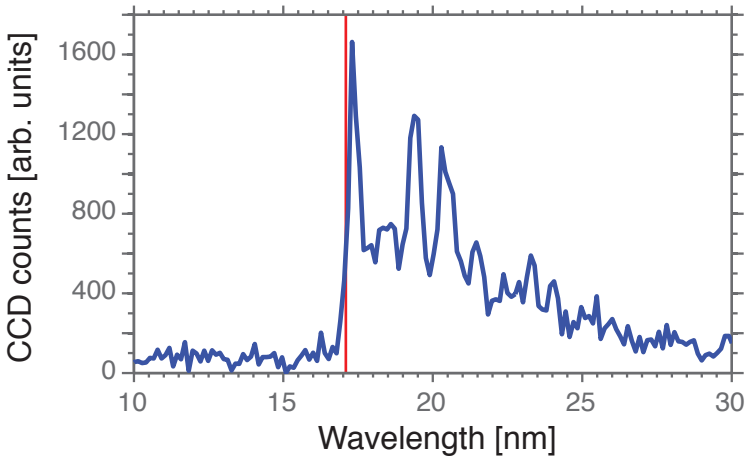

Figure 6.15. | **Spectrum of the plasma radiation.** The blue curve shows the spectrally resolved radiation originating from the plasma in the accelerator, integrated over the whole CCD (integrated over the vertical CCD distance from pixel 10:100 of figure 6.14). The red line indicates the cutoff of the aluminum filter at ~ 17.1 nm

The CCD-pixel to wavelength calibration of the spectrometer was done by defining the aluminum transmission cutoff at $\sim 17.1\,\mathrm{nm}$ for the + and - first diffraction orders. With this calibration, the diffraction angle $\alpha(\lambda)$ can be calculated using the diffraction grating equation

$$m\lambda = p \sin\alpha, \tag{6.9}$$

where m is the diffraction order, $p = 1\,\mu\mathrm{m}$ is the distance between two individual grating slits. The deflection distance on the CCD can be determined by the CCD pixel size ($20 \times 20\,\mu\mathrm{m}$) and considering the horizontal binning of a factor of 2 (4 vertical). This distance x and the diffraction angle α can be used to calculate the distance between the grating and the CCD chip d with the relation

$$d = \frac{x}{\tan\alpha}. \tag{6.10}$$

The calculation leads to a distance of $d = 305\,\mathrm{mm}$, which agrees with the measured distance of $299 \pm 10\,\mathrm{mm}$. Equations (6.9) & (6.10), and a grating-CCD distance of 305 mm were used for calibration and the determination of the corresponding wavelength to each pixel. Radiation from the plasma below a wavelength of 17 nm was verified by measuring the spectra with zirconium filters.

Deduction of Number of Photons from CCD Counts

Since the X-ray spectrometer setup could not be absolute calibrated, the **number of photons** have to be deduced from the counts of the CCD camera considering the following components and their properties:
the undulator radiation is reflected by the gold mirror in a $\sim 10°$ setup. The reflectivity of gold in grazing incidence decreases the number of undulator photons N_{ph} by a factor R_{mirror} ($R_{\mathrm{mirror}} = 0.65$ for 17 nm (70 eV) photons, see figure 6.11). A fraction of η_{grating} of these photons are diffracted into the + and - first diffraction order by the transmission grating (10% total for 17 nm, i.e. 5% is diffracted in each diffraction order) (see figure 6.12). Photons with an energy of E_{phot} are detected by the CCD camera with a quantum efficiency (probability) of QE (for 70 eV, QE ≈ 0.4, see figure 6.13). Photons with energies of $< 70\,\mathrm{keV}$ are mainly absorbed by the photo-electric effect. For silicone, an average energy of 3.65 eV is required to produce an electron-hole pair, i.e. an 70 eV photon produces $70/3.65 \approx 19\,\mathrm{e}^-$ [Inc]. The electronic of the CCD camera was operated in the low-noise, high-gain mode, in which for each 1.2 e^- one ADU (analog-to-digital unit, or CCD counts) is produced. Considering all these effects, the number of counts is related to the number of photons by

$$N_{\mathrm{counts}} = \underbrace{N_{\mathrm{ph}} \cdot R_{\mathrm{mirror}} \cdot \eta_{\mathrm{grating}}}_{\text{phot in first diffraction order}} \underbrace{\cdot \mathrm{QE} \cdot \frac{E_{\mathrm{phot}}[\mathrm{eV}]}{3.65} \frac{1}{1.2}}_{\text{counts in CCD}}. \tag{6.11}$$

For a 70 eV photon, this results in

$$N_{\mathrm{counts}} = 0.21 \cdot N_{\mathrm{ph}} \tag{6.12}$$

$$N_{\mathrm{ph}} = 4.81 \cdot N_{\mathrm{counts}} \tag{6.13}$$

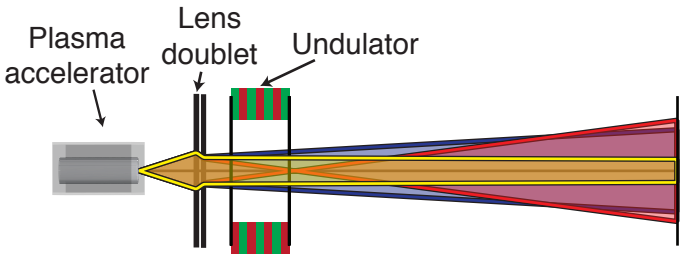

Figure 6.16. | Influence of magnetic lenses on electron beams with different energies. The divergence of electron beams with energies of 190 MeV (red), 215 MeV (yellow) and 240 MeV (blue) are shown after propagating through a doublet of magnetic lenses set to collimate an electron energy of 215 MeV.

6.1.4. Experimental Verification of Soft-X-Ray Undulator Radiation

In order to verify that the detected radiation is in fact undulator radiation in the soft-X-ray range, several tests have been conducted. In order to distinguish the short wavelength radiation from any background signal in other wavelength ranges, 150 and 450 nm Al and Zr filters (see section 6.1.3) were used which both have narrow transmission curves in the XUV range (figs. 6.8 & 6.9). Additionally a 5 cm long Quartz glass block was used to filter out any XUV radiation and determine the optical background. By simultaneously monitoring the signal on the X-ray spectrometer as well as the electron beam for these filter combinations with the undulator in the beam path and the undulator removed from the beam path, a soft-X-ray signal originating from the undulator when the electron beam was present could be verified.

6.2. Magnetic Quadrupole Lenses as Energy-Bandpass Filter for the Undulator Radiation

Calculation method for the bandpass filter
Analytical calculation
Simulation considering the on-axis flux peaks and beamline
Simulation considering the spectral broadening and overlapping of the on-axis fluxes
Details of the SRW simulations

A doublet of magnetic quadrupole lenses was used for beam transport from the accelerator through the undulator. The lenses are highly chromatic which means that only electrons with a particular energy are collimated, whereas the divergence of electrons with different energies is markedly increased (see figure 6.16). As each individual electron emits its radiation in a narrow cone along its propagation direction, the varying divergences of the electron beam strongly affect the undulator angular flux and even lead to an effective energy-bandpass filter as discussed below. In this section, this effect is

estimated by an analytical model based on a Gaussian approximation (see section 3.4.1) and computed in more detail by two undulator simulations, each describing different aspects of the process (sections 6.2.3 & 6.2.4).

Brief Summary: Undulator Flux

For the following sections, it is important to clearly differentiate between the spatial *on-axis* undulator flux and the *spectrally integrated* (total) undulator flux. Therefore, a quick summary of the formulas is given (for more details, see section 3.6).

The wavelength emitted electrons of energy γ propagating through an undulator with a periodic field of λ_u, an deflection parameter K, observed under an angle θ is given by

$$\lambda = \frac{\lambda_u}{2n\gamma^2}\left(1 + \frac{K^2}{2} + \gamma^2\theta^2\right), \tag{6.14}$$

where n is the harmonic number.

The **total angle-integrated flux** emitted by an electron beam with a current I and an undulator with a number of periods N_u and an undulator parameter K can be written for the undulator fundamental and for $K < 1$ as

$$\Phi_n = \frac{\pi}{2}\alpha N_u \frac{I}{e} K^2, \tag{6.15}$$

where $\alpha = 1/137$ is the fine-structure constant.

In the Gaussian approximation, the angular spectral flux can be written as ($\vec{\Psi} = (\theta_x, \theta_y)$)

$$\frac{\mathrm{d}\Phi}{\mathrm{d}\Omega}(\vec{\Psi}, \omega_n) = \left.\frac{\mathrm{d}\Phi}{\mathrm{d}\Omega}\right|_{\vec{\Psi}=0} \exp\left(-\frac{\theta_x^2}{2\Sigma_{x'}^2} - \frac{\theta_y^2}{2\Sigma_{y'}^2}\right), \tag{6.16}$$

where the total divergence $\Sigma_{x'}$ can be written in terms of the intrinsic undulator divergence $\sigma_{r'}$ and the electron beam divergence $\sigma_{x'}$ as $\Sigma_{x'} = \sqrt{\sigma_{r'}^2 + \sigma_{x'}^2}$. The on-axis flux is given by

$$\left.\frac{\mathrm{d}\Phi}{\mathrm{d}\Omega}\right|_{\vec{\Psi}=0} = \frac{\Phi_n}{2\pi\Sigma_{x'}\Sigma_{y'}}. \tag{6.17}$$

For a zero-emittance (filament) electron beam, the on-axis flux (for $K < 1$) can be written as

$$\left.\frac{\mathrm{d}\Phi}{\mathrm{d}\Omega}\right|_{\vec{\Psi}=0} = \alpha\frac{I}{e}N_u^2\gamma^2\frac{K^2}{1 + K^2/2}, \tag{6.18}$$

where γ is the electron energy in terms of the electron rest mass $m_e c^2$.

It can be seen that the on-axis flux scales quadratically with the electron energy owing to the smaller emission cones ($\sigma_{r'} \propto 1/\gamma$) for higher energies. Owing to emittance effects, the flux gets spatially washed out which leads to a decrease in the on-axis flux (see equation 6.17). Furthermore, a finite electron beam size and divergence also increases the on-axis bandwidth toward wavelengths that are larger than the resonance wavelength as discussed in section 3.6.2. Both these effects can be seen in figures 6.19 & 6.20 which show the spectrally resolved on-axis flux for varying electron energies and divergences corresponding to the chromatic effects of the magnetic lenses.

6.2.1. Analytical Calculation Method for the Bandpass Filter

The influence of the chromatic lenses on the undulator radiation (UR) can be quantified by the calculation of the radiation emitted by a thick (finite emittance) electron beam with a varying divergence and beam size. The beam size of the undulator radiation from a thick electron beam can be determined by a convolution of the single-electron emission with the electron beam distribution (see section 3.5.2). As described in section 3.4.1), both quantities can be approximated by a Gaussian distribution (which for the UR is only possible for the resonance frequencies). In this case, the UR beam size of a thick electron beam resulting from the convolution can be written as the quadratic sum of the beam size of the single-electron emission and the beam size of the electron beam. In order to determine the undulator radiation at an observation point after a free drift, the radiation has to be propagated. As shown in section 3.5.3, carrying out the convolution in the center of the undulator and propagating the resulting radiation is equivalent to first separately propagating the single-electron UR and the electron beam to the observation point and then performing the convolution.

Explicitly, this means that the undulator beam size *at the position of the detector* can be calculated by a convolution of the single-electron UR beam size with the electron beam size, both *at the position of the detector* which in the Gaussian approximation can be written as

$$\Sigma_{x,y}(s) = \sqrt{\sigma_{x,y}^2(s) + \sigma_r^2(s)}, \tag{6.19}$$

where $\sigma_{x,y}(s)$ is the horizontal/vertical electron beam size at the position s measured from the undulator center. The single-electron UR beam size $\sigma_r(s)$ is mainly given by the natural UR divergence for distances much larger than the undulator length ($s \gg L$). For a free drift, the beam size can be written as (see section 3.5.3)

$$\Sigma_{x,y}(s) = \sqrt{\sigma_{x,y}^2(s) + \frac{\lambda L}{2\pi^2} + \frac{\lambda}{2L} s^2}\,, \tag{6.20}$$

where L is the undulator length and λ the wavelength of the undulator emission. For a given λ and L (which are determined by undulator parameters and the electron energy), the undulator beam size only varies with the electron beam size at the detector. It can be seen that the on-axis flux which depends on the undulator beam size (see equation 6.17) thus can be modified by changing the electron beam size. Since the electron beam size can be adjusted by the magnetic lenses, they implicitly determine the on-axis flux intensity: The small size of an electron beam focused at the position of the detector leads to a small UR beam size and thus a high on-axis photon flux. The size of the electron beam for a particular energy is given by the specific setup of the quadrupole lenses: in our case the lenses are set-up to collimate a particular energy. Since the undulator radiation is observed at a relatively long distance ($\simeq 3$ m) downstream of the last lens, electron energies, slightly below the energy that is collimated, are focused at the position of the detector. Owing to the chromaticity of the quadrupole lenses, only electrons in a small bandwidth around this energy have a small electron beam size and therefore a small UR beam size at the detector. Both the energy-dependent spatial electron beam

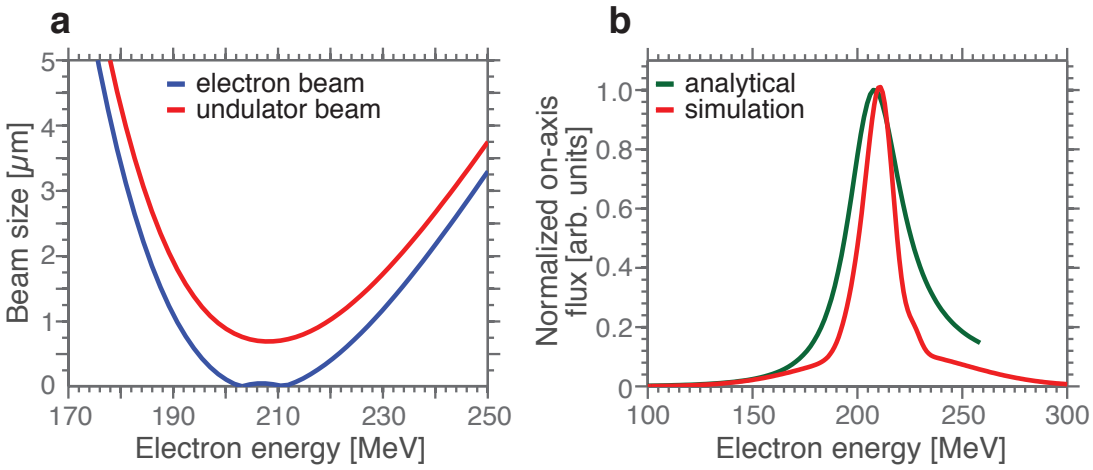

Figure 6.17. | **Electron and undulator beam areas as well as resulting energy band-pass filter through the effect of the magnetic lenses. a)** The electron beam area ($A_{\mathrm{el}} = \pi\,\sigma_x \cdot \sigma_y$) at the position of the detector is calculated for various electron energies considering the effect of the magnetic lenses (blue). The red curve shows the undulator beam area analytically calculated by the convolution of the electron beam size with the size of the single electron emission ($A_{\mathrm{UR}} = \pi\,\Sigma_x \cdot \Sigma_y$). The "wiggle" of the blue curve at $\approx 200 - 215$ MeV is due to an astigmatic focus of the electron beam. **b)** shows the system response curve of our setup, which corresponds to the calculated energy-dependent on-axis undulator flux at the position of the detector. The narrow bandwidth filter is due to the energy-dependent electron-beam divergence introduced by the the magnetic lenses as explained in the main text. The red curve is the result of the simulation of the undulator code SRW that includes the focusing effect of the gold-mirror (for details of the calculation refer to sec. 6.2.5). The green curve is a result of analytical calculations of the on-axis flux after a free drift using equation 6.17. Both consider the energy-dependent electron beam sizes given by the effect of the magnetic lenses and the wavelength-dependent UR beam size given by equation 6.20. In the green curve, the focusing effect of the the mirror is not included. The red curve has a FWHM-bandwidth of 9% around 211 MeV and the green curve a bandwidth of 15% FWHM around 209 MeV. Both the curves in **a** and in **b** are calculated for a lens setup that collimates an electron energy of 220 MeV. The natural focusing of the undulator is not considered in these curves.

area ($A_{\mathrm{el}} = \pi\,\sigma_x \cdot \sigma_y$) and the spatial undulator beam area ($A_{\mathrm{UR}} = \pi\,\Sigma_x \cdot \Sigma_y$) at the position of the detector for a lens setup that collimates an electron energy of 220 MeV can be seen in figure 6.17**a**.

Electron bunches with identical beam currents but different electron energies produce the same angle-integrated undulator spectral flux Φ_n (as it is independent of the electron energy (see equation (6.15)). However, the undulator radiation flux from electrons of energies within the small bandwidth that are focused to a small beam size at the detector is not as smeared out as that from electrons outside this energy band. This results in a higher *on-axis* flux of the radiation emitted by the focused electron energies.

Figure 6.17**b** shows the result of computations of this energy-bandpass filter for the setup used in this experiment: An electron beam with an energy that is focused to the smallest spot at the detector (for this lens setup $\simeq$ 210 MeV) yields the highest on-axis flux, whereas deviations of energies of a few tens of MeV causes the on-axis flux to drop sharply. In order to determine the undulator spectrum and the (spectral) fraction of the electron beam that primarily contributes to the measured undulator spectrum, the detected electron spectrum has to be filtered by this curve (see figure 6.22) which is therefore called the system response curve.

6.2.2. Comparison between the Utilized Calculation Methods

In the following sections the different utilized calculation methods including their results are presented. The methods include an analytical description (discussed above) and two simulations using the undulator code SRW (see section 6.2.5) which each describes different aspects but not the whole problem due to the restriction of reasonable computational time. In all three methods, the broad electron spectra are decomposed and for each electron energy the appropriate beam parameters (size and divergence) are determined considering the effect of the magnetic lenses. For each electron energy, the undulator radiation (UR) is calculated and propagated to the detector.

The analytical model uses a Gaussian approximation for the angular flux distribution which is only valid for the corresponding undulator resonance wavelength (eq 6.14) at each electron energy. The emittance effects are taken into account by considering the *spatial* increase of the electron beam size at the detector (and a corresponding decrease in on-axis flux). However, the model does not include the *spectral* broadening of the bandwidth of the on-axis flux due to emittance effects. For each electron energy, the on-axis flux is only calculated for one wavelength (the corresponding resonance wavelength). The distance between the undulator and the detector is taken into account as a free drift (neglecting the focusing of the gold mirror and the slit in front of the grating).

The first simulation method (see section 6.2.3) computes the undulator radiation for each electron energy but considers the focusing of the gold mirror and the slit in front of the detector. However, the code can only propagate a single frequency through such a beamline (within a reasonable computational time). Therefore, also only the corresponding resonance wavelength for each electron energy is propagated. The result in comparison to the analytical model can be seen in figure 6.17**b**

The second simulation method (see section 6.2.4) only considers a free drift between the undulator and the detector. This allows to propagate the whole undulator spectrum (which can be significantly broadened due to emittance effects) for each electron energy. Owing to this broadening, some of the undulator radiation contribution of different electron energies spectrally overlap. The resulting computed overall undulator spectrum (the sum over each energy contribution) leads to a slightly broader shape at a higher photon energy in comparison to the latter two methods. The comparison between this simulation and the analytical model can be seen in figure 6.20**b**.

6.2.3. Results of Analytical Calculation and Simulation Considering the Beamline

The shape of the curves in figure 6.17**b** is determined by multiple calculations of the on-axis undulator flux at the position of the detector for electron bunches with different electron energies, each with zero energy spread and consisting of the same amount of electrons. The calculations of both curves consider the wavelength-dependent natural undulator divergence and the energy-dependent electron beam size which is determined by the lens setup as discussed above. The on-axis flux for each electron energy is evaluated only for the corresponding resonance wavelength. The blue curve is calculated using equations 6.17 & 6.20, and as beamline between undulator and detector only considers a free drift of $\approx$ 2.7m after the undulator to the detector.

The red curve is a result of a simulation using the code Synchrotron Radiation Workshop (SRW) [Chubar and Elleaume, 1998] that includes the focusing effect of the spherical gold mirror and the slit in front of the X-ray spectrometer (for details of the simulation, see section 6.2.5). Although the blue curve is calculated using a Gaussian approximation and does not consider the focusing mirror, both curves give approximately the same result.

6.2.4. Simulation Considering the Spatial and Spectral Broadening of the on-Axis Fluxes

The computation methods described above do not consider the spectral broadening of the on-axis flux bandwidth to lower photon energies resulting from emittance effects. Therefore, a second simulation was performed, using SRW which calculates the whole spectrum of the emitted spatial flux for each electron energy (two individual contributions to the sum can be seen in figure 6.19). Within a reasonable computational time, the whole bandwidth can only be propagated through a free drift from the undulator to the detector (and therefore cannot consider the beamline consisting of a focusing mirror and an aperture). For a more detailed description of the calculation, see sec 6.2.5.

Similar to the methods mentioned above, in this simulation the spatial spectral fluxes were computed with the same amount of electrons (at zero energy spread) for each electron energy. Although the highest individual on-axis-flux peak is emitted by electrons with an energy of 210 MeV (at a corresponding photon energy of 70 eV), the overall flux peak of the sum of the contributions is at a higher photon energy.

This can be understood by the contributions to the sum of the fluxes from individual electron energies: An on-axis lineout of the sum over each flux (lineout along vertical position 0 mm of figure 6.18), as well as lineouts of the individual spatial fluxes produced by every fifth electron energy step are shown in figure 6.20 **a**. It can be seen in 6.20 **b** that the peak amplitude of each contribution approximately matches the value analytically calculated for the resonance frequencies in figure 6.17 (blue curve) and that the highest flux amplitude is emitted by electrons of $\simeq$ 210 MeV.

However, the peak of the sum over these contributions is at a higher photon energy than the individual highest on-axis peak flux: in contrast to higher or lower electron

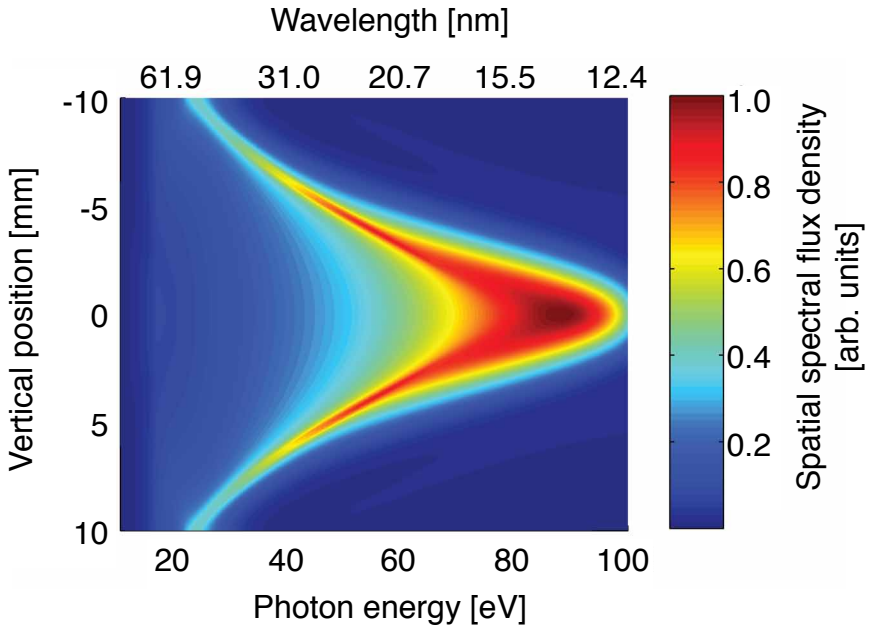

Figure 6.18. | Simulation of the spatial spectral flux density for a flat-top electron spectrum with the magnetic lenses set to collimate an energy of 220 MeV. The figure shows the sum of flux densities, each calculated for a mono-energetic electron beam at equal increments of the electron energy in a range from 100 - 250 MeV, each consisting of the same amount of electrons. The energy dependent electron beam size and divergence given by the lens setup is responsible for the sharp drop of flux for photon energies < 60 eV. Two individual contributions can be seen in figure 6.19.

energies, the spectrally narrow on-axis fluxes emitted by electron energies around 210 MeV do not (spectrally) overlap which reduces the sum of their contributions. At higher and lower electron energies, the electron beam has a larger divergence which spatially, and more importantly, spectrally washes out the flux to lower photon energies (which is a result from $\theta > 0$ contributions of the emitted UR wavelength, see equation (6.14) and can be seen in figure 6.19). This spectral overlap increases the value of the overall sum over these individual fluxes. As a result, the peak of the sum of the fluxes is at a photon energy of $\approx 90\,\mathrm{eV}$, whereas the largest amplitude of the on-axis fluxes is at an energy of $\approx 70\,\mathrm{eV}$.

Although the spectra of the individual on-axis fluxes for photon energies $< 70\,\mathrm{eV}$ also overlap, the overall peak of the sum is at higher photon energies. This is because the on-axis flux (of a filament electron beam) is proportional to the square of the electron energy ($\propto \gamma^2$) (see equation 6.18), since it is emitted into a smaller emission cone ($\sigma_{r'} \propto 1/\gamma$).

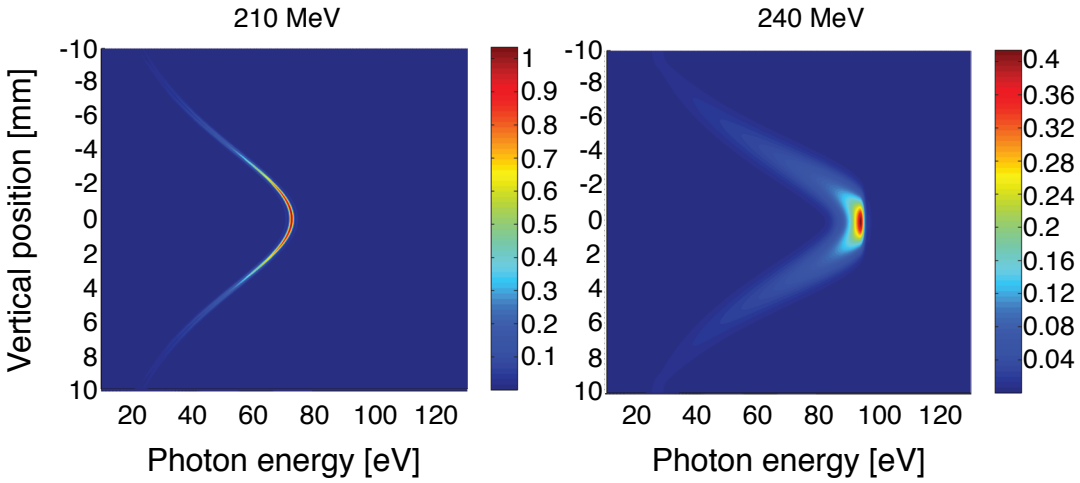

Figure 6.19. | **Comparison of the simulation of the 210 MeV and the 240 MeV angular flux.** Owing to the small electron beam size at the detector, the 210 MeV contribution closely resembles a filament-beam angular flux distribution. The 240 MeV contribution is both spatially and spectrally washed out. Its peak amplitude is only $\approx 40\%$ of that of the 210 MeV flux (both electron beams contain the same amount of charge but a different electron beam size and divergence due to the effect of the magnetic lenses). It can be seen that the 210 MeV contribution has a more distinct parabolic shape, whereas the high intensity (yellow to red-colored) part of the 240 MeV contribution rather resembles a vertical line.

Brief Summary

In conclusion, the energy-dependent electron beam divergence induced by the chromaticity of the magnetic lenses acts as an effective band-pass filter for the undulator radiation. The electrons that primarily contribute to the on-axis flux of the undulator radiation are determined by the filtering of the electron spectrum with the system response function, shown figure 6.17). However, the sum of the spectrally spread-out and thus overlapped on-axis fluxes shift the overall peak of the undulator emission from the highest spectral on-axis peak to higher photon energies (figure 6.18).

6.2.5. SRW Calculations

The code Synchrotron Workshop (SRW) computes the near-field synchrotron radiation by numerically solving equation (3.5). Radiation from thick (finite emittance) electron beams is calculated by a convolution of the radiation of a single electron with the electron beam distribution, both computed at the observation point. In order to take into account beamline components, such as mirrors, slits, etc. the single-electron photon distribution is propagated through these components in the frame of the scalar diffraction theory using Fourier optics. The distribution of a thick electron beam is taken into account by a convolution with the electron beam distribution after the propagation

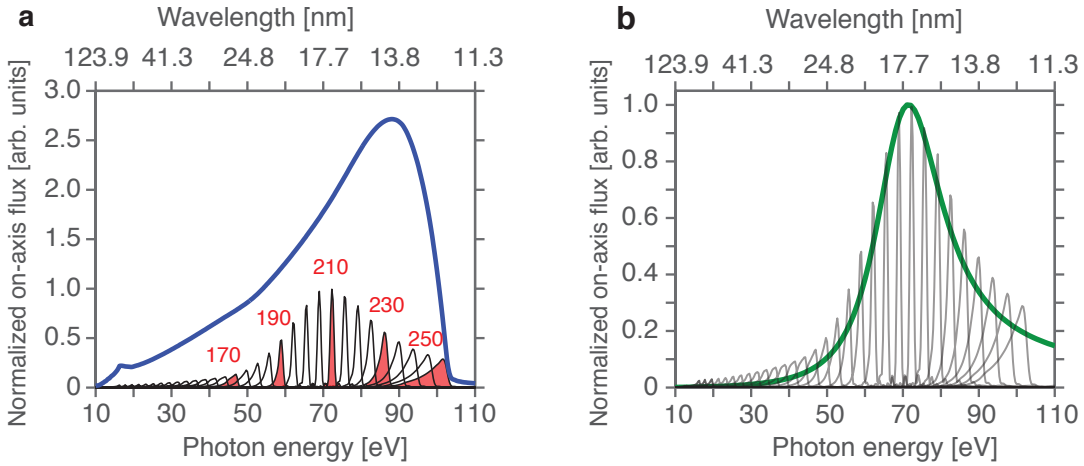

Figure 6.20. | Simulation results from on-axis lineouts of the sum and individual contributions. a) The blue curve shows the on-axis lineout of the sum of the spatial spectral fluxes of electron energies that are relevant for the experiment (100 - 250 MeV) which is the lineout at vertical position 0 mm of fig 6.18. The simulations include the effects on the electron beam size and divergence of the magnetic lenses. The on-axis spectral fluxes of every fifth energy step are shown as black lines. The red-filled contributions are labeled by the corresponding electron energies. The sharp drop of the lineout of the sum (blue) at photon energies >100 eV can be explained by the cutoff of the simulation at a maximum electron energy of 250 MeV (corresponding to a resonance photon energy of 103 eV). **b)** shows the comparison between the simulated spectral fluxes (black) to the analytical calculation (green). The simulated fluxes (black) are the same as in **a** and the envelope (green) shows the peak amplitude of the flux calculated at the resonance photon energy, calculated for an electron energy range of 100-250 MeV (same curve as in fig 6.17).

which delivers an accurate result in case of the well-defined, small-emittance electron beams of conventional synchrotrons. In our case, however, parts of the electron beam with energies that are not focused, have large divergences (see sec 6.2) which means that the propagation method described above does not yield the correct result for focusing mirrors and apertures.

In order to include these effects, one simulation was performed by decomposing the phase-space distribution of the electron beam and thus sampling it by several computations of the single-electron undulator radiation with different initial positions and angles which were all added up at the position of the detector. Owing to the chromaticity of the magnetic lenses, the electron beam size and divergence are different for each electron energy. Therefore, the electron beam has to be additionally spectrally decomposed and each phase-space distribution of each electron energy has to be simulated separately. Since SRW only allows the propagation of one particular photon energy through the beamline, only the *resonance* frequency (eq (6.14)) for each electron energy was propagated through the setup. As a result, the red curve in figure 6.17 shows the on-axis flux after the propagation through the beamline (mirror and slit) only of the resonance

frequencies for each electron energy.

In order to avoid the difficulties mentioned above, a second SRW simulation that does not consider the effect of the mirror and the aperture was performed. Here, the thick electron beam can be calculated by a convolution and the decomposing of the phase-space is not necessary. Furthermore, not only a single frequency but all photon energies can be calculated after a free drift. Therefore, this simulation computes for each electron energy the whole spectrum of the spatial flux at the observation point. However, only a free drift between the undulator exit and the location of the CCD detector has been taken into account. The results of these simulations are shown in figures 6.18 & 6.34.

6.3. Measured Undulator Spectra

Measured spectrum with a setup including the magnetic lenses
Comparison of measurement and simulation
Comparison of undulator spectra to a setup lacking the lenses
Comparison of undulator spectra from different lens setups
Tuning of the undulator radiation
Undulator as diagnostic tool

A typical detected undulator spectrum from an electron beam collimated by the magnetic lenses (the lenses were set to collimate an electron energy of 220 MeV) can be seen in figure 6.21. The corresponding detected electron spectrum is shown as a blue curve in figure 6.22. The undulator spectrum has an energy bandwidth of 22% (FWHM) at the observation angle $\theta = 0$ (after deconvolving the instrument function, deduced from the (spatial) width of the zeroth diffraction order). Since the radiation is spectrally resolved by a transmission grating, the measurements show a zeroth as well as a positive and negative first diffraction order. Each first diffraction order shows an undulator fundamental and a second harmonic. The fundamental of the shot shown in figure 6.21 peaks at a wavelength of 17 nm, the second harmonic peaks at 9 nm. The observation of second harmonic radiation on axis and the fact that its wavelength is slightly longer than half the fundamental results from finite-emittance electron beams and the imaging of the undulator radiation with the spherical mirror: although the spectrum is detected after a slit, the spherical mirror horizontally focuses off-axis (second harmonic) radiation onto the axis and thus effectively increases the horizontal width of the slit (vertically, the divergence of the undulator emission is practically not affected by the spherical mirror, see section 6.1.3). In contrast to the fundamental, the intensity of second harmonic undulator radiation is peaked off-axis and thus at a longer wavelength (as can be seen from the resonance condition, eq (6.14)). Owing to the horizontally focusing mirror, these components are propagated through the slit onto the detector, shifting the peak of the observed on-axis spectrum to longer wavelengths. Figure 6.31**a** shows an undulator simulation of the approximated setup (for details to the approximations, see section 6.3.1) for a collimated electron beam versus the horizontal observation angle, the green lines indicate the effective width of the slit. Each horizontal lineout of the measured spectra

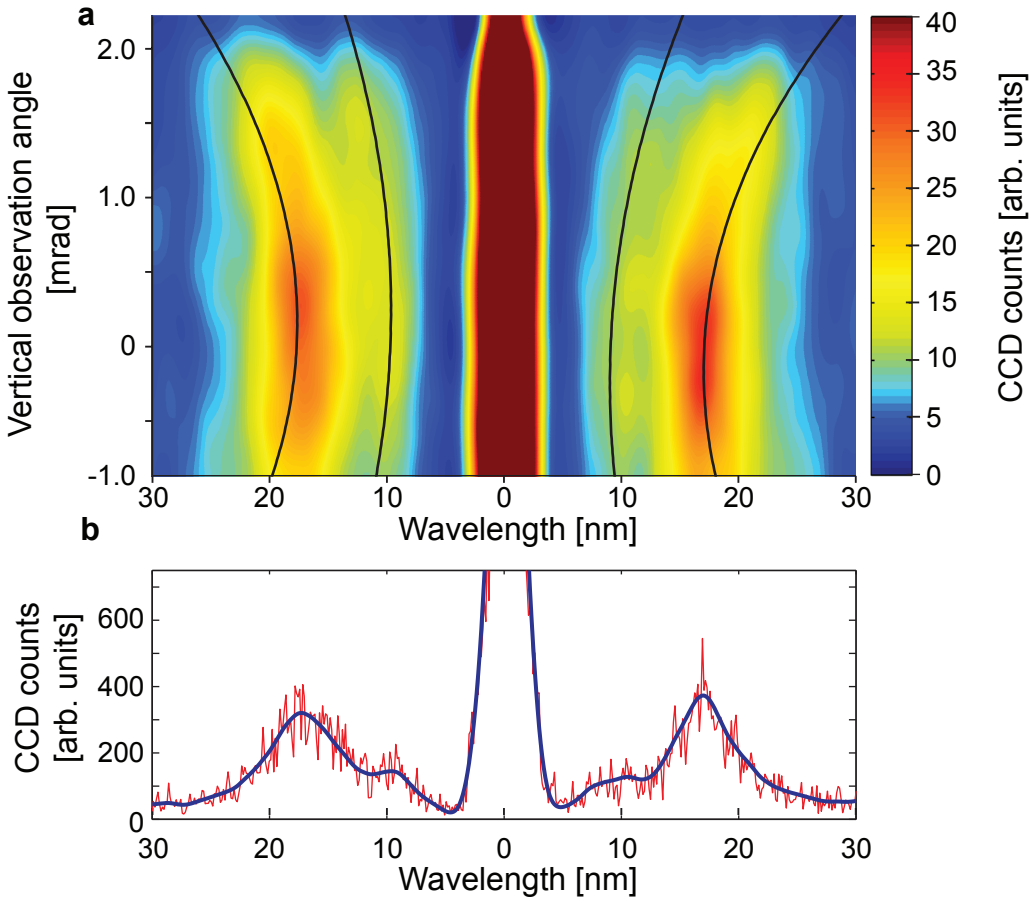

Figure 6.21. | **Detected, spatially-resolved single-shot undulator spectrum.** **a)** shows a smoothed representation of an undulator spectrum measured with the magnetic lenses set to collimated electrons with an energy of 220 MeV. The figure shows the vertical observation angle in one dimension and the spectrum of the undulator radiation in the other dimension. The radiation is spectrally dispersed by the transmission grating and a zeroth (center) and the $\pm$ first diffraction orders can be seen. Each diffraction order shows an undulator fundamental, peaked at 17 nm and a second harmonic , peaked at 9 nm. The theoretical parabolic dependence of the wavelength on the observation angle θ for a filament electron beam is shown by the black solid lines. An electron energy of 207 MeV corresponding to the peak of the effective electron spectrum of figure 6.22 was used as a parameter. For the different emission characteristics of the second harmonic, our simulation yields an on-axis radiation spectrum peaked at a wavelength of 9.2 nm, which defines the parameter chosen for the corresponding parabola. It can be seen that the opening angle of the parabola is half as that of the fundamental as expected by theory. Since the transmission grating is rotated by an angle of $2.5°$ with respect to the slit and the CCD camera, the black parabola lines have been rotated by the same angle. **b)** shows a lineout integrated over 10 pixel rows around $\theta = 0$ (corresponding to an observation angle of $\Delta\theta \simeq 300\,\mu\mathrm{rad}$). The blue line shows the smoothed data and the underlying raw data is shown in red. The smoothed data is obtained by utilizing a thin-plate smoothing spline algorithm after [Buckley, 1994].

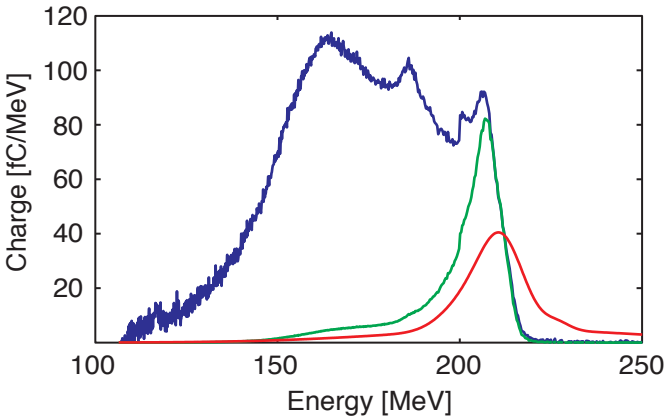

Figure 6.22. | **Electron spectrum corresponding to the undulator radiation of figure 6.21.** The blue curve shows the measured electron spectrum corresponding to the simultaneously measured undulator spectrum shown in figure 6.21. The red curve is the system response curve for a magnetic lens setup that collimates an electron energy of 220 MeV (as described in section 6.2). The curve is peaked at 211 MeV and has a bandwidth of 9% (FWHM). The green curve depicts the electron spectrum filtered by the system response curve which represents the electrons that primarily contribute to the undulator emission. This curve is peaked at an energy of 207 MeV and has a bandwidth of 6% (FWHM).

(at a certain vertical observation angle) represents the spectrally-resolved flux integrated over the effective horizontal slit width. In figure 6.30 the integrated flux through the slit marked by the green lines in figure 6.31 can be seen. It shows significant second harmonic radiation at a slightly longer wavelength than half the fundamental which agrees well with the results obtained in the experiment.

The relatively narrow bandwidth of the undulator radiation is a result of the spectral band-pass filter effect of the magnetic lenses as described in section 6.2. Without the band-pass filter, the undulator would be expected to have a bandwidth of $\simeq 65\%$, corresponding to the width of the measured electron spectrum. The energy bandwidth of the electrons that are filtered by the magnetic lenses and primarily contribute to the undulator spectrum (green curve in fig 6.22) is 6% (FWHM). Since the emitted wavelength depends quadratically on the electron energy (see eq (6.14)), an electron beam with an energy spread of 6% (FWHM) produces undulator radiation with a bandwidth of 12% (FWHM).

However, as explained in section 6.2.4, the sum over spectrally-broadened emission lines, leads to a broadening of the overall photon spectrum. The simulated undulator spectrum computed from the measured electron spectrum (fig 6.22) which considers this effect, is shown in figure 6.23. The comparison between the simulation and the measured lineout is shown in figure 6.25. The focusing of the second harmonic on axis (as described above) is not considered in this simulation. The on-axis lineout of the simulations has an FWHM-bandwidth of 28% where in order to compare to the measured data, the photon-energy detection efficiency of the CCD camera is taken into account. A fit over a lineout

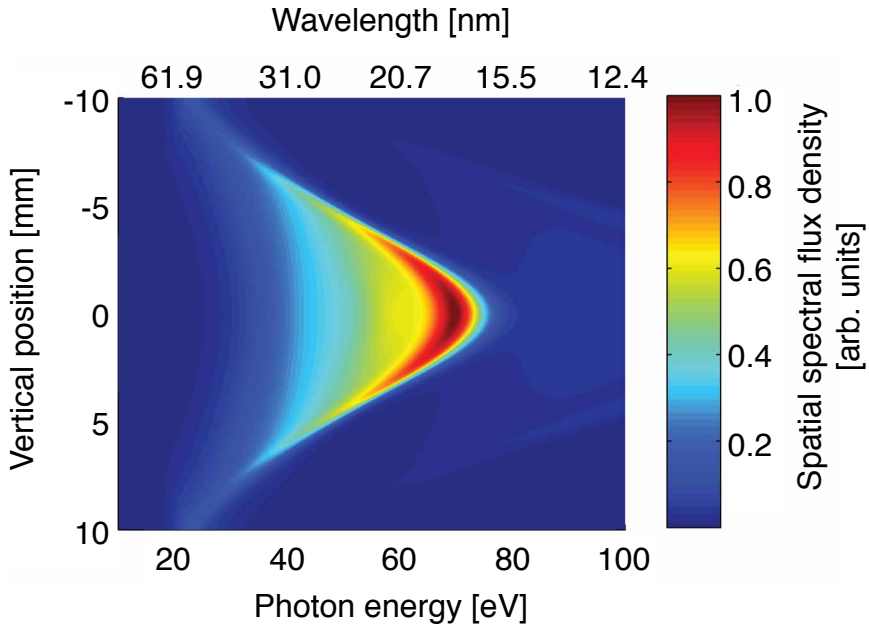

Figure 6.23. | Simulated spatial spectral undulator flux produced by a real electron spectrum. The figure shows the undulator flux simulated similarly to that shown in figure 6.18 but instead of a flat-top electron spectrum the radiation from the measured electron spectrum shown in figure 6.22 has been used. This simulation does not take into account the horizontal focussing of the spherical mirror.

of the measured data integrated over 10 pixel rows (corresponding to an observation angle of $\Delta\theta \simeq 300\,\mu\text{rad}$) gives a linewidth of 34% (FWHM).

From the measured spectrum shown in figure 6.21 an on-axis flux[1] of 16,400 ± 6,200 photons per shot per mrad^2 per 0.1% bandwidth can be deduced. The estimated on-axis flux by equation (6.18) gives for a charge of 1.3 pC in the effective electron spectrum (green curve in fig 6.22) 9,500 ± 2,100 photons per shot per mrad^2 per 0.1% bandwidth. However, this estimation is only valid for the resonance frequency. For a photon frequency ω' slightly below the resonance frequency, the angle integrated flux is twice that for the resonance frequency (as discussed in section 3.4.1). For a filament electron beam, radiation at this frequency is emitted on a cone with a dip on axis. However, the measured radiation is produced by a finite-emittance electron beam which spectrally and spatially washes out the radiation. Therefore, the maximum flux is that emitted at ω' which is estimated to be $\sim 19,000$ photons per shot per mrad^2 per 0.1% bandwidth.

The number of measured photons is deduced from the counts detected by the CCD camera using equation (6.11). The estimated error is the result of a number of measurement uncertainties: (1) the number of counts is deduced from the first diffraction order of the CCD image after smoothing and averaging over several pixel rows which leads to an estimated uncertainty of 20%. (2) the accuracy of the grating efficiency as measured

[1]The on-axis flux and brilliance given in reference [Fuchs et al., 2009] was underestimated by a factor of 2 owing to an inaccuracy in the conversion from CCD counts into number of photons

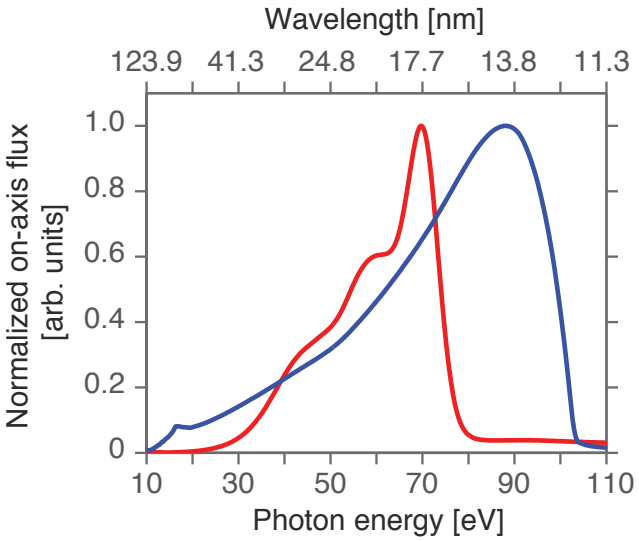

Figure 6.24. | **Lineout of the simulated UR for a flat spectrum and the electron spectrum of figure 6.22.** The blue curve shows a lineout of the system response curve for a flat-top electron spectrum (lineout at position 0 of fig 6.18). The red curve shows a lineout through figure 6.23 at position 0 which is the simulated undulator flux for the measured electron spectrum, blue in figure 6.22. The cutoff at high photon energies of the red curve is due to the cutoff in electron energies. The curve has a FWHM bandwidth of 28%.

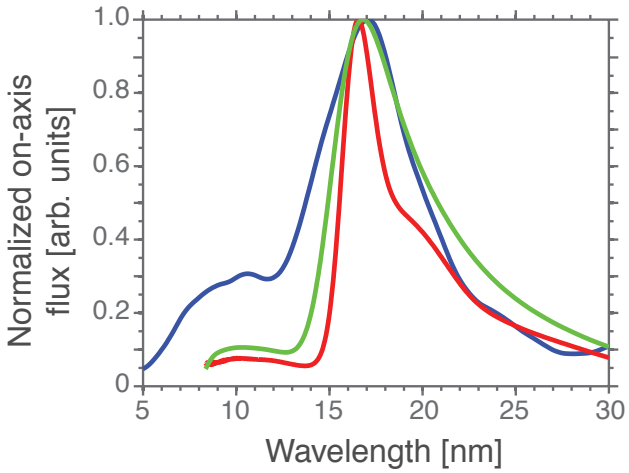

Figure 6.25. | **Comparison between simulation and experiment.** The blue curve shows the lineout (over 10 pixel) from the measured undulator spectrum shown in figure 6.21. The red curve is a lineout of a simulation which computes the radiation from the measured electron spectrum shown in figure 6.22. The green curve considers the instrument function of the X-ray spectrometer. Second harmonic radiation is in this simulation not present on axis since the focusing of the gold mirror is not included.

for a different grating of the same production series (fig 6.12) is estimated to be 5%. (3) an uncertainty of the reflection angle (and therefore the reflectivity) of the gold mirror and the surface roughness of the coating leads to an uncertainty of the reflectivity of 20%. The estimated uncertainty in the case of the simulated photon number is a result from the accuracy of the measurement of the undulator field (5%), the calibration of the electron bunch charge measurement (10%) as well as the uncertainty of the exact position of the magnetic quadrupole lenses which influence the amount of charge in the effective spectrum (10% error in charge).

The brilliance of the source can be estimated from the photon flux, the estimated electron beam emittance and the estimated elecron bunch duration. From an electron beam divergence of 1 mrad and plausibility arguments of the typical dimensions in a laser-wakefield accelerator which lead to a source diameter of $\simeq 2\ \mu$m, the normalized electron beam emittance in our case (electron energy of 200 MeV) can be estimated to be $\epsilon_n = \beta\gamma\epsilon \simeq 0.8\,\text{mm mrad}$. With the settings of the quadrupole lenses, this leads to a rms photon-beam size in the undulator of $270\,\mu$m vertically and $630\,\mu$m horizontally and respective rms photon-beam divergences of $180\,\mu$rad and $170\,\mu$rad. With an assumed bunch duration of 10 fs, the peak (on-axis) brilliance can be estimated to be (see eq (3.37)) $\mathcal{B}|_0 \sim 8 \times 10^{18}$ photons/(s mrad^2 mm^2 0.1% b.w.). In reference [Fuchs et al., 2009], the brilliance (determined by integrating the measured photon flux over 10 pixel around $\theta = 0$ and the spectral bandwidth of this curve) was estimated to be $\mathcal{B} \sim 4\times 10^{17}$ photons/(s mrad^2 mm^2 0.1% b.w.). However, this estimation is strictly speaking not the (on-axis) peak brilliance as defined in section 3.5.2, but a brilliance calculated over an averaged angular flux which leads to a decreased value.

The setup using the magnetic lenses proved to be very reproducible: over 37 shots of the run with the lenses set to collimate an energy of 220 MeV, we could observe in 70% of consecutive laser shots spectrally resolved undulator radiation in the first diffraction orders which is a very remarkable stability for a LWFA experiment. In the remaining 30% of laser shots, the amount of charge in the effective spectrum was not high enough to produce enough radiation that could be spectrally resolved. The average charge within the effective electron spectrum was $0.6 \pm 0.3\,\text{pC}$ which produced $140,000 \pm 50,000$ photons in the undulator fundamental integrated over a detection cone of $K/(2\gamma) = \pm 0.7\,\text{mrad}$. The observed spectra show a fundamental wavelength at 18 nm and a second harmonic peak at 10 nm, with shot-to-shot standard deviations of about 5% which is discussed in more detail in section 6.3.1.

Verification of the Second Harmonic of the Undulator Radiation

The peak at smaller wavelengths in undulator spectra produced with collimated electron beams (by magnetic lenses) has been verified to be the second harmonic: spectra of undulator radiation that is filtered with a 150 nm thick aluminum foil (that filters out radiation with photon energies of $\simeq 5 - 17\,\text{nm}$, see figure 6.9) do not show any radiation smaller than 17 nm (see figure 6.26). This means that the features detected at positions closer to the zeroth diffraction order in fact do have small wavelengths. Additionally, the ratio of the fundamental peak to the second harmonic peak measured

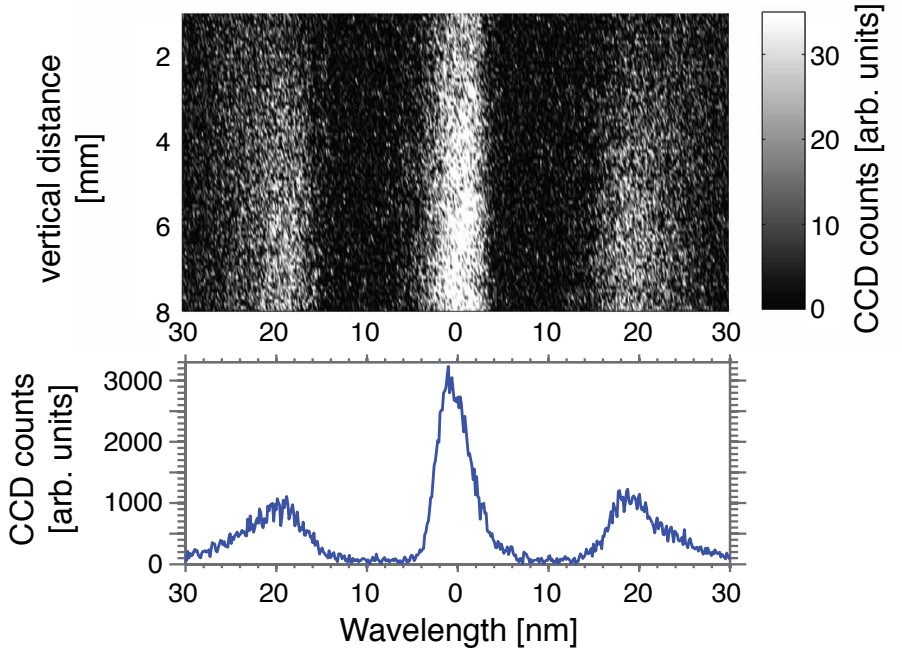

Figure 6.26. | **Undulator radiation spectrum filtered by a 150 nm thick aluminum foil.** The figure shows undulator radiation filtered by an aluminum foil, which has a transmission cutoff at $\sim 17\,\mathrm{nm}$. The lower part of the figure is a line-out vertically integrated over the whole CCD image. It can be clearly seen that the radiation closer to the zeroth order diffraction that can typically be seen (see figure 6.21) is filtered by the aluminum foil. This means that this part of the radiation has in fact wavelengths $< 17\mathrm{nm}$ and the second harmonic radiation is not a measurement artifact.

in the experiment is in good agreement with that computed by undulator simulations (see figure 6.30). Finally, the parabola describing the wavelength dependence on the observation angle in figure 6.21 shows for the second harmonic half the opening angle than for the fundamental as it is expected from theory (eq (6.14)).

6.3.1. Comparison of Undulator Spectra from Setups with Different Lens Settings

Undulator radiation has been detected for different lens setups. The section above describes in detail radiation emitted by an electron beam that is collimated by the magnetic lenses set to collimate an energy of 220 MeV. The following sections compare these results to radiation produced by a diverging electron beam from a setup lacking the magnetic lenses and a collimated beam with the lenses set to collimate an energy of 180 MeV. Figure 6.27 shows typical measured undulator spectra for different lens settings and figure 6.28 the corresponding electron spectra.

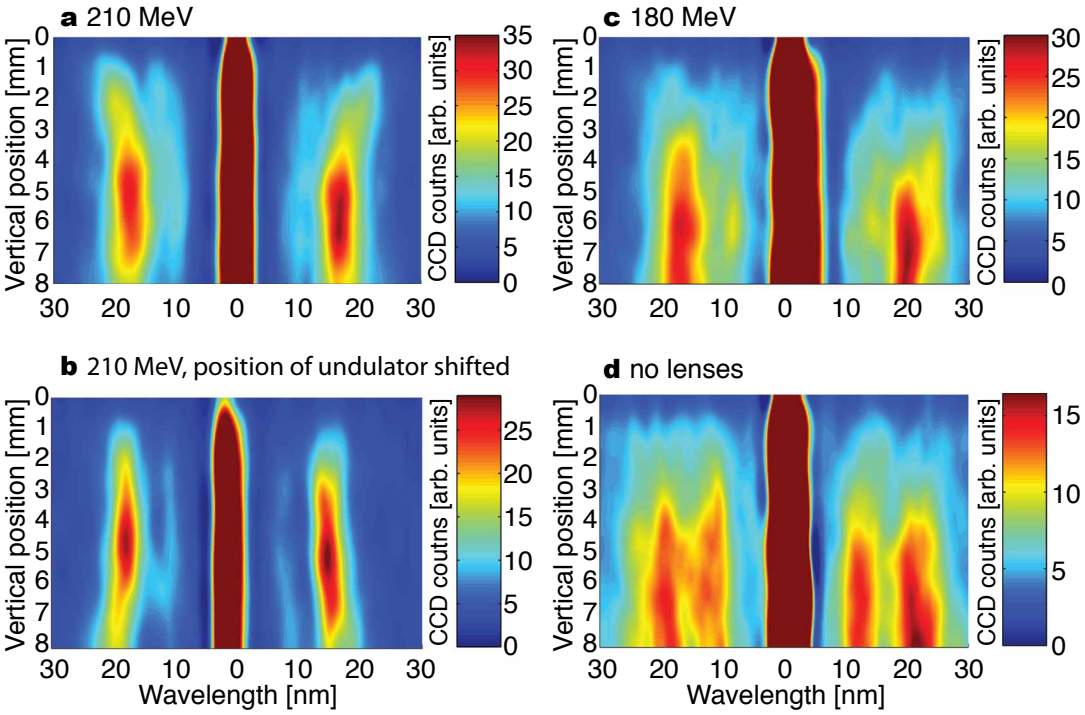

Figure 6.27. | Typical measured undulator spectra for different lens settings. Typical measured undulator spectra show the vertical position on CCD (at a distance 2.6m after the undulator center) versus the wavelength. Note that the CCD counts are color-coded and each of the measurements are represented with a different scale. **a** shows a spectrum emitted from an electron beam that is collimated by the magnetic lenses set to collimate 220 MeV. **b** shows a spectrum from the same setup but with the undulator vertically slightly shifted. **c** shows a spectrum measured with the lenses set to collimate 180 MeV. **d** shows the spectrum emitted by a diverging electron beam from a setup lacking the magnetic lenses.

Comparison of Undulator Spectra Produced by a Divergent and a Collimated Electron Beam

The undulator spectra produced from a setup lacking the magnetic lenses show a clearly separated, more distinct second harmonic peak with a higher intensity in comparison to the fundamental than those produced by a collimated electron beam (see figures 6.27 & 6.29).

The shapes of these *vertically-resolved* spectra can be explained by the characteristics of the *horizontal* distribution of the undulator spectra. Since the detected undulator spectra are vertically spatially and horizontally energy resolved the lineout at each vertical position shows the spectrally-resolved photon flux horizontally *integrated over a finite horizontal observation angle*. Such a lineout is computed by simulating the horizontal undulator spectra at $\theta_{\mathrm{vert}} = 0$. The results closely resemble the measurements (see right-hand side of figure 6.30) and give an interpretation of the experimental data which is discussed below.

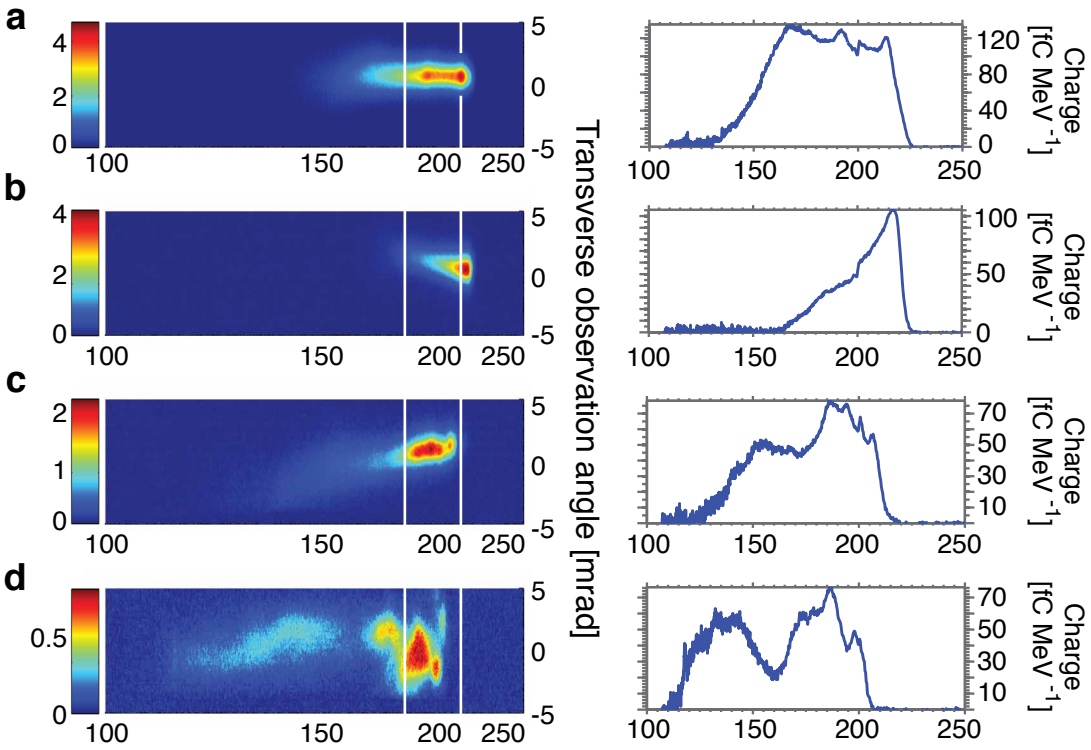

Figure 6.28. | **Electron spectra corresponding to the measured undulator radiation of figure 6.27.** The left-hand side of the figure shows the horizontally angular-resolved spectral distribution of the electrons beams which produced the undulator spectra shown in figure 6.27 (the labels in this figure corresponds to that in figure 6.27). Color-coded are the CCD counts. The vertical white lines correspond to an electron energy of 180 and 220 MeV. The right-hand side shows the corresponding electron spectra with a linear energy scale. The electron beams in **a** and **b** are collimated by the magnetic lenses set to collimate an energy of 220 MeV and have overall integrated charge of 8.4 pC and 4 pC, respectively. The electron beam in **c** is collimated by the lenses set to 180 MeV and has an overall charge of 2.8 pC. **d** shows the an electron spectrum of a beam propagating through a setup without lenses and has a charge of 4 pC. Note that these electron spectra are measured at a different distance to the capillary (1.94 m) than the undulator radiation ($\sim$ 3m) which means that a different electron energies are focussed at each positions.

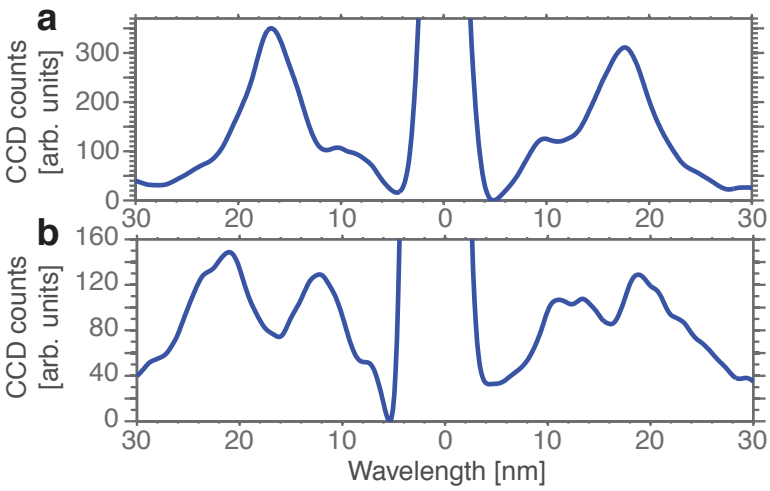

Figure 6.29. | **Lineouts of undulator spectra produced in a setup with lenses and without lenses.** **a** shows a lineout of the undulator spectrum produced by a beam collimated by the magnetic lenses set to collimate 220 MeV (lineout of figure 6.21). The lineout in **b** is taken from an undulator spectrum emitted from a diverging electron beam which propagating through a setup without magnetic lenses (the spectrum is shown in figure 6.27**d**. Note that the intensity scale is different in each plot and that the undulator spectra are produced from electron beams with different charge (a: 8.4 pC, b: 4pC). Both lineouts are (vertically) integrated over 10 CCD pixel which corresponds to an observation range of $\Delta\theta \sim 300\,\mu\mathrm{rad}$. The spectrum in **a** shows a fundamental peaked at a wavelength of 17 nm with a bandwidth of 13.6% (rms) and a second harmonic peaked at 9 nm with a bandwidth of 11.3% (rms). The spectrum in **b** shows a fundamental peaked at a wavelength of 20.5 nm with a bandwidth of 16% (rms) and a second harmonic peaked at 11.9 nm with a bandwidth of 15.9% (rms).

In order to perform simulations in a reasonable time, the computationally fast convolution algorithms of undulator simulations have been utilized. This is only possible by approximating some experimental conditions as follows:

(1) The filtering through the magnetic lenses has been taken into account by assuming a collimated electron beam at 210 MeV with an rms-energy spread of 6%. The energy spread is chosen slightly larger than the effective spectrum of figure 6.22 in order to take account for the results obtained from the simulation that includes the spectral overlap of individual flux distributions from different electron energies (which lead to a slightly larger bandwidth) which can be seen in figure 6.20. The computation is simplified by assuming the same collimation (divergence angle distribution) for all electron energies (and thus neglecting the chromatic effects introduced by the magnetic lenses). For the simulation of the spectra produced from a beam lacking the lenses, a divergence of 1 mrad and an energy spread of 4% rms (which is the typical bandwidth of the quasimonoenergetic peaks of the electron beam, see section 5.3) has been assumed.

(2) The effect of the horizontal focusing of the undulator radiation by the spherical mirror can be approximated by computing the undulator spectrum after a slit and

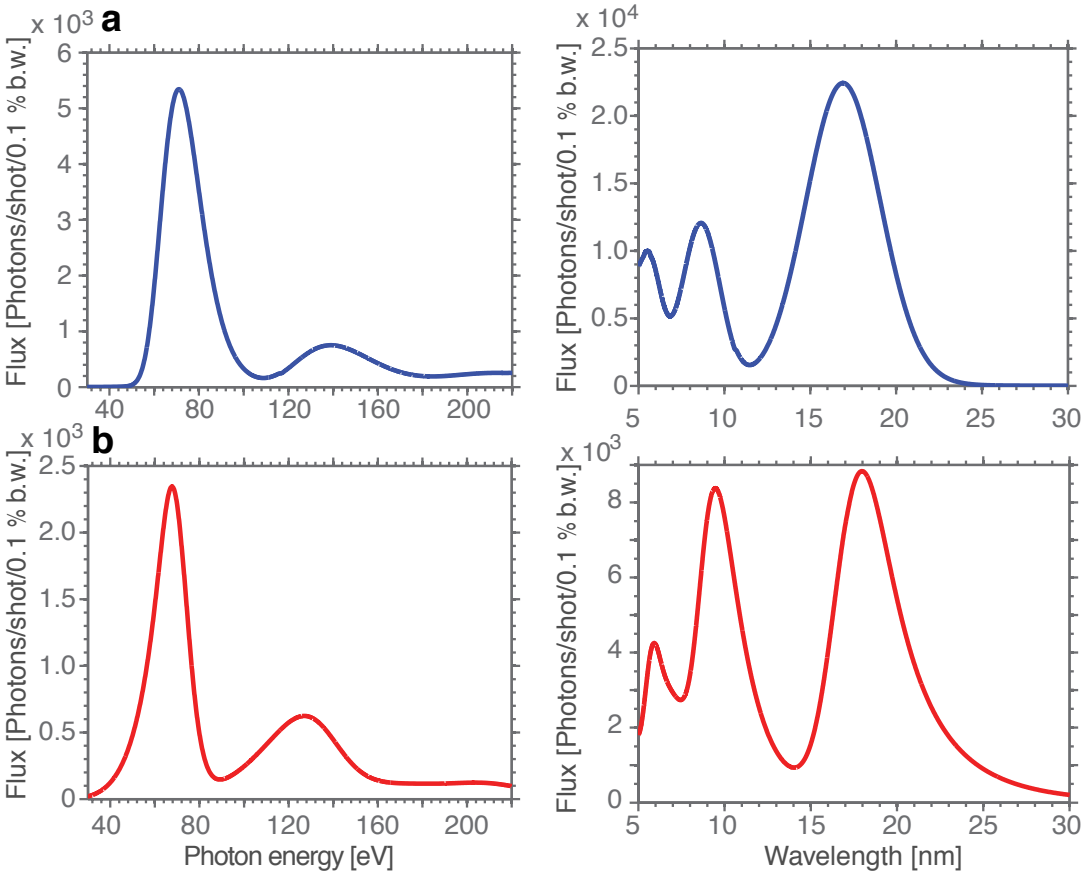

Figure 6.30. | **Simulated undulator spectra through a slit for setups with and without lenses.** The left-hand side of the figure shows simulated undulator spectra from lens setups with (**a**) and without magnetic lenses (**b**) versus the photon energy. The right-hand side shows the corresponding spectra in a linear wavelength scale. For details of the transformation procedure, see the main text and footnote mark[2]. The simulation is performed with the undulator code SPECTRA [Tanaka and Kitamura, 2001]. For details of the choice of parameters, see the main text. In the wavelength representation of the spectra from a collimated electron beam (**a**, right-hand side) shows an undulator fundamental peaked at 16.9 nm, a second harmonic peaked at 8.6 nm and a third harmonic at 5.5 nm, however since the reflectivity-cutoff of gold is around 7.5 nm (see figure 6.11), these low wavelengths cannot be detected in the experiment. For the spectrum produced by a divergent electron beam (lacking the magnetic lenses), the peaks are shifted to longer wavelengths (fundamental: 17.9 nm, second harmonic 9.6 nm, third harmonic 5.9 nm) through emittance effects. The second harmonic is more pronounced in the representation using a linear wavelengths scale in comparison to the linear photon-energy scale. The broadening of the measure spectra through the instrument function of the X-ray spectrometer is not considered in these simulations.

setting the effective horizontal slit width (the horizontal observation angle) to 1400 μrad. This horizontal observation angle has been determined through raytracing of the optical setup for a typical undulator radiation beam size and the maximum divergence which is imaged to typical transverse dimensions measured in the zeroth order of the spectra (the raytracing is shown in figure 6.10).

(3) The spectral response of the CCD camera has been taken into account by scaling the spectra with the photon energy (for further details to the spectral CCD response, see section 6.1.3).

The simulations assume a beam charge of 10 pC and an geometric emittance of $2 \cdot 10^{-9}\,\mathrm{m} \cdot \mathrm{rad}$.

The results of the simulation can be seen in figure 6.30 which shows the undulator spectrum through a slit versus the photon energy (on the left-hand side) and versus a linear wavelength scale (as measured in the experiment) on the right-hand side. In order to ensure the correct transformation of the curve from a linear energy to a linear wavelength scale (which is inversely proportional to each other), the function has to be scaled accordingly[2]. The spectra plotted with a linear wavelength scale (right-hand side of figure 6.30) show a more pronounced second harmonic radiation which is a result of the transformation from a linear photon-energy to a linear wavelength scale: the corresponding wavelength bin for an energy bin at a low energy is larger than a corresponding wavelength bin for the same energy bin width at higher energies (for example: the energy bin at 50...51 eV corresponds to a wavelength bin width of 0.5 nm, whereas the energy bin of 100...101 eV corresponds to a wavelength bin width of 0.13 nm).

The reason for the higher intensity ratio of the second harmonic to fundamental intensity for the radiation from the diverging electron beam (no lenses) in comparison to the collimated beam can be seen from simulation of (horizontal) spatially resolved spectra which are shown in figure 6.31. The spectra shown in figure 6.30 are integrated over the horizontal range between the green lines in figure 6.31. The undulator spectra emitted from the diverging electron beam (fig. 6.31**b**) are spatially and spectrally washed out to a higher degree relative to the spectra from collimated electron beams (fig. 6.31 **a**). This emittance effect is mainly due to the divergence of the electron beam, which leads to a finite (observation) angle between the propagation direction of the electron (and thus the $\theta = 0$ axis) and the observer. As a result, off-axis radiation characteristics of filament electron beams such as longer wavelengths and a peaked second harmonic emission can be observed on-axis. This leads to both an increase in bandwidth of the fundamental (to longer wavelengths) and an increase in the intensity of the second harmonic radiation on-axis. The undulator radiation produced by the collimated electron beam shows a spectrum more similar to a filament electron beam. It can be seen that the slit width (green lines in fig. 6.31) includes only a small portion of the second harmonic radiation in case of the collimated beam, whereas almost the whole distribution lies inside the slit in the case of the divergent electron beam. As a second effect, the peak intensity

[2] it has been ensured that the integral over each energy bin is the same as that over the corresponding transformed wavelength bin. Mathematically, this requirement can be expressed by $\int f(E)\mathrm{d}E = \int f[g(\lambda)] \cdot g'(\lambda)\mathrm{d}\lambda$. The curve $f[g(\lambda)]$ has to be scaled by the factor $g'(\lambda) = \mathrm{d}E/\mathrm{d}\lambda$

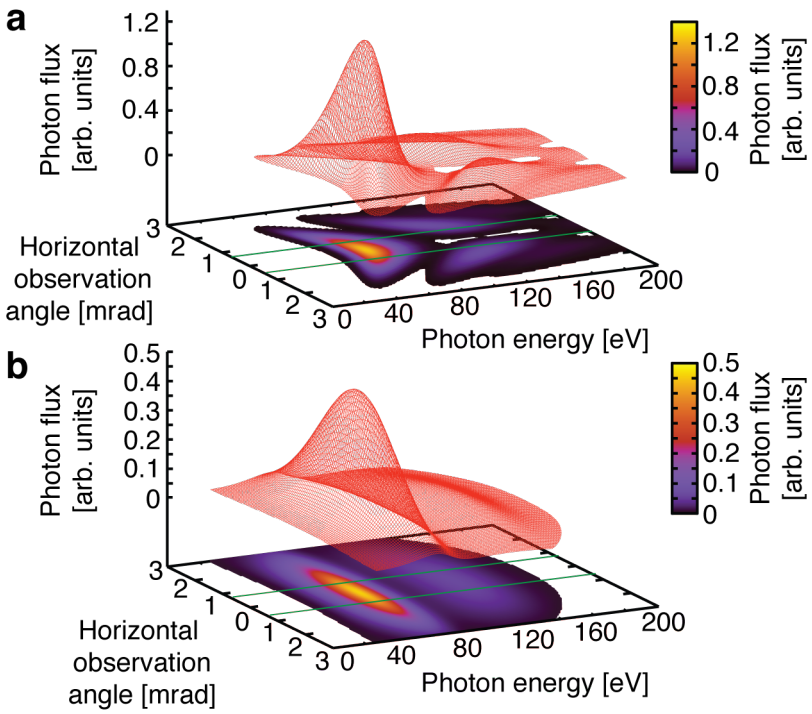

Figure 6.31. | **Simulated undulator spectra from a setup with lenses and without lenses versus horizontal observation angle. a)** shows the horizontally-resolved undulator spectrum for an electron beam collimated by the magnetic lenses and **b)** that of a freely-drifting (divergent) electron beam. Electron beam sizes and divergences typical to those of the experiment were used for the simulation: the beam sizes in case of the collimated beam are $\sigma_{\mathrm{hor}} = 400\,\mu\mathrm{m}$ and $\sigma_{\mathrm{vert}} = 224\,\mu\mathrm{m}$ with divergences of $\sigma'_{\mathrm{hor}} = 18\,\mu\mathrm{rad}$ and $\sigma'_{\mathrm{vert}} = 10\,\mu\mathrm{rad}$. In case of **b**, the beam sizes are $\sigma_{\mathrm{hor}} = \sigma_{\mathrm{vert}} = 380\,\mu\mathrm{m}$ with a divergence of $\sigma'_{\mathrm{hor}} = \sigma'_{\mathrm{vert}} = 1\,\mathrm{mrad}$. In both cases simulations were performed with the same charge of 10 pC and emittance of $2 \cdot 10^{-9}\,\mathrm{m} \cdot \mathrm{rad}$. The spectrum produced by the collimated electron beam shows features similar to undulator radiation from a filament electron beam such as second harmonic radiation peaked off-axis, a high on-axis intensity of the fundamental radiation and a pronounced parabolic dependence of photon energy with respect to the observation angle. In the case of the radiation from a divergent electron beam, these features are washed out through emittance effects. The green lines show the size of the effective slit width of $\pm 750\,\mu\mathrm{rad}$ which was used to simulate the angle-integrated spectra shown in figure 6.30.

of the fundamental is more washed out in the case of the divergent electron beam in comparison to the collimated beam. Both of these effects lead to a larger ratio of the second harmonic to the fundamental in case of the undulator radiation observed through a slit produced in a setup lacking the magnetic lenses.

In addition to a different ratio of the fundamental to the second harmonic peaks, the spectra show differences in angular variation in wavelengths: in contrast to the parabolic shape of the spectrum from the collimated electron beam, the spectrum from the divergent electron beam does not show such a behavior (see figure 6.27 **a** & **d**). The reason for this are emittance effects which wash out these filament beam features as can also be seen from the simulation in figure 6.31.

The width of the fundamental peaks of the undulator spectrum from a collimated electron beam does not correspond to the full width of the detected electron spectrum since only a part of the electrons contribute to the measured radiation as described in section 6.2. The undulator spectra produced by the diverging electron beam shows a bandwidth of 16% (rms) which suggests that the radiation mainly originates from the "quasimonoenergetic" feature of the electron beam (which has a rms-width of $\approx 7.2\%$, see figure 6.28 **d**). In figure 5.6, it can be seen that the quasimonoenergetic features of the electron beams have a smaller divergence compared to the spectral plateau background and contain a higher amount of charge.

The peak of the quasimonoenergetic feature is at 186 MeV (which corresponds to an emitted undulator wavelength of 21.7 nm), whereas the detected undulator wavelength peaks at 20.5 nm (corresponding to 192 MeV). However, the (vertical) spatially-resolved undulator spectrum is detected at the lower end of the CCD camera which means that the electron beam is pointed vertically "downwards" (has an angle with the ∞-energy axis of the magnetic spectrometer). An analysis of the magnetic spectrometer shows that an electron beam with a vertical angle of -1 mrad with respect to the ∞-energy axis can have an $\sim 10\%$ higher electron energy than actually measured (see section 5.2).

Comparison of Undulator Spectra Produced by a Setup with the Lenses set to 220 MeV and 180 MeV

The following section discusses the comparison between two undulator runs with the magnetic lenses set to collimate an electron energy of 180 ("180 MeV setup") as well as 220 MeV ("220 MeV setup"). The spatially resolved spectra can be seen in figure 6.27 **a**, **b** and **c**. The fundamental and second harmonic of the radiation in both the positive and negative first diffraction orders each is fitted by a sum of three Gaussian distribution (for the fundamental, for the second harmonic and for the background). The properties of the radiation, obtained by averaging the fits of the positive and negative first orders for each shot are listed in table 6.2. The 180 MeV run consists of 16 shots, the 220 MeV run of 20 shots with a sufficiently high number of CCD counts in the diffraction orders. The undulator radiation of both setups was produced by electron beams with very similar properties, since the runs were measured consecutively. The characterization of undulator radiation from a setup without the magnetic lenses was done with significantly less shots due to the high risk of hitting the undulator walls (gap

	180 MeV	220 MeV
	Fundamental	
wavelength [nm]	19.2 ± 1.4 (7.3%)	17.8 ± 0.6 (3.5%)
rms width of peak [nm]	3.4 ± 1 (28%)	2.4 ± 0.6 (24%)
bandwidth (rms)	18% ± 5.5%	13.4% ± 3%
	Second harmonic	
wavelength [nm]	11 ± 1.2 (11%)	10.3 ± 0.8 (7.6%)
rms width of peak [nm]	1.8 ± 0.8 (43%)	1.4 ± 0.4 (28%)
bandwidth (rms)	16% ± 6%	13.7% ± 3%

Table 6.2. | Comparison between the 180 and 220 MeV lens setup. The table shows a comparison between the undulator radiation produced in a setup with the magnetic lenses set to collimate 180 and 220 MeV. Attributes like wavelength, peak width and relative bandwidth are compared for the two setups. The relative deviation are given in parenthesis. The values are obtained by averaging fits of each diffraction order of a 10 pixel lineout (300 μrad observation angle) as discussed in the main text. The widths are given after the deconvolution of the X-ray spectrometer instrument function which is mainly given by the slit width. The slit width is deduced by the width of the zeroth order diffraction on the CCD camera.

= 1.2 mm). Therefore, they cannot be compared with the values presented in table 6.2.

The characteristics of the measured undulator radiation produced with the setup including the lenses confirm the properties expected from the simulations described above: The undulator radiation produced by the "220 MeV setup" exhibits a smaller average wavelength than the "180 MeV setup". This is also expected from the corresponding electron spectra, where the focused spectral part of the beam can be seen to clearly shift in energy for the two setups (see figure 6.28 **a,b** and **c**). The undulator peaks produced by the "220 MeV setup" have a smaller variation in the emitted wavelengths and additionally smaller peak widths. Both of these effects result from the fact that the low as well as the high photon-energy cutoff for the 180 MeV band-pass filter are given by the lens setup and the produced undulator radiation exhibits the fluctuations of the spectral electron beam properties. In the case of the 220 MeV band-pass filter, only the low-energy cutoff is given by the lenses, whereas the high-photon energy cutoff is given by the high-energy cutoff of the electron spectra. The quasi-monoenergetic features of the electron beams used in this experiment have a higher fluctuation in energy (of 6%) than the high-energy cutoff of the beams (3%) [Osterhoff et al., 2008] which manifests itself in smaller variations in the undulator radiation produced with the "220 MeV setup". However, since the band-pass of the "180 MeV setup" is at a spectrally more central part of the electron spectrum, the effective spectrum (electrons that primarily contribute to the undulator radiation) comprises a larger fraction of the electron

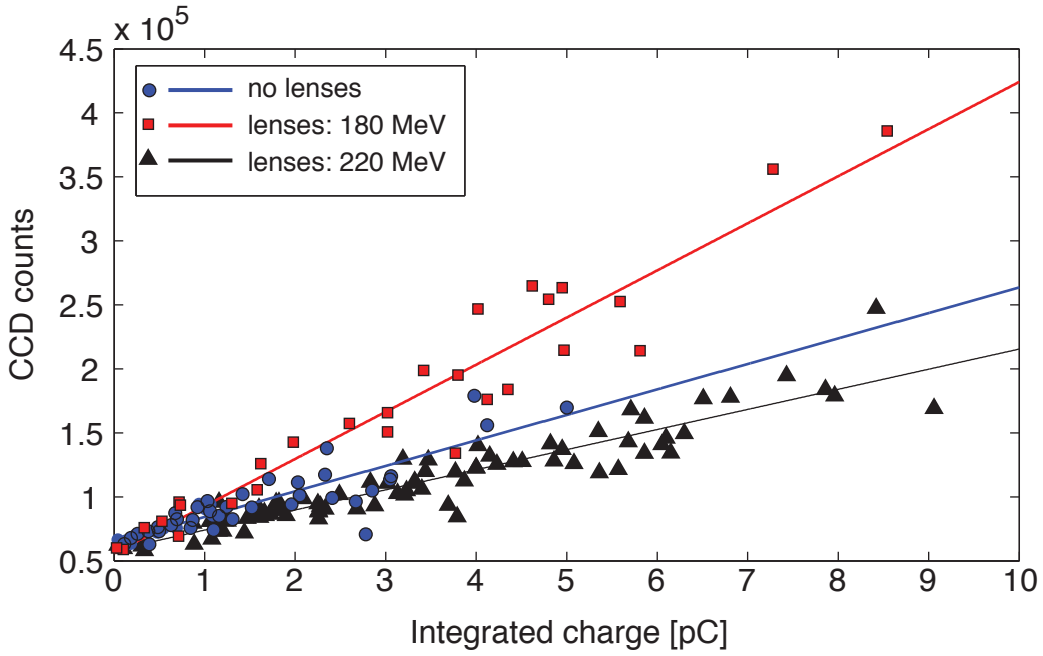

Figure 6.32. | **Integrated CCD counts vs charge.** The figure shows the CCD counts integrated over the vertical CCD area of the positive first diffraction order of the detected undulator spectra versus the integrated charge of the detected electron spectra. Three different cases are compared: (1) no magnetic lenses (blue), (2) lenses set to collimate 180 MeV (red) and (3) lenses set to collimate 220 MeV (black). The lines represent linear fits. It can be seen that the 220 MeV setup filters out a small part of the electron beam which mainly produces the undulator radiation. In the case of the setup lacking the lenses, the undulator radiation is mainly produced by the quasi-mononenergetic features in the electron beam which leads to an increase in detected CCD counts versus charge in comparison to the 220 MeV setup. The 180 MeV setup collimates a spectrally more central region of the electron beam and thus a large amount of electrons emits detectable undulator radiation but in a larger bandwidth in comparison to the 220 MeV setup (see table 6.2).

beam. This can also be seen in figure 6.32 which shows the number of detected CCD counts, integrated over the positive first diffraction order versus the integrated charge of the corresponding (whole) electron beam (not only the charge in the effective spectrum). The two different lens setups and the setup lacking the magnetic lenses are compared: The ratio of CCD counts to charge for the "180 MeV setup" is higher than that for the setup without lenses, because a larger fraction of the electron beam has a relatively small divergence and thus produces a highly collimated beam. In the electron spectra detected without lenses (for example fig 6.28, **d**), only the quasi-monoenergetic features exhibit relatively small divergences (of $\sim$ 700 µrad, see LWFA experimental chapter) and thus mainly contributes to the detected undulator radiation. This fact can also be seen from the relatively small bandwidth of the undulator radiation which is in good agreement to the width of the quasi-monoenergetic peak. Since the "220 MeV setup"

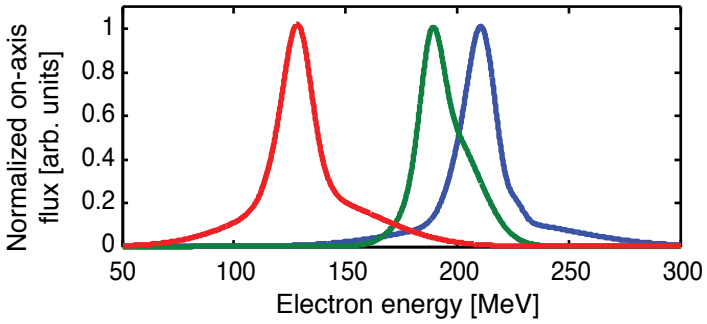

Figure 6.33. | Tuning of the energy-band-pass curve for different lens settings. The figure shows the calculated energy-band-pass curve (see section 6.2) for a lens settings that collimates an energy of 120 MeV (red), 180 MeV (green) and 220 MeV (blue). The curves are simulated by SRW for the resonance wavelength at each electron energy and considering the focusing gold mirror (with the method used to produce the system response curve, red in figure 6.17**b**).

cuts out only a relatively small (high energy) fraction (see green curve in fig 6.22) of the electron beam, it exhibits the lowest integrated CCD counts to charge ratio.

In figure 6.27 it can be seen that the parabolic shape of the wavelength-dependence on the observation angle is most pronounced for the 220 MeV setup. For the setup lacking the lenses, emittance effects wash out this shape as discussed above. In contrast to the 180 MeV setup, the 220 MeV setup is set to focus the electron energies of the quasi-monoenergetic feature and thus the peak of the spectral electron distribution. The simulation of the spatial spectral fluxes show that an electron energy that is focused at the position of the detector in comparison to one that is not in focus exhibit a more distinct parabolic shape in the angular distribution (see figure 6.19). For the 180 MeV setup, a spectrally more central part of the electron spectrum (and thus not the spectral peak) is focused which leads to a washing out of the parabolic angular shape into a more linear structure.

Tuning of the band-pass curve

As can be seen in table 6.2, the undulator wavelength can be tuned by setting the lenses to collimate a different electron energy. This leads to a tuning of the band-pass curve which can be adjusted by changing the lens positions according to table 6.1. The tuning of the system response for different lens settings can be seen in figure 6.33. The result of a SRW simulation that computes the sum of angular fluxes for each electron energy in the range of 100-250 MeV (similar to that shown in figure 6.18) but for a lens setting that collimates an electron energy of 180 MeV can be seen in figure 6.34. A comparison of the lineouts of the simulations for the 180 MeV and the 220 MeV lens settings can be seen in figure 6.35.

Owing to the broad spectra of the laser-accelerated electron beams used in this experiment, the tunability could also be quantified. The correlation of the detected undulator wavelength with the corresponding peak of the effective electron spectrum (after the

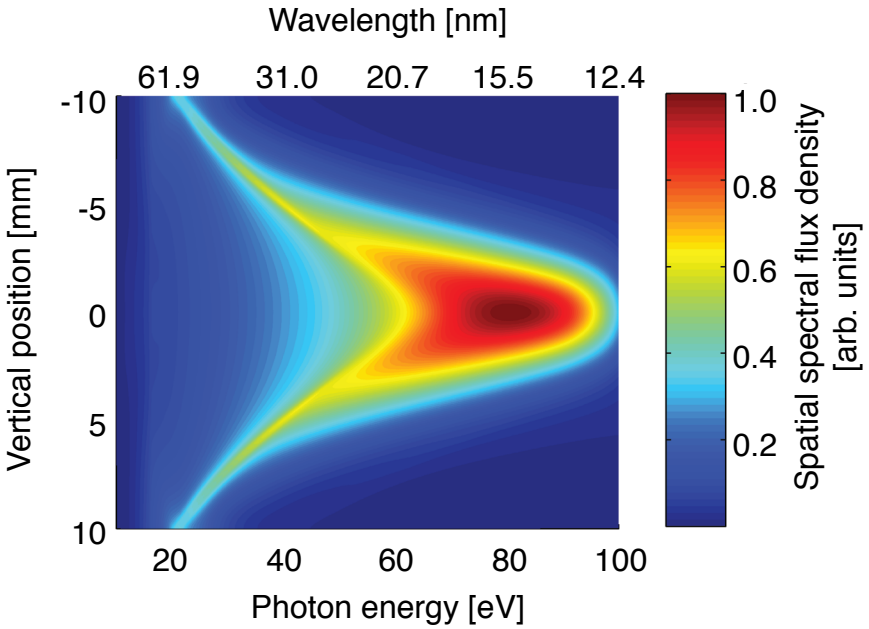

Figure 6.34. | Simulation of the spatial spectral flux density for a flat electron spectrum with the magnetic lenses set to collimate an energy of 180 MeV. The figure shows the simulated spatial spectral undulator flux density emitted by an electron beam with a flat-top energy spectrum propagating through a doublet of magnetic lenses set to collimate an electron energy of 180 MeV. The results were obtained with the methods described in section 6.2 (similar to that shown in figure 6.18).

band-pass filter due to the magnetic lenses) for different lens setting can be seen in figure 6.36. Electron beams that are transported by a lens setup that collimates an electron energy of 180 MeV (marked by blue dots) produce undulator radiation with an -on average- longer wavelength than electron beams transported by the 220 MeV setup which demonstrates the tunability of the source. The dependence of wavelength on the electron energy as predicted by equation (6.14) is in excellent agreement with the measured data.

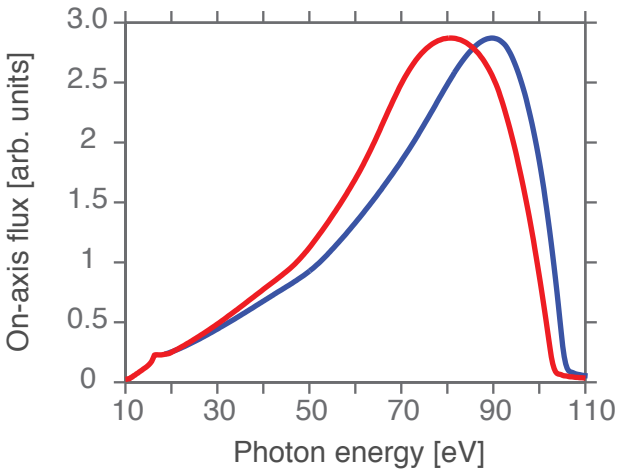

Figure 6.35. | Lineout of the simulated UR for a flat spectrum for different lens settings. The curves show lineouts at vertical position 0 mm of the simulated undulator emission (taken from figures 6.18 & 6.34) for a lens setting that collimates an electron energy of 180 MeV (red) and a setting that collimates 220 MeV (red). The curve shows the possibility to tune the wavelength of the undulator radiation with the help of the settings of the magnetic lenses. Between these settings, the peak can be shifted about 10 eV (or $\approx 1.7\,\mathrm{nm}$). The curves were simulated for for an energy range of 100-250 MeV which are the electron energies relevant for the experiment described here. The high-energy cutoff of the blue curve is due to the cutoff at 250 MeV of the simulation range.

6.3.2. Undulator as Diagnostic Tool

This section discusses the use of an undulator as a diagnostic tool for the electron beam. More specifically, the discussion focuses on the characterization of laser-accelerated beam in terms of the electron energy distribution [Gallacher et al., 2009] and the electron beam emittance.

Since the pointing as well as the energy spectrum can be measured simultaneously, the spectral characterization of the electron-energy distribution by undulator radiation is very powerful. This is especially important for laser-wakefield accelerated beams, because of their large pointing fluctuations (compared to conventional accelerators). Section 5.2 discusses the error in the deduced electron energy arising from the variation in electron-beam pointing for a spectrometer based on a magnetic dipole. Since in undulator spectra the wavelength depends quadratically on the observation angle, the pointing of the electron beam can be deduced from the position of the smallest wavelength ($\theta = 0$). Additionally, the electron energy as well as the energy spread of the electron beam can be deduced from undulator radiation that is spectrally resolved in one and spatially resolved in the other dimension. Additionally, X-ray spectrometer for diagnosing the undulator radiation are relatively compact and therefore offer the possibility for an absolute energy and intensity calibration by a defined X-ray source (such as a synchrotron source). This typically cannot be done for magnetic spectrometer setups

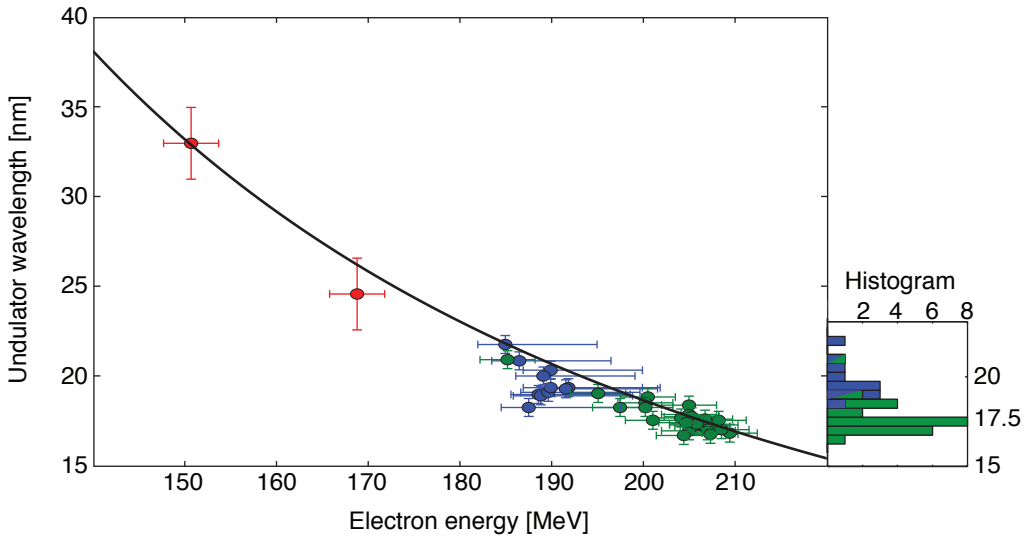

Figure 6.36. | **Undulator wavelength versus electron energy.** Detected fundamental undulator radiation wavelengths plotted against the corresponding maxima of the effective electron spectra (determined by the method of figure 6.17). The green and blue points correspond to consecutive shots with two different positions of the magnetic lenses, demonstrating the wavelength-tunability of the source (see figure 6.33). The error bars arise from measurement errors of the electron spectrometer, the X-ray spectrometer, magnetic lens distances and the undulator field. The asymmetric error bars of the blue points are due to a non-zero angle of the electron beam with the spectrometer axis. The red points represent shots that lie outside the stable electron acceleration regime. The theoretical behavior described in equation (6.14) is shown as a solid line.

that are needed to measure high electron energies since they require very long and strong magnets in order to achieve a sufficiently high energy resolution. Undulators can be a much more compact, *non-perturbative* diagnostic for the characterization of the electron energy distribution.

The electron beam emittance has a strong influence on the detected undulator spectrum: the angular flux of the undulator harmonics gets spatially as well as spectrally washed out as can be seen in figure 3.5. For an on-axis undulator spectrum, filtered by a slit, these emittance effects lead to a decrease of the on-axis flux of odd harmonics, whereas the on-axis flux increases for even harmonics (which for a filament electron beam are peaked off-axis). A simulated undulator spectrum after a slit for different emittances can be seen in figure 6.37.

Thus undulator radiation could be used as a diagnostic tool for the electron beams. However, laser-wakefield accelerated electron beams have a very large initial divergence and a small source size at the exit of the accelerator. The emittance effects mentioned above are only significant if the variation in emittance originates from a higher electron beam divergence rather than a larger source size as can be seen in figure 6.37. The emittance of LWFA beams can be estimated by the product of the divergence and the

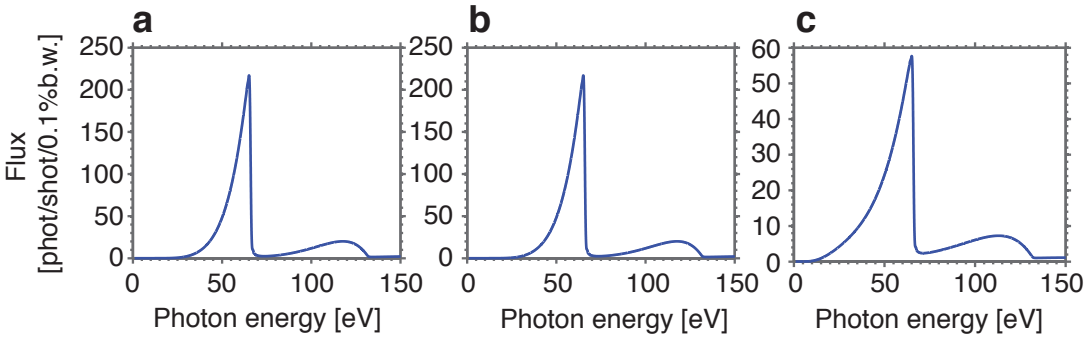

Figure 6.37. | **Simulated undulator flux through a slit for different emittances.** The curves show simulations of the undulator spectrum of an electron beam with an energy of 200 MeV, an energy spread of 0.1% and a charge of 10 pC filtered by a slit of vertical size of $500\,\mu\mathrm{m}$ and horizontal size of $200\,\mu\mathrm{m}$ at a distance of 1 m for different emittances. The undulator is that used in the experiments described above ($K = 0.55$, $\lambda_u = 5\,\mathrm{mm}$ and $L = 30\,\mathrm{cm}$. **a)** shows the spectrum emitted by an electron beam with a source size of $1\,\mu\mathrm{m}$ and a divergence of $1\,\mathrm{mrad}$, **b)** the spectrum for $10\,\mu\mathrm{m}$ and $1\,\mathrm{mrad}$, and **c)** for $1\,\mu\mathrm{m}$ and $2\,\mathrm{mrad}$. Note that the flux scales are different for the curves in **a** and **b** in comparison to that in **c**.

beam size at the accelerator exit. For the beams used in this experiment with a measured average divergence of $\approx 1\,\mathrm{mrad}$ and an estimated source size of $2\,\mu\mathrm{m}$, this leads to a geometrical emittance of $\epsilon \approx 2\,\mathrm{nm}\cdot\mathrm{rad}$. In figure 6.37, it can be seen that it is difficult to determine the electron beam source size with the help of undulator radiation: even a tenfold larger emittance (by increasing the initial electron beam size of a factor of 10, while leaving the divergence constant at 1 mrad) does not result in a different spectrum through a slit, whereas the increase of the divergence by a factor of 2 changes the spectral distribution significantly (see figure 6.37).

The possibility to use the undulator radiation from an electron beam that is collimated by magnetic lenses is discussed in the following. In order to examine emittance effects on the spatial spectral flux, SRW calculations for the "220 MeV" lens setup for different emittances have been conducted: for a "reference" beam with $\epsilon = 1 \times 10^{-9}\,\mathrm{nm}$ ($1\,\mu\mathrm{m}$ initial source size and 1 mrad inital divergence), and for two beams with $\epsilon = 10\times10^{-9}\,\mathrm{nm}$ (one with $10\,\mu\mathrm{m}$ source and 1 mrad divergence and one with $\sqrt{10}\,\mu\mathrm{m} \times \sqrt{10}\,\mathrm{mrad}$). The effects are only simulated for the undulator fundamental. The results can be seen in figure 6.38. As expected, in comparison to the reference beam, only the spectral flux emitted by the electron beam with the variation in beam size *and* the divergence shows a significantly different flux distribution. In the case of an emittance increase only due to an increased electron beam source size, the differences in the undulator flux distribution to the reference beam are insignificant.

In order to get a more detailed understanding of the differences between the fluxes, each flux distribution has been subtracted from that of the reference beam (see figure 6.39). It can be seen that the difference is only a few-percent effect for a variation in the source size (and thus the emittance) of a factor of 10. The difference in distribution is

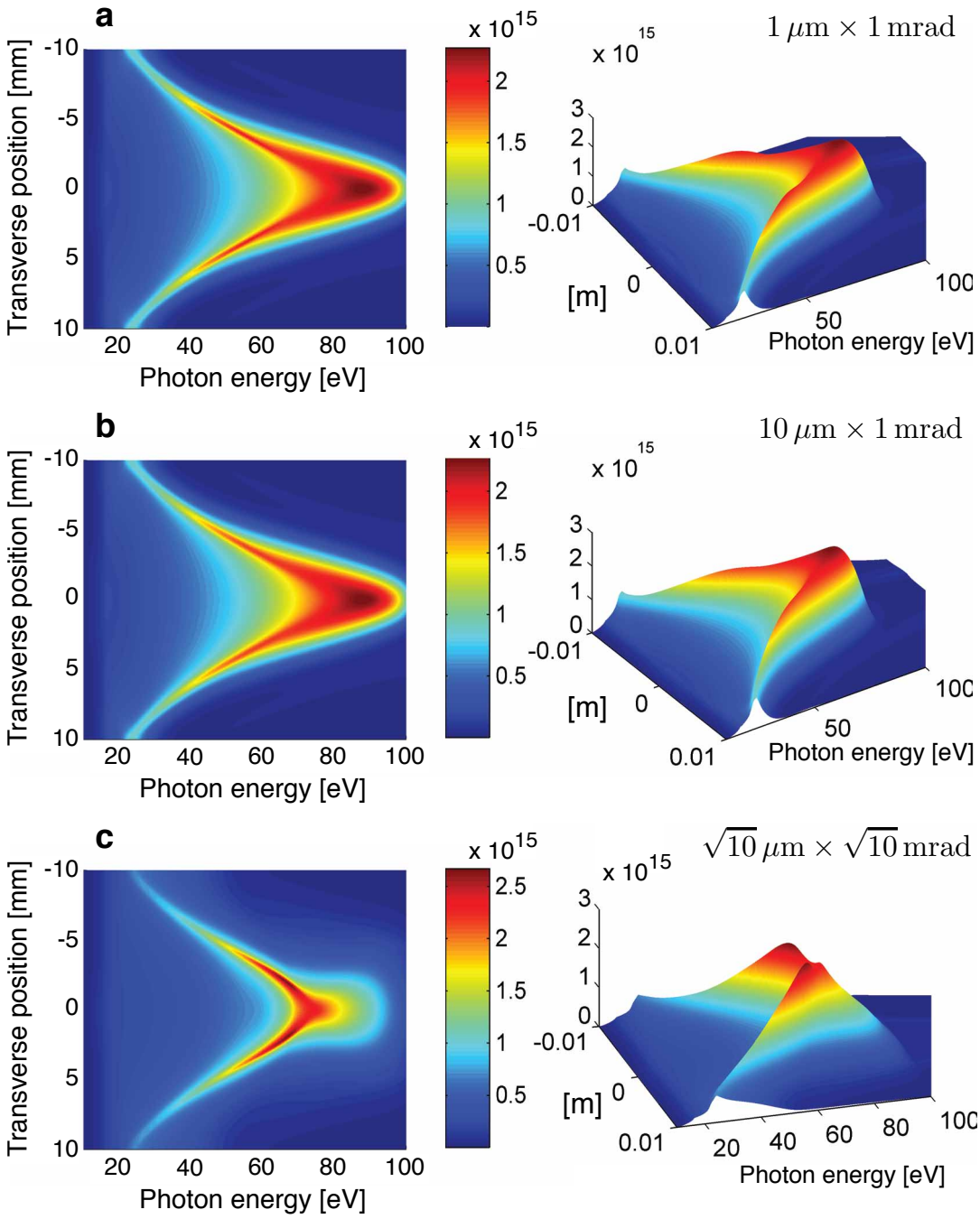

Figure 6.38. | **Simulated spatial spectral undulator flux for beams of three different emittances.** A SRW simulation similar to that shown in figure 6.18 with a flat-top electron energy spectrum of 100 - 250 MeV and the 220 MeV lens setup is performed for different emittances: **a)** shows the spectrum for an electron beam with an initial beam size and divergence of $1\,\mu\mathrm{m}$ and $1\,\mathrm{mrad}$, **b)** for $10\,\mu\mathrm{m}$ and $1\,\mathrm{mrad}$ and **b)** for $\sqrt{10}\,\mu\mathrm{m}$ and $\sqrt{10}\,\mathrm{mrad}$. The figures on the right-hand side show a 3D representation of those on the left-hand side.

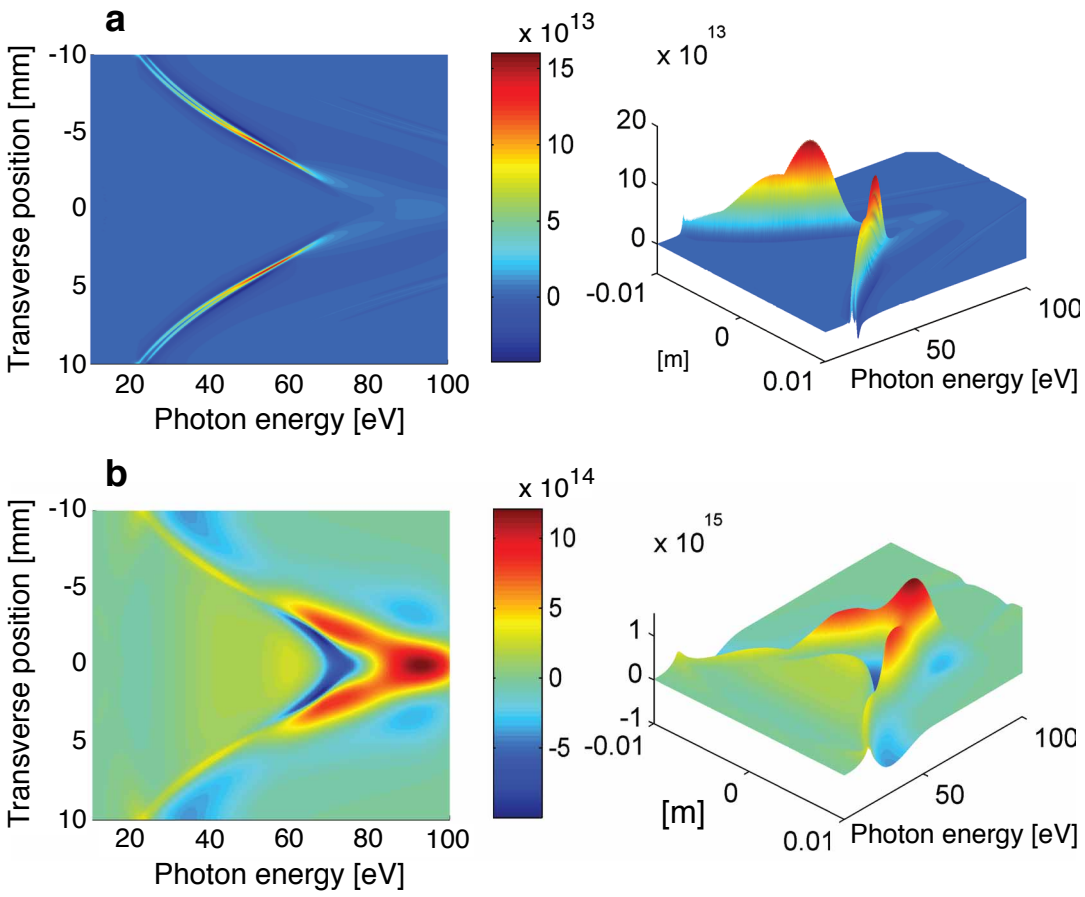

Figure 6.39. | **Difference between the undulator flux distributions of the beams of figure 6.38. a)** shows the result of the flux distribution emitted by the electron beam with a $10\,\mu\mathrm{m}$ source size and 1 mrad divergence subtracted from the reference beam. **b)** shows the difference between the flux from the $\sqrt{10}\,\mu\mathrm{m} \times \sqrt{10}\,\mathrm{mrad}$-beam subtracted from the reference-beam flux distribution. The figures on the right-hand side show a 3D representation of those on the left-hand side.

mainly in the wings of the parabolic angular shape of the flux emitted by the electron energy that is focussed at the position of the detector. In contrast to the difference in flux distribution from the reference beam and the beam with initially $\sqrt{10}\,\mu\mathrm{m} \times \sqrt{10}\,\mathrm{mrad}$ which are significantly distinct from each other. The differences can be explained by the electron beam sizes at the position of the detector: figure 6.40 shows the energy-dependent electron beam cross-sectional area ($\pi \cdot \sigma_x \cdot \sigma_y$) for the three different cases.

In case of the beam with an equally increased divergence and beam size, the beta function β_{Twiss} of the system does not change. Since the beam size can be calculated from $\sigma = \sqrt{\beta_{\mathrm{Twiss}} \cdot \epsilon}$, this means that both the beam size in focus is larger for the higher emittance case and its beam size is growing faster with the electron energy than the lower emittance beam (see black line in figure 6.40). This results in a significantly different spectral photon flux distribution as can be seen in figure 6.39.

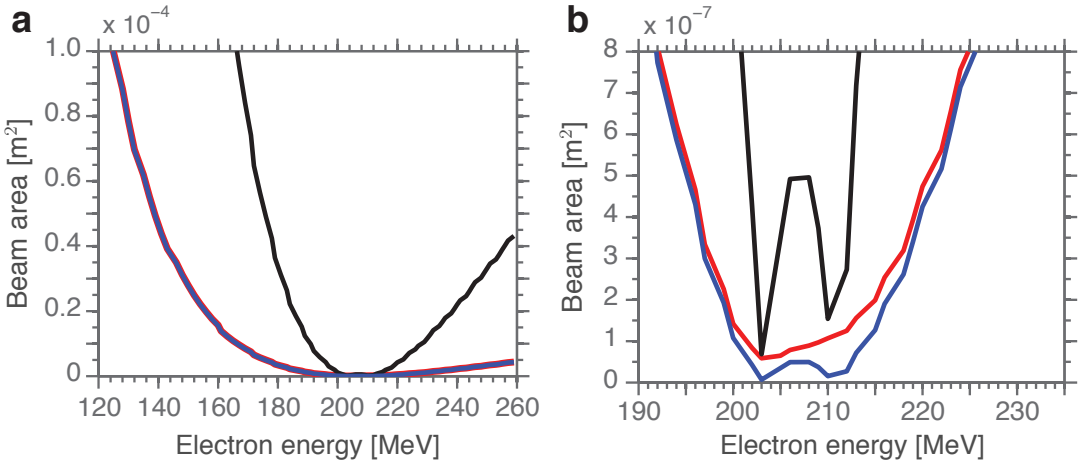

Figure 6.40. | **Electron beam cross-section area.** The figure shows the cross-sectional area ($\pi \cdot \sigma_x \cdot \sigma_y$) at the position of the detector of the electron beams with an initial beam size and divergence of $1\,\mu\mathrm{m}$ and $1\,\mathrm{mrad}$ (blue), $10\,\mu\mathrm{m}$ and $1\,\mathrm{mrad}$ (red) and $\sqrt{10}\,\mu\mathrm{m} \times \sqrt{10}\,\mathrm{mrad}$ (black) propagated through the "220 MeV lens setup" for a larger electron energy range **a** and a zoom at the focused beam in **b**. The wiggles in the beam area in **b** originate from the astigmatic focus.

In case of a different electron beam source size (and same divergence as the reference beam), the beam sizes at the position of the detector are almost identical except for the size of the focussed (imaged) electron energy (see red and blue curve in figure 6.40**b**). In order to determine the beam size of the undulator radiation, the electron beam size has to be convoluted with the natural undulator beam size which for wavelengths in the soft-X-ray range dominates over this effect and no significant difference can be seen. Only the angular spectral flux distribution shows a slight difference (few-percent effect) in the opening angle of the parabolic angle-wavelength dependence (figure 6.39).

Since the divergence of the electron beam is routinely measured by the determination of the electron beam size at a defined distance, only the measurement of the electron beam source size leads to additional information about the emittance. However, since for the detected undulator radiation, the pixel-to-pixel fluctuations in photon counts on the CCD is significantly larger than the (few-percent) effect of a tenfold increase in electron beam source, no significant information about the electron beam emittance can be deduced from the measurements described above.

Undulator-based emittance measurements that are typically used in conventional synchrotron facilities such as the imaging of the source [Elleaume et al., 1995] require a detailed knowledge of the beamline (Twiss parameters) and a well-behaved electron beam with a small energy spread. For LWFA beams these requirements are not given since it has (in comparison to conventional facilities) a relatively large energy spread and large shot-to-shot variations in divergence, pointing (which vary the Twiss parameters for a given setup). However, the possibility of single-shot emittance measurements of LWFA beams using undulator radiation in combination with measurements of the electron beam properties is currently being investigated.

7. CONCLUSIONS AND OUTLOOK

The experiments described in this thesis mark a milestone on the path towards a new generation of undulator-based X-ray sources with dimensions on the university-laboratory scale: Radiation in the soft X-ray range (with wavelengths down to $\sim 7\,\mathrm{nm}$) was generated by an undulator source driven by laser-wakefield accelerated electron beams with energies of $\sim 210\,\mathrm{MeV}$. The radiation was detected and spectrally characterized in 70% of consecutive driver laser shots which is a remarkable stability for a proof-of-principle experiment using ultra-high intensity lasers. This high reproducibility is due to both the stable laser-wakefield accelerator and the electron beam transport consisting of a doublet of high-gradient miniature magnetic quadrupole lenses. The electron beam collimated by the magnetic lenses showed significantly decreased effective shot-to-shot pointing fluctuations on target (however the intrinsic pointing fluctuations of the LWFA beam cannot be changed with this method). In addition, it was shown that the magnetic lenses act as an effective spectral-bandpass filter for the undulator radiation: owing to their chromaticity, the lenses only collimate electrons of a particular energy whereas for electrons of energies outside this band, the divergences significantly increase. This leads to a variation in the electron (and thus undulator) beam divergence which results in a high on-axis undulator flux only for radiation emitted from electrons that are collimated or slightly converging. These electrons constitute the energy-bandpass. Experimentally this was verified by the small undulator radiation bandwidth of 20% (FWHM) (where 65% would be expected from the electron spectrum) and small spectral shot-to-shot fluctuations of only 3.5%. By setting the magnetic lenses to collimate a different electron energy, this effect was used to show the wavelength-tunability of the undulator radiation within a few nanometers.

Both the detected angular spectral (parabolic) shape of the undulator radiation and its wavelength dependence on the electron energy are in excellent agreement with the theoretical prediction. The detected on-axis flux of 16,000 photons per shot per mrad^2 per 0.1% bandwidth is emitted by the fraction of the electron spectrum that lies within the band-pass originating from the spectral filtering through the magnetic lenses. This part of the electron beam was measured to have a charge of 1.3 pC, which agrees with theoretical computations of the on-axis flux that estimates a required bunch charge of 1.1 pC.

The pulse duration of an undulator source emitting short-wavelengths is mainly given by the duration of the electron bunch. In the case of laser-wakefield accelerators it is predicted by theory and simulations to be only $\sim 10\,\mathrm{fs}$. This implies three orders of magnitude improvement in temporal resolution compared to third-generation synchrotron sources. The ultrashort pulse duration and their perfect synchronization to the driver laser makes LWFA-driven sources ideal candidates to provide radiation with

the properties required for ultrafast four-dimensional imaging using pump-probe techniques. These unique properties, in combination with the compact size holds the promise for widespread application in university-scale laboratories. However, the ability to perform four-dimensional imaging on the atomic scale requires pulses with wavelengths in the Ångström range, sub-picosecond to a few femtosecond duration and a sufficiently high flux. In order to provide such pulses with peak brilliances comparable to third-generation synchrotron sources, the electron beam parameters need to be significantly improved: the laser-wakefield accelerator must deliver beams with a charge of a few hundred pico-Coulombs and energies of a few giga-electronvolt and less than a few percent-level energy spreads. Additionally, the shot-to-shot stability in energy, charge and pointing of the electron beams needs to be increased.

First promising improvements towards this end have already been obtained: LWFA-accelerated electron beams with an energy of 1 GeV have been shown, however with an energy spread of 2.5% (rms) and a charge of 30 pC [Leemans et al., 2006]. Charges of several hundred pico-Coulombs have been reported in [Faure et al., 2004], [Geddes et al., 2004] & [Mangles et al., 2004] however only at an electron energy of $\sim 100\,\mathrm{MeV}$. Methods of separating the electron injection mechanism from the acceleration (see section 2.7.2), such as the density-downramp injection scheme [Bulanov et al., 1998] or the injection by colliding laser pulses [Faure et al., 2006], have the potential to increase the shot-to-shot stability and decrease the electron energy spread at the same time. A 1% (rms) energy-spread has been reported using the latter method [Rechatin et al., 2009], however with an accelerated charge of 10 pC at energies around $\sim 200\,\mathrm{MeV}$. Additionally, finer control over laser parameters contributes to a higher shot-to-shot stability.

These developments show the rapid progress in the field of laser-wakefield accelerators and its potential to realize the aforementioned demands on the beams. Since many properties of the LWFA electrons can be improved by a higher laser intensity, the fast-paced advances in laser technology additionally help to move the field forward. For LWFA-driven lightsources, this means that they could soon be operating in the targeted regime.

Figure 7.1 shows a plot of brilliances of sources driven by LWFA electron beams with parameters that can potentially be achieved in the near- to mid-term future. The brilliances are compared to that of the source presented in this dissertation and to that of a state-of-the art third generation synchrotron source. It can be seen that a source driven by LWFA electron pulses of 10 fs duration, 100 pC of charge, an energy of 3 GeV and an energy spread of 1% could compete with the peak brilliance of a state-of-the synchrotron (15 ps pulse duration, 40 nC of charge, 6 GeV and 0.1% energy spread). They both use a 5m undulator, but with different parameters (for parameters see caption of figure 7.1) From the electron beam parameters it can be seen that the two sources operate in a completely different regime: in the case of the LWFA driven source, the high brilliance is reached by a high photon flux and an extremely short pulse duration, whereas the conventional synchrotrons provide pulses that are more than two orders of magnitude higher in flux and are produced by electron beams with extremely small emittance. However, with a duration of these pulses is three orders of magnitude longer than that of the LWFA pulses. Through sophisticated techniques such as femto-slicing

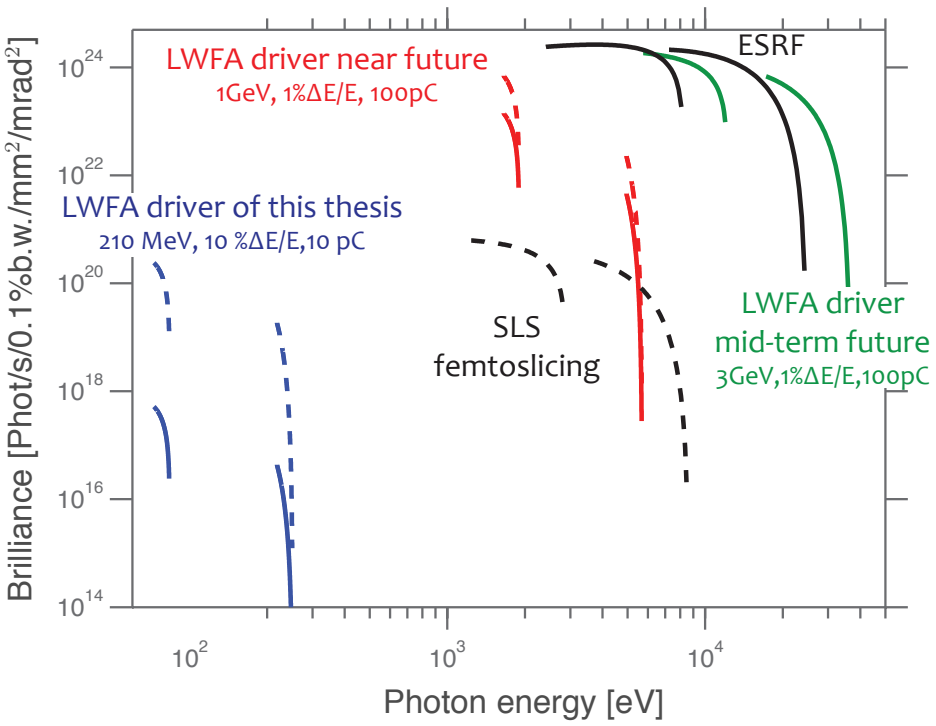

Figure 7.1. | **Estimated peak brilliances.** The estimated peak brilliances of the undulator fundamental and the third harmonic in using the parameters of the experiment presented in this thesis (blue), electron parameters than can potentially be reached by LWFA accelerators in the near (red) and in the mid-term future (green) in comparison to existing state-of-the art third generation synchrotron sources (black). The LWFA electron beams are assumed to have a pulse duration of 10 fs and an emittance of $1\,\mathrm{nm}\cdot\mathrm{rad}$. The electron energy spread is taken into account by normalizing the charge of the bunches to 0.1% energy spread. The parameters used to create these curves are: in the case of this experiment (blue solid lines) an electron beam with a charge of 10 pC, energy of 210 MeV and energy spread of 10%, horizontal and vertical beam sizes and divergences of $360\,\mu\mathrm{m}$, $200\,\mu\mathrm{m}$, $9\,\mu\mathrm{rad}$ and $7\,\mu\mathrm{rad}$. The undulator has a period of $\lambda_u = 5\,\mathrm{mm}$, a length of $L = 30\,\mathrm{cm}$ with $K = 0.55$. The beta-matched case (section 3.5.2, $\alpha_{\mathrm{Twiss}} = 0$, $\beta_{\mathrm{Twiss}} = L/(2\pi)$) with beam sizes of $7\,\mu\mathrm{m}$ and divergences of $141\,\mu\mathrm{rad}$ (blue dashed lines). The near-term LWFA electron beams are assumed to have an energy of $1\,\mathrm{GeV}$ with a spread of 1% and a charge of $100\,\mathrm{pC}$. The same undulator parameters as above are used but with a length of $L_1 = 1\,\mathrm{m}$ (red solid line) and $L_2 = 5\,\mathrm{m}$ (red dashed line). The mid-term brilliances assume beams with $3\,\mathrm{GeV}$ with a spread of 1% and a charge of $100\,\mathrm{pC}$ and an undulator of $5\,\mathrm{m}$ length with a period of $7\,\mathrm{mm}$ and $K = 1.5$. ESRF (ID23) (black lines): $6\,\mathrm{GeV}$ energy and a spread of 0.1%, a bunch charge of $40\,\mathrm{nC}$ and $15\,\mathrm{ps}$ duration. The horizontal and vertical emittances are $4\,\mathrm{nm}\cdot\mathrm{rad}$ and $0.03\,\mathrm{nm}\cdot\mathrm{rad}$ and the undulator parameters are $L = 5\,\mathrm{m}$, $\lambda_u = 42\,\mathrm{mm}$ and $K = 2.2$. The dashed black line depicts the femtoslicing source at the SLS [Beaud et al., 2007] with the parameters of 60 A peak current at 2.4 GeV, an emittance of $5\,\mathrm{nm}\cdot\mathrm{rad}$, an undulator with $\lambda_u = 19\,\mathrm{mm}$, 96 periods and 0.92 T magnetic field.

[Khan et al., 2006] the pulses of conventional synchrotrons can be shortened to $\sim$100 fs, however, with the drawback of a significant loss in bunch charge (for a comparison of the sources, see figure 7.1).

This means that the X-ray pulses of conventional and LWFA-driven sources are suited for different applications. With their short pulse durations and the synchronization to the driver laser, the LWFA-driven sources are perfectly tailored for ultrafast pump-probe measurements, whereas conventional synchrotron sources are best for applications that require sheer photon flux. Owing to their high flux per pulse and their high repetition rates of several hundreds of MHz, the *average* flux of conventional (storage-ring-based) undulator sources is orders of magnitude higher than that of LWFA-driven sources. Typical laser-wakefield accelerators currently operate at a repetition rate of 10 Hz which is limited by the driver laser. However, advances in laser technology, such as more efficient pump lasers like diode-pumped solid-state lasers or fiber-based lasers with a high repetition rate or new amplification schemes such as optical parametric chirped-pulse amplification (OPCPA) are pushing on this frontier.

In order to apply the X-ray beams of LWFA-based sources in experiments, the divergent undulator radiation needs to be refocused. Focusing systems that are typically used in synchrotron sources such as Fresnel zone plates, grazing incidence Kirkpatrick-Baez arrangements or bent crystals require extremely well-defined X-ray beams. The performance of these focusing methods is markedly degraded if the radiation has a large spectral bandwidth or fluctuations in photon energy or pointing (as is the case for laser-driven sources). In order to cope with these properties of current laser-driven sources in the short-term application, a lossless focusing scheme based on the compact magnetic lenses described in 6.1.1 is proposed: the lenses are used to produce a convergent electron beam with a focus located at a short distance after the undulator. As discussed in chapter (3.24), the photon beam size at target can be calculated by the convolution of the electron beam size and the natural (single-electron) undulator beam size, both determined at the position of the target. Thus, a tightly focused electron beam leads to a focused photon beam. However, this method of focusing is limited by the intrinsic undulator radiation divergence which depends on the square root of the emitted wavelength.

An example is shown in figure 7.2 in the case of an electron beam with an energy of 220 MeV (however with negligible energy spread). The electron beam is focused by a magnetic-lens triplet to a beam size of 5 µm in both directions at a distance of 0.5m after the undulator center. An undulator of length 0.3 m and a period of 5 mm emits radiation with $\sim$ 15 nm and an intrinsic divergence $\theta \simeq 160$ µrad. In this setup, this intrinsic undulator divergence leads to a spot size of 80 µm 0.5 m after the undulator center. This distance is required to deflect the electrons in order not to hit the target. For a higher electron energy (and thus a smaller wavelength), the undulator divergence is decreased: for example, radiation with a wavelength of 1 nm is emitted with a divergence of $\theta \simeq$ 40 µrad which leads to a smaller spot size of the undulator radiation. A small undulator length is required in order to achieve a small electron beam focus and minimize the increase in undulator beam size due to the intrinsic undulator divergence (the divergence scales as $\sigma_{r'} \propto L^{-1/2}$ and the beam size at the undulator exit as $\sigma = \sigma_{r'} \cdot L/2 \propto \sqrt{L}$).

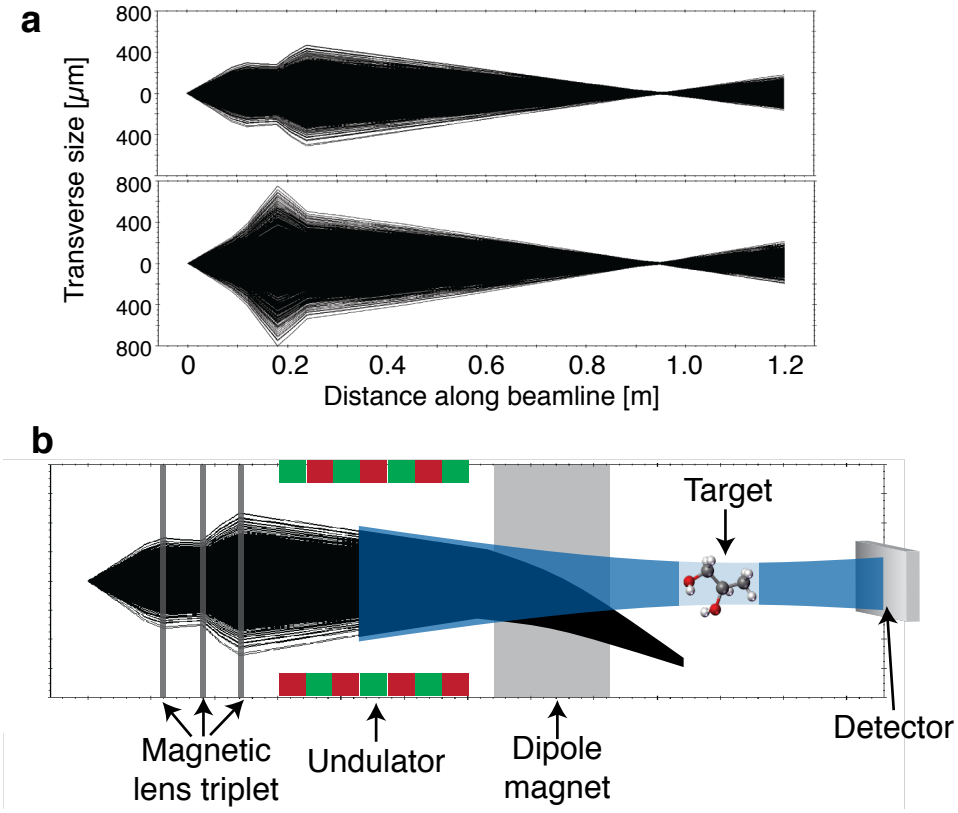

Figure 7.2. | **Simulation of electron beam focusing and schematic setup. a)** shows a simulation of an electron beam with an energy of 220 MeV and negligible energy spread focused by a magnetic lens triplet (courtesy B. Zeitler). **b)** shows a schematic drawing of a potential application of such a beam.

Although the beam sizes are on the few tens of micrometers scale, this setup can cope with fluctuations in pointing and energy that are present in a laser-wakefield accelerator and does not require lossy X-ray optics.

The experiment described in this thesis can be used as a testbed for future developments which in the long-term future may culminate in a laboratory-sized X-ray free-electron laser (FEL). The radiation emitted by an FEL is coherent which leads to a brilliance that is more than six orders of magnitude larger than that of the incoherent sources described above. Typical dimensions of conventional X-ray FELs are on the kilometer-scale. However, the unique properties of laser-wakefield accelerated electron beams such as an ultrashort pulse duration (and a correspondingly high peak current) and a relatively low emittance have the potential to significantly decrease the dimensions of FELs to the university-laboratory scale. The FEL (saturation) length depends on the peak current density as $L_{\mathrm{sat}} \propto (I_{\mathrm{peak}})^{-1/3}$, where I_{peak} is the peak current (see chapter 4). The increased peak current in the LWFA scenario, along with a different choice of undulator parameters and a smaller electron beam energy lead to an FEL length that is one order of magnitude shorter than that of conventional FELs ($\sim$ 10 m instead of typically $\sim$ 100 m) [Gruener et al., 2007]. However, the FEL process sets extremely

high demands on the electron beam properties: Necessitating a bunch charge of several hundred pico-Coulombs and energy spreads on the sub one-per-cent level makes them a rather long-term development process. The required parameters for first proof-of-principle LWFA-driven FELs are currently being investigated.

In order for the FEL process to occur and the radiation to become coherent, the electron beam has satisfy the conditions [Schmüser et al., 2008]: (1) the electrons energy must have nearly the same energy, (2) the electron beam size and divergence must be similar, "matched", to that of the X-ray beam and (3) since the FEL is relatively long, the gain in radiation intensity must be large enough to overcome diffraction losses of the radiation. More specific, the normalized electron beam energy spread has to fulfill the condition [Schmüser et al., 2008]

$$\frac{\sigma_\gamma}{\gamma} < 0.5\rho, \tag{7.1}$$

where ρ is the Pierce parameter which is a central parameter in the FEL theory. It is defined as

$$\rho = \frac{1}{2\gamma}\left[\frac{I_{\mathrm{peak}}}{I_A}\left(\frac{A_u\lambda_u}{2\pi\sigma_x}\right)^2\right]^{1/3}, \tag{7.2}$$

where γ is the relativistic factor, I_{peak}/I_A is the peak current of the electron bunch normalized to the Alfvén current $I_A = 17\,\mathrm{kA}$, λ_u the undulator period and σ_r the transverse electron beam size. The Bessel function factor is given by $A_u = K/\sqrt{2}\,[J_0(\xi) - J_1(\xi)]$ where J_i are Bessel functions which depend on the undulator K parameter through $\xi = K^2/(4 + 2K^2)$.

The properties of laser-accelerated electron beams that could potentially be achieved on a near-term timescale constitute bunches of 10 fs duration (FWHM), with a charge of 100 pC (corresponding to a peak current of 10 kA) at an energy of 300 MeV with 1% energy spread. Focused to a beam size of $\sigma_x = 25\,\mu\mathrm{m}$ into an undulator with a period of $\lambda_u = 10\,\mathrm{mm}$ and an on-axis magnetic field of $B_0 = 1\,\mathrm{T}$ ($K = 0.93$), this leads to

$$\rho = 0.8\%. \tag{7.3}$$

Under these conditions, such an electron beam would almost fulfill the required condition on the energy spread (eq. 7.1).

The gain length (e-folding length of the radiation power) can be estimated under consideration of the degrading effects of space charge, energy spread and emittance in 3D by [Xie, 2000]

$$L_g = L_{g0}(1 + \Lambda), \tag{7.4}$$

where

$$L_{g0} = \frac{\lambda_u}{4\pi\sqrt{3}\rho} \tag{7.5}$$

is the 1D gain length and the correction term Λ is determined by a fit of 3D numerical studies. Owing to the relatively large energy spread, $\Lambda = 4.8$ for the parameters given above. For such a large correction term, the treatment of the degrading effects as a perturbation is inaccurate and the results have to be regarded with great caution and

only as approximate estimates. Nevertheless, electron beams with such parameters are anticipated to drive demo FELs which might show first signatures of SASE amplification of a factor of approximately 3-5 from 2-4 gain lengths (Saturation in typical SASE FELs is achieved after 15 - 25 gain lengths). The determination of parameters for such a demo FEL requires full 3D FEL simulations (for example with the code described in [Reiche, 1999]).

In order to complete the discussion and show the potential of LWFA-driven FELs, an electron beam (100 pC, 300 MeV, 10fs) with an energy spread of 0.5% (which might become accessible through novel injection schemes, as discussed in chapter 2) is assumed. This drop in energy spread decreases the correction term to $\Lambda = 0.9$ which means that a treatment using the Ming-Xie perturbation methods gives a rough estimate of the resulting parameters.

The parameters given above lead to a gain length of $L_g = 11\,\mathrm{cm}$ and an approximate total length of the undulator (until saturation is reached) of $L_{\mathrm{sat}} \approx 20 \cdot L_g = 2.2\,\mathrm{m}$.

The radiation is emitted at a wavelength of 20 nm. Its power can be approximately determined by [Xie, 2000]

$$P_{\mathrm{sat}} \approx 1.6 \cdot \rho \frac{1}{(1+\Lambda)^2} \cdot P_{\mathrm{e-beam}}, \tag{7.6}$$

where $P_{\mathrm{e-beam}}$ is the power of the electron beam. For these electron beam properties: ($P_{\mathrm{e-beam}} = 30\,\mathrm{mJ}/10\,\mathrm{fs} = 3\,\mathrm{TW}$)

$$P_{\mathrm{sat}} \approx 10\,\mathrm{GW}, \tag{7.7}$$

or correspondingly 1×10^{13} photons per pulse. Considering the bandwidth of the radiation of $2 \cdot \rho$ and assuming a Gaussian TEM_{00} mode, this results in a peak brilliance of

$$\mathcal{B} \approx 7 \cdot 10^{29}\ \mathrm{photons/sec/mm^2/mrad^2/0.1\%b.w.} \tag{7.8}$$

As the wavelength becomes smaller, the requirements on the electron beam become more stringent. Especially for smaller wavelengths and in order to correctly include degrading effects numerical simulations are required to compute the FEL process. The comparison between this estimation and full 3D simulations for a similar and a hard X-ray case can be seen in table 7.1. In addition, the table shows a comparison between LWFA-driven FELs and machines based on conventional rf-technology. It can be seen that laser-driven FELs have the potential to reach peak brilliances similar to conventional facilities with intrinsically ultra-short pulse durations at a significantly smaller undulator (saturation) length.

The required laser parameters that can accelerate electron bunches with the properties described above can -in the bubble regime- be estimated by the following formulas (for a more detailed discussion of the formulas, refer to chapter 2). In the bubble regime, the accelerator "knobs" are mainly given by the power of the laser, its focus size and

	Estimation	TT-VUV FEL	TT XFEL	FLASH (fs)	LCLS
peak current	10 kA	50 kA	160 kA	1.3 kA	3.5 kA
norm. emitt.	1 μm	1 μm	1 μm	6 μm	0.5 μm
beam size	25 μm	30 μm	30 μm	170 μm	
energy	300 MeV	150 MeV	1.74 GeV	461.5 MeV	13.6 GeV
rel. energy spread	0.5%	0.5%	0.1%	0.04%	0.01 %
und. period	10 mm	5 mm	5 mm	27.3 mm	30 mm
wavelength	20 nm	32 nm	0.25 nm	30 nm	0.15 nm
Pierce par.	0.8%	1%	0.15%	0.2%	
sat. length	2.2 m	0.8 m	5 m	19 m	60 m
pulse duration	10 fs	4 fs	4 fs	55 fs	70 fs
sat. power	10 GW	2.0 GW	58 GW	0.8 GW	40 GW
photons/pulse	$1 \cdot 10^{13}$	$1.3 \cdot 10^{12}$	$3 \cdot 10^{11}$	$1.2 \cdot 10^{12}$	$2.3 \cdot 10^{12}$
brilliance[1]	$7 \cdot 10^{29}$	$6.3 \cdot 10^{28}$	$1.6 \cdot 10^{33}$	$6.7 \cdot 10^{28}$	$2 \cdot 10^{33}$

Table 7.1. | **Comparison of FEL parameters.** The FEL parameters estimated in main text for a 100 pC, 10 fs LWFA electron bunch are compared to results of simulations (with different electron beam parameters, denoted as TT-VUV FEL and TT XFEL) [Gruener et al., 2007]. The results of the 3D estimation have to be considered as rough estimates since the large degrading effects violate the treatment as a perturbation. Note that the simulations (TT-VUV FEL and TT XFEL) do not consider wall wakefields and are no start-to-end simulations. The parameters of LWFA-driven FELs are compared to conventional FELs. The brilliances are estimated assuming a Gaussian TEM_{00} mode.
[1]brilliance is given in units of [photons/s/mm^2/mrad^2/0.1%b.w.]

the plasma density. The electron energy depends on the laser power P and the plasma density n_p as [Lu et al., 2007]

$$\Delta E[\mathrm{GeV}] \simeq 1.7 \left(\frac{0.8}{\lambda_0[\mu\mathrm{m}]}\right)^{4/3} \left(\frac{10^{18}}{n_p[\mathrm{cm}^{-3}]}\right)^{2/3} \left(\frac{P[\mathrm{TW}]}{100}\right)^{1/3}, \tag{7.9}$$

where λ_0 is the laser wavelength. The accelerated charge can be estimated from [Lu et al., 2007]

$$N \simeq 2.5 \times 10^9 \, \frac{\lambda_0[\mu\mathrm{m}]}{0.8} \sqrt{\frac{P[\mathrm{TW}]}{100}}. \tag{7.10}$$

A small energy spread can be achieved by a triangular shaped injected electron bunch and a maximum charge of [Tzoufras et al., 2008]

$$Q[\mathrm{nC}] \simeq 7.5 \times 10^7 \sqrt{\frac{1}{n_0[\mathrm{cm}^{-3}]}} \; a_0^{3/2}, \tag{7.11}$$

where

$$a_0 \simeq \lambda\,[\mu\mathrm{m}] \cdot \sqrt{\frac{I_0\,[\mathrm{W/cm}^2]}{1.4 \times 10^{18}}} \tag{7.12}$$

is the normalized laser intensity (I_0 is the laser intensity in units of W/cm^2).

The plasma density and the laser power are related to each other through the following equations. For a given plasma density the laser group velocity and thus the plasma wave velocity is given by [Esarey and Leemans, 1999]

$$\gamma_p \simeq \left(\frac{\omega_p^2}{\omega^2} + 2\frac{c^2}{\omega^2 w_0^2} \right)^{-1/2}, \tag{7.13}$$

where ω is the laser frequency, ω_p the plasma frequency and w_0 the laser spot size. Electron self-injection into the bubble requires the bubble radius R (and thus the laser spot size) to have the dimension of [Kostyukov et al., 2009]

$$k_p R \gtrsim \sqrt{2}\,\gamma_p. \tag{7.14}$$

For an acceleration in the pure bubble regime and for the bubble to exhibit a spherical shape, the normalized laser intensity has to fulfill the condition of $a_0 \geqslant 4$ [Lu et al., 2007]. For each plasma density, the required focus size and the requirement on a_0 lead to a required laser power which in turn leads through equations (7.9 - 7.11) to the electron energy and the bunch charge.

In order to accelerate an electron bunch with a charge of $\simeq 100$ pC to an energy of 300 MeV, a plasma density of $1.4 \cdot 10^{19}\,\mathrm{cm}^{-3}$ and a 110 TW laser pulse focused to a beam spot of 22 µm are required. The charge scaling at optimum beam loading (leading to a small energy spread, equation 7.11) leads to a charge of 160 pC.

In order to achieve higher electron energies in the few-GeV range (to produce hard X-ray FEL radiation), the plasma density has to be lowered, which leads to a higher plasma wave velocity and thus leads to a larger laser focus size in order to get injection. This in turn requires a larger laser power to drive an accelerator in the bubble regime. The additional large bunch charges in the TT XFEL scenario (table 7.1) require few-petawatt laser systems. For example, a 3 PW system could accelerate an electron bunch of 2.5 nC (not considering optimal shapes of the injected bunches required to circumvent beam loading effects which leads to an increased energy spread, equation 7.10) to energies of 3 GeV. These values are in rough agreement with recent particle-in-cell (PIC) simulations [Lu et al., 2007; Martins et al., 2010].

Since first commercial petawatt laser systems are expected to be developed within the next few years, this is rather a more mid-term research goal. Novel schemes are currently being explored in which the electron injection is separated from the acceleration mechanism. This could lead to the injection of high quality electrons that can subsequently be accelerated in a quasi-linear regime by more modest laser pulse powers than those required by the bubble regime.

Advances in laser-wakefield acceleration, beam transport and undulator design will lead to a new generation of compact lightsources, based on the results presented in this thesis. In the short- to mid-term future, we expect this approach to spawn laboratory-sized ultrafast hard-X-ray undulator sources. In the long term, these developments may culminate in the development of compact ultra-brilliant X-ray free-electron lasers.

A. ADDITIONAL DERIVATIONS: LWFA THEORY

A.1. Ponderomotive Force

The fields of a tightly focused, ultrashort laser pulse vary radially as well as longitudinally. An electron placed in such a field experiences a non-linear transverse acceleration since the electric field $\vec{E}$ varies with the radius. Furthermore, the electron is accelerated in the direction of the propagation of the laser pulse due to the $\vec{v}\times\vec{B}$ term in the Lorentz force equation. This acceleration is at a phase of π with the $\vec{E}$ field which means that when $\vec{E}=0$ and the electron has the maximum velocity, that the $\vec{B}$-field and therefore the longitudinal acceleration is maximal. In order to quantify these forces which both are included in the ponderomotive force, we solve the equation of motion for an electron in electro-magnetically wave with a spatially- and temporally-varying field amplitude $\vec{E}_0(\vec{r},t)$. This can be done using the Lorentz force equation

$$m\frac{\mathrm{d}\vec{v}}{\mathrm{d}t} = -e\left[\vec{E}(\vec{r},t)+\vec{v}\times\vec{B}(\vec{r},t)\right] \tag{A.1}$$

For a light field that is changing in time and space, this equation can be solved by: (1) considering the first order term (neglect the $\vec{v}\times\vec{B}$ -part) at an initial position $\vec{r}_0$ and then (2) determine the electric field and velocity at a slightly different position $\vec{r}_0+\delta\vec{r}$. For an electric field of the form $\vec{E}=\vec{E}(\vec{r})\cos(\omega t)$, the solutions of the first order equation are (numbers in superscript indicate order):

$$m\frac{\mathrm{d}\vec{v}^{(1)}}{\mathrm{d}t} = -e\vec{E}(\vec{r}_0) \tag{A.2}$$

$$\vec{v}^{(1)} = -\frac{e}{m\omega}\vec{E}(\vec{r}_0)\sin(\omega t) = \frac{\mathrm{d}\vec{r}^{(1)}}{\mathrm{d}t} \tag{A.3}$$

$$\delta\vec{r}^{(1)} = \frac{e}{m\omega^2}\vec{E}(\vec{r}_0)\cos(\omega t) \tag{A.4}$$

In order to calculate the second-order equation of motion we need the Taylor expansion of the electric field around $\vec{r}_0$:

$$\vec{E}(\vec{r}) = \vec{E}(\vec{r}_0) + (\delta\vec{r}^{(1)}\cdot\vec{\nabla})\vec{E}|_{r=r_0} + ...$$

and the second order $\vec{v}^{(1)}\times\vec{B}^{(1)}$ term, where $\vec{B}^{(1)}$ is given by Maxwells equation ($\vec{\nabla}\times\vec{E} = -\frac{\mathrm{d}\vec{B}}{\mathrm{d}t}$):

$$\vec{B}^{(1)} = -\frac{1}{\omega}\vec{\nabla}\times\vec{E}(\vec{r})\sin(\omega t). \tag{A.5}$$

The second-order equation of motion reads:

$$m\frac{\mathrm{d}\vec{v}^{(2)}}{\mathrm{d}t} = -e\left[(\delta\vec{r}^{(1)}\cdot\vec{\nabla})\vec{E}|_{r=r_0} + \vec{v}^{(1)}\times\vec{B}^{(1)}\right] \tag{A.6}$$

with equations (A.3), (A.4) and (A.5) and averaging over one oscillation period, this becomes:

$$m\left\langle\frac{\mathrm{d}\vec{v}^{(2)}}{\mathrm{d}t}\right\rangle = -\frac{e^2}{m\omega^2}\frac{1}{2}\left[(\vec{E}(\vec{r})\cdot\vec{\nabla})\vec{E}(\vec{r}) + \vec{E}(\vec{r})\times(\vec{\nabla}\times\vec{E}(\vec{r}))\right] \tag{A.7}$$

Rewriting the second term by using the vector identity $[\vec{a}\times(\vec{b}\times\vec{c}) = \vec{b}\cdot(\vec{a}\cdot\vec{c}) - \vec{c}\cdot(\vec{a}\cdot\vec{b})]$ cancels the $(\vec{E}_0\cdot\vec{\nabla})\vec{E}_0$ and the effective non-linear ponderomotive force reads:

$$\vec{F}_{\mathrm{NL}} = -\frac{1}{4}\frac{e^2}{m\omega^2}\vec{\nabla}E(r)^2. \tag{A.8}$$

A.1.1. Dispersion Relation

Derivation after [Goldston and Rutherford, 1998]
Start from relevant Maxwell equation:

$$\vec{\nabla}\times\vec{E} = -\frac{\partial\vec{B}}{\partial t} \tag{A.9}$$

$$\vec{\nabla}\times\vec{B} = \mu_0\vec{j} + \frac{1}{c^2}\frac{\partial\vec{E}}{\partial t} \tag{A.10}$$

just consider plane waves:

$$\vec{E} = \vec{E}_0\mathrm{e}^{\mathrm{i}(\vec{k}\vec{r}-\omega t)}$$

$$\vec{B} = \vec{B}_0\mathrm{e}^{\mathrm{i}(\vec{k}\vec{r}-\omega t)}$$

make use of $\vec{\nabla}\times\vec{E} = \mathrm{i}\vec{k}\times\vec{E}$:

$$\mathrm{i}\vec{k}\times\vec{E} = \mathrm{i}\omega\vec{B} \tag{A.11}$$

$$\mathrm{i}\vec{k}\times\vec{B} = \mu_0\vec{j} + \mathrm{i}\frac{\omega}{c^2}\vec{E} \tag{A.12}$$

$k\times$eqn(A.11), use vector identity $A\times(B\times C) = (A\cdot C)B - (A\cdot B)C$ and insert eqn(A.12) into eqn(A.11)

$$k^2\vec{E} - \vec{k}\cdot(\vec{k}\cdot\vec{E}) = \frac{\omega^2}{c^2}\left(\frac{\vec{j}}{\mathrm{i}\epsilon_0\omega} + \vec{E}\right) \tag{A.13}$$

for e-m waves $\vec{k}\perp\vec{E}$
also: for high frequencies, the ions stay stationary which means that the current results

just from the electron motion: $\vec{j} = -n_e e \vec{v}_e$ and from first order equations of motion which can be derived with the help of the Lorentz force: $\vec{F} = q\left(\vec{E} + \vec{v} \times \vec{B}\right)$

$$m_e \frac{\mathrm{d}\vec{v}}{\mathrm{d}t} = -e\vec{E} \tag{A.14}$$

the current dependence on the electric field (for a plane wave) can be calculated as:

$$\vec{j} = -n_e e \vec{v} = \frac{n_e e^2}{m_e} \frac{1}{\mathrm{i}\omega} \vec{E}$$

using this in (A.13), gives:

$$(c^2 k^2 - \omega^2)\vec{E} = -\frac{n_e e^2}{m_e \epsilon_0} \vec{E} \tag{A.15}$$

where the expression for $\omega_{p,e}^2$ is recognizable on the on the right-hand side of the equation. This gives the dispersion relation for electromagnetic waves propagating in a plasma: (wave with high frequency in an unmagnetized plasma)

$$\omega^2 = \omega_p^2 + c^2 k^2 \tag{A.16}$$

Light frequencies below the plasma frequency can't propagate in the plasma but are reflected or attenuated, because the plasma electrons shield fields which oscillate at a frequency below ω_p. Since the plasma frequency depends on the electron density, a critical density for $\omega = \omega_p$ can be defined as:

$$n_\mathrm{c} = \frac{m_e \epsilon_0 \omega^2}{e^2}$$

For densities above n_c incident light waves are reflected from the plasma. Furthermore, from equation (A.16) can be seen that the wave number k is imaginary and a wave decays as

$$\exp\left(-x\sqrt{\frac{\omega_p^2 - \omega^2}{c}}\right)$$

The skin depth

$$\delta = |k|^{-1} = \frac{c}{(\omega_p^2 - \omega^2)^{1/2}}$$

is defined as the distance over which the field is attenuated by a factor 1/e.
The non-relativisitic index of refraction can also be deduced from the dispersion relation equation (A.16):

$$\eta = \frac{c}{v_\mathrm{ph}} = \sqrt{1 - \left(\frac{\omega_p}{\omega}\right)^2}$$

where $v_\mathrm{ph} = \omega/|\vec{k}|$ is the phase velocity of the light wave.

A.1.2. Linear Plasma Waves

A linear 3D plasma wave excited by a non-evolving laser pulse can be described by the cold fluid equations, i.e. the continuity equation, the moment equation and Poisson's equation:

$$\frac{\partial}{\partial t}\delta n + n_0 \vec{\nabla}\cdot\vec{u} \simeq 0 \tag{A.17}$$

$$\frac{\partial \vec{u}}{\partial t} \simeq \nabla\phi - \nabla a_0^2/2 \tag{A.18}$$

$$\nabla^2\phi \simeq k_p^2 \frac{\delta n}{n_0} \tag{A.19}$$

Combining these equations results in equations describing a linear plasma wave and wakefield for an initially uniform plasma:

$$\left(\frac{\partial^2}{\partial t^2} + \omega_p^2\right)\frac{\delta n}{n_0} = c^2\nabla^2\frac{a_0^2}{2} \tag{A.20}$$

$$\left(\frac{\partial^2}{\partial t^2} + \omega_p^2\right)\phi = \omega_p^2\frac{a_0^2}{2} \tag{A.21}$$

where δn is the perturbation in electron density and a_0 is the normalized intensity of the driver-laser pulse.

A solution of equations (A.20) and (A.21) for the density perturbation and the associated electric field are given by

$$\frac{\delta n}{n_0} = \frac{c^2}{\omega_p}\int_0^t \mathrm{d}t' \sin[\omega_p(t-t')]\nabla^2\frac{a^2(\vec{r},t')}{2} \tag{A.22}$$

$$\vec{E}(\vec{r},t) = -\frac{m_e c^2\omega_p}{e}\int_0^t \mathrm{d}t' \sin[\omega_p(t-t')]\vec{\nabla}\frac{a^2(\vec{r},t')}{2} \tag{A.23}$$

more specifically, the solutions for a Gaussian laser pulse $a^2 = a_0^2\exp(-\frac{2r^2}{r_s^2})\sin^2(\frac{\pi\xi}{L})$, where $\xi = z - ct$ are the co-ordinates of a frame co-moving with the laser pulse are:

$$\frac{\delta n}{n_0} = -\frac{\pi}{4}a_0^2\left[1 + \frac{8}{k_p^2 r_s^2}\left(1 - \frac{2r^2}{r_s^2}\right)\right]\exp\left(-\frac{2r^2}{r_s^2}\right)\sin(k_p\xi) \tag{A.24}$$

$$\frac{E_z}{E_0} = -\frac{\pi}{4}a_0^2\exp\left(-\frac{2r^2}{r_s^2}\right)\cos(k_p\xi) \tag{A.25}$$

A.1.3. Nonlinear Plasma Waves

nonlinear momentum equations
transformation into the comoving frame
simplification for $\gamma_g \gg 1$

Symbol	Description
ϕ	electrostatic potential
n	plasma density
$a(z)$	normalized laser pulse intensity with an amplitude a_0
$\beta_z = v_z/c$	normalized longitudinal plasma fluid velocity
$\beta_\perp = v_\perp/c$	normalized transverse plasma fluid velocity
$\gamma = 1/(1-\vec{\beta}^2)$	relativistic factor associated with the electrons[1]
$\gamma_z = 1/(1-\beta_z^2)$	longitudinal part of the relativistic factor
$\gamma_\perp = (1+a^2)$	transverse part of the relativistic factor
β_p	normalized velocity of the plasma wave[2]
$p = \gamma\beta$	electron fluid momentum, normalized to $m_0 c$

Table A.1. List of Symbols: Appendix of the LWFA chapter

The cold *relativistic* fluid equations can be written as [Sprangle et al., 1990]:
longitudinal electron fluid momentum equation

$$\frac{d(\gamma\beta_z)}{dt} = c\frac{\partial\phi}{\partial z} - \frac{c}{2\gamma}\frac{\partial a^2}{\partial z} \tag{A.26}$$

continuity equation

$$\frac{\partial n}{\partial t} + c\frac{\partial(n\beta_z)}{\partial z} = 0 \tag{A.27}$$

The expressions can be greatly simplified by transforming into a co-moving frame of reference (a frame moving the group velocity of the laser $v_g = v_z$) with the coordinates

$$\xi = z - v_g t \quad \text{and} \quad \tau = t. \tag{A.28}$$

The spatial and temporal derivatives become

$$\frac{\partial}{\partial t} = \frac{\partial}{\partial \tau} - v_g\frac{\partial}{\partial \xi} \quad \text{and} \quad \frac{\partial}{\partial z} = \frac{\partial}{\partial \xi} \tag{A.29}$$

In order to transform the momentum equation into this frame of reference, the total differential

$$\frac{df}{dx} = \frac{\partial f}{\partial x} + \sum_j \left(\frac{\partial f}{\partial y_j}\frac{dy_j}{dx}\right) \tag{A.30}$$

of the left-hand side of equation (A.26) reads

$$\frac{d}{dt}(\gamma\beta_z) = \frac{\partial(\gamma\beta_z)}{\partial t} + \frac{\partial(\gamma\beta_z)}{\partial z}\cdot\frac{dz}{dt}, \tag{A.31}$$

[1] $\gamma = \gamma_\perp\gamma_z = \left(1-(\beta_\perp^2+\beta_z^2)\right)^{-1/2}$

[2] for lasers as driver: $\beta_p \simeq \beta_g$

where $dz/dt = c\beta_z$. The dependence of the relativistic factor on the laser intensity:

$$\gamma^2 = \frac{1}{1-(\beta_\perp^2+\beta_z^2)} = \frac{1+a^2}{1-\beta_z^2} \tag{A.32}$$

$\gamma_\perp = 1 + a^2$ leads to

$$\frac{\partial a^2}{\partial z} = \frac{\partial}{\partial z}\Big[\gamma^2 - \gamma^2\beta_z^2 - 1\Big] = 2\gamma\left(\frac{\partial\gamma}{\partial z} - \beta_z^2\frac{\partial\gamma}{\partial z} - \gamma\beta_z\frac{\partial\beta_z}{\partial z}\right). \tag{A.33}$$

Transforming equation (A.31) using equation (A.29) gives

$$\frac{d}{dt}(\gamma\beta_z) = \frac{\partial(\gamma\beta_z)}{\partial\tau} - c\beta_g\frac{\partial(\gamma\beta_z)}{\partial\xi} + c\beta_z\frac{\partial(\gamma\beta_z)}{\partial\xi}. \tag{A.34}$$

With equation (A.34) and equation (A.31), the **fluid momentum equation** equation (A.26) reads

$$\frac{1}{c}\frac{\partial(\gamma\beta_z)}{\partial\tau} = \frac{\partial}{\partial\xi}\Big[\phi - \gamma(1-\beta_g\beta_z)\Big]. \tag{A.35}$$

In a similar way, the **continuity equation** equation (A.27)

$$\frac{\partial}{\partial\xi}\Big[n(\beta_g-\beta_z)\Big] = \frac{1}{c}\frac{\partial n}{\partial\tau}, \tag{A.36}$$

and the **Poisson's equation**

$$\frac{\partial^2\phi}{\partial\xi^2} = k_p^2\left(\frac{n}{n_0} - 1\right) \tag{A.37}$$

can be transformed.

In order to integrate the equations, the quasi-static approximation (QSA) has to be made which means that the plasma fluid quantities are functions only of the co-moving variable ξ (neglecting the $\partial/\partial\tau$ derivatives). Taking into account the boundary conditions for the region $\xi \geqslant 0$ (upstream of the laser pulse), $\vec{a} = 0$, $n = n_0$, $\beta_z = 0$ and $\gamma = 1$, gives the integration constants $C_1 = -1$ for equation (A.35) and $C_2 = n_0\beta_g$ for (A.36) which leads to the integrated expression:

$$\gamma(1-\beta_g\beta_z) - \phi = 1 \tag{A.38}$$

$$n(\beta_g - \beta_z) = n_0\beta_g \tag{A.39}$$

Using equation (A.39), the Poisson's equation (eq. A.37) can be written as

$$\frac{\partial^2\phi}{\partial\xi^2} = k_p^2\left(\frac{\beta_z}{\beta_g-\beta_z}\right) \tag{A.40}$$

and with the explicit expression for β_z reads [Esarey et al., 2009]

$$\frac{\partial^2\phi}{\partial\xi^2} = k_p^2\gamma_g^2\left[\beta_g\left(1 - \frac{1+a_0^2}{\gamma_g^2(1+\phi)^2}\right)^{-1/2} - 1\right]. \tag{A.41}$$

These expressions can be further simplified in the case of $\gamma_g \gg 1$. Equation (A.40) becomes

$$\frac{\partial^2\phi}{\partial\xi^2} \simeq k_p^2 \left(\frac{\beta_z}{1-\beta_z}\right) \tag{A.42}$$

and with the help of equation (A.32), the square of equation (A.38) can be written as

$$\frac{1+a_0^2}{(1+\phi)^2} \simeq \frac{1+\beta_z}{1-\beta_z}. \tag{A.43}$$

Since

$$\frac{\beta_z}{1-\beta_z} = \frac{1}{2}\left(\frac{1+\beta_z}{1-\beta_z} - 1\right), \tag{A.44}$$

the **Poisson's equation** equation (A.40) can finally be simplified to

$$\frac{\partial^2\phi}{\partial\xi^2} = \frac{k_p^2}{2}\left(\frac{1+a_0^2}{(1+\phi)^2} - 1\right) \tag{A.45}$$

Electron Trapping and Acceleration

To get the Hamiltonian of a test electron in phase-space, we start with the fluid momentum equation

$$H(\gamma_z, \xi) = \gamma(1-\beta_p\beta_z) - \phi(\xi) = \gamma - \beta_p p_z - \phi(\xi). \tag{A.46}$$

Using equation (A.32)

$$\beta_z^2 = 1 - \frac{1+a^2}{\gamma^2} \tag{A.47}$$

and from $p_z = \gamma\beta_z$, we get

$$\gamma^2 = p_z^2 + 1 + a^2, \tag{A.48}$$

which substituted into equation (A.46) leads to

$$H(p_z, \xi) = \sqrt{p_z^2 + 1 + a^2} - \beta_p p_z - \phi(\xi) \tag{A.49}$$

A.2. Electron Trapping in the Bubble Regime

The motion of electrons under the influence of the fields of the bubble in the co-moving frame can be described by the Hamiltonian [Kostyukov et al., 2004], neglecting the laser fields, since trapping happens at the back side of the bubble.

$$H = \sqrt{1 + (\vec{p} + \vec{A})^2 + a^2)} - \beta_p p_z - \phi, \tag{A.50}$$

from which the equations of motion can be derived

$$\frac{\mathrm{d}p_z}{\mathrm{d}t} = -\beta_z\frac{\partial A_z}{\partial\xi} - \beta_y\frac{\partial A_y}{\partial\xi} + \frac{\partial\phi}{\partial\xi}, \tag{A.51}$$

$$\frac{\mathrm{d}p_y}{\mathrm{d}t} = -\beta_z \frac{\partial A_z}{\partial y} - \beta_y \frac{\partial A_y}{\partial y} + \frac{\partial \phi}{\partial y}, \tag{A.52}$$

$$\frac{\mathrm{d}\xi}{\mathrm{d}t} = \frac{p_z}{\gamma} - \beta_p = \beta_z - \beta_p, \tag{A.53}$$

$$\frac{\mathrm{d}y}{\mathrm{d}t} = \frac{p_y}{\gamma} = \beta_y, \tag{A.54}$$

with $\gamma = (1+p_z^2+p_y^2)^{1/2}$. The electric potential of the bubble is determined by the model of a sphere with a uniform ion background and the fields in cylindrical coordinates are given by (2.57) & (2.58). The bubble with a radius R is surrounded by an electron sheath, that screens its ion field and the resulting fields are given by [Kostyukov et al., 2009]

$$E_z = f(r) k_p \frac{\xi}{2} E_0 \tag{A.55}$$

$$E_y = B_z = f(r) \frac{y}{4}, \tag{A.56}$$

where $f(r) = [\tanh(R/d - r/d) - 1]/2$ describes the electron sheath of the width d. Since (A.51) & (A.52) are the Lorentz forces and the equations of motion (lengths normalized to k_p and fields to E_0) can be written as

$$\frac{\mathrm{d}p_z}{\mathrm{d}t} = -f(r)\frac{\xi}{2} + f(r)\frac{p_y}{\gamma}\frac{y}{4}, \tag{A.57}$$

$$\frac{\mathrm{d}p_y}{\mathrm{d}t} = -f(r)\left(1 + \frac{p_z}{\gamma}\right)\frac{y}{4}, \tag{A.58}$$

$$\frac{\mathrm{d}\xi}{\mathrm{d}t} = \frac{p_z}{\gamma} - \beta_p, \qquad \frac{\mathrm{d}y}{\mathrm{d}t} = \frac{p_y}{\gamma}, \tag{A.59}$$

This set of differential equations can be numerically solved for an electron located on the radius of the bubble, initially at rest: (at $t = 0$): $\vec{p} = 0$, $y = R$ and $\xi = 0$. p_z depends on the initial radius: for $y < R$, the electron gains negative momentum due to the interaction with the "front half" of the bubble fields.

B. ADDITIONAL DERIVATIONS: UNDULATOR THEORY

B.1. Propagation of Single-Electron Brilliance: Free Drift

The propagation of the brilliance through a free drift space of length ℓ can be calculated by

$$\mathcal{B}(\vec{x},\vec{\varphi},s+\ell)=\mathcal{B}(\vec{x}-\ell\cdot\vec{\varphi},\vec{\varphi},s). \tag{B.1}$$

Starting from $s=0$, the brilliance at position ℓ can be written as

$$\mathcal{B}(\vec{x},\vec{\varphi},\ell)=\mathcal{B}|_0\exp\left(-\frac{(x-\ell\varphi)^2}{2\sigma_r^2}-\frac{\varphi^2}{2\sigma_{r'}^2}\right). \tag{B.2}$$

The spatial flux density at the position ℓ can be calculated from the brilliance as follows:

$$\frac{\mathrm{d}\Phi}{\mathrm{d}x}=\int\mathcal{B}(\vec{x},\vec{\varphi},\ell)\mathrm{d}\varphi, \tag{B.3}$$

which leads to

$$\frac{\mathrm{d}\Phi}{\mathrm{d}x}=\mathcal{B}|_0\exp\!\left(-\frac{x^2}{2\sigma_r^2}\right)\int\exp\left[-\varphi^2\left(\frac{\ell^2\sigma_{r'}^2+\sigma_r^2}{2\sigma_r^2\sigma_{r'}^2}\right)+\varphi\frac{\ell x}{\sigma_r^2}\right]\mathrm{d}\varphi. \tag{B.4}$$

Using

$$\int_{-\infty}^{\infty}\mathrm{e}^{-ax^2-2bx}\,\mathrm{d}x=\sqrt{\frac{\pi}{a}}\;e^{(b^2/a)} \tag{B.5}$$

and by doing this for both dimensions (radial symmetry) leads to

$$\frac{\mathrm{d}\Phi}{\mathrm{d}\mathcal{S}}=\frac{2\pi\sigma_r^2\sigma_{r'}^2}{\sigma_r^2+\ell^2\sigma_{r'}^2}\mathcal{B}|_0\exp\!\left(-\frac{x^2+y^2}{2(\sigma_r^2+\ell^2\sigma_{r'}^2)}\right) \tag{B.6}$$

since

$$\mathcal{B}|_0=\frac{\Phi}{(2\pi\sigma_r\sigma_{r'})^2} \tag{B.7}$$

the spatial flux density at the longitudinal position ℓ can be written as

$$\frac{\mathrm{d}\Phi}{\mathrm{d}\mathcal{S}}=\frac{\Phi}{2\pi(\sigma_r^2+\ell^2\sigma_{r'}^2)}\exp\!\left(-\frac{x^2+y^2}{2(\sigma_r^2+\ell^2\sigma_{r'}^2)}\right). \tag{B.8}$$

By integrating this expression over the spatial coordinates, it can be seen that the total flux is conserved.

B.2. Equality of Propagation of Convoluted Beam and the Convolution after Propagation

The beam size after propagation of the radiation from a thick electron beam can be written as

$$\Sigma_r(\ell)^2 = \Sigma_r(0)^2 + \Sigma_{r'}^2\ell^2 = \sigma_{e,0}^2 + \sigma_{r,0}^2 + \ell^2(\sigma_{r'}^2 + \sigma_{e'}^2), \tag{B.9}$$

which is exactly the beam size computed by propagating each distribution separately to the position ℓ and then do the convolution (which corresponds to the quadratic sum of the standard deviations)

$$\Sigma_r(\ell)^2 = \sigma_r^2(\ell) + \sigma_e^2(\ell) = \sigma_{r,0}^2 + \ell^2\sigma_{r'}^2 + \sigma_{e,0}^2 + \ell^2\sigma_{e'}^2 = \sigma_{e,0}^2 + \sigma_{r,0}^2 + \ell^2(\sigma_{r'}^2 + \sigma_{e'}^2) \tag{B.10}$$

Bibliography

A. I. Akhiezer and R. V. Polovin. Theory of wave motion of an electron plasma. *SOVIET PHYSICS JETP-USSR*, 3(5):696–705, 1956. ISSN 0038-5646.

C. Amsler and *et al.* Review of particle physics. *Physics Letters B*, 667 (1-5):1 – 6, 2008. ISSN 0370-2693. doi: DOI:10.1016/j.physletb.2008.07.018. URL http://www.sciencedirect.com/science/article/B6TVN-4T4VKPY-2/2/2fe3ceb40a4d144f48321db99160ecb2. Review of Particle Physics.

T. Auguste, P. Monot, G. Mainfray, C. Manus, S. Gary, and M. Louis-Jacquet. Focusing behavior of multiterawatt laser pulse in a h2 gas jet. *Optics Communications*, 105(5-6):292 – 296, 1994. ISSN 0030-4018. doi: DOI:10.1016/0030-4018(94)90398-0. URL http://www.sciencedirect.com/science/article/B6TVF-46MDG39-43/2/84227e41b9129bcc9a21106842253823.

P. Beaud, S. L. Johnson, A. Streun, R. Abela, D. Abramsohn, D. Grolimund, F. Krasniqi, T. Schmidt, V. Schlott, and G. Ingold. Spatiotemporal stability of a femtosecond hard–x-ray undulator source studied by control of coherent optical phonons. *Phys. Rev. Lett.*, 99(17):174801, Oct 2007. doi: 10.1103/PhysRevLett.99.174801.

S. Becker, M. Bussmann, S. Raith, M. Fuchs, R. Weingartner, P. Kunz, W. Lauth, U. Schramm, M. El Ghazaly, F. Grüner, H. Backe, and D. Habs. Characterization and tuning of ultrahigh gradient permanent magnet quadrupoles. *Phys. Rev. ST Accel. Beams*, 12(10):102801, Oct 2009. doi: 10.1103/PhysRevSTAB.12.102801.

A. V. Brantov, T. Z. Esirkepov, M. Kando, H. Kotaki, V. Y. Bychenkov, and S. V. Bulanov. Controlled electron injection into the wake wave using plasma density inhomogeneity. *Physics of Plasmas*, 15(7):073111, 2008. doi: 10.1063/1.2956989. URL http://link.aip.org/link/?PHP/15/073111/1.

A. Buck, K. Zeil, A. Popp, K. Schmid, A. Jochmann, S. D. Kraft, B. Hidding, T. Kudyakov, C. M. S. Sears, L. Veisz, S. Karsch, J. Pawelke, R. Sauerbrey, T. Cowan, F. Krausz, and U. Schramm. Absolute charge calibration of scintillating screens for relativistic electron detection. *Review of Scientific Instruments*, 81(3):033301, 2010. doi: 10.1063/1.3310275. URL http://link.aip.org/link/?RSI/81/033301/1.

M. J. Buckley. Fast computation of a discretized thin-plate smoothing spline for image data, 1994.

S. Bulanov, N. Naumova, F. Pegoraro, and J. Sakai. Particle injection into the wave acceleration phase due to nonlinear wake wave breaking. *Phys. Rev. E*, 58(5):R5257–R5260, Nov 1998. doi: 10.1103/PhysRevE.58.R5257.

S. V. Bulanov, F. Pegoraro, A. M. Pukhov, and A. S. Sakharov. Transverse-wake wave breaking. *Phys. Rev. Lett.*, 78(22):4205–4208, Jun 1997. doi: 10.1103/PhysRevLett.78.4205.

A. Butler, D. J. Spence, and S. M. Hooker. Guiding of high-intensity laser pulses with a hydrogen-filled capillary discharge waveguide. *Phys. Rev. Lett.*, 89(18):185003, Oct 2002. doi: 10.1103/PhysRevLett.89.185003.

F. F. Chen. *Introduction to plasma physics and controlled fusion. Volume 1, Plasma physics*. Springer, 1984.

O. Chubar and P. Elleaume. Accurate and efficient computation of synchrotron radiation in the near field region. *Proceedings of the EPAC98 Conference*, pages 1177–1179, 1998.

J. A. Clarke. *The Science and Technology of Undulators and Wigglers*. Oxford University Press, 2004.

C. E. Clayton, K. A. Marsh, A. Dyson, M. Everett, A. Lal, W. P. Leemans, R. Williams, and C. Joshi. Ultrahigh-gradient acceleration of injected electrons by laser-excited relativistic electron plasma waves. *Phys. Rev. Lett.*, 70(1):37–40, Jan 1993. doi: 10.1103/PhysRevLett.70.37.

CXC. Chandra x-ray center. http://cxc.harvard.edu/proposer/POG/html/chap9.html, 2009.

CXRO. The center for x-ray optics. http://www-cxro.lbl.gov/.

J. M. Dawson. Particle simulation of plasmas. *Rev. Mod. Phys.*, 55(2):403–447, Apr 1983. doi: 10.1103/RevModPhys.55.403.

J. M. Dawson. Plasma particle accelerators. *Scientific American*, 260:54, 1989.

A. D. Debus, M. Bussmann, U. Schramm, R. Sauerbrey, C. D. Murphy, Z. Major, R. Hörlein, L. Veisz, K. Schmid, J. Schreiber, K. Witte, S. P. Jamison, J. G. Gallacher, D. A. Jaroszynski, M. C. Kaluza, B. Hidding, S. Kiselev, R. Heathcote, P. S. Foster, D. Neely, E. J. Divall, C. J. Hooker, J. M. Smith, K. Ertel, A. J. Langley, P. Norreys, and J. L. Collier. Electron bunch length measurements from laser-accelerated electrons using single-shot thz time-domain interferometry. *Phys. Rev. Lett.*, 104(8):084802, Feb 2010. doi: 10.1103/PhysRevLett.104.084802.

C. D. Decker and W. B. Mori. Group velocity of large amplitude electromagnetic waves in a plasma. *Phys. Rev. Lett.*, 72(4):490–493, Jan 1994. doi: 10.1103/PhysRevLett.72.490.

R. J. Dejus and M. S. del Rio. Xop: A graphical user interface for spectral calculations and x-ray optics utilities. *The 9th National conference on synchrotron radiation instrumentation*, 67(9):3356–3356, 1996. doi: 10.1063/1.1147376. URL `http://link.aip.org/link/?RSI/67/3356/2`.

T. Eichner. Aufbau und charakterisierung eines undulators aus permanentmagneten. Master's thesis, Ludwig-Maximilians Universität München, 2007.

T. Eichner, F. Grüner, S. Becker, M. Fuchs, D. Habs, R. Weingartner, U. Schramm, H. Backe, P. Kunz, and W. Lauth. Miniature magnetic devices for laser-based, table-top free-electron lasers. *Phys. Rev. ST Accel. Beams*, 10(8):082401, Aug 2007. doi: 10.1103/PhysRevSTAB.10.082401.

F. R. Elder, A. M. Gurewitsch, R. V. Langmuir, and H. C. Pollock. Radiation from Electrons in a Synchrotron. *Physical Review*, 71:829–830, June 1947. doi: 10.1103/PhysRev.71.829.5.

P. Elleaume, C. Fortgang, C. Penel, and E. Tarazona. Measuring Beam Sizes and Ultra-Small Electron Emittances Using an X-ray Pinhole Camera. *Journal of Synchrotron Radiation*, 2(5):209–214, Sep 1995. doi: 10.1107/S0909049595008685. URL `http://dx.doi.org/10.1107/S0909049595008685`.

P. Emma. First lasing of the lcls x-ray fel at 1.5. Particle Accelerator Conference, Vancouver, 2009.

E. Esarey and W. P. Leemans. Nonparaxial propagation of ultrashort laser pulses in plasma channels. *Phys. Rev. E*, 59(1):1082–1095, Jan 1999. doi: 10.1103/PhysRevE.59.1082.

E. Esarey and M. Pilloff. Trapping and acceleration in nonlinear plasma waves. *Physics of Plasmas*, 2(5):1432–1436, 05 1995. URL `http://link.aip.org/link/?PHP/2/1432/1`.

E. Esarey, P. Sprangle, J. Krall, and A. Ting. Overview of plasma-based accelerator concepts. *Plasma Science, IEEE Transactions on*, 24(2):252–288, Apr 1996. ISSN 0093-3813. doi: 10.1109/27.509991.

E. Esarey, R. F. Hubbard, W. P. Leemans, A. Ting, and P. Sprangle. Electron injection into plasma wakefields by colliding laser pulses. *Phys. Rev. Lett.*, 79(14):2682–2685, Oct 1997. doi: 10.1103/PhysRevLett.79.2682.

E. Esarey, C. B. Schroeder, B. A. Shadwick, J. S. Wurtele, and W. P. Leemans. Nonlinear theory of nonparaxial laser pulse propagation in plasma channels. *Phys. Rev. Lett.*, 84(14):3081–3084, Apr 2000. doi: 10.1103/PhysRevLett.84.3081.

E. Esarey, C. B. Schroeder, and W. P. Leemans. Physics of laser-driven plasma-based electron accelerators. *Reviews of Modern Physics*, 81(3), 08 2009. URL `http://link.aps.org/abstract/RMP/v81/p1229`.

J. Faure, Y. Glinec, A. Pukhov, S. Kiselev, S. Gordienko, E. Lefebvre, J. P. Rousseau, F. Burgy, and V. Malka. A laser-plasma accelerator producing monoenergetic electron beams. *Nature*, 431(7008):541–544, 09 2004. URL `http://dx.doi.org/10.1038/nature02963`.

J. Faure, C. Rechatin, A. Norlin, A. Lifschitz, Y. Glinec, and V. Malka. Controlled injection and acceleration of electrons in plasma wakefields by colliding laser pulses. *Nature*, 444(7120):737–739, 12 2006. URL `http://dx.doi.org/10.1038/nature05393`.

R. P. Feynman, R. B. Leighton, and M. Sands. *The Feynman Lectures on Physics*. Addison-Wesley Longman, 1970.

S. Fritzler, E. Lefebvre, V. Malka, F. Burgy, A. E. Dangor, K. Krushelnick, S. P. D. Mangles, Z. Najmudin, J.-P. Rousseau, and B. Walton. Emittance measurements of a laser-wakefield-accelerated electron beam. *Phys. Rev. Lett.*, 92(16):165006, Apr 2004. doi: 10.1103/PhysRevLett.92.165006.

M. Fuchs, R. Weingartner, A. Popp, Z. Major, S. Becker, J. Osterhoff, I. Cortrie, B. Zeitler, R. Horlein, G. D. Tsakiris, U. Schramm, T. P. Rowlands-Rees, S. M. Hooker, D. Habs, F. Krausz, S. Karsch, and F. Gruner. Laser-driven soft-x-ray undulator source. *Nat Phys*, 5(11):826–829, 11 2009. URL `http://dx.doi.org/10.1038/nphys1404`.

J. G. Gallacher, M. P. Anania, E. Brunetti, F. Budde, A. Debus, B. Ersfeld, K. Haupt, M. R. Islam, O. Jackel, S. Pfotenhauer, A. J. W. Reitsma, E. Rohwer, H.-P. Schlenvoigt, H. Schwoerer, R. P. Shanks, S. M. Wiggins, and D. A. Jaroszynski. A method of determining narrow energy spread electron beams from a laser plasma wakefield accelerator using undulator radiation. *Physics of Plasmas*, 16(9):093102, 2009. doi: 10.1063/1.3216549. URL `http://link.aip.org/link/?PHP/16/093102/1`.

C. G. R. Geddes, C. Toth, J. van Tilborg, E. Esarey, C. B. Schroeder, D. Bruhwiler, C. Nieter, J. Cary, and W. P. Leemans. High-quality electron beams from a laser wakefield accelerator using plasma-channel guiding. *Nature*, 431(7008):538–541, 09 2004. URL `http://dx.doi.org/10.1038/nature02900`.

C. G. R. Geddes, K. Nakamura, G. R. Plateau, C. Toth, E. Cormier-Michel, E. Esarey, C. B. Schroeder, J. R. Cary, and W. P. Leemans. Plasma-density-gradient injection of low absolute-momentum-spread electron bunches. *Physical Review Letters*, 100(21): 215004, 2008. doi: 10.1103/PhysRevLett.100.215004. URL `http://link.aps.org/abstract/PRL/v100/e215004`.

M. Geissler, J. Schreiber, and J. M. ter Vehn. Bubble acceleration of electrons with few-cycle laser pulses. *New Journal of Physics*, 8(9):186, 2006. URL `http://stacks.iop.org/1367-2630/8/i=9/a=186`.

P. Gibbon. *Short Pulse Laser Interactions with Matter: An Introduction*. World Scientific Publishing Company, 2005.

R. Goldston and P. Rutherford. *Introduction to Plasma Physics*. Taylor & Francis, 1995.

R. J. Goldston and P. H. Rutherford. *Plasmaphysik*. Vieweg+Teubner, 1998.

S. Gordienko and A. Pukhov. Scalings for ultrarelativistic laser plasmas and quasi-monoenergetic electrons. *Physics of Plasmas*, 12(4):043109, 2005. doi: 10.1063/1.1884126. URL `http://link.aip.org/link/?PHP/12/043109/1`.

GPT. Pulsar physics and the general particle tracer (gpt) code. http://www.pulsar.nl/gpt, 2009.

F. Gruener, S. Becker, U. Schramm, T. Eichner, M. Fuchs, R. Weingartner, D. Habs, J. Meyer-ter Vehn, M. Geissler, M. Ferrario, L. Serafini, B. van der Geer, H. Backe, W. Lauth, and S. Reiche. Design considerations for table-top, laser-based vuv and x-ray free electron lasers. *Applied Physics B: Lasers and Optics*, 86(3):p431 – 435, 2007. ISSN 09462171. URL `http://search.ebscohost.com/login.aspx?direct=true&db=aph&AN=24109225&loginpage=Login.asp&site=ehost-live`.

F. J. Grüner, C. B. Schroeder, A. R. Maier, S. Becker, and J. M. Mikhailova. Space-charge effects in ultrahigh current electron bunches generated by laser-plasma accelerators. *Phys. Rev. ST Accel. Beams*, 12(2):020701, Feb 2009. doi: 10.1103/PhysRevSTAB.12.020701.

K. Halbach. Design of permanent multipole magnets with oriented rare earth cobalt material. *Nuclear Instruments and Methods*, 169:1–10, Feb. 1980. doi: 10.1016/0029-554X(80)90094-4.

R. Hockney and J. Eastwood. *Computer simulation using particles*. Bristol: Hilger, 1988, 1988.

W. Horton and T. Tajima. Pump depletion in the plasma-beat-wave accelerator. *Phys. Rev. A*, 34(5):4110–4119, Nov 1986. doi: 10.1103/PhysRevA.34.4110.

Z. Huang and K.-J. Kim. Review of x-ray free-electron laser theory. *Phys. Rev. ST Accel. Beams*, 10(3):034801, Mar 2007. doi: 10.1103/PhysRevSTAB.10.034801.

P. I. Inc. Princeton instruments inc. direct detection direct detection of x-rays (30ev to 20kev) using detectors based on ccd technology. http://www.princetoninstruments.com.

J. Jackson. *Classical Electrodynamics Third Edition*. Wiley, 08 1998. ISBN 047130932X.

S. Kalmykov, S. A. Yi, V. Khudik, and G. Shvets. Electron self-injection and trapping into an evolving plasma bubble. *Phys. Rev. Lett.*, 103(13):135004, Sep 2009. doi: 10.1103/PhysRevLett.103.135004.

T. Katsouleas, S. Wilks, P. Chen, J. Dawson, and J. Su. Beam loading in plasma accelerators. *Particle Accelerators*, 22(1):81–99, 1987. ISSN 0031-2460.

S. Khan, K. Holldack, T. Kachel, R. Mitzner, and T. Quast. Femtosecond undulator radiation from sliced electron bunches. *Physical Review Letters*, 97(7):074801, 2006. doi: 10.1103/PhysRevLett.97.074801. URL `http://link.aps.org/abstract/PRL/v97/e074801`.

K.-J. Kim. Characteristics of synchrotron radiation. *PHYSICS OF PARTICLE ACCELERATORS*, 184:565–632, 1989. doi: 10.1063/1.38046. URL `http://link.aip.org/link/?APC/184/565/1`.

P. Kirkpatrick and A. V. Baez. Formation of optical images by x-rays. *Journal of the Optical Society of America (1917-1983)*, 38:766–+, Sept. 1948.

I. Kostyukov, A. Pukhov, and S. Kiselev. Phenomenological theory of laser-plasma interaction in "bubble" regime. *Physics of Plasmas*, 11(11):5256–5264, 2004. doi: 10.1063/1.1799371. URL `http://link.aip.org/link/?PHP/11/5256/1`.

I. Kostyukov, E. Nerush, A. Pukhov, and V. Seredov. Electron self-injection in multidimensional relativistic-plasma wake fields. *Phys. Rev. Lett.*, 103(17):175003, Oct 2009. doi: 10.1103/PhysRevLett.103.175003.

W. P. Leemans, B. Nagler, A. J. Gonsalves, C. Toth, K. Nakamura, C. G. R. Geddes, E. Esarey, C. B. Schroeder, and S. M. Hooker. Gev electron beams from a centimetre-scale accelerator. *Nat Phys*, 2(10):696–699, 10 2006. URL `http://dx.doi.org/10.1038/nphys418`.

W. Lu, C. Huang, M. Zhou, W. B. Mori, and T. Katsouleas. Nonlinear theory for relativistic plasma wakefields in the blowout regime. *Phys. Rev. Lett.*, 96(16):165002, Apr 2006. doi: 10.1103/PhysRevLett.96.165002.

W. Lu, M. Tzoufras, C. Joshi, F. S. Tsung, W. B. Mori, J. Vieira, R. A. Fonseca, and L. O. Silva. Generating multi-gev electron bunches using single stage laser wakefield acceleration in a 3d nonlinear regime. *Phys. Rev. ST Accel. Beams*, 10(6):061301, Jun 2007. doi: 10.1103/PhysRevSTAB.10.061301.

K. Makino and M. Berz. Cosy infinity version 8. *Nuclear Instruments and Methods in Physics Research Section A: Accelerators, Spectrometers, Detectors and Associated Equipment*, 427(1-2):338 – 343, 1999. ISSN 0168-9002. doi: DOI:10.1016/S0168-9002(98)01554-X. URL `http://www.sciencedirect.com/science/article/B6TJM-3YSY5S6-28/2/742610627b6b86b8540725018bac9f13`.

V. Malka, S. Fritzler, E. Lefebvre, M.-M. Aleonard, F. Burgy, J.-P. Chambaret, J.-F. Chemin, K. Krushelnick, G. Malka, S. P. D. Mangles, Z. Najmudin, M. Pittman, J.-P. Rousseau, J.-N. Scheurer, B. Walton, and A. E. Dangor. Electron Acceleration by a Wake Field Forced by an Intense Ultrashort Laser Pulse. *Science*, 298(5598):1596–1600, 2002. doi: 10.1126/science.1076782. URL `http://www.sciencemag.org/cgi/content/abstract/298/5598/1596`.

S. P. Mangles, S. Kneip, C. McGuffey, S. S. Bulanov, V. Chvykov, F. Dollar, Y. Horovitz, C. Huntington, G. Kalintchenko, A. Maksimchuk, T. Matsuoka, C. Palmer, K. T. Phuoc, P. Rousseau, V. Yanovsky, K. Krushelnick, and Z. Najmudin. Coherent betatron radiation from laser-wakefield accelerated bunches of monoenergetic electrons. In *Conference on Lasers and Electro-Optics/International Quantum Electronics Conference*, page JWD4. Optical Society of America, 2009. URL `http://www.opticsinfobase.org/abstract.cfm?URI=CLEO-2009-JWD4`.

S. P. D. Mangles, C. D. Murphy, Z. Najmudin, A. G. R. Thomas, J. L. Collier, A. E. Dangor, E. J. Divall, P. S. Foster, J. G. Gallacher, C. J. Hooker, D. A. Jaroszynski, A. J. Langley, W. B. Mori, P. A. Norreys, F. S. Tsung, R. Viskup, B. R. Walton, and K. Krushelnick. Monoenergetic beams of relativistic electrons from intense laser-plasma interactions. *Nature*, 431(7008):535–538, 09 2004. URL `http://dx.doi.org/10.1038/nature02939`.

S. P. D. Mangles, A. G. R. Thomas, O. Lundh, F. Lindau, M. C. Kaluza, A. Persson, C.-G. Wahlstrom, K. Krushelnick, and Z. Najmudin. On the stability of laser wakefield electron accelerators in the monoenergetic regime. *Physics of Plasmas*, 14(5):056702, 2007. doi: 10.1063/1.2436481. URL `http://link.aip.org/link/?PHP/14/056702/1`.

S. F. Martins, R. A. Fonseca, W. Lu, W. B. Mori, and L. O. Silva. Exploring laser-wakefield-accelerator regimes for near-term lasers using particle-in-cell simulation in lorentz-boosted frames. *Nat Phys*, 6(4):311–316, 04 2010. URL `http://dx.doi.org/10.1038/nphys1538`.

P. Michel, E. Esarey, C. B. Schroeder, B. A. Shadwick, and W. P. Leemans. Efficient electron injection into plasma waves using higher-order laser modes. *Physics of Plasmas*, 13(11):113112, 2006a. doi: 10.1063/1.2378627. URL `http://link.aip.org/link/?PHP/13/113112/1`.

P. Michel, C. B. Schroeder, B. A. Shadwick, E. Esarey, and W. P. Leemans. Radiative damping and electron beam dynamics in plasma-based accelerators. *Phys. Rev. E*, 74 (2):026501, Aug 2006b. doi: 10.1103/PhysRevE.74.026501.

A. Modena, Z. Najmudin, A. E. Dangor, C. E. Clayton, K. A. Marsh, C. Joshi, V. Malka, C. B. Darrow, C. Danson, D. Neely, and F. N. Walsh. Electron acceleration from the breaking of relativistic plasma waves. *Nature*, 377(6550):606–608, 10 1995. URL `http://dx.doi.org/10.1038/377606a0`.

P. Mora and T. M. Antonsen. Electron cavitation and acceleration in the wake of an ultraintense, self-focused laser pulse. *Phys. Rev. E*, 53(3):R2068–R2071, Mar 1996. doi: 10.1103/PhysRevE.53.R2068.

K. Nakajima, D. Fisher, T. Kawakubo, H. Nakanishi, A. Ogata, Y. Kato, Y. Kitagawa, R. Kodama, K. Mima, H. Shiraga, K. Suzuki, K. Yamakawa, T. Zhang, Y. Sakawa,

T. Shoji, Y. Nishida, N. Yugami, M. Downer, and T. Tajima. Observation of ultrahigh gradient electron acceleration by a self-modulated intense short laser pulse. *Phys. Rev. Lett.*, 74(22):4428–4431, May 1995. doi: 10.1103/PhysRevLett.74.4428.

H. Onuki and P. Elleaume, editors. *Undulators, Wigglers and their Applications*. Taylor & Francis, London, 2003.

J. Osterhoff. *Stable, ultra-relativistic electron beams by laser-wakefield acceleration*. PhD thesis, Ludwig-Maximilians Universität München, 2008b.

J. Osterhoff, A. Popp, Z. Major, B. Marx, T. P. Rowlands-Rees, M. Fuchs, M. Geissler, R. Horlein, B. Hidding, S. Becker, E. A. Peralta, U. Schramm, F. Gruner, D. Habs, F. Krausz, S. M. Hooker, and S. Karsch. Generation of stable, low-divergence electron beams by laser-wakefield acceleration in a steady-state-flow gas cell. *Physical Review Letters*, 101(8):085002, 2008. doi: 10.1103/PhysRevLett.101.085002. URL `http://link.aps.org/abstract/PRL/v101/e085002`.

W. K. H. Panofsky and W. A. Wenzel. Some considerations concerning the transverse deflection of charged particles in radio-frequency fields. *Review of Scientific Instruments*, 27(11):967–967, 1956. doi: 10.1063/1.1715427. URL `http://link.aip.org/link/?RSI/27/967/1`.

PI. Princton instruments pi-sx:400 data sheet.

P. Predehl, H. Kraus, H. W. Braeuninger, W. Burkert, G. Kettenring, and H. Lochbihler. Grating elements for the axaf low-energy transmission grating spectrometer. *EUV, X-Ray, and Gamma-Ray Instrumentation for Astronomy III*, 1743(1):475–481, 1992. doi: 10.1117/12.130706. URL `http://link.aip.org/link/?PSI/1743/475/1`.

A. Pukhov and J. Meyer-ter Vehn. Relativistic magnetic self-channeling of light in near-critical plasma: Three-dimensional particle-in-cell simulation. *Phys. Rev. Lett.*, 76 (21):3975–3978, May 1996. doi: 10.1103/PhysRevLett.76.3975.

A. Pukhov and J. Meyer-ter Vehn. Laser wake field acceleration: the highly non-linear broken-wave regime. *Applied Physics B: Lasers and Optics*, 74(4):355–361, 04 2002. URL `http://dx.doi.org/10.1007/s003400200795`.

A. Pukhov, Z.-M. Sheng, and J. M. ter Vehn. Particle acceleration in relativistic laser channels. *Physics of Plasmas*, 6(7):2847–2854, 1999. doi: 10.1063/1.873242. URL `http://link.aip.org/link/?PHP/6/2847/1`.

A. D. Rakić. Algorithm for the determination of intrinsic optical constants of metal films: application to aluminum. *Appl. Opt.*, 34(22):4755–4767, 1995. URL `http://ao.osa.org/abstract.cfm?URI=ao-34-22-4755`.

C. Rechatin, J. Faure, A. Ben-Ismail, J. Lim, R. Fitour, A. Specka, H. Videau, A. Tafzi, F. Burgy, and V. Malka. Controlling the phase-space volume of injected electrons in a laser-plasma accelerator. *Physical Review Letters*, 102(16):164801, 2009.

doi: 10.1103/PhysRevLett.102.164801. URL http://link.aps.org/abstract/PRL/v102/e164801.

S. Reiche. Genesis 1.3: a fully 3d time-dependent fel simulation code. *Nuclear Instruments and Methods in Physics Research Section A: Accelerators, Spectrometers, Detectors and Associated Equipment*, 429(1-3):243 – 248, 1999. ISSN 0168-9002. doi: DOI:10.1016/S0168-9002(99)00114-X. URL http://www.sciencedirect.com/science/article/B6TJM-3WTWX9N-4H/2/58eab03f04264a4e7ded393045fc226e.

J. B. Rosenzweig, B. Breizman, T. Katsouleas, and J. J. Su. Acceleration and focusing of electrons in two-dimensional nonlinear plasma wake fields. *Phys. Rev. A*, 44(10): R6189–R6192, Nov 1991. doi: 10.1103/PhysRevA.44.R6189.

R. D. Ruth, A. W. Chao, P. L. Morton, and P. B. Wilson. A plasma wake field accelerator. *Particle Accelerators*, 17:171–189, 1985.

B. E. A. Saleh and M. C. Teich. *Fundamentals of Photonics*. Wiley-Interscience, 1991.

H. P. Schlenvoigt, K. Haupt, A. Debus, F. Budde, O. Jackel, S. Pfotenhauer, H. Schwoerer, E. Rohwer, J. G. Gallacher, E. Brunetti, R. P. Shanks, S. M. Wiggins, and D. A. Jaroszynski. A compact synchrotron radiation source driven by a laser-plasma wakefield accelerator. *Nat Phys*, 4(2):130–133, 2008. URL http://dx.doi.org/10.1038/nphys811.

P. Schmüser, M. Dohlus, and J. Rossbach. *Ultraviolet and Soft X-Ray Free-Electron Lasers: Introduction to Physical Principles, Experimental Results, Technological Challenges*. Springer, Berlin, 2008.

C. B. Schroeder, E. Esarey, B. A. Shadwick, and W. P. Leemans. Trapping, dark current, and wave breaking in nonlinear plasma waves. *Physics of Plasmas*, 13(3):033103, 2006. doi: 10.1063/1.2173960. URL http://link.aip.org/link/?PHP/13/033103/1.

C. B. Schroeder, E. Esarey, C. G. R. Geddes, C. Tóth, and W. P. Leemans. Design considerations for a laser-plasma linear collider. In C. B. Schroeder, W. Leemans, & E. Esarey, editor, *American Institute of Physics Conference Series*, volume 1086 of *American Institute of Physics Conference Series*, pages 208–214, Jan. 2009. doi: 10.1063/1.3080906.

P. Sprangle, E. Esarey, and A. Ting. Nonlinear theory of intense laser-plasma interactions. *Phys. Rev. Lett.*, 64(17):2011–2014, Apr 1990. doi: 10.1103/PhysRevLett.64.2011.

P. Sprangle, E. Esarey, J. Krall, and G. Joyce. Propagation and guiding of intense laser pulses in plasmas. *Physical Review Letters*, 69(15), 10 1992. URL http://link.aps.org/doi/10.1103/PhysRevLett.69.2200.

P. Sprangle, B. Hafizi, J. R. Peñano, R. F. Hubbard, A. Ting, C. I. Moore, D. F. Gordon, A. Zigler, D. Kaganovich, and T. M. Antonsen. Wakefield generation and gev acceleration in tapered plasma channels. *Phys. Rev. E*, 63(5):056405, Apr 2001. doi: 10.1103/PhysRevE.63.056405.

D. Strickland and G. Mourou. Compression of amplified chirped optical pulses. *Optics Communications*, 55:447–449, Oct. 1985. doi: 10.1016/0030-4018(85)90151-8.

T. Tajima. High energy laser plasma accelerators. *Laser and Particle Beams*, 3(04):351–413, 1985. doi: 10.1017/S0263034600001117. URL `http://journals.cambridge.org/action/displayAbstract?fromPage=online&aid=4286884&fulltextType=RA&fileId=S0263034600001117`.

T. Tajima. Laser acceleration and its future. *Proceedings of the Japan Academy, Series B*, 86(3):147–157, 2010.

T. Tajima and J. M. Dawson. Laser electron accelerator. *Phys. Rev. Lett.*, 43(4):267–270, Jul 1979. doi: 10.1103/PhysRevLett.43.267.

T. Tanaka and H. Kitamura. *SPECTRA*: a synchrotron radiation calculation code. *Journal of Synchrotron Radiation*, 8(6):1221–1228, Nov 2001. doi: 10.1107/S090904950101425X. URL `http://dx.doi.org/10.1107/S090904950101425X`.

A. G. R. Thomas, S. P. D. Mangles, C. D. Murphy, A. E. Dangor, P. S. Foster, J. G. Gallacher, D. A. Jaroszynski, C. Kamperidis, K. Krushelnick, K. L. Lancaster, P. A. Norreys, R. Viskup, and Z. Najmudin. Ultrashort pulse filamentation and monoenergetic electron beam production in lwfas. *Plasma Physics and Controlled Fusion*, 51 (2):024010, 2009. URL `http://stacks.iop.org/0741-3335/51/i=2/a=024010`.

A. Ting, E. Esarey, and P. Sprangle. Nonlinear wake-field generation and relativistic focusing of intense laser pulses in plasmas. *Physics of Fluids B: Plasma Physics*, 2(6): 1390–1394, 1990. doi: 10.1063/1.859561. URL `http://link.aip.org/link/?PFB/2/1390/1`.

M. Tzoufras, W. Lu, F. S. Tsung, C. Huang, W. B. Mori, T. Katsouleas, J. Vieira, R. A. Fonseca, and L. O. Silva. Beam loading in the nonlinear regime of plasma-based acceleration. *Phys. Rev. Lett.*, 101(14):145002, Sep 2008. doi: 10.1103/PhysRevLett.101.145002.

J. van Tilborg, C. B. Schroeder, C. V. Filip, C. Tóth, C. G. R. Geddes, G. Fubiani, R. Huber, R. A. Kaindl, E. Esarey, and W. P. Leemans. Temporal characterization of femtosecond laser-plasma-accelerated electron bunches using terahertz radiation. *Phys. Rev. Lett.*, 96(1):014801, Jan 2006. doi: 10.1103/PhysRevLett.96.014801.

R. Weingartner, M. Fuchs, A. Popp, S. Raith, S. Becker, S. Chou, M. Heigoldt, K. Khrennikov, J. Wenz, B. Zeitler, Z. Major, J. Osterhoff, F. Krausz, S. Karsch, and F. Grüner. Imaging laser-wakefield-accelerated electrons using miniature magnetic quadrupole lenses. *to be published.*

C. Welnak, G. Chen, and F. Cerrina. Shadow: A synchrotron radiation and x-ray optics simulation tool. *Nuclear Instruments and Methods in Physics Research Section A: Accelerators, Spectrometers, Detectors and Associated Equipment*, 347(1-3):344 – 347, 1994. ISSN 0168-9002. doi: DOI:10.1016/0168-9002(94)91906-2. URL `http://www.sciencedirect.com/science/article/B6TJM-46XYDK0-29/2/64df4c2cf5a7b2686aff716dae4157cb`.

H. Wiedemann. *Synchrotron Radiation*. Springer, Berlin, 2002.

H. Wiedemann. *Particle Accelerator Physics*. Springer, 2007.

E. Wigner. On the quantum correction for thermodynamic equilibrium. *Phys. Rev.*, 40 (5):749–759, Jun 1932. doi: 10.1103/PhysRev.40.749.

K. Wille. *The physics of particle accelerators: an introduction*. Oxford University Press, 2000.

M. Xie. Exact and variational solutions of 3d eigenmodes in high gain fels. *Nuclear Instruments and Methods in Physics Research Section A: Accelerators, Spectrometers, Detectors and Associated Equipment*, 445(1-3):59 – 66, 2000. ISSN 0168-9002. doi: DOI:10.1016/S0168-9002(00)00114-5. URL `http://www.sciencedirect.com/science/article/B6TJM-4091HMX-F/2/5b09880fcfd1449cb5cebc0ca6da730e`.

C. ACKNOWLEDGEMENTS

The work that is presented in this thesis can clearly not be accomplished by a single person. I want to thank all my colleagues for their contribution and their help. I enjoyed working with my colleagues, most of whom even became good friends over the years. It is hard thank individual persons and I hope nobody feels forgotten, therefore I want to thank (not exclusively) the following persons:

- **Prof. Dr. Florian Grüner**
  Florian convinced me to change research fields and join the LMU/MPQ laser-wakefield "accelerators". It was a good decision! I am very thankful for the trust and his great confidence he put in me in all situations: be it in succeeding with experiments or in substituting for him to give important presentations. He guides his group with a low hierarchy, always listens to criticism and persistently improves his team management. Thank you for the supervision over the years, for being a constant source of motivation when things were going well but also (and more importantly) when the situation was rough. Thank you for being my "Doktor-vati".

- **Prof. Dr. Stefan Karsch**
  Stefan supported and encouraged me to start at the MPQ by arranging a position in the beginning and mediating me into Florian's group. Not only is he a true "maestro" in the lab throughout all disciplines from whom I could learn a lot, but he has a very intuitive view on physics which lets him instantly understand complex physics problems. He is also very talented in all sort of applied physics such as telescope building, boat manufacturing or the practical demonstration of the injection and acceleration by (water) waves (however, slightly out-of-phase).

- **Prof. Dr. Ferenc Krausz**
  I am very thankful that I had the opportunity to be a doctoral student in Ferenc' group. He motivates and orchestrates such a big team in a way to completely use everyone's skills which leads to very impressive results. Within his group, he manages to create a world-wide unique scientifically stimulating environment.

- **Prof. Dr. Toshiki Tajima**
  I am very honored that one of the inventors of the field of the laser-wakefield accelerators kindly agreed to be a reviewer of this thesis.

- **Prof. Dr. Dieter Habs**
  Dieter was my advisor before Florian became able to supervise PhD students. He

is an electrifying person who is enthusiastic about physics and a constant source of stimulating new ideas.

- **Antonia Popp and Raphael Weingartner**
  Only with their help, dedication and countless hours in the lab it was it possible to achieve these results. I am highly in debt for their contributions to this work. Both were a constant source of motivation when things weren't going as well. Besides the amazing work in the lab Antonia is the "good soul" of all MPQ students, always putting a lot of effort in organizing social events. Raphael is fun to hang out with, play sports or go to rock concerts. Both have become very good friends.

- **Dr. Zsuzsi Major and Dr. Jens Osterhoff**
  Zsuzsi and Jens also put countless hours into these experiments and through their vast knowledge in lasers and laser-wakefield acceleration made invaluable contributions and taught me a lot. Jens was always a sure bet if I was in dire needs for a beer. Luckily I could pay him back his accommodation debts during my visits in Berkeley.

- **Dr. Stefan Becker**
  Stefan helped us a lot by adjusting the magnetic lenses and the undulator. Owing to his tremendous coffee consumption, he is always good for a short break and a long chat.

- **Michael Hofstetter**
  With Michael I enjoyed lots of fun discussions about physics and all other situations in life. He helps me to still dream of becoming rich by founding a parabola-company based on revolutionary new inventions.

- **FEL team**
  I want to thank the whole FEL crew for all the help and useful discussions. Especially Thorben Seggebrock, Benno Zeitler and Timon Mehrling (although not directly in the FEL team) I want to thank for their help with some figures in this thesis.

- **Andreas Maier**
  AC/DC rules!

- **All "Scientists from downstairs"**
  I want to thank all scientists from downstairs for their help when we needed a hand, for letting us borrow tools or giving good advice when we needed it.

- **Dr. Adrian Cavalieri, Dr. Ralph Ernstorfer, Markus Fiess, Dr. Ernst Fill, Dr. George Tsakiris**
  I am very thankful for important and necessary lab equipment that we could borrow.

- **The International Max-Planck Research School (IMPRS)**
  I want to thank all IMPRS coordinates, students and particularly Frau Wild for providing an excellent platform for activities outside of physics. Especially for the organization of block lectures, summer schools and all the fun social events.

- **Container Coffee Crew**
  I want to thank the CCC for all the interesting and fun discussion about physics and life during our after-lunch coffee breaks.

- **LMU and MPQ Workshop**
  Stellvertretend für die Belegschaft der LMU- und der MPQ- Werkstätten möchte ich mich recht herzlich bei Herrn Rolf Oehm und Herrn Thomas Strobl bedanken. Ohne die kompetente und schnelle Bearbeitung unserer teilweise eher kurzfristigen Anfragen wäre ein Erfolg bei diesem Experiment nicht möglich gewesen.

- **Herr Haas, Herr Fischer, Herr Fölsner** und **Herr Böswald**
  Für die Unterstützung in jeglicher Hinsicht möchte mich recht herzlich bedanken.

- **Frau Monika Wild**
  Frau Wild is an incredible support in any administrative matter. When I was in doubt which group to join at the MPQ, Frau Wild made her point pretty CLEAR. Thank you for this advice. She is also an infinite source of unbelievably good stories and a dedicated supporter against the extinction of all-capital-letter emails.

- **Dr. Carl Schroeder and Dr. Carlo Benedetti**
  Carl and Carlo were a big help in getting LWFA theory straight but in exchange, they forced me to include them in the acknowledgements. Trotzdem vielen Dank für die Diskussionen!

- all **my friends** who supported me not only through the years of being a graduate student but through all the ups and downs of my whole life

- **Emelie**
  Although we had to suffer from a distance of almost 6,000 miles, you were always there for me. Your love and humor always helped, and always will help me to go on and regain my strength.

- My parents **Ursula and Josef**
  Von ganzem Herzen möchte ich meinen Eltern danken. Sie haben mich während meines gesamten Lebens bei meinen Entscheidungen nach allen Kräften unterstützt und haben mir alle nur erdenklichen Möglichkeiten zu meiner freien Entfaltung geboten.

This thesis is dedicated to my dear friend Matthias Baar, who left this world long before his time.

D. Curriculum Vitae

Contact Information

Name	Matthias Fuchs
Address	Theresienstrassse 122
	80333 München
	Germany
email	matfuchs (at) gmx.de

Personal Data

Date and place of birth	August 06, 1980 in Ellwangen/Jagst, Germany
Citizenship	German
Gender	male

Education

since 08/2006 **Ludwig-Maximilians-Universität München and**
Max-Planck Institut für Quantenoptik, Germany
Ph.D Student (physics)
in the framework of the International Max-Planck Research School
for Advanced Photon Science (IMPRS-APS)
Subject: Laser-driven Undulator Source
Research advisor: Prof. Florian Grüner
in the group of Prof. Ferenc Krausz

09/04 – 06/06 **University of Oregon, Eugene, OR, USA**
Physics Department
Graduate Student
Master of Science 06/2006
Thesis topic: Development of a High-Power Stabilized Diode-Laser System
Research advisor: Prof. Daniel Steck

10/01 – 09/04 **University of Stuttgart, Germany**
Physics Department
Vordiplom 10/2003

06/2000 **Abitur**, Peutinger Gymnasium, Ellwangen, Germany

Awards and Honors

- Scholar of the International Max-Planck Research School (since 08/06)
- Scholar of the Baden-Württemberg Program (09/04- 07/05)
- Award of the German Physical Society (DPG) for an outstanding high school diploma in physics (06/00)

Invited Talks

- **FEL 2010**
  Malmö, Sweden, 23. - 27.08.2010
- **High brightness electron beams workshop (HBEB)**
  Maui, HI, USA, 16.-19.11.2009
- **DELTA Seminar**
  Dortmund, Germany, 11.09.2009
- **John Adams Institute Lecture series**
  Oxford, U.K., 30.07.2009
- **MLL Kolloquium für Kern-, Teilchen- und Beschleunigerphysik**
  Munich, Germany, 23.07.2009
- **SPIE Symposium on Optics and Optoelectronics 2009**
  Prague, Czech Republik, 20. 23.04.2009
- **DPG Frühjahrstagung**
  Darmstadt, Germany, 10.-14.03.2008

Teaching Experience

- **Terascale Accelerator School 2009**
  Dortmund, Germany, 11.09.2009
  Subject: Advanced Accelerator Concepts

Professional Services

- **Referee for:**
  Contributions to Plasma Physics
- **Mentor for:**
  Diploma student Benno Zeitler

- **Mentor for:**
  the Deutsche Akademischer Austauschdienst (DAAD) RISE exchange program for undergraduate students of the US and UK. Summer 2008, Summer 2009

Professional Affiliations

- Member of: the Deutsche Physikalische Gesellschaft (DPG, German Physical Society)

Activities and Leisure

- **Unterwegs gegen Krebs e.V.**
  Co-founder and vice president of the club Unterwegs gegen Krebs, which is devoted to fight cancer, especially leukemia, by fund-raising and by calling attention to cancer and leukemia in public and the necessity to register in bone marrow donor databases.

- **Leisure**
  Sports (soccer, volleyball (both as a player and as a coach), tennis, basketball), travelling, hiking, playing the guitar, reading.

Publications

Journal Articles

- **Laser-driven soft-X-ray undulator source**
  M. Fuchs, R. Weingartner, A. Popp, Zs. Major, S. Becker, J. Osterhoff, I. Cortrie, R. Hörlein, G. D. Tsakiris, U. Schramm, T. P. Rowlands-Rees, S. M. Hooker, D. Habs, F. Krausz, S. Karsch and F. Grüner
  Nature Physics **5**, 826-829 (2009)

- **First milestone on the path toward a table-top free-electron laser**
  M. Fuchs, R. Weingartner, A. Popp, Zs. Major, S. Becker, J. Osterhoff, R. Hörlein, G. D. Tsakiris, U. Schramm, T. P. Rowlands-Rees, S. M. Hooker, D. Habs, F. Krausz, S. Karsch and F. Grüner
  LEI 2009. AIP Conference Proceedings, **1228**, 295-299 (2010)

- **Imaging laser-wakefield-accelerated electrons using miniature magnetic quadrupole lenses**
  R. Weingartner, **M. Fuchs**, A. Popp, S. Raith, S. Becker, B. Zeitler, S. Chou, M. Heigoldt, K. Khrennikov, J. Wenz, Zs. Major, J. Osterhoff, F. Krausz, S. Karsch and F. Grüner
  in preparation

- **Characterization and tuning of ultra-high gradient permanent magnet quadrupoles**
  S. Becker, M. Bussmann, S. Raith, **M. Fuchs**, R. Weingartner, P. Kunz, W. Lauth, S. Schramm, M. El Ghazaly, F. Grüner, H. Backe and D. Habs
  Phys. Rev. ST Accel. Beams **12**, 102801 (2009)

- **All-optical steering of laser-wakefield-accelerated electron beams**
  A. Popp, J. Osterhoff, Zs. Major, R. Hörlein, **M. Fuchs**, R. Weingartner, T. P. Rowlands-Rees, J. Vieira, M. Marti, R. A. Fonseca, L. O. Silva, S. M. Hooker, F. Grüner, F. Krausz, and S. Karsch
  submitted

- **Generation of stable, low-divergence electron beams by laser-wakefield acceleration in a steady-state-flow gas cell**
  J. Osterhoff, A. Popp, Zs. Major, B. Marx, T. P. Rowlands-Rees, **M. Fuchs**, M. Geissler,R. Hörlein, B. Hidding, S. Becker, E. A. Peralta, U. Schramm, F. Grüner,D. Habs,F. Krausz,S. M. Hooker, and S. Karsch
  Phys. Rev. Lett. **101**, 085002 (2008)

- **GeV-scale electron acceleration in a gas-filled capillary discharge waveguide**
  S. Karsch, J. Osterhoff, A. Popp, T. P. Rowlands-Rees, Zs. Major, **M. Fuchs**, B. Marx, R. Hrlein, K. Schmid, L. Veisz, S. Becker, U. Schramm, B. Hidding, G. Pretzler, D. Habs, F. Grüner, F. Krausz, S. M. Hooker
  New Journal of Physics **9**, 415 (2007)

- **Miniature magnetic devices for laser-based, table-top free-electron lasers**
  T. Eichner, F. Grüner, S. Becker, **M. Fuchs**, D. Habs, R. Weingartner, U. Schramm, H. Backe, P. Kunz, and W. Lauth
  Phys. Rev. ST Accel. Beams **10**, 082401 (2007)

- **Design considerations for table-top, laser-based VUV and X-ray free electron lasers**
  F. Grüner, S. Becker, U. Schramm, T. Eichner, **M. Fuchs**, R. Weingartner, D. Habs, J. Meyer-ter-Vehn, M. Geissler, M. Ferrario, L. Serafini, B. van der Geer, H. Backe, W. Lauth, S. Reiche
  Applied Physics B **86**, 431-435 (2007)

Popular-Science Articles

- **Röntgenstrahlung mit einem Laserplasma Beschleuniger** (in German)
  M.Fuchs & F.Grüner
  Physik in unserer Zeit **41**, 11-12 (2010).